

**As-Grown Gallium Nitride Nanowire Electromechanical  
Resonators**

by

**Joshua R. Montague**

B.A., Colby College, 2006

M.S., University of Colorado, 2010

A thesis submitted to the  
Faculty of the Graduate School of the  
University of Colorado in partial fulfillment  
of the requirements for the degree of  
Doctor of Philosophy  
Department of Physics

2013

This thesis entitled:  
As-Grown Gallium Nitride Nanowire Electromechanical Resonators  
written by Joshua R. Montague  
has been approved for the Department of Physics

---

Charles Rogers and Victor M. Bright

---

Date \_\_\_\_\_

The final copy of this thesis has been examined by the signatories, and we find that both the content and the form meet acceptable presentation standards of scholarly work in the above mentioned discipline.

Montague, Joshua R. (Ph.D., Physics)

As-Grown Gallium Nitride Nanowire Electromechanical Resonators

Thesis directed by Profs Charles Rogers and Victor M. Bright

Technological development in recent years has led to a ubiquity of micro- and nano-scale electromechanical devices. Sensors for monitoring temperature, pressure, mass, etc., are now found in nearly all electronic devices at both the industrial and consumer levels. As has been true for integrated circuit electronics, these electromechanical devices have continued to be scaled down in size. For many nanometer-scale structures with large surface-to-volume ratio, dissipation (energy loss) becomes prohibitively large causing a decreasing sensitivity with decreasing sensor size.

In this work, gallium nitride (GaN) nanowires are investigated as singly-clamped (cantilever) mechanical resonators with typical mechanical quality factors,  $Q$  (equal to the ratio of resonance frequency to peak full-width-at-half-maximum-power) and resonance frequencies, respectively, at or above 30,000, and near 1 MHz. These  $Q$  values –in vacuum at room temperature– indicate very low levels of dissipation; they are essentially the same as those for bulk quartz crystal resonators that form the basis of simple clocks and mass sensors. The GaN nanowires have lengths and diameters, respectively, of approximately 15 micrometers and hundreds of nanometers. As-grown GaN nanowire  $Q$  values are larger than other similarly-sized, bottom-up, cantilever resonators and this property makes them very attractive for use as resonant sensors.

We demonstrate the capability of detecting sub-monolayer levels of atomic layer deposited (ALD) films, and the robust nature of the GaN nanowires structure that allows for their ‘reuse after removal of such layers. In addition to electron microscope-based measurement techniques, we demonstrate the successful capacitive detection of a single nanowire using microwave homodyne reflectometry. This technique is then extended to allow for simultaneous measurements of large ensembles of GaN nanowires on a single sample, providing statistical information about the distribution of individual nanowire properties. We observe nanowire-to-nanowire variations in the

temperature dependence of GaN nanowire resonance frequency and in the observed mechanical dissipation. We also use this ensemble measurement technique to demonstrate unique, very low-loss resonance behavior at low temperatures. The low dissipation (and corresponding large  $Q$  values) observed in as-grown GaN nanowires also provides a unique opportunity for studying fundamental energy loss mechanisms in nano-scale objects. With estimated mass sensitivities on the level of zeptograms ( $10^{-21}$  g) in a one second averaging time, GaN nanowires may be a significant addition to the field of resonant sensors and worthy of future research and device integration.

## Dedication

To my mother and father; your endless support has always empowered me to go after the next great thing, one bite at a time.

And to Sarah; your companionship provided me the stability to weather this long and sometimes arduous journey.

## Acknowledgements

The number of people who contributed in one way or another to the creation of this document is astounding. First and foremost, the past and present members of the Rogers and Bright groups; throughout the years, nearly everyone provided some amount of help and discussion, but next-level appreciation is due to Jason Gray, Long He, Brayden Hass, Joe Brown, Brad Davidson, Matt Brubaker, Harris Hall, Joel Weber, Keith Cobry, Wendy Altman, Chris Oshman, and Alicia Baca. The technical support of Sid Gustafson and Charlie Bowen got me through many a machining process. David Alchenberger's vast experience was priceless, and his willingness to use equipment in new, novel (and most-likely not recommended) ways enabled many of these projects to happen. The JILA machine and electronics shop employees provided many insights from their collective experiences. Eric Erdos kept the cryogenic liquids flowing and provided help for many of the construction-related and facilities-management aspects of this work. Extensive time, resources, and helpful conversations came from collaborating with Konrad Lehnert and some of his current and former students: Scott Hoch, Jen Harlow, and John Teufel. Many helpful conversations came from Kyle McElroy and his students Jixia Dai and Eduardo Calleja. Thanks for support from Y.C. Lee and the staff of the Department of Mechanical Engineering. None of this work would have been possible without the help and friendly collaboration of our NIST partners, Kris Bertness and Norm Sanford in particular. And, finally, thank you to Charles Rogers and Victor Bright for providing the guidance, knowledge, and trust needed to work through all of this together.

# Contents

## Chapter

<b>1</b>	Introduction	1
1.1	MEMS, NEMS, And Nanowires . . . . .	1
1.2	High- $Q$ Resonators . . . . .	2
1.3	Bottom-Up Cantilever Resonators . . . . .	4
1.4	$c$ -Axis Gallium Nitride Nanowires . . . . .	5
1.5	Measurement Readout Techniques . . . . .	11
<b>2</b>	From Simple Harmonic Oscillators To Nanowire Resonators	13
2.1	Resonator Eigenfrequencies And Modeshapes . . . . .	13
2.1.1	Zener's Model Of An Anelastic Solid . . . . .	16
2.2	Resonator Lineshapes . . . . .	19
2.2.1	Two-phase Lineshape . . . . .	19
2.2.2	Power Spectral Density Lineshapes . . . . .	22
2.3	Approximate Limits On $Q$ : Damping Mechanisms . . . . .	23
2.3.1	Gas Damping . . . . .	24
2.3.2	Anchor Loss . . . . .	25
2.3.3	Thermoelastic Loss . . . . .	26
2.3.4	Surface Loss . . . . .	27

<b>3</b>	<b>Scanning Electron Microscope-Based Measurements</b>	<b>29</b>
3.1	Origins . . . . .	29
3.2	SEM-Based Measurement Setup . . . . .	30
3.3	SEM-Based Measurement Techniques . . . . .	33
3.3.1	Power Spectral Density Measurement . . . . .	34
3.3.2	Phase-Sensitive Lock-In Measurement . . . . .	39
3.4	First Nanowire Ensemble Measurement . . . . .	42
3.5	Understanding SEM Results Through Finite Element Modeling . . . . .	42
3.5.1	Lifting Mode Degeneracy . . . . .	42
3.5.2	Nanowire Taper . . . . .	44
3.6	Effects Of Atomic Layer Deposition On Resonators . . . . .	45
3.6.1	Conformal Alumina ALD Films . . . . .	48
3.6.2	Conformal Metallic ALD Films . . . . .	55
3.6.3	Discontinuous Metallic ALD Films . . . . .	56
3.7	Transitioning From SEM- to Capacitance-Based Measurements . . . . .	58
3.7.1	Microwave Stripline Electrostatic Actuation . . . . .	60
<b>4</b>	<b>Capacitive Measurements: Theory &amp; Single-Nanowire Results</b>	<b>65</b>
4.1	Resonant Microwave Circuit Theory . . . . .	65
4.1.1	Ideal LC Tank Circuit . . . . .	66
4.1.2	Lossy LC Tank Circuit . . . . .	66
4.1.3	Microwave Network Analysis . . . . .	67
4.1.4	Detecting Nanowire Motion As A Variable Capacitance . . . . .	71
4.2	Capacitive Single-Nanowire Detection . . . . .	72
4.2.1	Connecting Physical Deflection And Measured Signal . . . . .	75
4.2.2	GaN Nanowire Mechanical Dissipation By Gas Damping . . . . .	78

<b>5</b>	Capacitive Measurements: Ensemble Extension	80
5.1	Microwave System Iteration . . . . .	80
5.1.1	Fabrication With Microwave Laminates . . . . .	81
5.1.2	Key Electrical Circuit Features And Components . . . . .	87
5.1.3	Resurrecting A $^4\text{He}$ Cryostat . . . . .	92
5.2	Capacitive Detection Of Nanowire Ensembles . . . . .	96
5.2.1	Quick Inspection: Pressure Dependence . . . . .	101
5.2.2	Resonance Parameter Distributions . . . . .	102
5.2.3	Temperature Measurements: Setup . . . . .	111
5.2.4	Temperature Measurements: Results . . . . .	115
5.2.5	Analysis Process . . . . .	122
5.3	Conclusions . . . . .	123
<b>6</b>	Future Work & Applications	126
6.1	Extensions Of This Work . . . . .	126
6.2	New Directions And Experiments . . . . .	134
	<b>Bibliography</b>	138
	<b>Appendix</b>	
<b>A</b>	Research Contributions	148
A.1	Peer-Reviewed Publications . . . . .	148
A.2	Presentations And Conference Proceedings . . . . .	148
<b>B</b>	Calculation Of Hexagonal Beam $I_y$	150
<b>C</b>	ANSYS Finite Element Models	153
C.1	File #1 . . . . .	153

C.2 File #2 . . . . .	156
<b>D</b> Atomic Force Microscope Scan of ALD Ruthenium	161
<b>E</b> Microwave Circuit Lithography Masks	162
<b>F</b> SolidWorks Sample Holder Model	163
<b>G</b> OriginPro Data, Scripts, And Fitting Functions	165
G.1 OriginPro Data Files . . . . .	165
G.2 OriginPro Scripts . . . . .	166
G.2.1 Independent Variable: Time . . . . .	167
G.2.2 Independent Variable: Frequency . . . . .	167
G.3 OriginPro Fitting Functions . . . . .	168
<b>H</b> LabView Tools	169
<b>I</b> Additional Ensemble Data	173

## Tables

### Table

2.1	Dissipation Calculation Parameters . . . . .	24
3.1	Results From Metallic ALD Coatings . . . . .	55

## Figures

### Figure

1.1	Resonator Quality Factor Vs. Size . . . . .	3
1.2	ZnO Nanowire Resonator . . . . .	5
1.3	SiC Nanowire Resonator . . . . .	6
1.4	a-Axis GaN Nanowire Resonator I . . . . .	7
1.5	a-Axis GaN Nanowire Resonator II . . . . .	8
1.6	c-Axis Gallium Nitride Nanowires . . . . .	9
1.7	GaN Nanowire Wurtzite Crystal Structure . . . . .	10
1.8	GaN Nanowire Crystal Planes . . . . .	11
2.1	Flexure Of A Prismatic Cantilever . . . . .	14
2.2	Allowed Frequencies For Singly-Clamped Beam . . . . .	15
2.3	First Four Cantilever Resonance Modeshapes . . . . .	17
2.4	Lorentzian Function: In-phase & Quadrature . . . . .	20
2.5	Lorentzian Function: Amplitude & Phase . . . . .	20
2.6	Phase Rotation of Lorentzian Response . . . . .	21
2.7	Squared Lorentzian . . . . .	22
2.8	Squared Lorentzian With Correlated Background . . . . .	23
3.1	Sample Holder For Early SEM-based Measurements . . . . .	31
3.2	SEM-based Measurement Schematic . . . . .	32

3.3	Identifying Nanowire Resonance Frequencies In A PSD . . . . .	35
3.4	Visually Verifying Nanowire Resonance Frequencies In An SEM . . . . .	36
3.5	Heterodyned PSD Resonance Measurements . . . . .	38
3.6	Two-Phase Lock-in Resonance Measurement . . . . .	40
3.7	Hysteretic Lock-in Resonance Measurement . . . . .	41
3.8	SEM-Based Nanowire Ensemble Measurement . . . . .	43
3.9	Example ANSYS Modal Analysis . . . . .	44
3.10	SEM Image Of Nanowire Taper . . . . .	46
3.11	Nanowire Resonance Frequency As Function Of Taper . . . . .	47
3.12	Predicted Resonance Frequency Shifts As A Function Of ALD Layer Thickness . . . . .	48
3.13	Peak Broadening And Resonance Frequency Shift Due To ALD Film . . . . .	49
3.14	ALD Alumina Peak Shifting . . . . .	50
3.15	Resonance Frequency As A Function of ALD Alumina Thickness . . . . .	51
3.16	GaN Nanowire Substrate Matrix Filling . . . . .	52
3.17	Resonance Frequency Shifts Per nm ALD Alumina . . . . .	53
3.18	Quality Factor As A Function Of ALD Thickness . . . . .	54
3.19	Nanowire Retrieval Process For Multiple SEM-Based Measurements . . . . .	59
3.20	Nanowire Retrieval Process For Multiple SEM-Based Measurements . . . . .	60
3.21	Electrostatic Actuation Of An As-Grown GaN Nanowire . . . . .	64
4.1	Capacitively Coupled Ideal Tank Circuit . . . . .	66
4.2	Capacitively Coupled Lossy LC Tank Circuit . . . . .	68
4.3	Calculated And Measured $S_{11}$ Smith Chart And Log-Magnitude . . . . .	70
4.4	Mixer I And Q Output Signals As Functions Of Frequency . . . . .	73
4.5	Capacitive Detection Single GaN Nanowire . . . . .	74
4.6	Capacitively Measured Two-Phase Resonance Data . . . . .	76

4.7	Calibrating Capacitive Measurement Amplitude With SEM-Measured Nanowire Deflections . . . . .	77
4.8	Gas Damping Of A GaN Nanowire Resonator . . . . .	78
5.1	An Early Microwave Laminate-Based LC Resonant Circuit . . . . .	82
5.2	Coplanar Common Sensing Electrode . . . . .	84
5.3	Example Transparency Etch Mask . . . . .	85
5.4	Cu Sample Holder With CSE . . . . .	90
5.5	Cryostat With Insert And Sample Chamber . . . . .	93
5.6	Cryostat Sample Ring And Components . . . . .	95
5.7	Schematic Of Full Capacitive Experiment . . . . .	97
5.8	SEM Images Of CSE-Nanowire Interface . . . . .	98
5.9	PSD With Ensemble Nanowire Observation . . . . .	99
5.10	Thermally Calibrated GaN Nanowire Resonance Peak . . . . .	101
5.11	Nanowire Resonator Gas Damping Crossover . . . . .	103
5.12	Ensemble Histogram Of Resonance Frequencies . . . . .	104
5.13	Ensemble Histogram Of Resonance Linewidths . . . . .	106
5.14	Ensemble Histogram Of Resonance $Q$ Factors . . . . .	107
5.15	Ensemble Histogram Of Calculated Loss Moduli . . . . .	109
5.16	Scatterplot And Histograms Of Ensemble Resonance Parameters . . . . .	110
5.17	Venting During LHe Transfer . . . . .	114
5.18	Temperature Dependent Ensemble Resonance Frequencies . . . . .	116
5.19	Temperature Dependent Ensemble Dissipation, $Q^{-1}$ . . . . .	118
5.20	Temperature Dependent Ensemble Dissipation, $Q^{-1}$ (Additional Data) . . . . .	119
5.21	Correlation Between Peak $Q^{-1}$ And Relative Frequency Shift . . . . .	120
5.22	Temperature Dependent PZT Structure . . . . .	121
6.1	Sacrificial Photoresist Base Layer . . . . .	129

6.2	Individual Nanowire Electrodes Via ALD . . . . .	130
6.3	MUMPs Design . . . . .	135
B.1	Calculations of $I_y$ . . . . .	151
D.1	Capacitively Coupled Lossy LC Tank Circuit . . . . .	161
E.1	Microwave Laminate Lithography Mask . . . . .	162
F.1	Cu Sample Holder SolidWorks Model II . . . . .	163
F.2	Cu Sample Holder SolidWorks Model I . . . . .	164
I.1	Additional Ensemble Frequency Data . . . . .	173
I.2	Additional Ensemble $Q$ Data . . . . .	174

# Chapter 1

## Introduction

Technological advancements of the late 20th and early 21st centuries have led to ubiquitous use of microelectromechanical systems (MEMS). Virtually everything we interact with, from desktop to hand-held electronics, automobiles, rooms and buildings, all have an array of processors and sensors (to monitor temperature, pressure, mass, inertia, orientation, etc.) built on MEMS technology. As MEMS technology has become more advanced and established, the length scales on which these devices are fabricated continues to decrease.

The industry is currently very adept at bulk- and surface-micromachining intricate structures on the micrometer scale (i.e. depositing and etching material onto and away from substrates). As this push continues into the sub-micron realm of nanoelectromechanical systems (NEMS), there is a growing need for patterning technology that can improve upon the existing, high-resolution standards of current optical- and electron-beam technologies. A complimentary approach to this kind of ‘top-down’ fabrication (e.g. lithography) has arisen in the form of ‘bottom-up’ fabrication (e.g. growth). It is in this sector –using grown, single-crystal structures– that the work presented here is found.

### 1.1 MEMS, NEMS, And Nanowires

Often the decision to fabricate via top-down, or bottom-up processes results from choices of both cost and processing capabilities. These structures can be made of many combinations of materials including (but not limited to): silicon (Si) [1–9], silicon carbide (SiC) [10], silicon nitride

(Si<sub>3</sub>N<sub>4</sub>) [11,12], aluminum nitride [13], nanocrystalline diamond [14–17], and also — as in this work — gallium nitride (GaN) [18–24]. Each choice of structural material (or combination of materials) results in unique material properties, and performance benefits or detriments. For some examples of the performance of various M/NEMS structures of varying material choice, see Refs [25,26] and for an example of the multitude of materials that can be micromachined, see Ref [27].

While these nanoscale structures can take many geometries, in this work we are particularly interested in nanowires — cantilever-like structures with very large aspect ratios and fixed at one end, illustrated schematically in Figure 2.1. Research into the utility of nanowires is growing rapidly and previous studies have shown them to have use in optical applications as light-emitting and laser diode structures [28–34], in electronic applications as selective filters for signal processing [35] and field effect transistors (FETs) [36–39], and, particularly relevant to this work, in mechanical applications as resonant sensors [6, 8, 10, 40, 41].

## 1.2 High- $Q$ Resonators

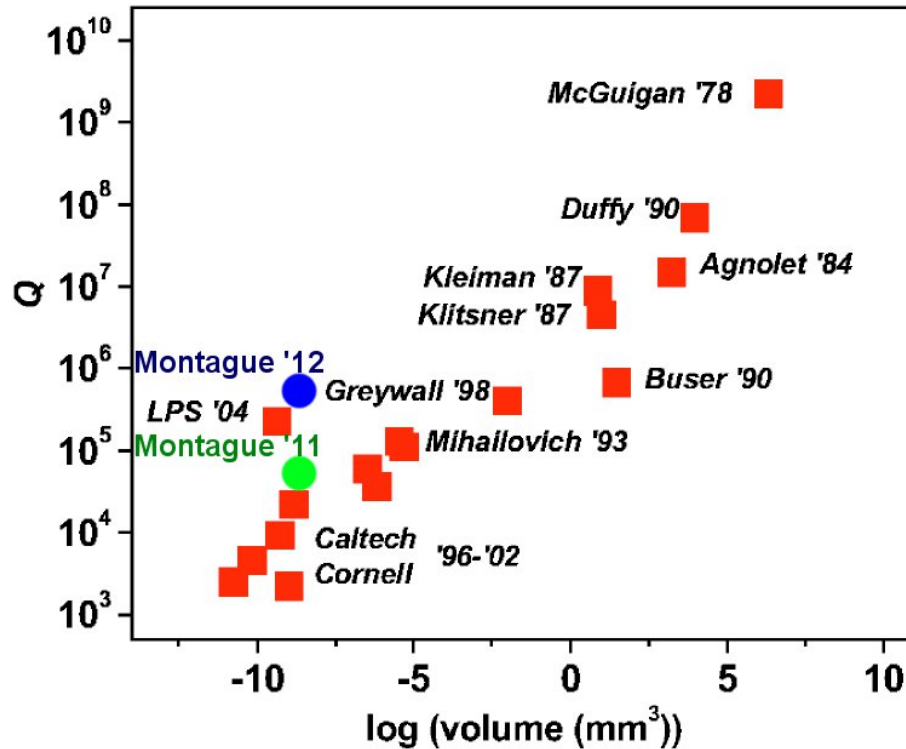
In using NEMS resonators for any of the applications mentioned above, nearly all pursuits are focused on attaining resonators with as little energy loss as possible. Such a low-loss resonator is one with large quality factor,  $Q$  (defined as the ratio of central resonance frequency to resonance peak full-width-at-half-maximum,  $Q = \omega_o/\Gamma$ ). As a result,  $Q^{-1}$  is a common parameter with which to discuss dissipation within resonator devices. As early as the 1990s, having large  $Q$  in a high-frequency communication system was understood to lead directly to lower insertion loss [35]. It is this parameter that sets the characteristic power level required for operation, determines the natural linewidth of the spectral peak, and ultimately limits the sensitivity for any practical detection scheme. External to the resonator itself, the main sources of dissipation are clamping or anchor losses. There are also dissipation mechanisms internal to the resonator: fundamental losses due to thermoelastic damping (caused by nonequilibrium interactions between thermal phonons and strain fields), losses due to internal defects and those on the resonator surfaces, electron-phonon and phonon-phonon coupling, and also air damping. These mechanisms and their manifestation

in this work will be discussed further in Chapter 2, but we can point out that each individual  $Q_i$  contributes to the overall resonator  $Q$  as

$$\frac{1}{Q} = \sum_i \frac{1}{Q_i}. \quad (1.1)$$

In their comprehensive review paper [42], Ekin and Roukes explicitly plot out the quite consistent downward trend in measured  $Q$  factors with decreasing resonator volume, suggesting a strong relationship between dissipation and e.g. surface-to-volume ratio. Figure 1.1 is adapted from that source, with the addition of two points resulting from major experiments included in this work. It is important to note that the resonators represented there cover a range of geometries and materials. It is also important to point out that resonator  $Q$  can be increased without reducing

Figure 1.1: Reported values of quality factor  $Q$  measured from mechanical resonators with sizes spanning many orders of magnitude. It is seen that  $Q$  scales down with decreasing resonator volume. The added green and blue circles represent typical values for, respectively, the room-temperature and low-temperature results reported in this work. Both are roughly above the linear fit one might add to the pre-existing data, sampled from a wide range of geometries and temperatures (mK to room temperature). Adapted from [42].



intrinsic energy loss, by the addition of tension. In this work, we specifically study resonators with no intrinsic stress or tension; the high  $Q$  of these resonators is due to low intrinsic energy loss.

### 1.3 Bottom-Up Cantilever Resonators

Once we have narrowed our scope of interest to bottom-up (i.e. grown) cantilever resonators, we find that the field is, surprisingly, quite limited. Much more effort is currently being exerted in the realm of micromachined, top-down systems. Moreover, the reported values of  $Q$  in such bottom-up structures tends to be lower than that of micromachined structures. However, the high crystalline quality of grown structures has kept them an active area of research. It is also important to note that much of the work on bottom-up structures (like that described below) involves removing the structure from its substrate and affixing it to another device (e.g. a macro-scale electrode tip). To help put this work in context, it is valuable to mention a few examples of bottom-up cantilever resonators in a similar parameter space to the GaN nanowires studied here.

In a 2006 article, Huang et al. [43] reported work on zinc oxide (ZnO) nanowire resonators with lengths and diameters, respectively, near 10  $\mu\text{m}$  and 100 nm, and with fundamental resonance frequencies in the range 100-500 kHz. With somewhat low data resolution, these resonators — an example is shown in Figure 1.2 — show  $Q$  near 500 at room temperature.

Previous results from Perisanu et al. [44] on silicon carbide (SiC) nanowires (shown in Figure 1.3) with lengths near 200  $\mu\text{m}$  and diameters near 100 nm show fundamental resonance frequencies near 10 kHz and  $Q$  near 40,000 at room temperature, reaching 150,000 after extreme high-temperature annealing. These structures reside somewhere between the bottom-up and top-down fabrication classes – the monocrystalline SiC nanowires are coated with nanometer-thick amorphous carbon layers.

Finally, work on GaN nanowires grown in a different crystallographic orientation (a-axis, versus the c-axis, studied here) has been carried out by both Nam et al. [45] and Henry et al. [22]. Examples of these as-grown resonators are shown in Figures 1.4 and 1.5. Both of these results were carried out on nanowires approximately 5  $\mu\text{m}$  in length and 50 nm in diameter, and both

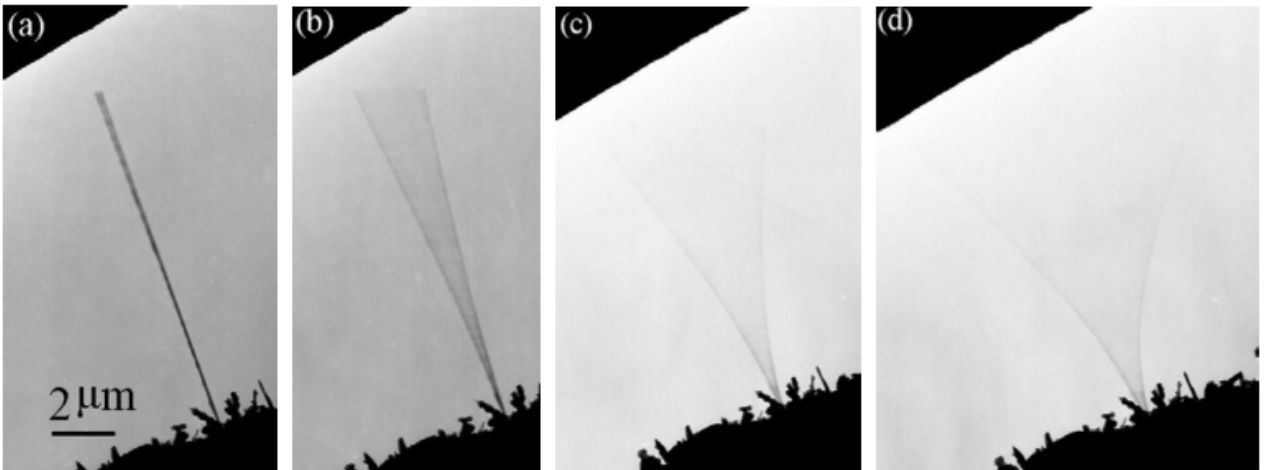
measured  $Q$  in the range of about 500-2000. Both of these studies were also on nanowires grown via the vapor-liquid-solid (VLS) mechanism [46], which is different from the catalyst-free nanowires studied in this work and described in further detail in Section 1.4.

In the realm of bottom-up nanowire resonators, it appears that typical structures have  $Q$  of order 1000. While useful for some applications, our group's earliest work on as-grown *c*-axis GaN nanowires showed typical  $Q$  larger by an order of magnitude: most above  $10^4$  and over  $10^6$  with positive feedback [47]. So, it is evident that we have an opportunity to branch out into a new area of low-loss (high- $Q$ ), bottom-up, cantilever resonators.

#### 1.4 *c*-Axis Gallium Nitride Nanowires

GaN is an important member of the III-V family of semiconductors. Its 3.4-eV bandgap (365 nm) has led to much interest in ultra-violet (UV) LED structures (e.g. [29]). When combined with materials like indium and aluminum, the various alloys allow for a tunable bandgap from UV through to infrared (IR) [48, 49]. GaN typically takes on zinc blende and wurtzite crystal structures. Here, we are interested in the wurtzite structure, comprising two interpenetrating hcp

Figure 1.2: Transmission electron microscope (TEM) images of large-amplitude mechanical resonance of a zinc oxide (ZnO) nanowire resonator mounted on a W tip. Such structures are reported to have fundamental resonance frequencies of order 100 kHz and  $Q$  near 500. Figure from [43].

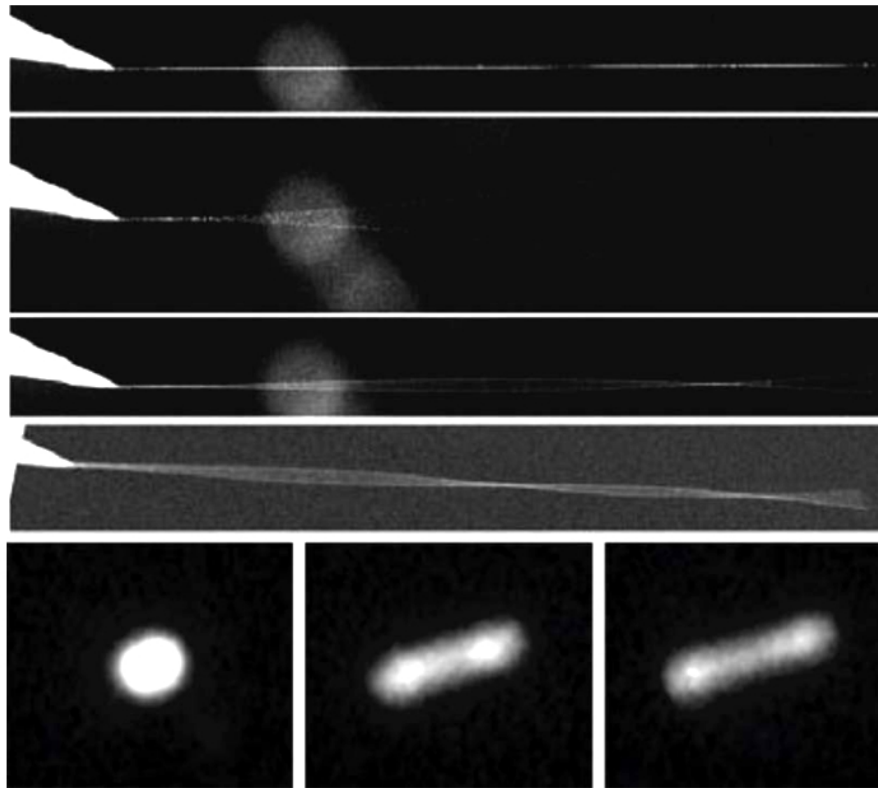


lattices along the  $c$ -axis. A scanning electron microscope (SEM) image of the nanowires used in this work is shown in Figure 1.6.

The GaN wurtzite structure and some important crystallographic planes are shown in Figures 1.7 and 1.8. In terms of materials properties,  $c$ -axis GaN nanowires are perhaps surprisingly similar to the accepted bulk values for elastic (Young's) modulus ( $E = 300$  GPa) and density ( $\rho = 6.15$  g/cm<sup>3</sup>) [50]. Combined results from tensile tests and atomistic simulations (using density functional theory and molecular dynamics) show that until nanowire radii are at or below approximately 20 nm, the values of  $E$  and  $\rho$  remain mostly constant.

The GaN nanowires studied here are provided by Drs. Kris Bertness and Norman Sanford at

Figure 1.3: Scanning electron microscope (SEM) images of a 243- $\mu$ m-long silicon carbide (SiC) nanowire mounted on a tungsten (W) tip. The nanowire is shown from top to bottom, respectively, stationary, in its first three resonance modes, and end-on in field emission imaging mode. Fundamental resonance frequencies of these structures are near 10 kHz and  $Q$ s are near 40,000. Figure from [44].



the National Institute of Standards and Technology (NIST-Boulder). Along with their team, they maintain an active research program in the growth and characterization of GaN nanowires. They have succeeded in obtaining spontaneous nanowire growth via molecular beam epitaxy (MBE) by thermodynamically-driven variations in surface sticking [53]. This is a unique growth mechanism that differs from the conventional VLS mechanism which typically requires a metallic nanoparticle catalyst at the nanowire tip. One reason for selecting nanowires grown by this spontaneous, catalyst-free mechanism is a reported tendency toward more consistent geometrical aspects.

GaN nanowires are grown in a gas-source MBE system from a sputtered GaN matrix layer. Below this matrix layer are a thin layer of aluminum and an aluminum nitride buffer layer on Si (1 1 1) wafers. These Al layers provide a means to relax the strain caused by a lattice mismatch

Figure 1.4: TEM image of an a-axis gallium nitride (GaN) nanowire showing its 2-MHz fundamental resonance frequency with  $Q$  near 3000. Figure from [45].

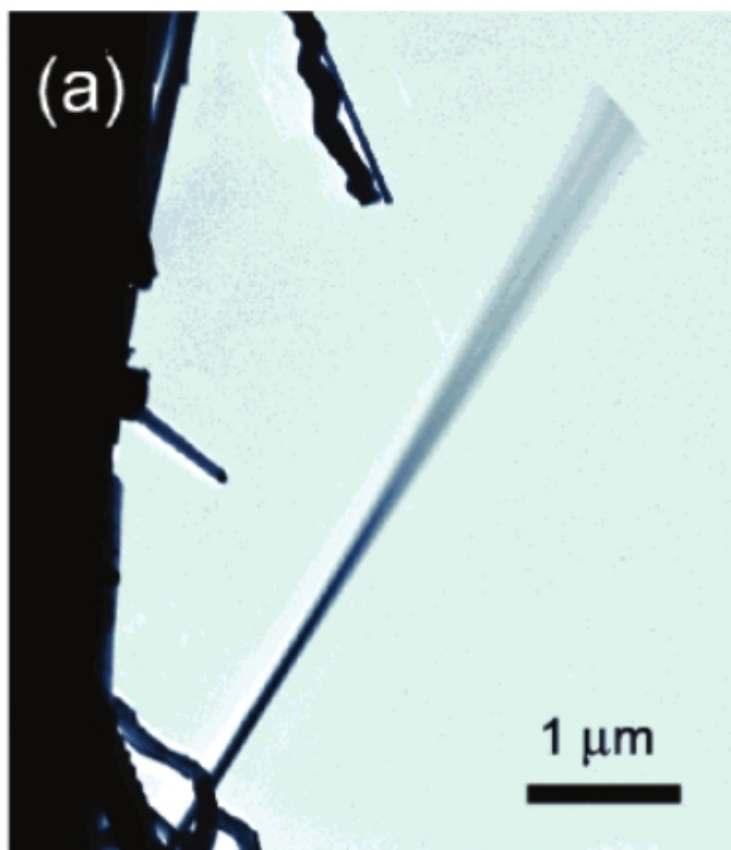


Figure 1.5: Fabrication schematic (a-d) and SEM images (e-f) of a-axis GaN nanowires grown on GaN mesas. These nanowires have lengths near  $4\ \mu\text{m}$ , diameters near  $50\ \text{nm}$ , fundamental resonance frequencies near  $2\ \text{MHz}$ , and  $Q$  near  $700$ . Figure from [22].

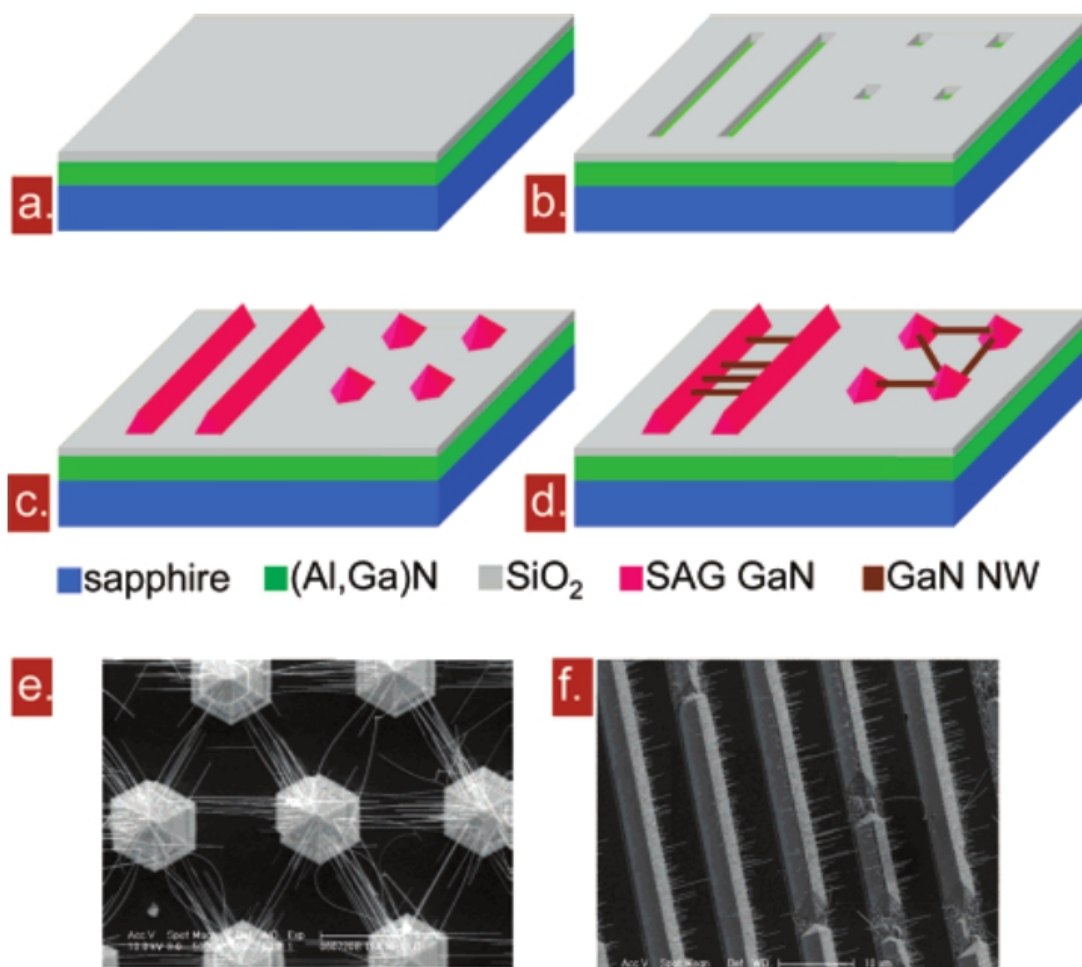


Figure 1.6: Scanning electron micrographs of as-grown gallium nitride (GaN) nanowires. (a) Hexagonal cross-section, typical of c-axis, wurtzite crystal structure. (b) Side view of GaN nanowire growth out of GaN matrix layer to a height of about 15  $\mu\text{m}$ . (c) Angled plan view of as-grown nanowires, showing approximate areal density of  $1 \mu\text{m}^{-2}$ . Variations in nanowire sidelength can be seen, along with occasional bonding of adjacent nanowires, likely due to Van der Waals forces.

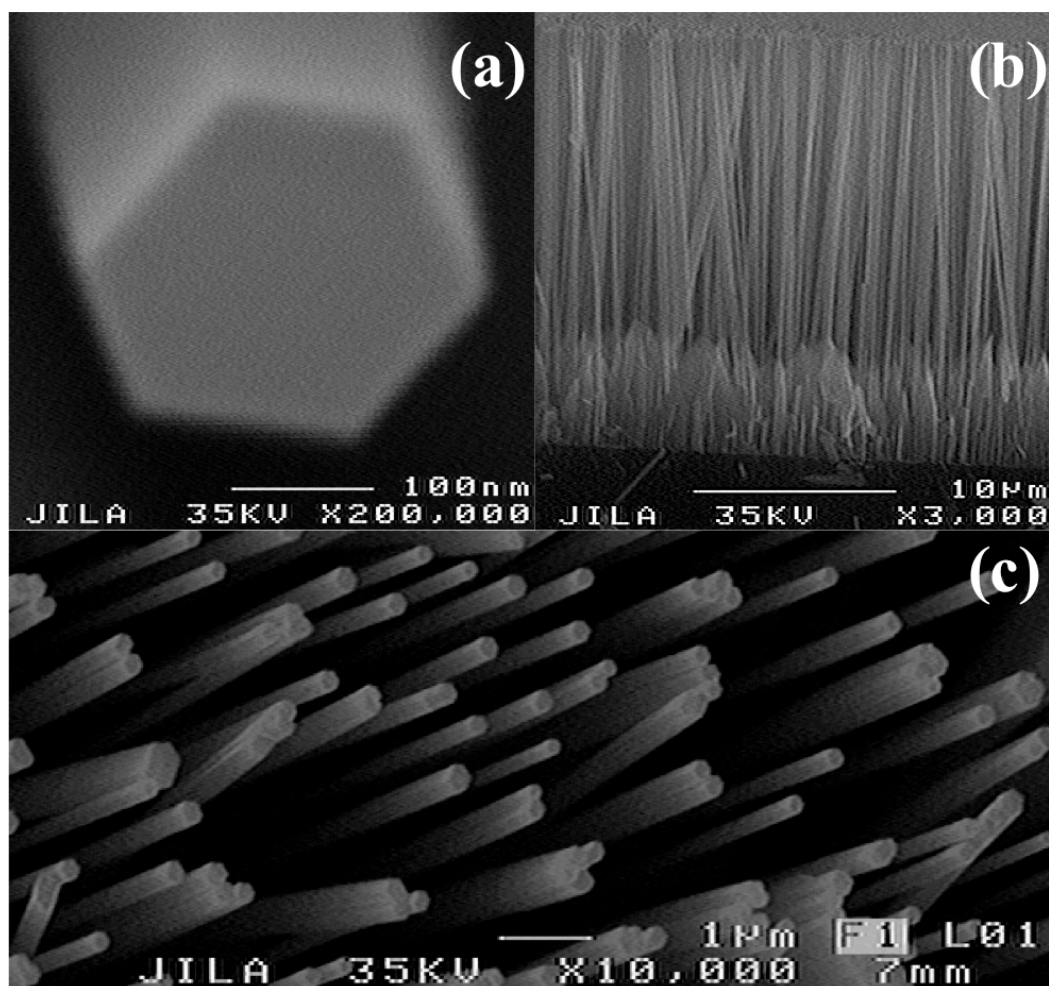


Figure 1.7: Ball-and-stick models of (a) full GaN nanowire wurtzite crystal structure and (b) corresponding unit cell. Gallium atoms are shown as large and yellow, nitrogen atoms are small and gray. Figure adapted from Ref. [51].

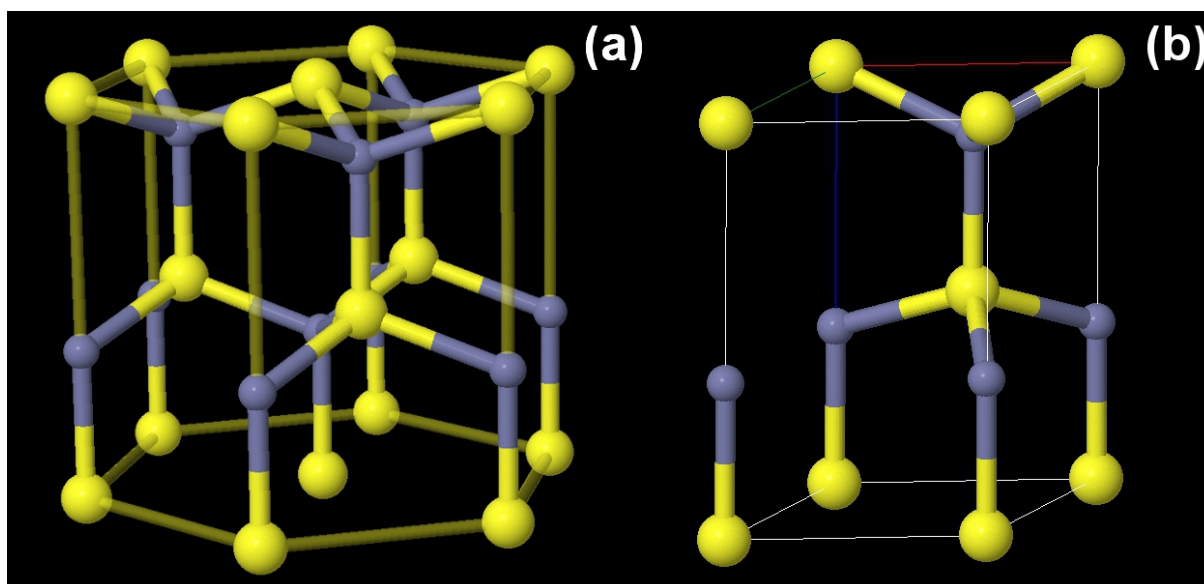
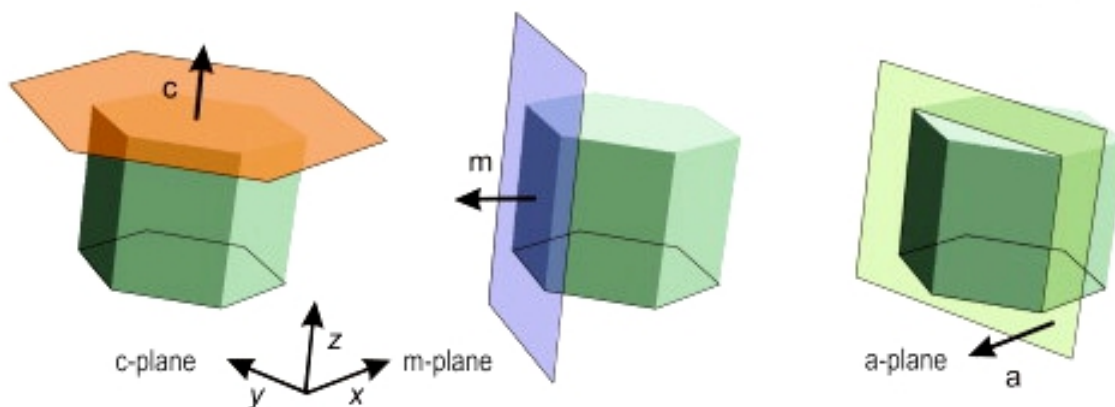


Figure 1.8: GaN nanowire crystallographic planes. For the nanowires studied in this work, the nanowire ends are c-plane (left) and the sidewalls are m-plane (center). Figure adapted from Ref. [52].



between the GaN ( $3.19 \text{ \AA}$ ) and Si (111) hexagonal constant ( $3.84 \text{ \AA}$ ) [48, 54].

The nanowires can be doped by substitutional impurities on the Ga sites. Intentional  $p$ -type doping is done through the introduction of magnesium and has recently furthered the development of GaN-based electronic components (e.g. p-n junctions) [55, 56]. Intentional  $n$ -type doping is done through the introduction of Si. Carrier densities for such doped nanowires can be on the order of  $10^{18} \text{ cm}^{-3}$ . Even the nanowires that are not intentionally doped can themselves be ‘unintentionally’  $n$ -type due to defects or impurities in the crystal, with carrier densities approximately  $10^{16} \text{ cm}^{-3}$ .

## 1.5 Measurement Readout Techniques

Once familiar with the material and its structure and properties, it is worth briefly discussing how one might go about interrogating the physical system; namely, how do we read out information from a nanoscale system? Below, I will briefly mention the common techniques in use in current literature. For more comprehensive discussions of these techniques, the reader is directed to Refs. [41] and [26]. In later Chapters, I will discuss further the techniques used in this work.

Despite the large number of experiments and variation in systems to be measured, the set of experimental readout techniques is relatively small. Virtually all of the technologies mentioned

below utilize some form of sensor whose output depends linearly on the displacement of the resonant structure. Practically, resonance analysis is carried out by recording the aforementioned signal (e.g. voltage) as a function of time, and then transforming it to frequency space. The expected shape of such a signal is discussed in Chapter 2.

Resonant cavity methods are among the most common readout techniques in use. These types of cavities can take some of the following forms: a Fabry-Pérot cavity [57] (one moveable mirror and one fixed), a moveable membrane within a rigid cavity [58], a microtoroid [59], or a superconducting microwave cavity [60]. Transmission detection methods involve observing modulations in measurements of electrons (e.g. through proximity transmission [61] or through piezoresistivity [18]), or photons [62]. Piezoelectric systems produce a electric polarization under strain and so can be used as displacement sensors by measuring the induced voltage on resonance [63]. Flux-based detectors commonly make use of the magnetomotive technique in fixed-fixed (doubly-clamped) beams [64] or superconducting quantum interference devices (SQUIDs) [65].

And, finally, the two principal readout techniques that are implemented in this work are the collection of backscattered electrons from an incident beam [47], and a capacitive detection scheme [66]. Note, also, that there can be overlap between these various detection methods. For instance – as in this work – a mechanical resonator can be capacitively coupled to some form of cavity.

## Chapter 2

### From Simple Harmonic Oscillators To Nanowire Resonators

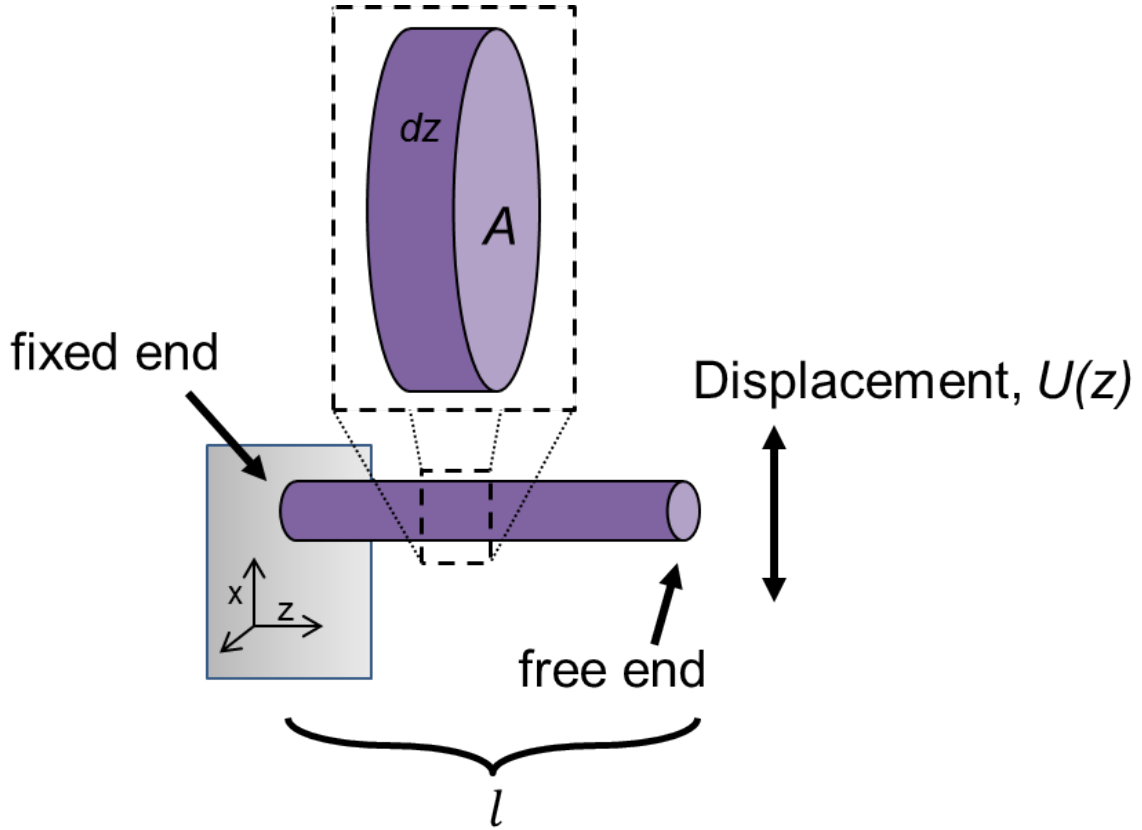
This chapter briefly covers some of the mathematics involved in quantifying resonance behavior from the point of view of strength-of-materials and from the equations of motion. For an accessible and quite comprehensive discussion that covers the full range from binary atom chains to lithographic recipes for microstructures, see Cleland's recent, comprehensive text [67]. The majority of the following analysis is explained in much more detail in that work.

#### 2.1 Resonator Eigenfrequencies And Modeshapes

When considering the small-deflection-amplitude limit of long thin beams, one common approach is to use Euler-Bernoulli (EB) beam theory [67, 68]. As discussed in Section 1.4, GaN nanowires have aspect ratios of order 100 and so can be considered within this category. EB theory deals with beams under applied forces leading to torque perpendicular to both the force and the beam axis, and is a subset of a more complete treatment that includes the effects of shear deformation, Timoshenko theory. In EB theory, we assume planes within the beam that are initially perpendicular to the beam axis remain perpendicular to the neutral axis under loading.

We want to consider the flexural vibrations in one dimension of a beam as shown in Figure 2.1. The treatment of a differential element of cross-sectional area  $A$  and thickness  $dz$  under load  $F_x$  requires balancing the linear forces and torques. Taylor expanding these balanced expressions about a point  $z$ , keeping only terms that are first-order in  $dz$ , one arrives at a wave equation for the beam displacement,  $U(z)$  [67]:

Figure 2.1: Schematic side-view – and blow-up of differential element  $dz$  – of a beam of length  $l$ , cross-sectional area  $A$ , and indicating transverse displacement  $U(z)$  of fixed-free cantilever beam.



$$\frac{\partial^2}{\partial z^2} \left( EI_y \frac{\partial^2 U}{\partial z^2} \right) = -\rho A \frac{\partial^2 U}{\partial t^2}, \quad (2.1)$$

where  $E$  is the beam's elastic modulus,  $I_y$  the second moment of inertia, and  $\rho$  the material density.

When we treat the modulus  $E$  and second moment of inertia  $I_y$  as not varying with  $z$  (true for prismatic, homogeneous beams), and assume a harmonic time dependence for the displacement,  $U(z, t) \propto e^{-i\omega t}$ , the spatial dependence satisfies the equation

$$\frac{d^4 U}{dz^4} = \beta^4 U(z), \quad (2.2)$$

where we have defined  $\beta = (\rho A / EI_y)^{1/4} \omega^{1/2}$ . If we now assume that the spatial dependence has the form  $U(z) = e^{\kappa z}$ , then the solutions are  $\kappa = \pm i\beta, \pm\beta$  and the general solution takes the form

(in real functions):

$$U(z) = a \cos(\beta z) + b \sin(\beta z) + c \cosh(\beta z) + d \sinh(\beta z). \quad (2.3)$$

At this point we can apply boundary conditions that are appropriate for a singly-clamped ('fixed-free') beam or cantilever. The beam clamp is taken to be at  $z = 0$ , and the free end at  $z = l$ . As such, the boundary conditions are  $U(0) = \frac{dU}{dz}(0) = \frac{d^2U}{dz^2}(l) = \frac{d^3U}{dz^3}(l) = 0$ . The third and fourth boundary conditions represent, respectively, the fact that there should be no transverse force or torque on the free end.

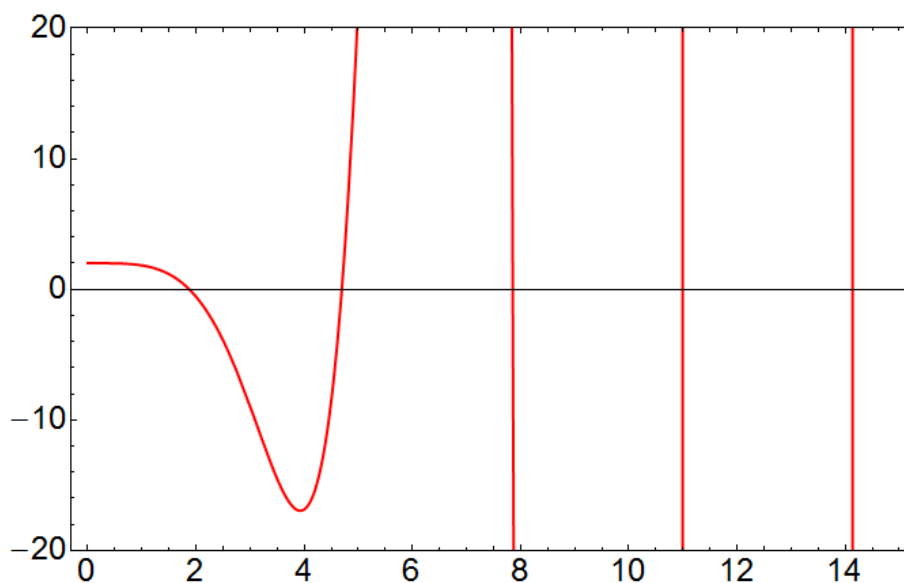
Applying these boundary conditions to Equation 2.3, the allowed values of  $\beta l$  (and thus, the frequencies  $\omega$ ) form a discrete set satisfying

$$\cos(\beta_n l) \cosh(\beta_n l) + 1 = 0, \quad (2.4)$$

which is shown graphically in Figure 2.2.

The solutions  $\beta_n l = 1.875, 4.694, 7.885, 10.996, \dots$  represent the first- ( $n = 1$ ), second- ( $n = 2$ ),

Figure 2.2: The function  $y = \cos x \cosh x + 1$ , whose zero crossings give the allowed mode frequencies for a singly-clamped (cantilever) beam.



..., order resonance modes, and plugging them into Equation 2.3 gives the corresponding relative amplitudes which allow us to plot the modeshapes shown in Figure 2.3. The frequency of each mode, labeled by  $n$ , is calculated by inverting from  $\beta_n$ . For the fundamental ( $n = 1$ ) mode, the resonance frequency  $\omega_1$  (typically written  $\omega_o$ ) for a cantilever of arbitrary geometry is given by

$$\omega_o = \sqrt{\frac{EI_y}{\rho A}} \left( \frac{1.875}{l} \right)^2. \quad (2.5)$$

We can make Equation 2.5 slightly more specific by writing out explicitly the form of  $I_y/A$  for the hexagonal cross-section of the GaN nanowires (discussed in Section 1.4). A regular hexagon with sidelength  $a$  has cross-sectional area  $A = \frac{3\sqrt{3}}{2}a^2$ . In calculating the beam second moment  $I_y$ , it would seem that two orthogonal directions could be equivalently chosen: one with the neutral plane between vertices, and another with the neutral plane between facets. As is shown in Appendix B.1, for a regular hexagon these moments are equivalently  $I_y = \frac{5\sqrt{3}}{16}a^4$ . Combining these results, the degenerate fundamental resonance frequency becomes

$$\omega_o = \frac{1.875^2}{2} \sqrt{\frac{5}{6}} \sqrt{\frac{E}{\rho}} \left( \frac{a}{l^2} \right), \quad (2.6)$$

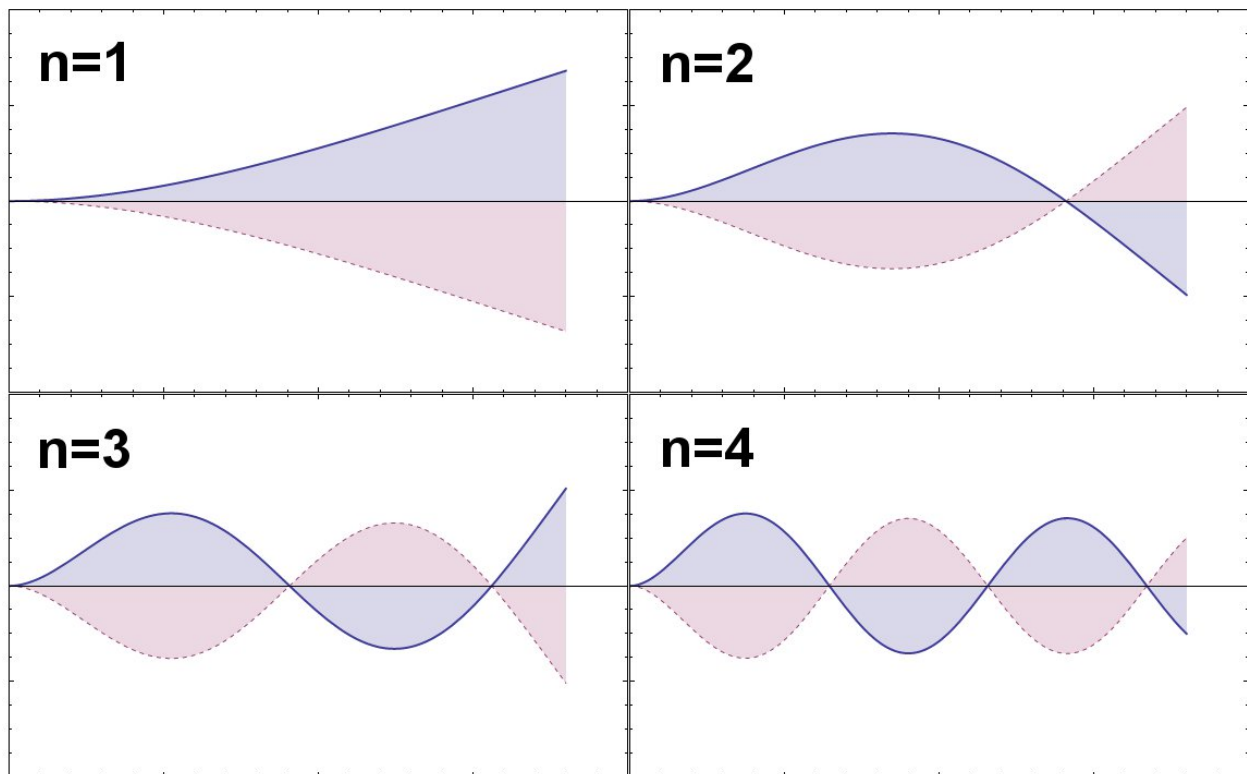
and differs from the equivalent expression for a cylindrical beam of radius  $a$  by the factor  $\sqrt{\frac{5}{6}} \sim 0.91$ .

### 2.1.1 Zener's Model Of An Anelastic Solid

It is also possible to introduce the concept of energy loss – or dissipation – into the governing equations described in Section 2.1. In the 1930s, Clarence Zener incorporated anelastic mechanical response in a theory of deformable materials, which we now refer to as the ‘Zener Model.’ Zener’s model is a generalization of Hooke’s law  $\sigma = E\epsilon$  (considered in one dimension), where  $\sigma$  is the stress,  $\epsilon$  the strain, and  $E$  the elastic modulus. Zener’s approach was to incorporate the first derivatives of both the stress  $\sigma$  and strain  $\epsilon$  to allow for mechanical relaxation:

$$\sigma + \tau_\epsilon \frac{d\sigma}{dt} = E_R \left( \epsilon + \tau_\sigma \frac{d\epsilon}{dt} \right). \quad (2.7)$$

Figure 2.3: Four lowest allowed resonance frequency modeshapes for a singly-clamped (cantilever) beam geometry, given by Equation 2.3. Values of  $n$  are associated with the corresponding values  $\beta_{nl}$  in Equation 2.4.



Here, the two relaxation constants,  $\tau_i$  allow one to consider the rate at which the dissipative processes occur, and the modulus  $E_R$  is an explicitly relaxed value of the Young's modulus. The unrelaxed value is given by  $E_U = \frac{\tau_\sigma}{\tau_\epsilon} E_R$ .

When we consider harmonic time dependence in  $\sigma$  and  $\epsilon$ ,  $X = X_o e^{-i\omega t}$ , we can write an expression for the complex Young's modulus (where  $\sigma_o = E(\omega)\epsilon_o$ ):

$$E(\omega) = E_{eff}(\omega) \left( 1 - \frac{i\omega\bar{\tau}}{1 + \omega^2\bar{\tau}^2} \Delta \right), \quad (2.8)$$

where we have simplified this expression with the help of:

$$\begin{aligned} \bar{\tau} &= \sqrt{\tau_\epsilon \tau_\sigma}, \\ \Delta &= \frac{E_U - E_R}{E_R}, \\ E_{eff}(\omega) &= \frac{1 + \omega^2 \bar{\tau}^2}{1 + \omega^2 \tau_\epsilon^2} E_R. \end{aligned}$$

We can now see explicitly that the complex modulus suggests a phase difference between the stress  $\sigma$  and the strain  $\epsilon$ . This is the source of our energy loss.

The key motivation for all of this being that for small  $\Delta$ , we can now also define the quality factor  $Q$  as the ratio of the imaginary part of  $E$  to the real part:

$$Q^{-1} = \frac{\omega\tau}{1 + \omega^2\bar{\tau}^2} \Delta, \quad (2.9)$$

showing that the dissipation  $1/Q$  is frequency dependent with a maximum value where  $\omega = 1/\bar{\tau}$ . By including this effective elastic modulus in the Euler-Bernoulli formula, we can rewrite Equation 2.1 as:

$$E(\omega)I_y \left( 1 - \frac{i}{Q} \right) \frac{\partial^4 U}{\partial z^4} = \omega^2 \rho A U, \quad (2.10)$$

which has the same spatial solutions as Equation 2.1, and also the same real-valued resonance frequency. But, it also now incorporates dissipation via the imaginary component of the complex-valued resonance frequency. Seeing the resonator loss in this form is instructive, but for the rest of the derivations, we will largely consider the real-valued resonance given in Equation 2.5.

## 2.2 Resonator Lineshapes

Once we understand the origins of a fundamental resonance frequency due to Euler-Bernoulli beam theory, we can look at how this frequency and the associated measurable lineshapes come out of the equations of motion. Beginning with the canonical simple harmonic oscillator (SHO), we'll consider the force  $F$  on a mass  $m$  resulting in acceleration  $a$ , as given by Newton's second law  $F = ma$ . In the presence of energy loss (damping) specified by parameter  $\Gamma$  (proportional to  $Q^{-1}$ , as introduced in Section 2.1.1), the center of mass equation of motion in one dimension  $x = x(t)$  is given in terms of the restoring harmonic force  $-m\omega_o^2x$  (where  $\omega_o = 2\pi f_o$  is the angular resonance frequency), a frictional force  $-m\Gamma\frac{\partial x}{\partial t}$  proportional to velocity, and an applied force  $F_{app} = F_{app}(t)$ :

$$-m\omega_o^2x - m\Gamma\frac{\partial x}{\partial t} + F_{app} = m\frac{\partial^2 x}{\partial t^2}. \quad (2.11)$$

If we assume similar harmonic time dependence in both  $x = xe^{i\omega t}$  and  $F_{app} = F_{app}e^{i\omega t}$ , carry out the differentiation and then divide out the common time dependence, we arrive at the following expression for  $x$  in frequency space:

$$x(\omega) = \frac{F_{app}/m}{(\omega_o^2 - \omega^2) + i\omega\Gamma}. \quad (2.12)$$

### 2.2.1 Two-phase Lineshape

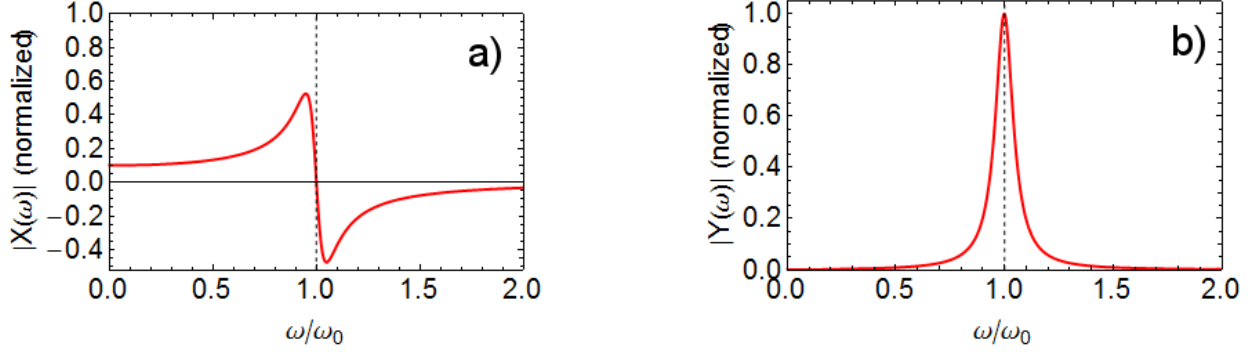
Equation 2.12 is a complex expression which can be split into real and imaginary components  $x = X + iY$ :

$$X(\omega) = \frac{F_{app}}{m} \frac{\omega_o^2 - \omega^2}{(\omega_o^2 - \omega^2)^2 + (\omega\Gamma)^2} \quad (2.13)$$

$$Y(\omega) = \frac{F_{app}}{m} \frac{\omega\Gamma}{(\omega_o^2 - \omega^2)^2 + (\omega\Gamma)^2}. \quad (2.14)$$

$X$  and  $Y$  are, respectively, referred to as the 'in-phase' and 'quadrature' components of the lineshape and are shown in Figure 2.4. Phase-sensitive data presented in this work will typically be in the

Figure 2.4: An (a) in-phase and (b) quadrature representation of the Lorentzian response function (Equation 2.12), normalized and in terms of the dimensionless parameter  $\omega/\omega_o$ .



form of Equations 2.13, 2.14, and Figure 2.4, but Equation 2.12 can be equivalently expressed in terms of its amplitude and phase,

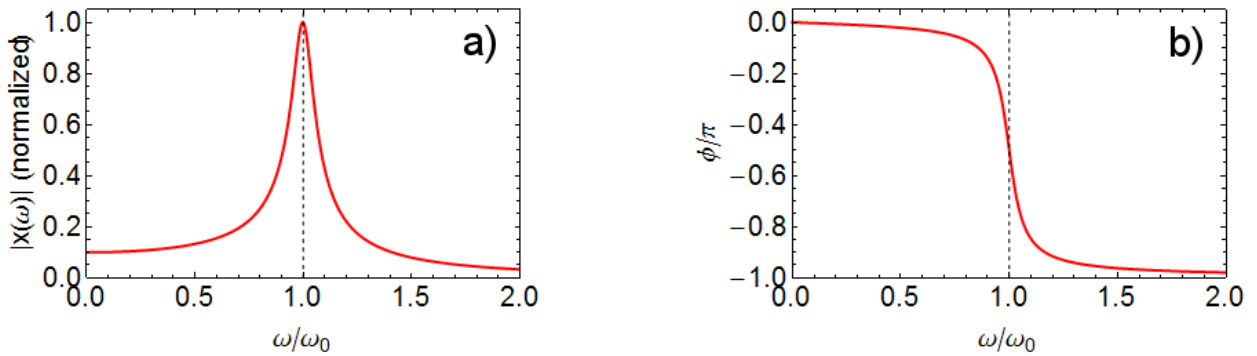
$$|x(\omega)| = \frac{F_{app}}{m} \frac{1}{\sqrt{(\omega_o^2 - \omega^2)^2 + (\omega\Gamma)^2}} \quad (2.15)$$

$$\tan^{-1} \phi(\omega) = \frac{\omega\Gamma}{\omega_o^2 - \omega^2}, \quad (2.16)$$

shown graphically in Figure 2.5.

In practice, during a phase-sensitive measurement, the introduction of physical, signal-carrying cables and reactive circuit components leads to a finite transmission length and an overall

Figure 2.5: An (a) amplitude and (b) phase representation of the Lorentzian response function (Equation 2.12), normalized and in terms of the dimensionless parameter  $\omega/\omega_o$ .



phase shift of Equation 2.12. Subsequently, the signal we actually detect and save (e.g. as described in Section 3.3.2) is  $xe^{i\theta}$ :

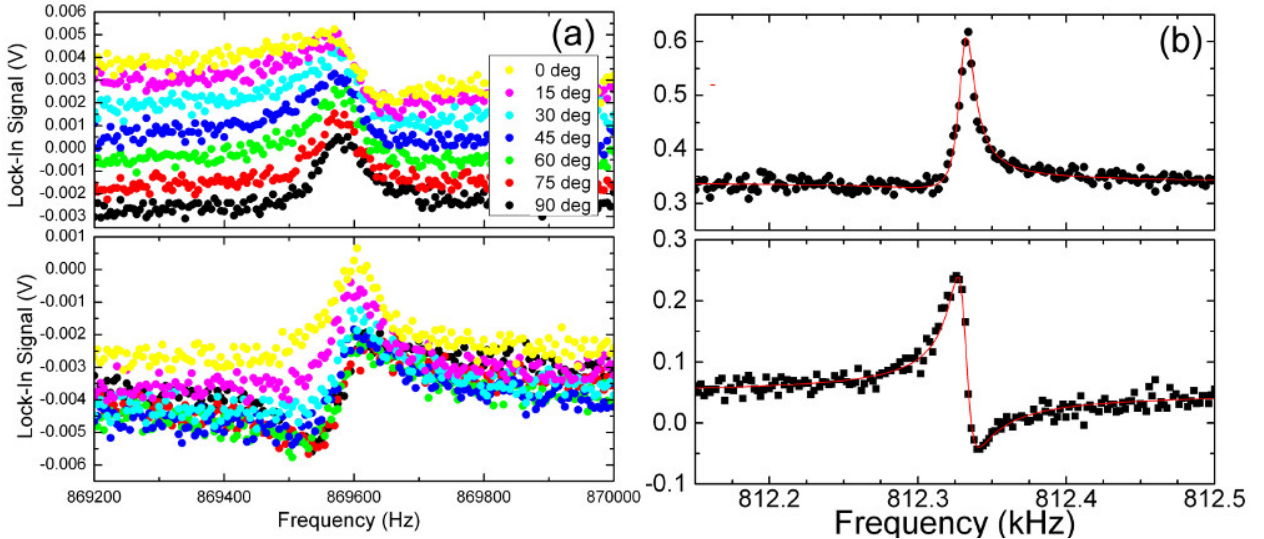
$$\tilde{X} = X \cos \theta - Y \sin \theta \quad (2.17)$$

$$\tilde{Y} = X \sin \theta + Y \cos \theta. \quad (2.18)$$

This overall phase shift is seen in Figure 2.6 as a kind of ‘rotation’ of both sets of data. With the functional form of the resonator response expression in hand, we can then fit our datasets of measured responses to these parameters.

From these fit results we can calculate one of the more commonly-used figures of merit in resonators, the quality factor  $Q$ . Defined as the ratio between the central resonance frequency  $\omega_o$  and the full-width-at-half-maximum (FWHM) power  $\Gamma$ ,  $Q = \omega_o/\Gamma$ ,  $Q$  can also be interpreted as the energy lost per cycle of oscillation. Low-loss resonators will typically possess high  $Q$ , though it is important to note that a resonator with equal damping and linewidth  $\Gamma$  but significantly higher

Figure 2.6: Phase-rotated Lorentzian responses of a GaN nanowire. (a) The effect of manually adjusting phase angle  $\theta$  – from Equations 2.17 and 2.18 – through  $90^\circ$  on the in-phase and quadrature Lorentzian response functions. (b) Arbitrary  $\theta$  observed in nanowire response data. Solid red line is a simultaneous fit to both  $\tilde{X}$  and  $\tilde{Y}$ , sharing the parameters  $f_o = 812,331.5 \pm 0.2$  Hz and  $\Gamma/2\pi = 13.0 \pm 0.3$ . With these fit values, we can calculate  $Q = \omega_o/\Gamma = 62,000 \pm 1000$ .



resonance frequency will have higher  $Q$ .

### 2.2.2 Power Spectral Density Lineshapes

An additional form in which data will be presented is that of a power spectral density (PSD). When recording data in terms of power, we are measuring the square of Equation 2.12,  $|x(\omega)|^2$ . For measurements in which the two components of Equation 2.12 have no offset, the resulting squared Lorentzian lineshape is shown in Figure 2.7 and is independent of the offset angle  $\theta$ .

An interesting situation arises when there is a contribution to the measured signal that is not associated with the resonant motion of the nanowire resonator. As will be illustrated in Chapter 5, when there exists additional background signal that is synchronous with  $F_{app}$ , the result is a constant offset in one or both phase components. The resulting PSD  $|x(\omega)|^2$  then possesses a more complicated overall shape. Figure 2.8 shows an example with the offsets of the two phases chosen arbitrarily.

Figure 2.7: (a) In-phase and quadrature Lorentzian responses ( $\tilde{X}$ ,  $\tilde{Y}$ ) without coherent background, and (b) the corresponding symmetrical, squared Lorentzian  $|x(\omega)|^2$  that results, as might be measured in an SEM (cf. Chapter 3). Shading indicates region between curve and  $x$  axis.

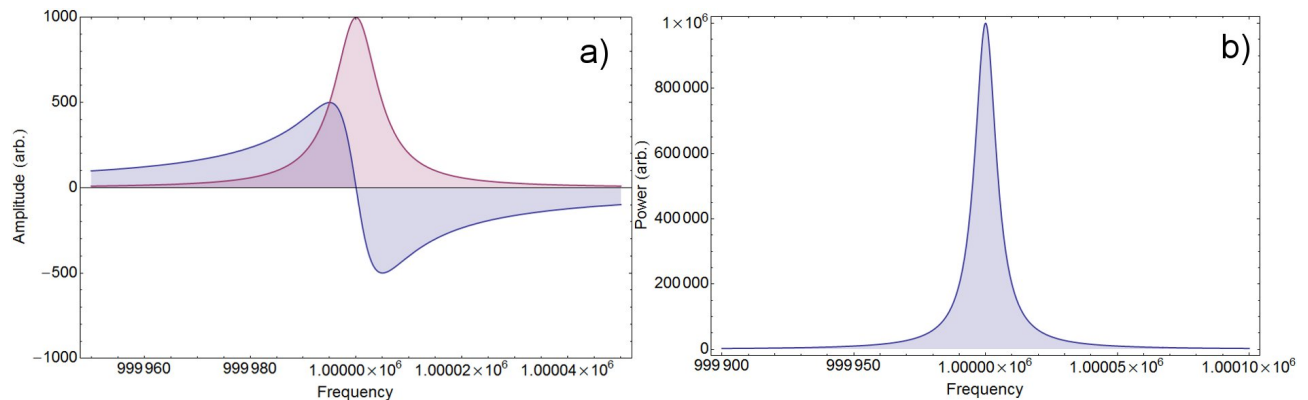
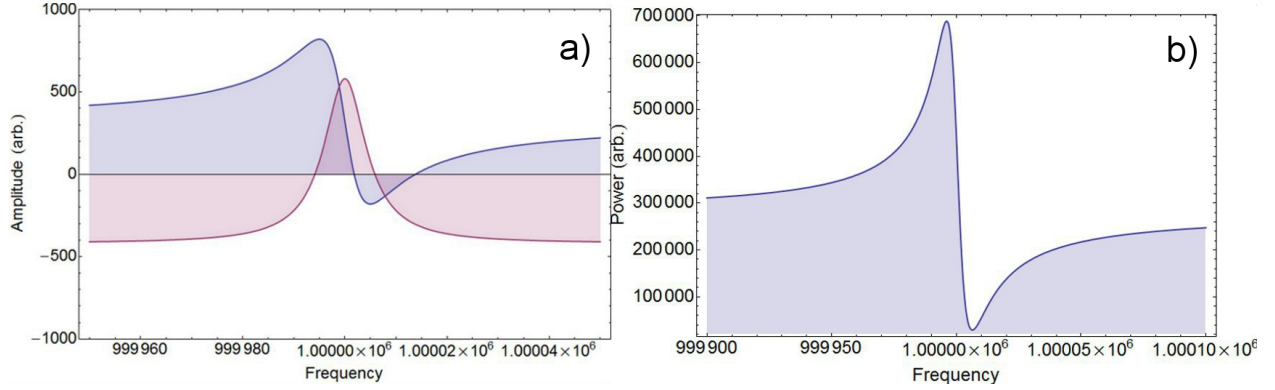


Figure 2.8: (a) In-phase and quadrature Lorentzian responses ( $\tilde{X}$ ,  $\tilde{Y}$ ) with arbitrarily chosen coherent background levels (offsets), and (b) the corresponding asymmetrical, squared Lorentzian  $|x(\omega)|^2$  that results, as might be measured capacitively (cf. Chapters 4 and 5). Shading indicates region between curve and  $x$  axis.



### 2.3 Approximate Limits On $Q$ : Damping Mechanisms

In the last decade, there has been extensive research carried out in the areas of sources and relative sizes of dissipation mechanisms in other micro- and nanomechanical resonator systems. For some examples, the reader is directed to Refs [9, 15, 17, 42, 69–87] – though this list is by no means comprehensive. However, since there is very little pre-existing work on dissipation in the GaN nanowire mechanical resonator system –and none on the as-grown geometry, as far as the author can tell – we make an attempt below to estimate the influence some of these mechanisms may have on our system. The references listed above include varying levels of theoretical foundations for their analyses of dissipation. One that appears to do a decent job of pulling together concise and manageable results from the original works is by Ono et al. [9]. That work also incorporates some of the more recent theory work from the last couple of decades. The estimates below follow a similar path through the calculations for four sources of dissipation described therein. Two are ‘external’ (air damping and support or anchor loss), and two are ‘internal’ (thermoelastic loss and surface loss). Each of these calculations result in a limit on  $Q$  for that source of loss, such that the inverse sum of all the  $Q^{-1}$  determines the overall resonator  $Q$ , as described in Equation 1.1.

To begin, Table 2.1 will set some parameters and values that will be used throughout these

Table 2.1: Parameters for use in GaN nanowire dissipation estimates.

<b>GaN nanowire parameter, symbol</b>	<b>Value</b>	<b>Units</b>
Resonance frequency, $f_o$ <sup>a</sup>	1	MHz
Length, $L$	12	$\mu\text{m}$
Radius/sidelength, $r$	150	nm
Effective ‘thickness’ <sup>b</sup> , $t = 2 \times r$	300	nm
Young’s (elastic) modulus, $E$	300	GPa
Density, $\rho$	6150	$\text{kg m}^{-3}$
Mass, $m$	1	pg
Spring constant, $k$	0.01	$\text{N m}^{-1}$
Linear thermal expansion coefficient, $\alpha$	$3.17 \times 10^{-6}$	$\text{K}^{-1}$
Specific heat, $c_p$	455 <sup>c</sup>	$\text{J kg}^{-1} \text{K}^{-1}$
Thermal diffusivity, $\chi$	$0.43 \times 10^{-4}$	$\text{m s}^{-2}$
<b>Environmental parameter, symbol</b>		
Temperature, $T$	300	K
Pressure, $p$	0.01 (1.33)	Torr (Pa) <sup>d</sup>

<sup>a</sup> This frequency does not explicitly correspond to the other dimensions listed in this table (e.g.  $r, L$ ), but represents a typical nanowire resonance frequency. For details about the difference between calculated and measured resonance frequencies, see Section 3.5.2.

<sup>b</sup> The referenced calculations are often carried out for a beam with rectangular cross-section. Here, we suggest the diameter of a cylindrical (or hexagonal) beam cross-section will not differ substantially from the width of a rectilinear cross-section.

<sup>c</sup> Calculated by converting  $38.1 \text{ J mol}^{-1} \text{ K}^{-1}$  [88] via molecular weight.

<sup>d</sup> Unless explicitly measuring pressure dependence, experiments are carried out at pressures on the order of  $10^{-6}$  Torr. This value represents a ‘worst case’ scenario for our vacuum system.

calculations. Beyond the those already discussed in Section 1.4, these material properties largely come from Levinshstein’s canonical text on semiconductor properties [88], or are reasonable order of magnitude estimates (e.g. nanowire geometry, mass). Additional environmental parameters are included, as well.

### 2.3.1 Gas Damping

Dissipation from gas damping is a common concern for sub-micron resonators due to the large surface-to-volume ratio. In their oft-cited work, Blom et al. specify three pressure regions: viscous, molecular, and intrinsic [86]. In the first region, the surrounding air acts as a viscous fluid, rapidly damping out oscillatory behavior. In the third region, the intrinsic region, air damping is

negligible. It is the middle region where particularly interesting behavior is observed. In Chapter 4 we return to the notion of the molecular damping region. In this molecular region, the limiting  $Q$  factor is given by [9, 86]

$$Q = \frac{k^2}{k_m p} \left( \frac{t}{L} \right)^2 \sqrt{\frac{E\rho}{12}}, \quad (2.19)$$

where  $k_m$  is defined for clarity as

$$k_m = \sqrt{\frac{32m}{9\pi RT}}, \quad (2.20)$$

where  $R$  is the gas constant.

With the parameters specified in Table 2.1, the resulting limit on  $Q$  is approximately  $3 \times 10^{10}$ . Recall that the environmental pressure for this calculation is orders of magnitude higher than that typically observed in our measurement chambers. As shown in Equation 2.19, the dissipation is proportional to the pressure, so the corresponding  $Q$  limit will only go up at lower pressures. Though air damping is certainly a component of our observed  $Q$ , it is negligible at our typical operating pressures.

### 2.3.2 Anchor Loss

Depending on the assumptions made about the nature of the substrate (infinitely rigid or elastic), the effect of the substrate on the resonator's natural frequency can vary. However, in either case there is a coupling between the phonon modes of the resonator beam and those of the substrate that allows for phonon radiation. Hosaka et al. estimate the support loss<sup>1</sup> limited  $Q$  factor when considering our substrate as an infinite elastic plate as [76]

$$Q = 4.35 \left( \frac{L}{t} \right)^3. \quad (2.21)$$

Note that in Ref [9], the authors appear to have made a mistake in their transcription of the

---

<sup>1</sup> Equivalently called anchor or clamping loss.

prefactor for this equation. Digging into the chain of references that start in [9] shows that the numerical prefactor is predominantly a result of integrals over the beam geometry of temperature-independent quantities (neglecting the linear expansion coefficient). This will be an important point when considering our temperature-dependent results in Chapter 5.

There is also quite extensive, recent work in this area by Wilson-Rae and colleagues (cf. Refs [73, 77, 84]). Ono et al. mention, off-hand, that for  $L/t < 100$ , support loss should probably be considered a significant contribution to resonator dissipation. For our resonators,  $L/t \approx 40$ , and for the parameters of Table 2.1, we obtain a limiting  $Q$  of about  $3 \times 10^5$ . While certainly a contribution to our observed  $Q$  values, support loss does not appear to be necessarily the dominant source of dissipation at higher temperatures. As will be discussed near the end of Chapter 5, it is possible that support loss is observed at low temperatures. For additional discussion of support loss and how it might be mitigated in future experiments, see also Chapter 6.

### 2.3.3 Thermoelastic Loss

In a typical solid, there is a coupling between the strain fields and the temperature fields, most simply embodied by the standard thermal expansion coefficient:

$$\alpha = \frac{1}{L} \frac{\partial L}{\partial T}. \quad (2.22)$$

During deformation (in this case, transverse motion) of the beam, the opposings sides of the resonating beam are alternately subject to tension and compression. As a result a thermal gradient is established between the sides of the solid, and the irreversible flow of heat between them leads to energy dissipation known as thermoelastic dissipation. This process was first identified back in the 1930s by Clarence Zener, who was able to approximate its effect on macro-scale metallic objects. In the realm of micro- and nano- structures, Zener's theory has been formalized exactly (see, in particular, Lifshitz and Roukes [87]), and is in very close agreement with Zener's original approximation.

In particular, we can write a similar expression for the limiting  $Q$  [9, 89–91]:

$$Q = 80 \frac{\chi}{f_o t^2} \frac{E}{\delta E}, \quad (2.23)$$

where  $\delta E$  is the difference between adiabatic and isothermal Young's moduli, approximated by:

$$\delta E = \frac{E^2 T \alpha^2}{9 c_p}. \quad (2.24)$$

Again, with the parameters specified in Table 2.1, we can evaluate this expression and the resulting limit on  $Q$  is approximately  $2 \times 10^5$ . Though not necessarily the dominant source of loss, this is relatively close to the contribution of support loss.

### 2.3.4 Surface Loss

Finally, a slightly more difficult dissipation source to quantify is that of the surface. As resonator beams become much smaller (particularly as dimensions can reasonably be measured in terms of discrete atoms or molecules), the surface-to-volume ratio increases and the contribution of the surface dynamics to the overall behavior becomes more significant. Ono et al. discuss how adsorbates can lead to charge transfer and electrostatic forces between both the resonator material and adsorbates, and also between multiple adsorbates. One way to represent these dissipation sources is via the following combination of geometry and complex moduli of the resonator and lossy layer [9,92]:

$$Q = \frac{\pi r}{8\delta} \frac{E}{E_{SL}}, \quad (2.25)$$

where  $\delta$  and  $E_{SL}$  are, respectively, the thickness and Young's modulus of a hypothetical surface layer on the resonator.

In Chapter 3, we will talk more about the lack of major surface contamination on GaN nanowires. But, for illustrative purposes, we can use Equation 2.25 for an example with some rough numbers. Consider a thin surface layer,  $\delta = 0.1$  nm, that has a modulus of only 0.1% that of GaN. Combined with the results of Table 2.1, we find a limiting  $Q$  of approximately  $10^5$ . Given the small scale of our resonators, this is an illustrative example of how nanoscale objects – particularly

those at the ‘small’ end of ‘nano’ – can easily be influenced by surface effects. For this made-up-but-not-completely-unrealistic example, we see a limited  $Q$  that is approaching that of our observed nanowire  $Q$  factors. As is discussed further in Chapter 6, for absolute maximization of  $Q$  in these GaN nanowire resonators, some attention should also be paid to the surface.

These are four sources of dissipation that are routinely discussed in the literature of nanomechanics – particularly nanoscale beams. If we again recall Equation 1.1, which combines these sources of dissipation into a single value of limiting- $Q$ , we obtain:

$$Q_{tot} = \left( \sum_i Q_i^{-1} \right)^{-1} \approx 6 \times 10^4. \quad (2.26)$$

Though no single contribution to the limit on  $Q$  was of order  $10^4$ , we see that the combination of the four terms brings our estimate very near to the observations of GaN nanowire  $Q$  factors from own experiments.

## Chapter 3

### Scanning Electron Microscope-Based Measurements

Initial studies of GaN nanowire resonances are carried out in a somewhat unconventional environment: a scanning electron microscope (SEM) chamber. From there, the structures can be both imaged for geometrical analysis and, as we see later, measured in the midst of mechanical resonance. This Chapter presents the progression from the earliest fundamental measurements of GaN nanowires, to ‘applied’ use in a sensitive thin-film detection experiments, and then the transition from the SEM into capacitance-based measurements.

#### 3.1 Origins

The first work on GaN nanowires in the Rogers Lab was by two previous graduate students (now Drs. Jason Gray and Shawn Tanner) and their proof-of-concept work studying the nanowires in a scanning electron microscope (SEM). In their publication, Tanner et al. presented the first report of as-grown c-axis GaN nanowire mechanical resonances [47]. Importantly, they reported unexpectedly large mechanical quality factors,  $Q$ , typically of order  $10^4$ . At the time of publication, these values were reported to be approximately ten times larger than previously reported values for similar-sized structures comprising a-axis GaN nanowires [45], carbon nanotubes [93], and single-crystal silicon micro-structures [94]. In that work, Tanner et al. demonstrated the potential utility of GaN nanowire resonators as sensitive mass sensors. During his own graduate career, Dr. Gray continued to study GaN nanowire resonators in fixed-fixed beam geometry [95]. His experiments isolated individual nanowires and combined them with lithographic structures to investigate res-

onance properties [18, 95]. Some of the measurement techniques employed in these earlier studies have been continued and extended in this work.

### 3.2 SEM-Based Measurement Setup

As described in Section 1.4, the GaN nanowire MBE growth process produces a densely populated substrate with an areal nanowire density ranging from 1–10  $\mu\text{m}^{-2}$  (cf. Figure 1.6). Subsequently, this large number of nanowires allows for many opportunities to investigate the properties of individual nanowires. Measurement techniques involving an SEM allow us to obtain a variety of experimental results rapidly, though with some sacrifice in scalability. However, as reported below, many interesting results are obtained with this SEM measurement technique. In this document, most discussions of an SEM refer to the JEOL 6400 SEM in the JILA Keck Lab, typically operating at pressures on the order of  $10^{-7} - 10^{-6}$  Torr, and at room temperature.<sup>1</sup>

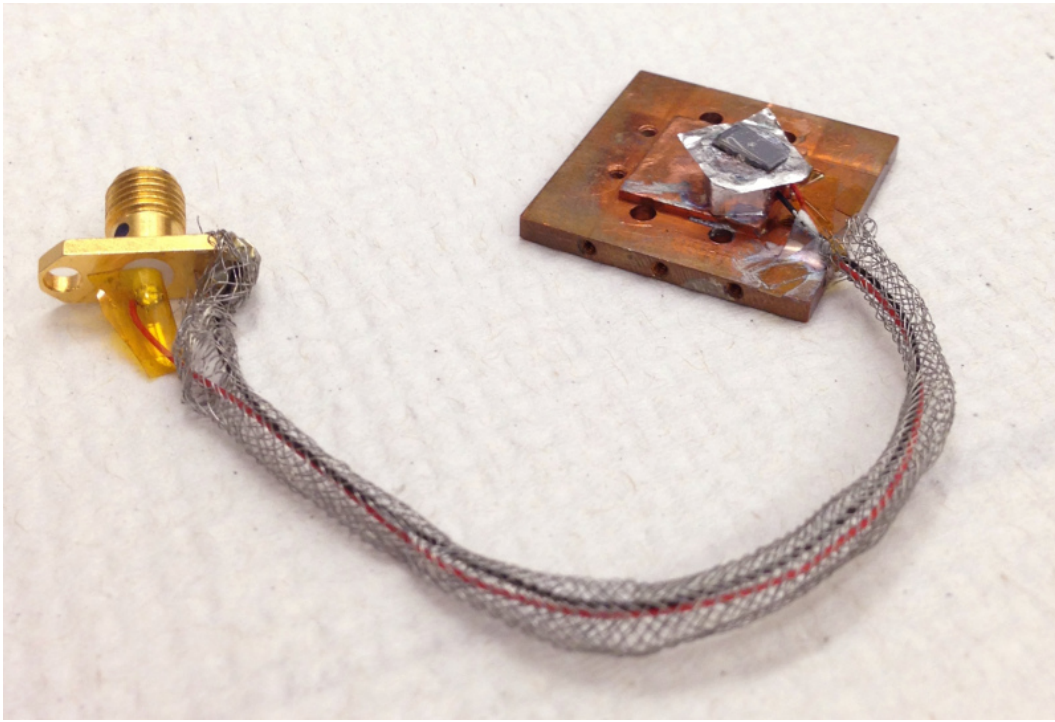
Since we are interested in the mechanical resonance properties of the GaN nanowires, it is necessary to have a source of excitation. An easy-to-implement method involves mounting a nanowire substrate portion (typically  $<1 \text{ cm}^2$ ) atop a Physik Instrumente lead-zirconate-titanate piezoelectric P-121.01 shear actuator (PZT). The PZT is fixed on a copper sample stage with silver paste (Ted Pella Leitsilber 200 Silver Paint). The assembled sample holder is shown in Figure 3.1. An attempt to electrostatically shield the PZT element is made by silver-pasting aluminum foil around the outside. The nanowire substrate is also fixed atop the foil with silver paste. Electrical connection to the PZT is made through an SMA connector attached at the end of the provided PZT leads. To relieve stress on the vulnerable PZT lead inserts, the wires are held down on the copper stage with kapton tape (barely visible in Figure 3.1 in the bottom-right corner of the copper).

The PZT actuator enables the transduction of electrical drive signals to physical nanowire motion. Explicitly, we can connect a signal source (e.g. a function generator) to the PZT through electrical feedthroughs in the sidewall of the SEM sample chamber. The ability to image nanowires

---

<sup>1</sup> Near the end of this thesis work, we also demonstrate some early success in replicating these experiments in the Keck Lab’s newer field emission SEM – an FEI NanoSEM 640 – under similar operation conditions (pressure and temperature).

Figure 3.1: The sample holder for initial SEM-based GaN nanowire measurements. A  $\sim 1$  in<sup>2</sup> copper stage holds the PZT element (covered in aluminum foil), and the nanowire substrate sample (dark gray rectangle) is on the top of the foil.

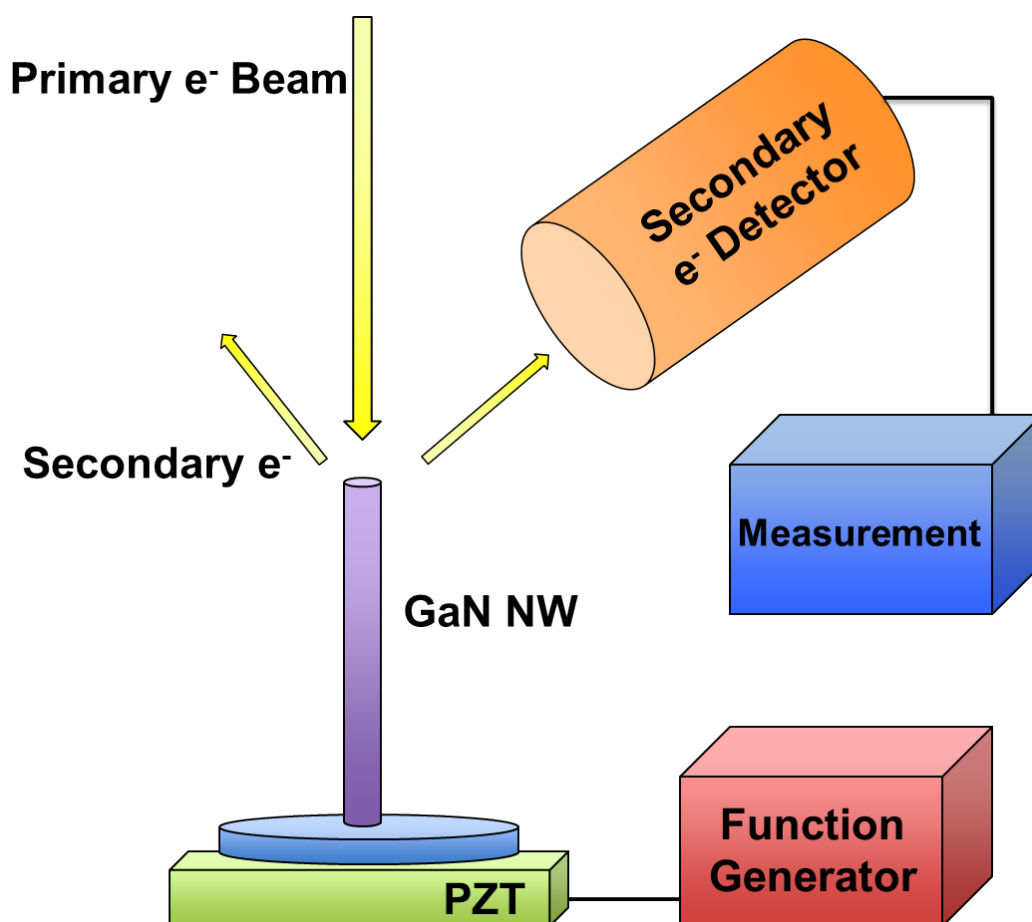


in the SEM by collection of the secondary electrons scattered by the nanowire surface is precisely the mechanism used to acquire information about time-dependent mechanical motion, as shown in Figure 3.2.

In so-called ‘Spot Mode,’ the SEM electron beam is switched from the conventional raster mode to a tightly focused, stationary point near the center of the field of view with a Gaussian beam profile a few nanometers in width. To acquire resonance data on an individual nanowire, the sample stage and beam location are adjusted until one of the high-contrast top edges of the hexagonal nanowire cross section is centered in the beam spot. Subsequent motion of the nanowire results in time-dependent modulation of the number of scattered secondary electrons collected by the photomultiplier tube (PMT) and the resultant electronic output voltage.

The PMT electronics are capable of digitizing at a maximum rate of  $\sim 3$  MHz. It is possible for similar GaN nanowires to resonate above this frequency, but the geometries of those investigated

Figure 3.2: General schematic illustrating the experimental setup for SEM-based measurements. The primary electron beam (typically in 'Spot Mode') is incident on a particular nanowire of interest. The scattered secondary electrons are collected by the scintillator and the photomultiplier output signal is collected for analysis.



here (particularly their 10–15  $\mu\text{m}$  length) tend to lead to values in the vicinity of 1 MHz. The aforementioned large areal nanowire density means that sampling even a small population of the available nanowires still yields a large number of potential resonances to study. For example, measuring just 1% of the nanowires on a  $0.25\text{ cm}^2$  chip with a  $1\ \mu\text{m}^{-2}$  density yields a total of 250,000 possible nanowires. With such a large number of possible nanowires, and an understanding of how the scattered electron beam signal may be used for analysis, we now must decide what to do with the output signal.

### 3.3 SEM-Based Measurement Techniques

The two SEM-based techniques employed in this work are a noise-driven power spectral density (PSD) measurement and a phase-sensitive lock-in measurement. Both have advantages, depending on what information you would like to acquire and how fast you would like to do so.

To begin data acquisition using either of these techniques, we begin by using a function generator to apply a frequency-independent, broadband white noise signal ( $\leq 10\text{ MHz}$ ) to the PZT and nanowire sample. In this experiment, we use a Stanford Research Systems DS345 function generator. Assuming ideal, uniform transduction of this noise signal to the sample, we would expect that all nanowires with fundamental resonance frequencies below 10 MHz to be excited at some level. However, the PZT response to applied voltages falls off at higher frequencies due to its own fundamental resonance near 300 kHz. Nevertheless, we observe nanowire resonances as high as 3 MHz using this PZT. The susceptibility of a particular nanowire to physically deflect is expected to be a function of its unique geometry, nearest neighbors, and possibly variations in internal structure (e.g. defects). Empirically, the majority of investigated nanowires have a visible response when subjected to noise drive. The small number of nanowires that do not move are lacking obvious common attributes. However, as a result of the large nanowire aspect ratio it is difficult to observe beyond the top few microns of a sample under plan-view (cf. Figure 1.6), excepting nanowires along a wafer edge. Therefore, it is possible that there exists an obstruction or other form of contamination between nanowires that impedes motion.

Once an particular nanowire has been chosen, the applied noise drive is chosen such that the nanowire is barely observed to move. Practically speaking, when viewing the nanowires with a properly aligned, focused, and stigmated, rastering electron beam, small-amplitude motion is assumed when the high-contrast nanowire tip edges begin to blur. Deflection amplitude in this scenario is approximately at the level of nanometers. At this point, the electron beam is switched from rastering to Spot Mode and centered on a nanowire vertex. The location of the electron beam spot can be precisely identified by the on-screen crosshairs and adjusted by the corresponding SEM control panel knobs. In order to retain the ability to image the nanowire sample without excessive connection and disconnection of cables, the coaxial PMT output is split between the control panel display and our measurement apparatus.

### 3.3.1 Power Spectral Density Measurement

SEM-based power spectral density (PSD) measurements progress through an evolution of equipment. For the sake of preservation, I'll briefly run through the sequence of work, ultimately describing the most useful version.

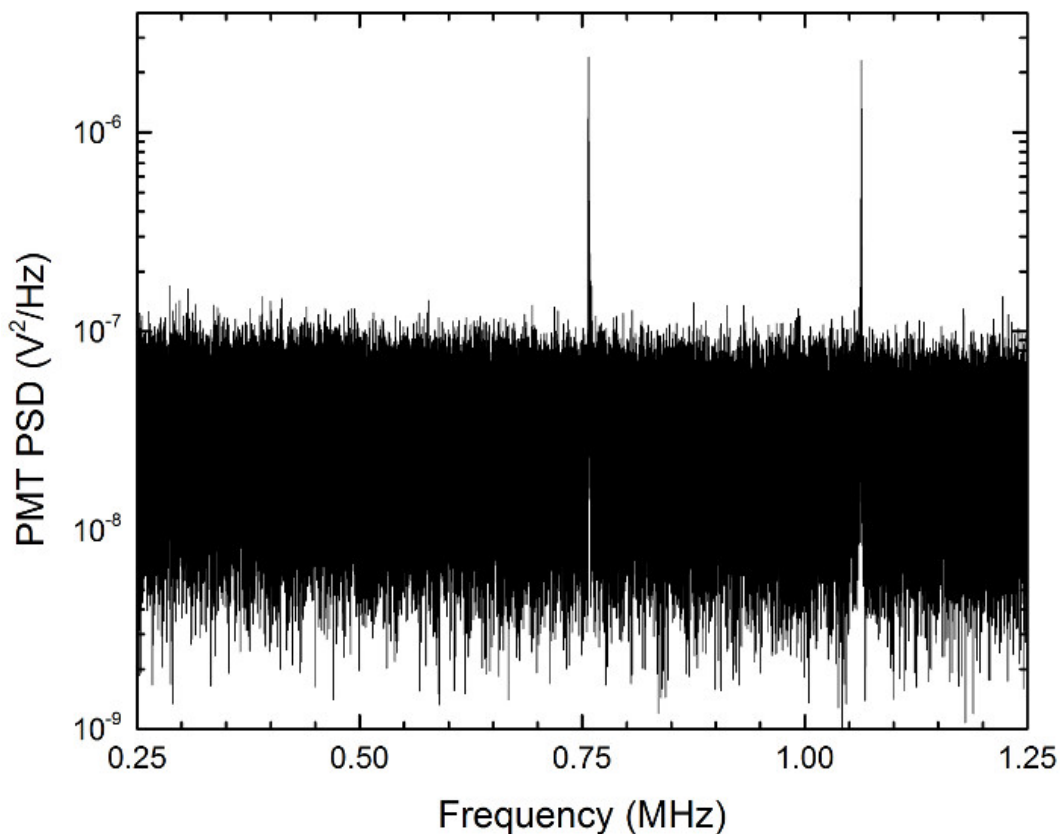
The earliest measurements in this work are taken by connecting the PMT output directly to the input of a Tektronix RSA5000 spectrum analyzer. This setup is extremely simple, fast to set up, and allows for local saving (and later retrieval) of data. However, the limited amount of internal memory within the RSA5000 leads to broadband measurements – the type in which we are predominantly interested – of rather low frequency resolution (e.g. 10s of Hz). We prefer to have greater resolution in order to accurately measure resonance linewidths on the order of 5 – 10 Hz. Furthermore, the RSA5000 is a shared piece of equipment and is frequently in use by many other research groups.

In order to both have more control over the measurement equipment and to increase resolution, we begin acquiring data with a 'homemade' power spectrum analyzer. PSD measurements in this arrangement were facilitated by the use of a LeCroy 9304A oscilloscope, Stanford Research Systems SR844 200-MHz lock-in amplifier — both addressed via General Purpose Interface

Bus (IEEE-488, GPIB) connections — and National Instruments LabView software running on a Windows-based computer.

The first step — as with the RSA5000 before — is to identify the fundamental resonance frequencies of the selected nanowire. To do this, we produce a broadband PSD (typically dc–1.5 MHz bandwidth) by taking the PMT output to the oscilloscope input. The corresponding time record data is brought into LabView where a PSD is calculated and displayed on-screen. This data is typically quite clean, with large signal to noise ratio (SNR) in the nanowire resonance peaks. A higher-resolution version of such a dataset (taken with equipment to be discussed below) is shown in Figure 3.3 and reveals two resonance peaks. This observation of two peaks instead of one is discussed further in Section 3.5.

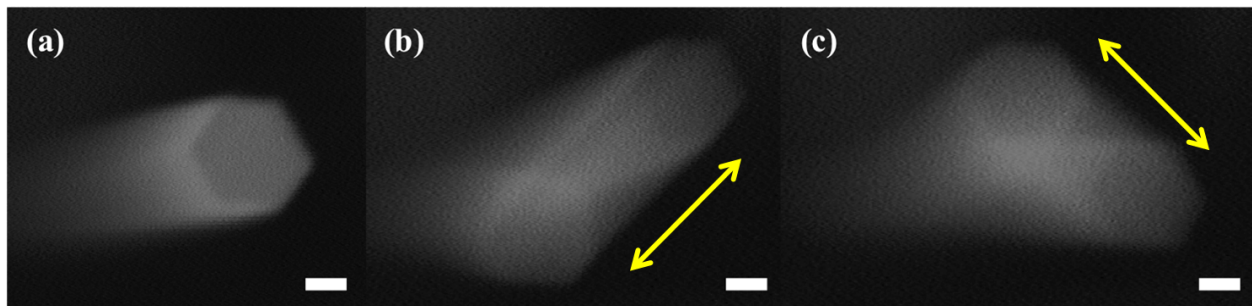
Figure 3.3: Typical PSD of SEM PMT output, taken with a high-resolution National Instruments NI-Scope. The peaks near 750 kHz and 1.05 MHz are the two fundamental resonance modes of the nanowire being investigated.



Though these observed lower-resolution PSD peaks are typically orders of magnitude above the background signal, it is possible to definitively identify the peak positions by driving the resonance modes and visually confirming nanowire response. By choosing to drive the PZT at a fixed tone (e.g. sinusoidal function generator output) sufficiently above or below the resonance – that is, much greater than the resonance half-width – and sweeping the tone frequency through the observed resonances, the rastering SEM image clearly shows the resonant displacement of the nanowire tip grow from zero (off resonance) to large-amplitude displacement (on resonance), as shown in Figure 3.4 (cf. the fundamental modeshape discussed in Section 2.1). Having identified the frequencies of interest, we can proceed with either the higher-resolution PSD or two-phase measurement.

The frequency resolution and bandwidth of a Fourier-transformed time record is determined completely by the parameters of the data acquisition. One way to parametrize this is in terms of the number of samples  $N_s$  (#), and the sampling rate  $R_s$  (Hz). A measurement made with these parameters will require an acquisition time  $N_s/R_s$  (s). When transformed to frequency space, the resulting spectrum has a maximum frequency (bandwidth)  $R_s/2$  Hz and resolution of  $R_s/N_s$  (Hz). As does most hardware, the LeCroy oscilloscope has a fixed amount of internal memory that limits the number of samples possible in a single acquisition. Once we have utilized the maximum number

Figure 3.4: Nanowire fundamental resonance frequencies are confirmed visually by sweeping the PZT actuation signal through the frequencies seen in the PSD. The visible fanning of the nanowire tip (consistent with fundamental cantilever modes) is observed. For the nanowire seen in (a), the modes shown in (b) and (c), respectively, are near 851 kHz and 691 kHz. The existence of two non-degenerate frequencies is discussed in Section 3.5.1. All scale bars are 100 nm.



of samples, the only way to further increase frequency resolution is to decrease the measurement bandwidth. Once the maximum PSD frequency is reduced below the resonance frequency of interest, the measurement is no longer capable of detecting the nanowire. However, we can circumvent the issue of limited oscilloscope memory with the use of non-linear circuit components that heterodyne (or ‘mix down’) the SEM PMT signal to lower frequencies.

Briefly, heterodyning is a signal processing technique that uses a nonlinear element — typically some form of frequency mixer — combining two unique frequencies to shift one of them into a new frequency range. Often (as in this work), it is used to move a difficult-to-measure high-frequency signal to a lower frequency. In the language of an ideal mixer, the high-frequency (RF) signal  $\omega_{RF}$  is multiplied by an arbitrary local oscillator (LO) signal  $\omega_{LO}$  and the two resultant signals are given by the trigonometric identity:

$$\sin(\omega_{RF}t) \sin(\omega_{LO}t) = \frac{1}{2} \cos[(\omega_{RF} - \omega_{LO})t] - \frac{1}{2} \cos[(\omega_{RF} + \omega_{LO})t]. \quad (3.1)$$

Thus, the desired, difference intermediate frequency (IF)  $\omega_{IF} = \omega_{RF} - \omega_{LO}$  is obtained by low-pass filtering the mixer IF products. For a more detailed discussion of radio frequency electronics techniques, see Ref. [96]

Though any non-linear mixer-like component would work, we make use of the SRS SR844 lock-in amplifier and its built-in frequency source. This provides us with the option of selectively choosing the LO frequency and determining the position of the resulting IF frequency that contains the nanowire resonance information. The lock-in amplifier provides two outputs which are the detected phase-sensitive signal levels (one  $90^\circ$  phase adjusted from the other) in addition to the digital LED displays. These output signals are then both IFs, either of which we can use as the input to the digital oscilloscope.

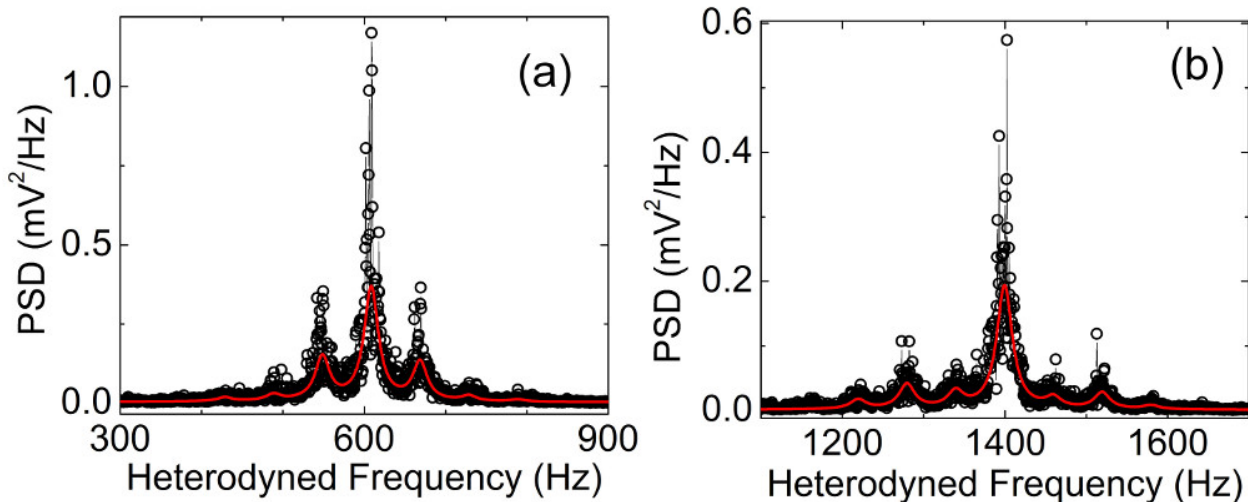
The IF signal of interest — along with all other signals contained in the PMT output — is now at  $\omega_{IF} = |\omega_{RF} - \omega_{LO}|$ . In order to extract the correct absolute nanowire resonance frequency, we measure two PSDs with unique LO frequencies — one above the expected nanowire frequency

and one below. For simplicity, the LO frequencies are typically chosen to be at the nearest or next-nearest kilohertz, both above and below the nanowire resonance. After fitting this data, we can use the known LO frequency to algebraically determine the central nanowire frequency. Figure 3.5 shows an example of two heterodyned PSD peaks.

Typically observed in these SEM-based heterodyned nanowire PSDs are 60-Hz sideband peaks, attributed to frequency mixing between the nanowire central resonance peak and 60 Hz noise in the PMT electronics. These sidebands share a shape identical to the central nanowire peak, but appear at uniform 60 Hz distances from — both above and below — the central peak. They are easily incorporated into the peak-fitting algorithm by including copies of the central peak at 60 Hz intervals, with decreasing amplitudes, as shown in Figure 3.5. We then fit these PSD data using a squared Lorentzian response function appropriate for such a damped harmonic oscillator (as described in Chapter 2).

Finally, our data acquisition currently benefits from the use of a dedicated high-speed digitizer, a National Instruments USB-5133 ‘NI Scope.’ This device has a larger on-board memory (32

Figure 3.5: Two heterodyned PSD measurements for one mode of a GaN nanowire. The local oscillator (LO) frequencies for (a) and (b) are, respectively 458 kHz and 460 kHz. Solid red lines are squared Lorentzian fits to the data including 60 Hz sidebands resulting from mixing products with SEM circuitry noise. The combined fit results show  $f_o = 458, 608.7 \pm 0.3$  Hz and  $Q = 21, 500 \pm 600$ .



or 64 MB), and is capable of sampling at 100 MHz. With this, we can convert the PMT output directly into PSD data faster and with higher resolution than before. An example of this type of data is seen in Figure 3.3.

Whichever our method of data acquisition, the PSD technique allows broadband measurements that contain the relevant mechanical resonance information — central frequency and peak width — that allows us to calculate  $Q$  values. As long as the acquisition parameters are within the hardware specifications, we can record data over a large bandwidth. It is still possible that we may run into issues of resolution and sampling rate that can be resolved with another type of measurement scheme; namely, a two-phase lock-in measurement.

### 3.3.2 Phase-Sensitive Lock-In Measurement

The second method of acquiring nanowire resonance data in the SEM environment is with a phase sensitive lock-in measurement. The main advantage of using lock-in detection is that the measurements are no longer bandwidth-limited (the sampling time at each individual frequency determines the acquisition time). Having the two phase components separated can also be beneficial in some circumstances. For a reminder of the functional form of the two signal phases, see Section 2.2.

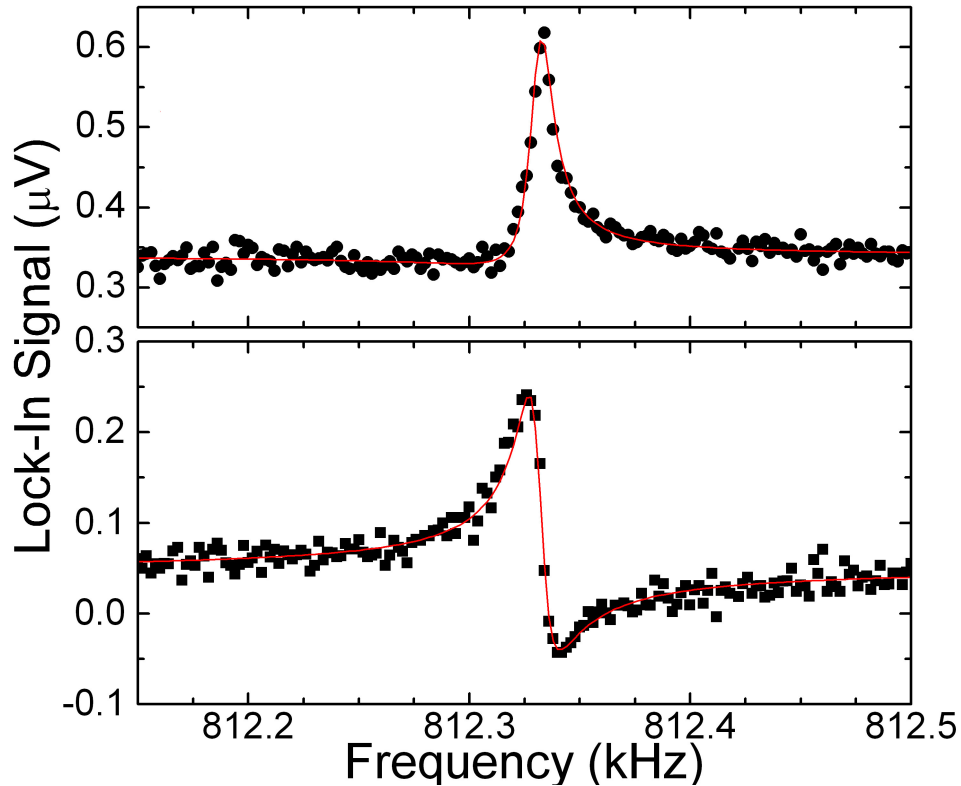
This type of measurement effectively uses a lock-in amplifier as a sensitive homodyne mixer. Once the nanowire resonance frequencies have been identified in a low-resolution PSD — as described in Section 3.3 — we take the full PMT output signal into the lock-in amplifier input (RF) while sweeping the PZT drive frequency (via function generator) through the nanowire resonance. The function generator output is simultaneously sent to the lock-in to serve as an external frequency (LO) and phase reference.

A typical lock-in measurement involves specifying a starting frequency, an ending frequency, and an incremental frequency step between them. At each specified frequency, the amplifier will acquire data according to the chosen parameters. The key front-panel data acquisition parameter on the SRS SR844 (and SR830) lock-in amplifier is the time constant (often  $\tau$ ). It is helpful to

select a time constant that is a few times larger than the characteristic damping time of nanowire oscillation. This means we often choose  $\tau \approx 3 \times (\text{resonance peak FWHM-power, } \Gamma)^{-1}$ . This allows the resonator sufficient time to ‘ring-up’ or ‘-down’ at each drive frequency and produce a consistent lock-in signal. After being collected and saved, the resulting data from the two phases can be fit simultaneously — the two data sets share parameters such as resonance frequency and peak width — to produce a result like that shown in Figure 3.6.

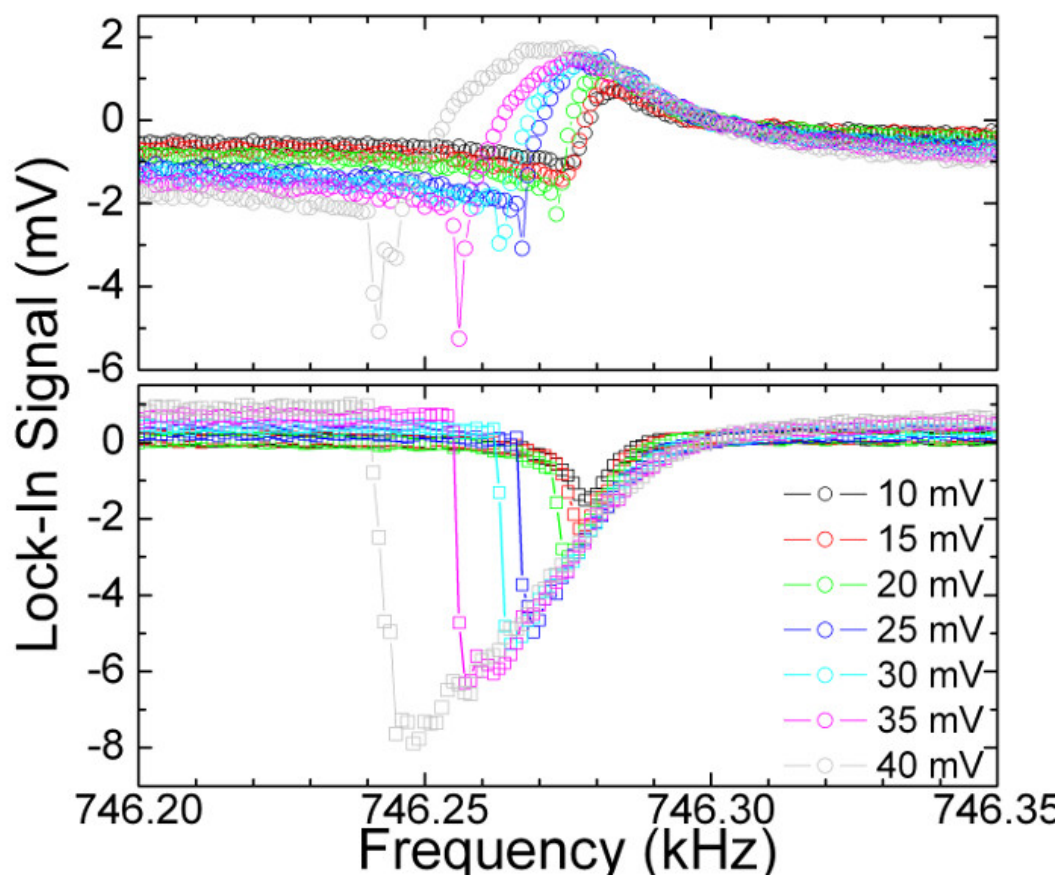
The typical lock-in measurement acquires data while sweeping from starting frequency to ending frequency, then back to starting frequency, etc, for a specified number of (forward-backward) sweeps. These sweeps (or the separate forward or backward traces) can be averaged at runtime – or afterward – to reveal small signals embedded in noise. Due to this tracing of the data, the lock-in

Figure 3.6: Data from a phase-sensitive lock-in measurement of a nanowire resonance in an SEM. Red curve is a simultaneous fit to both datasets resulting in  $f_o = 812,250 \pm 0.2$  Hz and  $Q = 62,000 \pm 1000$ .



measurement has the advantage of more easily showing deviations from linearity and transitions into nonlinearity via hysteretic response. The type of hysteretic trace shown in Figure 3.7 is commonly observed when the amplitude of the drive source is large enough to elicit a non-linear response. As is mentioned later in the context of Section 4.2.1, further investigation into the transition from linear response to non-linear response is one of the more interesting and approachable future directions for this work.

Figure 3.7: An example of the hysteretic, nonlinear response observed when a nanowire is over-driven during a two phase, lock-in measurement. The degree of nonlinearity can be seen to increase at increasing PZT drive amplitude (key in lower right).



### 3.4 First Nanowire Ensemble Measurement

During our SEM-based measurements we also make a first attempt at simultaneously detecting the motion of an ensemble of nanowires. As introduced in Section 3.2, the measurements described thus far took advantage of ‘Spot Mode’ and focused the electron beam into a tight region trained on the edge of a single nanowire. However, in this ensemble experiment, the electron beam is left in rastering mode — the mode in which it typically produces a continuous image — and a large (e.g. a few volts rms) white noise signal is applied to the PZT actuator.

The PMT output is again sent to the NI Scope digitizer and we can process the signal to produce a similar PSD to that described in Section 2.2.2. The signal to noise ratio of the resulting spectrum is quite low, and so a larger-than-usual PZT drive is required (e.g. 100 mV – 1 V for a single nanowire in Spot Mode versus 1–10 V for this ensemble measurement). But, at the few-volt level of white noise, we begin to see peaks emerge from the PSD background. An example PSD is shown in Figure 3.8. After identifying the central frequency in these peaks, we proceed to drive the PZT at these frequencies and observe the fanning effect described in Section 3.3.1 and shown in Figure 3.4. For one particular nanowire (A), both modes are seen in the PSD, separated by approximately 200 kHz.

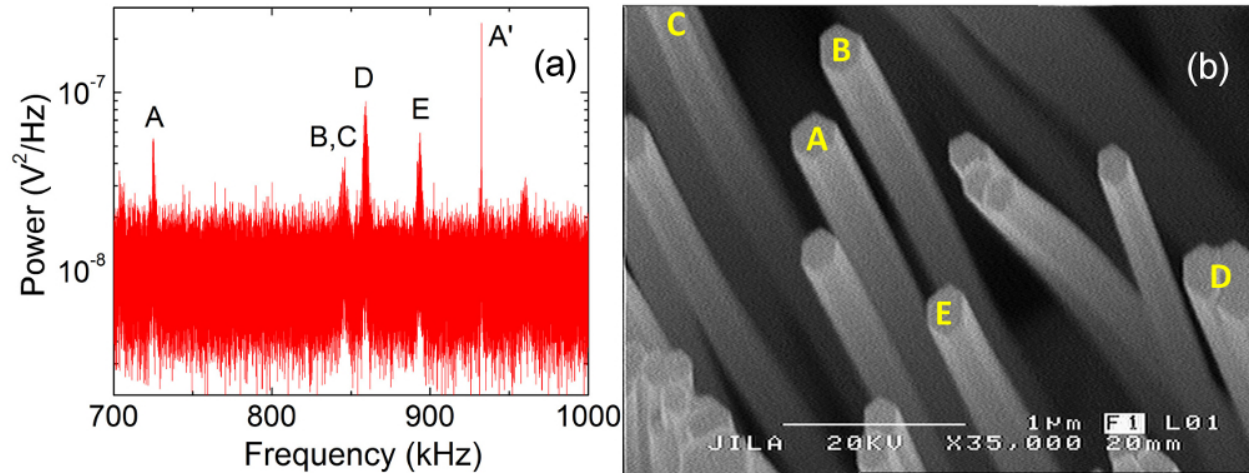
Though this technique is not explored very thoroughly in the SEM environment, such an ensemble measurement will later become a significant technological development in this project.

### 3.5 Understanding SEM Results Through Finite Element Modeling

#### 3.5.1 Lifting Mode Degeneracy

Despite the discussion of the symmetry-induced degenerate fundamental resonance frequencies in Section 2.1, the measurements described above nearly always result in two low-lying, non-degenerate resonance modes (cf. Figure 3.3). To understand the origin of this observation, the singly-clamped GaN nanowire resonator system is simulated within the commercial finite element modeling (FEM) software package ANSYS Mechanical (see also Appendix C for code and in-

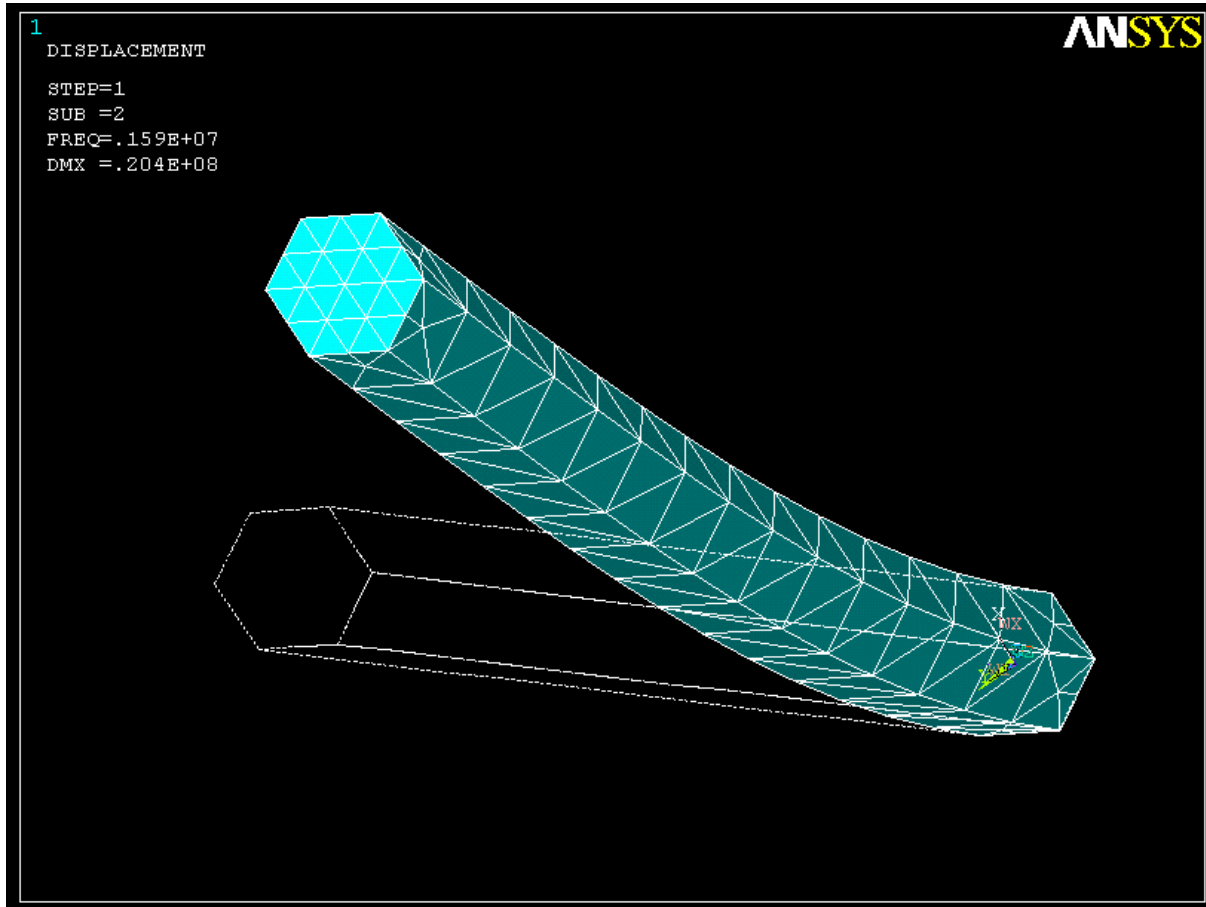
Figure 3.8: One of the early attempts at simultaneously measuring an ensemble of nanowire resonators, within an SEM. Large drive signals are required to bring nanowire resonance peaks out of PSD noise. Peaks in the PSD are identified by letters in (a) and are confirmed using the tone-drive verification technique shown in Figure 3.4 and arise from the motion of the corresponding labeled nanowires in (b). Peak A and A' in (a) are the two modes of the nanowire labeled A in (b).



structions). Given a right volume with regular hexagonal cross section and appropriate material properties (density and elastic modulus) and geometry, the harmonic analysis of the nanowire mechanical resonance modes does indeed produce two degenerate resonance frequencies (to within the numerical precision of the simulation) at approximately the frequency predicted by Equation 2.5. A screenshot from such a modal analysis on a nanowire 15  $\mu\text{m}$  in length and with 200 nm side-length is shown in Figure 3.9. The numerical solution of this analysis gives a fundamental frequency near 1.5 MHz.

However, when a small irregularity is added to the hexagonal cross section – while maintaining interior  $120^\circ$  angles, as has been observed by SEM imaging – the same harmonic analysis shows two non-degenerate fundamental resonance modes. The strength of the mode separation is proportional to the difference in the hexagonal side lengths. A difference in opposing side lengths of only a few nanometers results in a mode split on the order of kHz. Appendix C contains the simulation code and further information on these ANSYS models. Based on a long history of imaging these GaN nanowires in an SEM, it is certainly the case that a typical nanowire will have such side length

Figure 3.9: Screen capture from a finite element modal analysis of a cantilever GaN nanowire resonator using ANSYS Mechanical simulation software. Using the GaN material properties described in Section 1.4, a length of 15  $\mu\text{m}$  and radius of 200 nm, the solution converges to a fundamental frequency of about 1.5 MHz. This is in good agreement with a calculation using Equation 2.5.



differences.

### 3.5.2 Nanowire Taper

Additional insights into our results are gained through FEM analysis of the effects of c-axis taper on nanowire resonance frequencies. The standard Euler-Bernoulli beam theory discussed in Section 2.1 and [67] deals with right-volumes. That is, in our case, the nanowire sidewall should meet the substrate at a  $90^\circ$  angle. However, SEM images have shown that this is not usually the case. As described in [53], the MBE growth environment produces preferential sticking at the

nanowire tip. Because of the lower sticking coefficient on the m-plane nanowire sidewalls, Ga atoms impinging on the surface will likely desorb back into the chamber. The result is a tapered thickness along the length of the nanowire, most obvious near the base section. In Figure 3.10, this effect can be seen.

As one might expect, when the geometry of the nanowire changes, so too does the resulting resonance frequency. To see this, we use the same ANSYS model described above with a regular hexagonal cross section. Then, we vary the shape of the nanowire by linearly connecting top and bottom surfaces with different relative cross-sectional area. Figure 3.11 shows the results: decreasing the relative size of the nanowire base (consistent with an etching process) lowers the fundamental resonance frequency. By combining these models and results, we are able to both resolve the discrepancy between our initial calculations and experimental results, and also corroborate the original GaN nanowire work of Tanner and Gray [47].

### 3.6 Effects Of Atomic Layer Deposition On Resonators

One of the ways in which the SEM-based measurement techniques are used in a practical application, is to observe the effects of atomic layer deposition (ALD) films on GaN nanowire resonance properties [19]. ALD film technology has long been an active research area with substantial roots here at the University of Colorado in Prof. Steven George's research group [97]. In collaborating with the George group and others, we find that nanowire vibrational frequencies can readily distinguish conformal film growth from island growth, and that  $Q$  factors are sensitive to mechanical dissipation losses in the ALD films. Thus, GaN-NW mechanical resonators have great potential for monitoring ALD film growth mechanisms.

A simple picture of how nanowire resonators are sensitive to thin film processes is provided by the beam theory for the cantilever flexural resonance modes given by Equation 2.5. As an illustrative example, consider how this formula as applies to a right cylindrical cantilever with radius  $r$ , second moment  $I_y = \pi r^4/4$ , material properties  $X_1$ , and with the addition of a thin material layer of thickness  $t$  and with material properties  $X_2$ . In this situation, the Euler-Bernoulli

analysis of Section 2.1 gives a resonance frequency:

$$\omega_o = \frac{1}{2} \left( \frac{E_1 r^4 + E_2 ((r+t)^4 - r^4)}{\rho_1 r^2 + \rho_2 ((r+t)^2 - r^2)} \right)^{1/2} \left( \frac{1.875}{L} \right)^2. \quad (3.2)$$

For ALD films, we consider  $t \ll r$ , and can consider the first-order shift in resonance frequency  $\delta\omega$  –from the  $t = 0$  value– due to the additional of the ALD layer,

$$\delta\omega = \omega_o \cdot (2\tilde{E} - \tilde{\rho}) \cdot \frac{t}{r}, \quad (3.3)$$

where  $\omega_o$  is the original resonance frequency and  $\tilde{E}$  and  $\tilde{\rho}$  are, respectively the ratios of the film's elastic modulus to GaN's modulus and film density to GaN density. We note that for long, thin beams such as these GaN nanowires, the ratio  $\omega_o/r$  is independent of radius, indicating that  $\delta\omega_o$  should be similar even for nanowires of rather different initial  $\omega_o$  and  $r$ .

Figure 3.10: SEM micrograph of GaN nanowire growth C144. The dark portion at the bottom is the silicon wafer, topped by the GaN matrix layer. Out of this, the nanowires are seen growing to a height of approximately 12  $\mu\text{m}$ . (Figure courtesy of NIST)

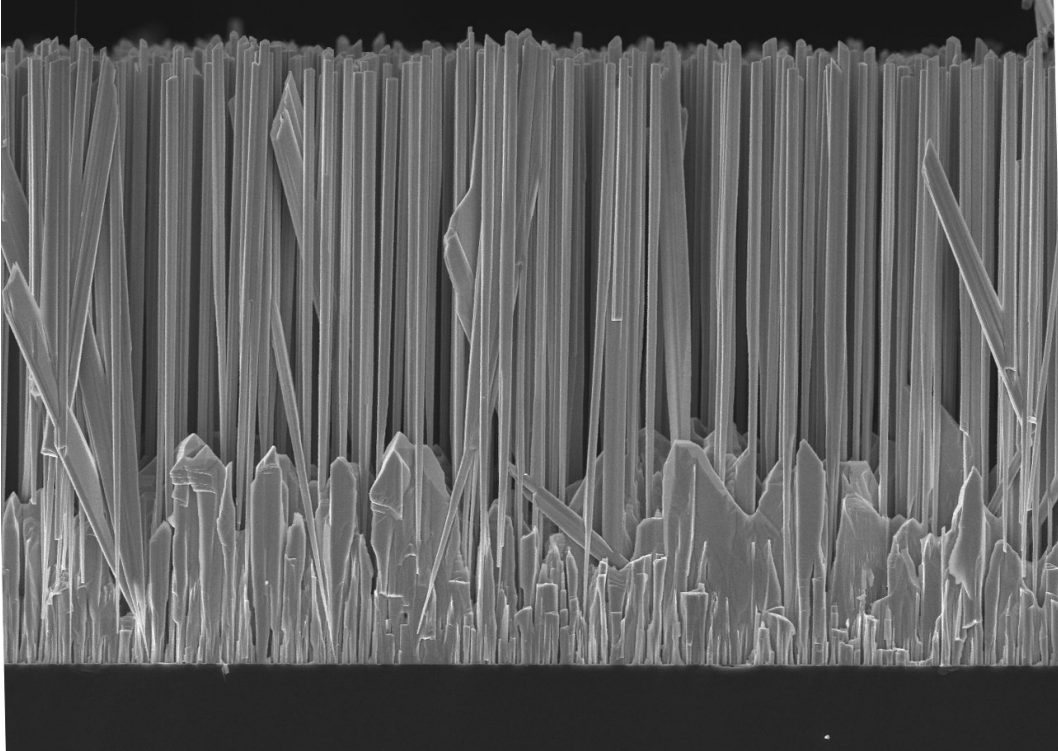
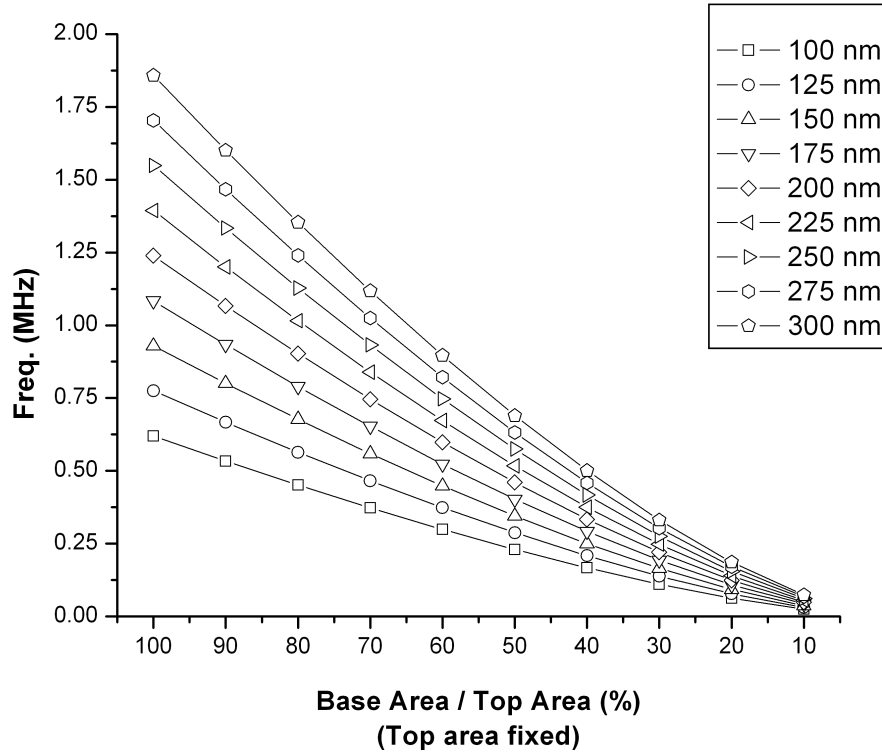


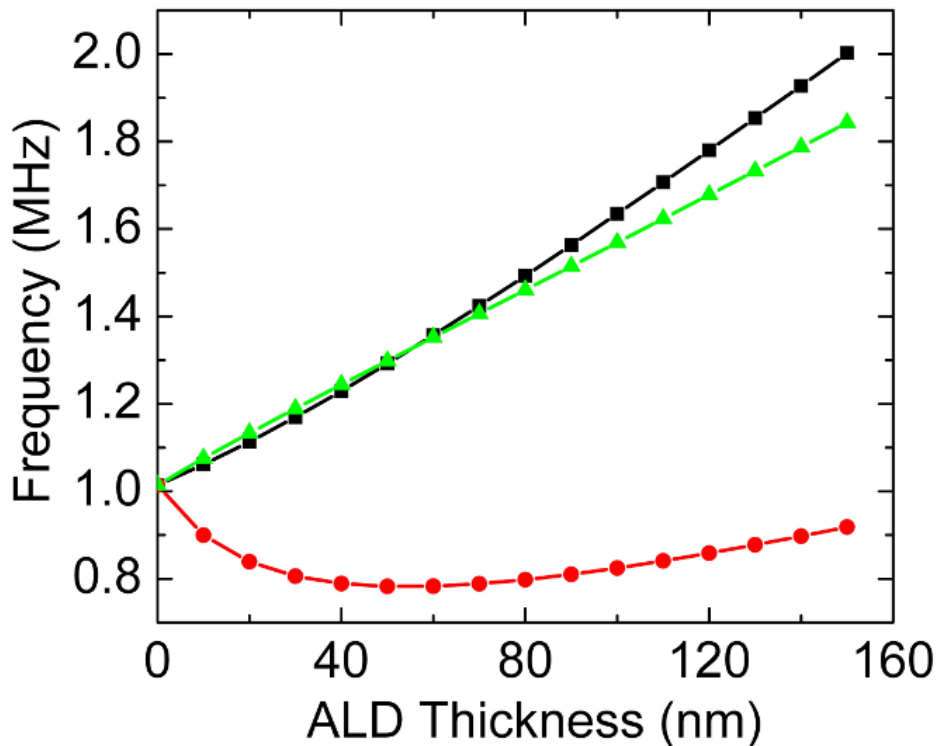
Figure 3.11: Model results from ANSYS simulation of the effect of nanowire tape on fundamental resonance frequency. Nanowire lengths are fixed at 15  $\mu\text{m}$  and side lengths / radii are varied as indicated in the legend.



Equation 3.3 demonstrates that for any particular nanowire, the behavior of the resonance frequency depends on the relationships between the film and GaN properties. As an example, Figure 3.12 shows theoretical resonance frequencies versus ALD film thickness based on Equation 3.2. The data represent the effects of ALD  $\text{Al}_2\text{O}_3$  (alumina), ruthenium (Ru), and platinum (Pt), all starting with an initial resonance mode at 1 MHz.

Figure 3.12 shows that for alumina and Ru, effective stiffening of the nanowire-ALD composite resonator dominates, causing an overall increase in resonance frequency. For high-density Pt, effective mass loading dominates initially, followed by effective stiffening for thicker films. Our experimental results qualitatively confirm these trends.

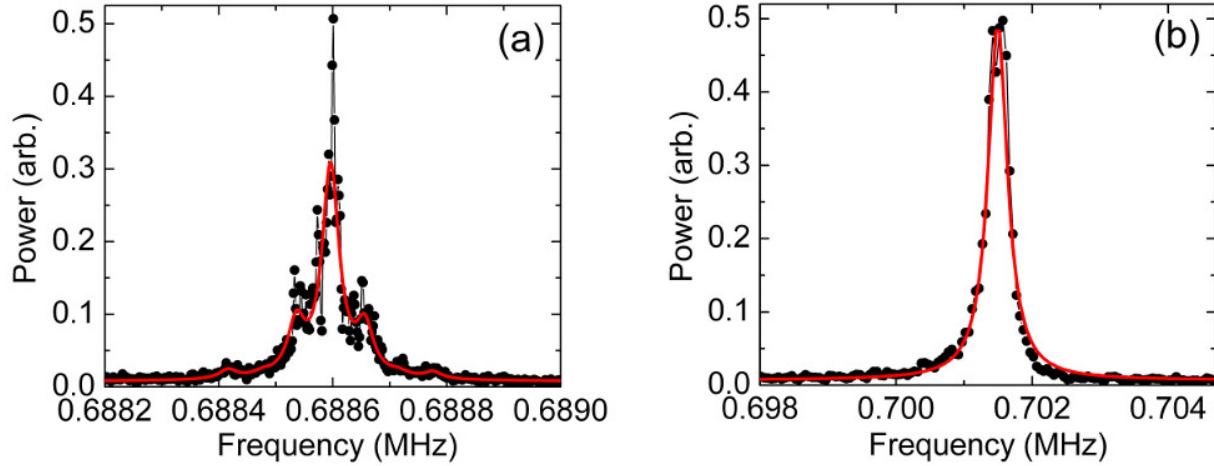
Figure 3.12: Predicted resonance frequency shifts for conformal growth of ALD materials on GaN nanowires from Equation 3.2. Black squares, green triangles, and red circles represent, respectively, alumina, Ru, and Pt. Initial, bare nanowire resonance frequency is set to 1 MHz. The ALD material properties are described in the text.



### 3.6.1 Conformal Alumina ALD Films

An example set of data showing the effects of a 4.6-nm ALD alumina deposition on nanowire resonance frequency and linewidth is shown in Figure 3.13. This work is done in collaboration with graduate students in Prof. Steve George's chemistry group. ALD alumina films are deposited on nanowire samples at 120°C, with  $\text{Al}(\text{CH}_3)_3$  and  $\text{H}_2\text{O}$  as precursors. The growth rate is about 1.2 Å/cycle. The mechanical properties of these ALD alumina films have been characterized previously: Tripp et al. [98] reported a Young's modulus in the range  $E = 168 - 182$  GPa and a density  $\rho = 3.03$  g/cm<sup>3</sup>. These values differ somewhat from the respective bulk values of  $E = 370$  GPa and  $\rho = 3.97$  g/cm<sup>3</sup>. Using these reported ALD material properties, Equation 3.3 predicts a shift in

Figure 3.13: Fundamental resonance peak for a single GaN nanowire mode. (a) Spectrum of a bare nanowire, before ALD coating. Solid curve indicates a Lorentzian fit showing  $f_o = 688,596 \pm 1$  Hz,  $Q = 19,000 \pm 2000$ . (b) Spectrum of same nanowire peak after 4.6-nm ALD alumina coating. Solid curve indicates a Lorentzian fit showing  $f_o = 701,495 \pm 9$  Hz,  $Q = 2000 \pm 200$ . Note enlarged frequency scale and increase in linewidth obscuring 60-Hz sidebands.

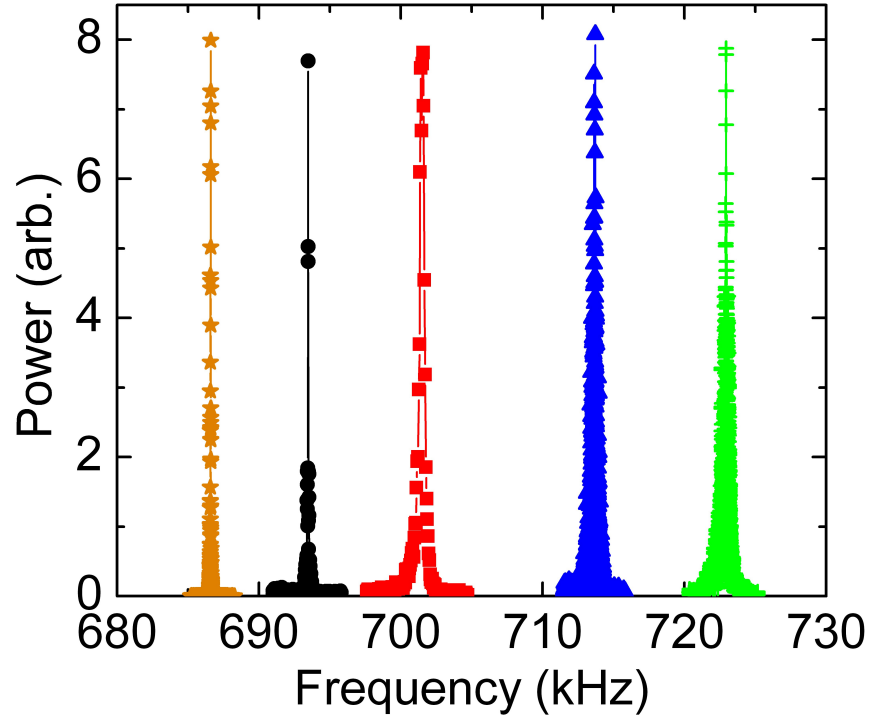


resonance frequency of 4-5 kHz per nanometer of added alumina.

The progression of resonance frequency shifts for a single mode of one nanowire-ALD composite resonator after three consecutive ALD depositions is shown in Figure 3.14. The initial peak is near 695 kHz and the ALD depositions are, respectively, 4.6 nm, 4.5 nm, and 3.9 nm, as measured by ellipsometry on a separate silicon wafer. With the first ALD alumina deposition, a Lorentzian fit to the peak reveals roughly an order of magnitude increase in the linewidth — approximately from 30 Hz to 330 Hz, in addition to an increase of about 13 kHz in frequency. As seen in Figure 3.14, measurements after successive ALD depositions show the peak linewidth does not increase much more, but the frequency continues to increase. After three depositions, the nanowire substrate and ALD layers were etched in an aqueous hydrofluoric acid (HF) bath and oxygen ( $O_2$ ) plasma reactive ion etch (RIE). After this process, the nanowire resonance is observed to return very close to its original frequency and linewidth, demonstrating how robustness of the GaN nanowire structure.

A collection of data similar to Figure 3.14 for a collection of six unique nanowire modes is shown in Figure 3.15. Here, we see that with each successive ALD alumina deposition, resonance

Figure 3.14: Change in resonance behavior for one mode of a single GaN nanowire after ALD alumina depositions and removal. The bare nanowire (black circles) is sequentially coated with ALD alumina layers of thickness 4.6 nm (red squares), 4.5 nm (blue triangles), and 3.9 nm (green crosses). After aqueous HF etching to remove the ALD alumina, followed by a brief O<sub>2</sub> RIE exposure to remove organics, the resonance frequency drops to near original value (orange stars). Note also the increased linewidth in ALD spectra, as compared with bare and etched peaks.



frequencies increase nearly linearly with deposition thickness. Occasionally, we observe abrupt increases in nanowire resonance frequencies, as seen in the pink-square data ( $f_o(t = 0 \text{ nm}) \sim 530 \text{ kHz}$ ) in Figure 3.15.

This data follows the trend common to the other five nanowires until the third alumina deposition. At this point, the resonance frequency is observed to increase by  $\sim 125 \text{ kHz}$ . Such large increases are observed infrequently, occur only once for any one nanowire, and simultaneously affect both orthogonal modes. We have attributed this behavior to an effective shortening of the nanowire due to the ALD film filling the matrix layer at the nanowire base, as illustrated schematically in Figure 3.16. The GaN matrix layer can also be seen in Figure 3.10. The resulting

Figure 3.15: Increase in GaN nanowire-ALD composite resonator frequency after ALD alumina coatings of 4.6, 4.5, and 3.9 nm. "HF etch" and "RIE" correspond, respectively, to a hydrofluoric acid etch and O<sub>2</sub> plasma RIE that remove the ALD film and return the nanowires very near to their original resonance positions. In order of increasing original resonance frequency, the data correspond to nanowires with side lengths of 128 nm (dark yellow circles), 115 nm (pink squares), 150 nm (light blue, up-pointing triangles), 154 nm (dark blue, down-pointing triangles), 137 nm (green diamonds), and 128 nm (red, left-pointing triangles). The abrupt increase in the resonance frequency near 13 nm of ALD of the nanowire starting at ~530 kHz is attributed to the shortening of the nanowire by filling of the matrix layer.

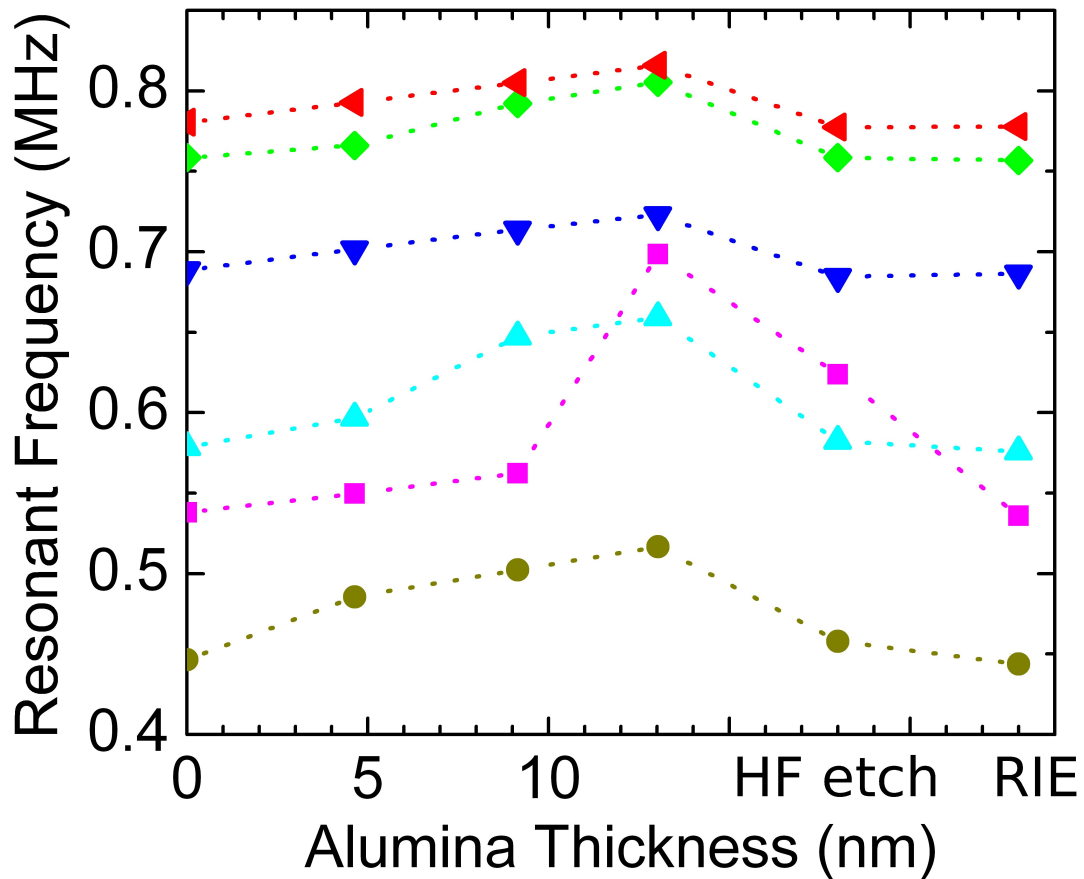
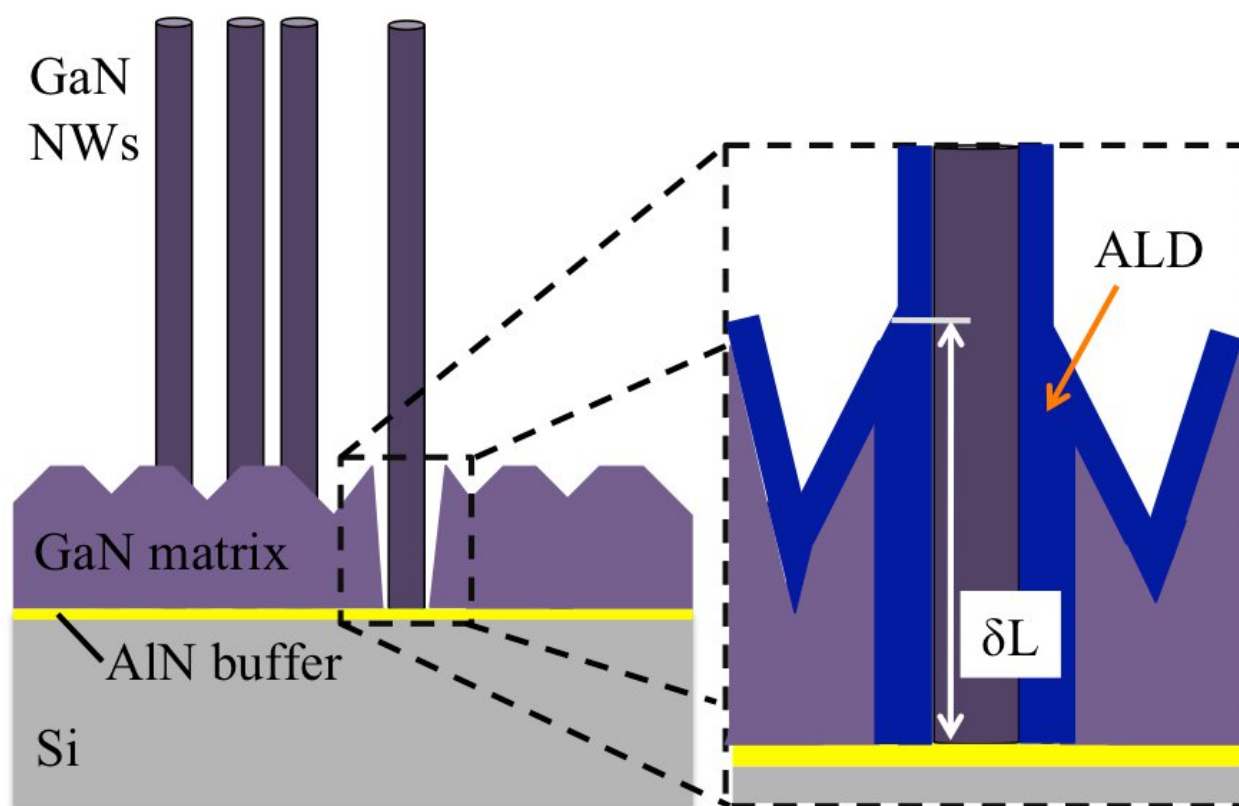


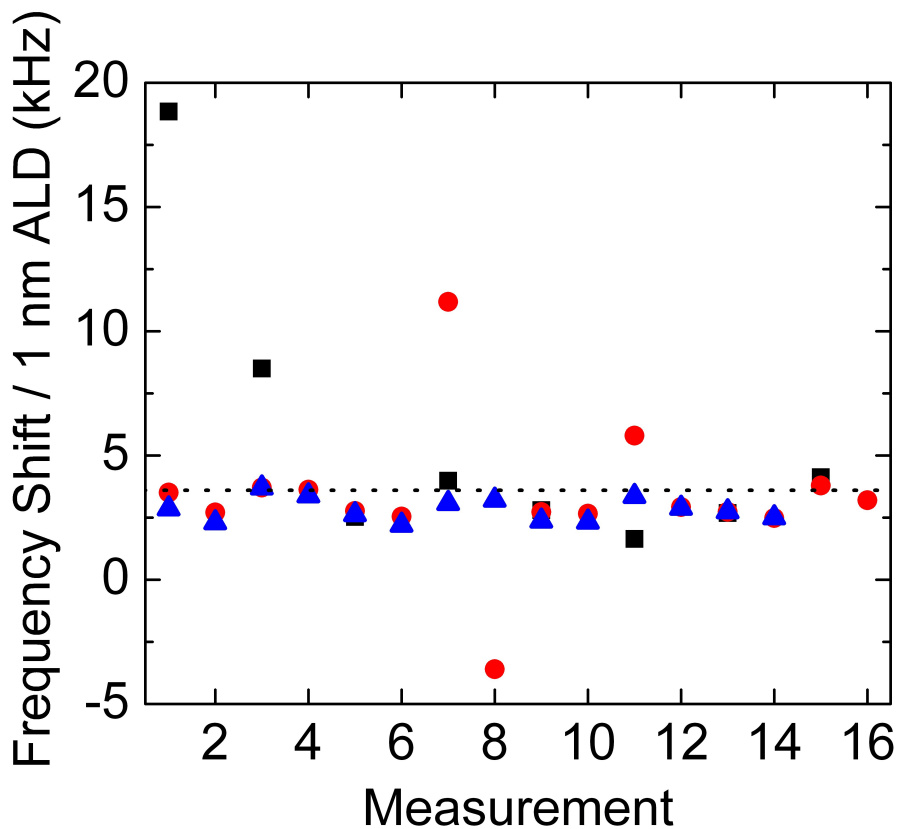
Figure 3.16: Schematic of GaN matrix layer filling. When the conformal film on the nanowire and surrounding GaN matrix material come into contact, the nanowire is effectively shortened by a length  $\delta L$ , increasing its resonance frequency.



clamping of the nanowire at a physically higher position reduces the effective beam length and increases the resonance frequency, cf. Equation 3.2. If we look at the shift in resonance frequency per nanometer of deposited ALD alumina for both modes of each nanowire and across all three stages of deposition, we find a consistently positive shift of  $\delta f = \delta\omega/2\pi \sim 3.6$  kHz/nm. This is in reasonable agreement with the first-order calculation in Equation 3.3, and is shown in Figure 3.17.

The as-grown nanowire FWHM linewidths  $\Gamma$  are typically of order 10-100 Hz, leading to quality factors  $Q$  of order 10,000. After the initial deposition of an ALD alumina film, we observe

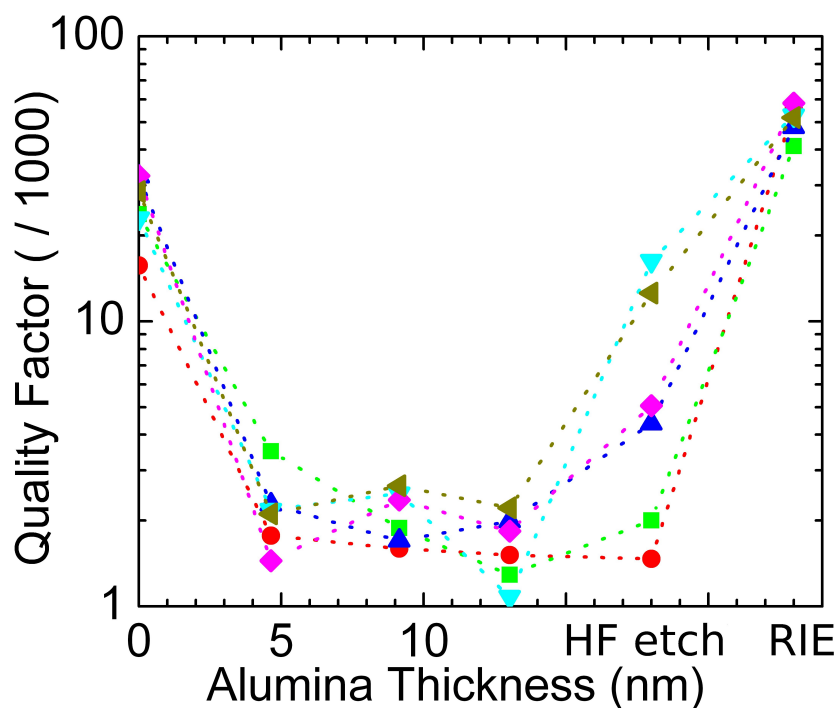
Figure 3.17: Distribution of resonance frequency shifts  $\delta f = \delta\omega/2\pi$  per nanometer of deposited ALD for all alumina-coated GaN nanowires studied. Each pair of "Measurements" (i.e. points at  $x = 1$  and  $x = 2$ ,  $\{3,4\}$ ,  $\{5,6\}$ , etc) corresponds to the two modes of a single nanowire. Black squares, red circles, and blue triangles correspond, respectively, to frequency shifts resulting from the addition of 4.6 nm, 4.5 nm, and 3.9 nm of alumina. The average shift of  $\delta f \sim 3.6$  kHz/nm ALD alumina is shown by the dotted line.



the resonator  $Q$  drop to order 1000, as shown in Figure 3.18. Though the resonance frequency continues to be affected by subsequent depositions (e.g. Figure 3.15), we see that  $Q$  remains approximately constant at its new, lower value. The nanowires in Figure 3.18 begin with a range of approximately 11,000-40,000, then drop to a range of 1,000-4,000 with the first ALD deposition. After a sequence of HF wet etch,  $\text{CO}_2$  critical point dry, and  $\text{O}_2$  plasma RIE, the nanowire  $Q$  is restored to or is greater than the initial as-grown range, spanning approximately 40,000–60,000. Since the GaN nanowires have been shown to be largely free of native oxide growth [99], this increase in  $Q$  may indicate an accumulation of organic contaminants on the nanowire after growth, but prior to use for ALD sensing.

We can compare these changes in  $Q$  to the surface loss described in Section 2.3.1. If we

Figure 3.18: Decrease in GaN nanowire-ALD composite resonator quality factor  $Q$  after ALD alumina coatings of 4.6 nm, 4.5 nm, and 3.9 nm, followed by ‘restoration’ via etching. Symbols correspond to the same nanowires as in Figure 3.15. “HF etch” and “RIE” correspond, respectively to an aqueous hydrofluoric acid etch and  $\text{O}_2$  plasma reactive ion etch. Note that after plasma RIE, all  $Q$  factors have been improved relative to their initial values.



assume that such a large change in the measured  $Q$  factor is due predominantly to the addition of a lossy surface layer, we can use Equation 2.25 to back out a surface layer loss modulus. Using the calculated  $Q$  factors for the initial alumina deposition (4.6 nm) on the eight nanowires shown in Figure 3.18, we calculate an alumina loss modulus of  $1.0 \pm 0.4$  GPa. This is just under 1 % the value reported in [98]. This is nearly three orders of magnitude larger than the GaN loss modulus we later calculate in Section 5.2.2.

### 3.6.2 Conformal Metallic ALD Films

In collaboration with the Cambridge, MA-based ALD company Cambridge NanoTech, we study ALD films of the transition metals Pt and Ru, which provide a qualitative confirmation of the behavior predicted by Equation 3.2, and established by our alumina studies in Section 3.6.1. A summary of the results is listed in Table 3.1.

Pt films are deposited at 270°C, with a  $(\text{Me}_3\text{PtCpMe})$  or  $(\text{CH}_3)_3(\text{CH}_3\text{C}_5\text{H}_4)\text{Pt}$  precursor and with  $\text{O}_2$  as a reactant. The growth rate is 0.33 Å/cycle. For this Pt film, the average measured resonance shift is  $\delta f \sim -28$  kHz. Most of the measured nanowires (10 of 16) have a reduced resonance frequency consistent with addition of a high-density material, as predicted by both Equation 3.2 and Figure 3.12. The remaining six resonances showed the increase in resonance position consistent with matrix filling, as described in Figure 3.16. Disregarding the nanowires that show matrix filling, the average shift was  $\delta f \sim 110$  kHz. The addition of a conformal Pt film also typically leads to

Table 3.1: Results from ALD coatings of Pt and Ru on GaN nanowire resonators.

ALD Material	ALD thickness (nm)	Nanowires [modes] (#)	Average resonance frequency shift (kHz)
Pt	40	10 [20]	-108±44
Ru	12.7 <sup>a</sup>	11 [19]	+289±142
Ru	2 <sup>b</sup>	12 [24]	-19±5

<sup>a</sup> Greater precision results from XRR measurements of film.

<sup>b</sup> The 150-cycle growth of Ru was not a continuous film, as described in Section 3.6.3. AFM measurements of a similar film showed islands of vertical height less than or equal to 2 nm.

a broadening of the resonant peak. Most measured nanowires demonstrate a decrease in their  $Q$  factor. The initial  $Q$  range of about 2000 to near 100,000 (most of order  $10^4$ ) was reduced to a post-ALD Pt range of about 2000-10,000.

Ru films are deposited at 270°C, with a  $(C_5H_5)_2Ru$  precursor and  $O_2$  as a reactant. After nucleation, the growth rate is 0.45 Å/cycle. For this Ru film, the average measured resonance shift is  $\delta f \sim 289$  kHz. Again, this shift (11 of 16 nanowires) toward higher resonant frequency is qualitatively consistent with the behavior shown in Figure 3.12. As was the case with both conformal films of alumina and Pt, the conformal coating of Ru also leads to resonance broadening. For all nanowires measured,  $Q$  decreases from its initial value. Here, the original range of about 11,000-80,000 decreases to a post-ALD Ru range of about 1000-4000.

For comparison with our results, it would be useful to have well-established values for the material properties of these ALD metals. The use of ALD alumina in the field of MEMS and NEMS has led to a decent characterization of its properties. Hopefully in the future, similar investigation of the Pt and Ru films used in this work can be compared to known bulk properties (Pt:  $E = 168$  GPa,  $\rho = 21,450$  kg/m<sup>3</sup>; Ru:  $E = 447$  GPa,  $\rho = 12,450$  kg/m<sup>3</sup>).

### 3.6.3 Discontinuous Metallic ALD Films

During the early growth stages of some ALD materials, surface nucleation occurs in physically isolated regions. Before these ‘islands’ coalesce, the discontinuous film will increase the effective resonator mass without necessarily contributing significantly to the resonators effective stiffness. By measuring a shift in the resonant frequency we can calculate the amount of material that was deposited on the resonator.

The ALD Ru presented in Section 3.6.2 is also studied as a discontinuous film on GaN nanowires. We measure nanowire resonance frequencies and  $Q$  factors after just 150 ALD cycles. This deposition period is chosen because it is believed to occur between the initial nucleation of the material and island coalescence. Most of the nanowires studied (13 of 16) demonstrate a decrease in frequency, with the average decrease being  $\delta f \sim 7$  kHz. Disregarding the data points indicating

an increase in resonant frequency (again attributed to the matrix filling mechanism mentioned in Section 3.6.1), the average resonance shift is  $\delta f \sim -19$  kHz. This result is included in Table 3.1. Using the Ru material data presented in Section 3.6.2, Equation 3.3 gives good agreement, also predicting a resonance frequency shift of  $\delta f \sim 16$  kHz. We can rewrite Equation 2.5 in terms of effective stiffness  $\kappa$  and mass  $\mu$ ,

$$\omega_o = \sqrt{\frac{\kappa}{\mu}} \left( \frac{1.875}{l} \right)^2 \quad (3.4)$$

and then expand it to find a relationship between the measured shift in resonance frequency  $\delta\omega_o$  and the addition of small mass  $\delta\mu$ :

$$\delta\mu = -2 \frac{\mu}{\omega_o} \delta\omega_o \quad (3.5)$$

After measuring the nanowire dimensions in the SEM, using the measured  $\delta f$ , and using XRR data from the Ru film, we calculate an average mass  $\delta\mu = 0.2$  fg of material added to the nanowires by the discontinuous ALD Ru. An atomic force microscope (AFM) is also used to analyze substrates with 150 cycles of the same Ru film (scan shown in Appendix D). Using the areal island density and height measured from that analysis, together with the XRR material data, we calculate the mass that should have been deposited to be on the order of 0.1 fg, in good agreement with  $\delta\mu$  calculated from the frequency shifts.

Though the surface coverage of the 150-cycle ALD Ru material should be far less than that of the continuous films, there was still a significant decrease in the nanowire Q. The initial, bare nanowire Q range of about 2000-70,000 is reduced to a range of about 400-50,000. Along with the effects seen after initial alumina depositions, this suggests that the GaN nanowire surface plays a significant role in the measured Q factors.

During the resonance measurements on discontinuous Ru, typical resonance frequency uncertainties were on the order of 10 Hz. Considering the measured 16 kHz shift in resonance position for 0.2 fg, we calculate an approximate mass resolution on the order of 0.2 ag with a 1-s averaging

time. This resolution is high enough to detect single cycles of the ALD process.

### 3.7 Transitioning From SEM- to Capacitance-Based Measurements

An issue that has heretofore been implicit is the notion that multiple measurements can be made – at disparate times, and after arbitrary processes – on a single nanowire. Though it may sound straightforward, this task requires many iterations to be successful. A quick glance at Figure 1.6 and the discussion in Section 3.2 gives the reader an idea of the vast number of nanowires that are **not** the one we seek at any given moment.

Ultimately, the relatively straightforward procedure that is adopted consists of saving a ‘breadcrumb trail’ of SEM images at varying levels of magnification, detailing the progress from single nanowire- to full-sample-view. To return to a particular nanowire for additional measurements, the sequence of images is ‘inverted’: starting with the full-sample-view, we make a series of manual steps of image recognition – that is, recognizing patterns by eye – followed by magnification, and repeat this process until arriving at the nanowire desired. An example series of such micrographs is shown in Figure 3.19. A key point in saving and reusing these images is that a small change in the angle of view (e.g. from the sample being mounted slightly unevenly) makes the manual image recognition extremely difficult to impossible. Care should be taken in establishing a repeatable sample-mounting procedure for the sake of reproducibility.

The aforementioned process of going back into the SEM for repeated measurements is a significant bottleneck to the throughput of this type of experiment. As such, it is also one of the motivations for transitioning to a more versatile and efficient measurement technique. Having observed a large amount of success in the realm of sensitive nanomechanical displacement detection using capacitive measurement techniques (see, for example Refs [40, 60]), we begin to experiment with incorporating electrostatic control and detection methods into our pre-existing SEM-based experiments.

Figure 3.19: An example of a ‘breadcrumb trail’ of SEM images used to locate a previously-measured GaN nanowire for further measurements. Though the series of images is created by going in the opposite direction, the process by which we recover a particular nanowire is as follows. Upon observing (most of) a full nanowire chip (substrate) at low magnification, we align the field of view with the corresponding, previously-saved image (a) and proceed to zoom directly in. At the magnification level of the next image (indicated in (a) by the red square), we identify any large-scale structures that assist in orienting our field of view. In this example, the disturbed region of nanowires in the lower-right and the contamination in the upper left will both assist in this process. Once we have aligned our current view to match another previously saved image (b), we repeat the process (c), and continue to higher magnification until we identify our desired nanowire within our field of view (d) – here, the isolated nanowire in the center of the image.

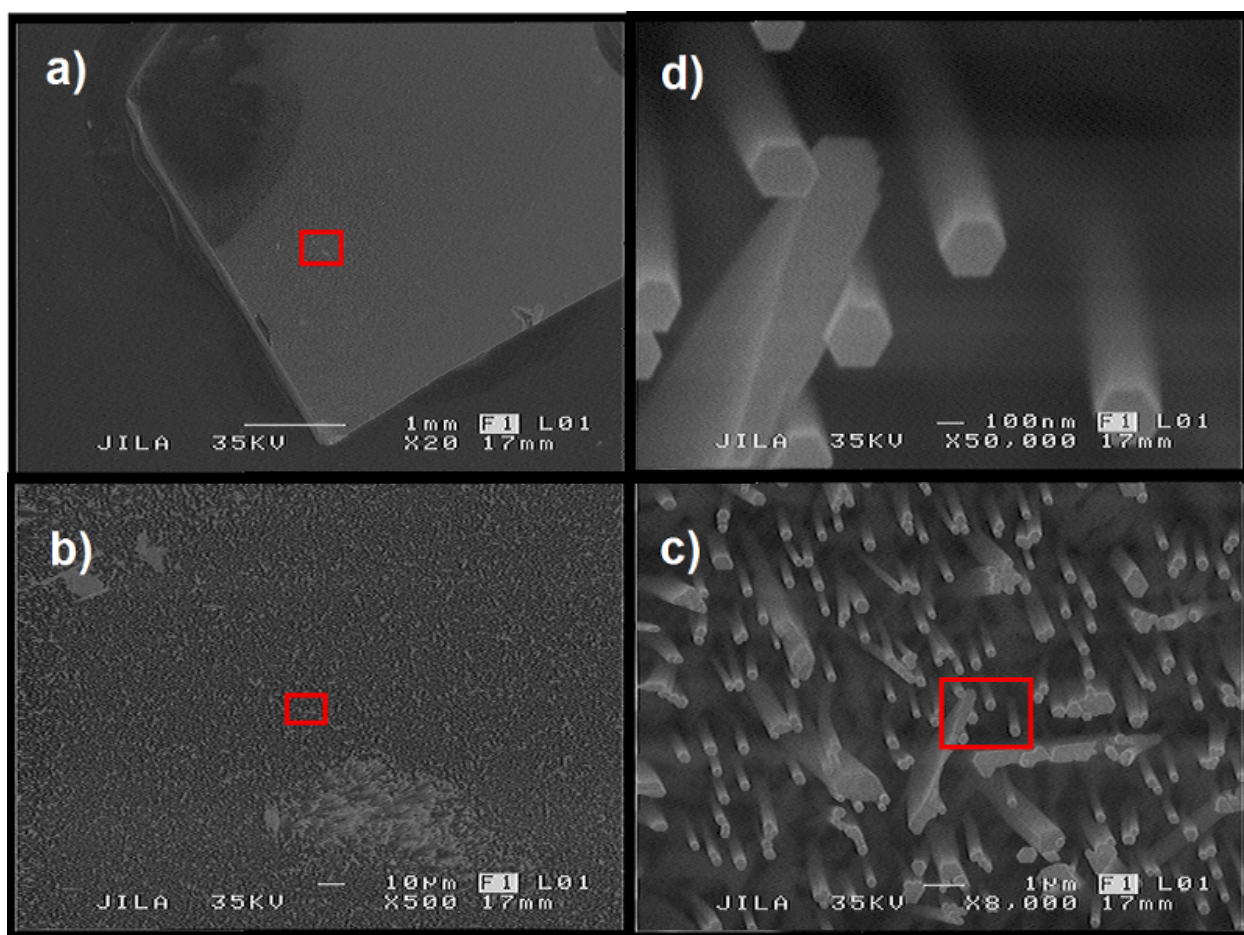
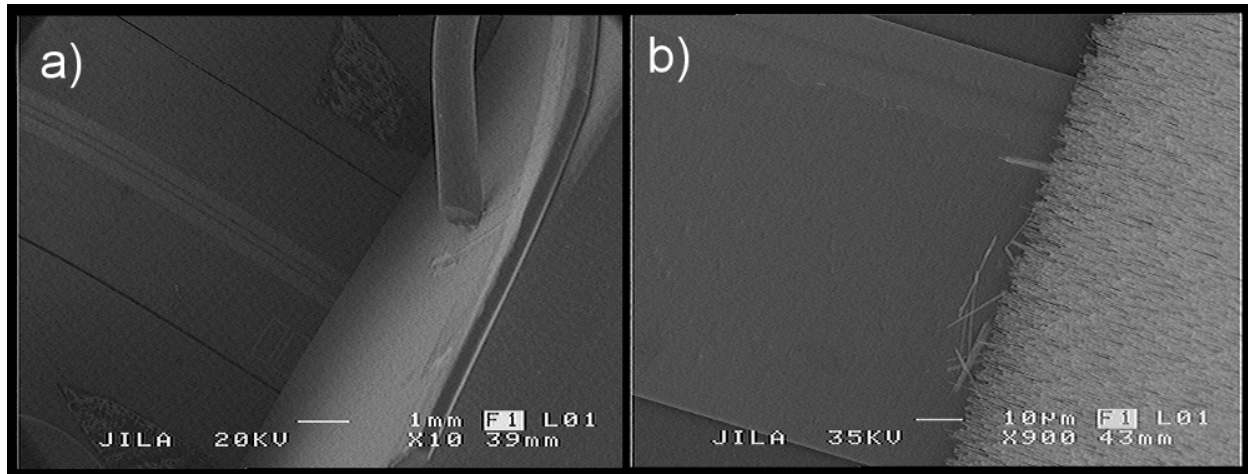


Figure 3.20: SEM micrographs showing one of the earliest attempts at electrostatic actuation of as-grown GaN nanowires. a) Low magnification, plan-view of coplanar microwave stripline (angling from top-left, toward center), with GaN nanowire substrate (lighter in color) grounded and clamped (via spring-loaded finger) normal to both the stripline plane and its direction. b) Higher magnification image of the stripline central conductor, with GaN nanowires now resolvable on the substrate. Additional broken and dislodged nanowires can be seen lying on the conductor. This central conductor is used as an electrostatic gate in an attempt to actuate those nanowires closest to the substrate edge (nearest the conductor).



### 3.7.1 Microwave Stripline Electrostatic Actuation

One of the earliest attempts to incorporate electrostatics into our actuation and detection is to simply mount a nanowire substrate on top of – and normal to – a microwave stripline and attempt to use it for electrostatic actuation. The experimental apparatus shown in Figure 3.20 shows both a low-magnification view of the apparatus and a higher-magnification view showing individual nanowires adjacent to the conducting strip at the center of the stripline. The outer stripline conductors are grounded, as is the conducting block to which the nanowire substrate is fixed. We intend to apply forces to the nanowires by controlling the voltage on the central stripline conductor.

For this experiment, we are interested in actuating a nanowire into resonance via the conducting strip, so we first must know its fundamental resonance frequency. In order to achieve this goal, we continue to zoom in to the nanowires on the substrate edge above the central stripline

conductor and somewhat arbitrarily choose to investigate one that is modestly isolated from the others (in terms of line-of-sight, for our observational purposes). As Figure 3.20 shows, the angle of the substrate makes it more difficult to resolve the individual nanowires than, say, from the nearer-normal angle shown in Figure 1.6. To find the chosen nanowire's resonance frequency, we use the power spectral density technique described in Section 3.3.1. While the process of focusing the beam on our nanowire in Spot Mode and analyzing the modulated photomultiplier output is the same, we no longer have use of the PZT for mechanical actuation. Given this situation, we can try two approaches to successfully actuate our nanowire.

Given that we don't know *a priori* what the natural resonance frequency is, we could potentially apply a broadband noise signal to the electrode, in parallel to our approach with the PZT technique. However, since we know nothing about the distance between the conducting electrode and the nanowire, they may be quite separated. Our arbitrary function generator is capable of producing 10 V<sub>rms</sub> white noise, but when distributed over a large bandwidth (10 MHz), the applied force at the (presumably narrow) resonance frequency of the nanowire is very small. Though we try this technique, we observe no obvious resonance structure in the PSD signal. While we could potentially introduce some form of gain on the drive signal, that is not an available option at the time of this measurement. Instead, we next, try a technique that is described in the original GaN publication from our lab by Drs. Tanner and Gray [47]. That is, we focus the beam on the nanowire and rely on the spontaneous oscillation of the resonator. In this situation, we do observe a small peak in the PSD signal that corresponds to a resonance. With knowledge about the location of the resonance frequency, we take a brief diversion into electrostatic actuation of nanowires.

The origin of electrostatic forces between capacitively-coupled conductors is in the changing charge on the conductor surfaces; that is, creating a voltage difference between the conductors. Recall that, as always, the force  $F$  is proportional to the gradient of the potential energy  $U$ . For this situation, we can write the force in terms of the capacitance  $C$  between our conductors and the (applied) voltage difference  $V_a$  as

$$F = -\nabla U = -\frac{1}{2} \frac{dC}{dx} V_a^2, \quad (3.6)$$

where the spatial derivative is with respect to the distance  $x$  between the nanowire and electrode.

Given the large aspect ratio of the nanowire, we can reasonably approximate the capacitance of the electrode-nanowire system as that of a thin cylinder near an infinite plane, which gives us an expression for the capacitance (to first order):

$$C = \frac{2\pi\epsilon_o L}{\ln(2x/r)}. \quad (3.7)$$

Here, the nanowire length and radius are given, respectively, by  $L$  and  $r$ , and the usual free-space permittivity is  $\epsilon_o = 8.854 \times 10^{-12}$  F/m [100].

For typical nanowire dimensions used in this work (e.g.  $r = 150$  nm,  $L = 12\mu\text{m}$ , and a spacing between 1 and 10  $\mu\text{m}$ ), the resulting capacitance is on the order of  $10^{-16}$  F.

When including the derivative of Equation 3.7, Equation 3.6 becomes

$$F = \frac{\pi\epsilon_o L}{x[\ln(2x/r)]^2} V_a^2, \quad (3.8)$$

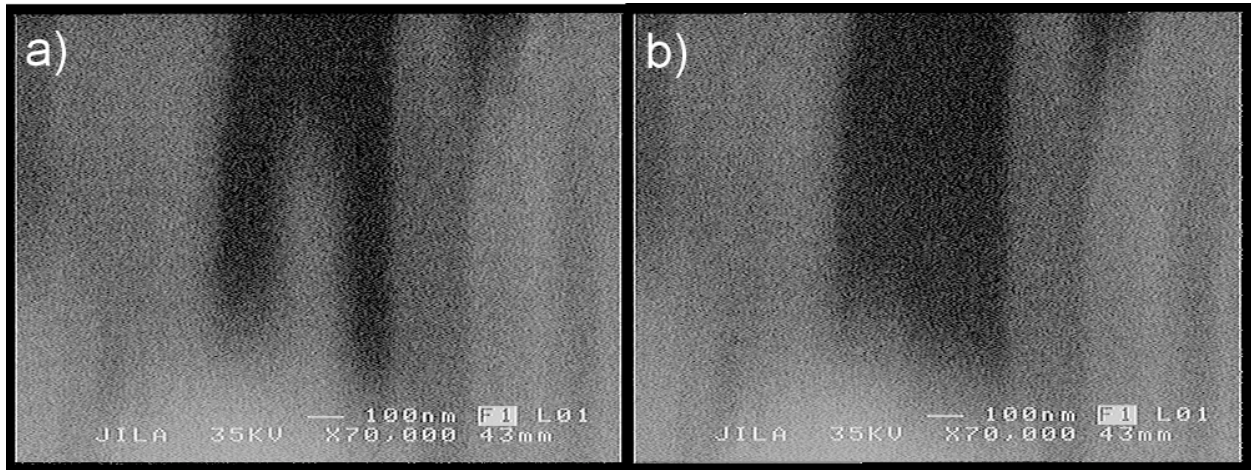
and we can see that the force drops off very rapidly with distance as  $1/(x \cdot \ln(x)^2)$ .

In both Equations 3.6 and 3.8, we see that the force is proportional to the square of the voltage difference. If both an ac ( $V_a^{ac}(\omega, t)$ ) and dc ( $V_a^{dc}$ ) component are included in  $V_a$ , then the resulting force on the nanowire will go as  $F \propto (V_a^{ac}(\omega, t))^2 + 2V_a^{ac}(\omega, t)V_a^{dc} + (V_a^{dc})^2$ . Now we can consider the effect of each of these terms. The third, constant,  $V_a^{dc}$  term will apply a force that simply tensions the nanowire. If  $V_a^{ac}(\omega, t) \propto \cos(\omega t)$ , then the second term will apply a periodic force at frequency  $\omega$ . And finally, the first term will apply a force at  $2\omega$ , since  $\cos^2(\omega, t) \propto \cos(2\omega, t)$ . This means that we can actually choose how we want to actuate a nanowire with resonance frequency  $\omega_o$ : only an ac voltage at  $V_a^{ac}(\omega_o)$ , or a combination of  $V_a^{dc}$  and  $V_a^{ac}(\omega_o/2)$ . In this stripline experiment, we choose to use the latter technique.

For this particular experiment, we observe a small peak we believe corresponds to the

nanowire resonance near  $\omega_o/2\pi = 310$  kHz (relatively low-frequency). We then proceed to sweep the ac drive frequency through a region centered on  $\omega_o/4\pi \approx 155$  kHz, while also applying a dc voltage (with opposite sign) of a few volts. Figure 3.21 shows the main image results of this experiment: at drive frequencies away from  $\omega_o/4\pi$ , we observe no visible change in the electron micrograph, but as we reach the resonance frequency  $\omega_o/4\pi$ , we observe a blurring of the nanowire (cf. Figure 3.21b) consistent with the typical motion-blur seen in other measurements. At first appearance, this could be an indication of a stuck resonator (due to Van der Waals forces between an adjacent surface or nanowire), but when we sweep through the resonance to off-resonance frequencies on either side, we observe the image shown in (a). An extremely rough estimate of the resonance linewidth can be estimated by recording the frequencies over the range of observable change in the SEM image and approximating the midpoint between, say, Figure 3.21(a) and (b). For this resonator the  $Q$  works out to be approximately 15,000, consistent with other nanowire measurements. Though the micrographs in Figure 3.21 are of admittedly low resolution, this is a proof-of-concept experiment and we believe we have demonstrated the successful electrostatic actuation of an as-grown GaN nanowire.

Figure 3.21: One of our earliest attempts at electrostatic actuation of an as-grown GaN nanowire. We fix a nanowire substrate normal to a coplanar stripline (as shown in Figure 3.20 and identify the resonance frequency of a single nanowire by measuring the secondary electron modulations due to spontaneous nanowire oscillation. While also applying a dc signal to the central stripline conductor, we sweep an additional ac signal from off-resonance (a), through the measured resonance frequency. On resonance, we observe a blurring of the image consistent with the typical nanowire fanning while undergoing resonant motion (b). A very rough estimate of the resonance linewidth (by visual observation of the resonance) suggests a quality factor  $Q$  of about 15,000 for this resonator, consistent with other as-grown GaN measurements.



## Chapter 4

### Capacitive Measurements: Theory & Single-Nanowire Results

In this next phase of this work, we implement a robust system for capacitive detection of nanowire motion. As compared to the SEM-based measurements described in Chapter 3, this technique benefits from not requiring any contact with the nanowires (e.g. without the constant bombardment by an electron beam). It also avoids potential heating effects resulting from piezoresistive measurements (Joule heating) and optical measurements (laser pumping). As a result, we suspect our interrogation tools have less of a perturbative effect on the ‘true’ intrinsic system behavior. In this chapter, we present a discussion of the microwave measurement system used for capacitive nanowire resonance detection, some of the theory behind its operation, and the first results measuring the behavior of a single as-grown GaN nanowire. The results of these measurements also help to corroborate the SEM-based results of Chapter 3.

#### 4.1 Resonant Microwave Circuit Theory

Choosing to convert more parts of our experiment to simple electrical signals provides a number of benefits. Circuit elements can be organized in a wide variety of topologies, leading to interesting and useful behavior. Furthermore, obtaining high quality components that are linear over a wide range of operation is relatively easy, as is interfacing them with each other via standard cables and devices. We make use of a resonant, microwave, inductor-capacitor (LC) tank circuit embedded in a homodyne reflectometer. The process through which we analyze, tune, and then utilize this microwave system is described below.

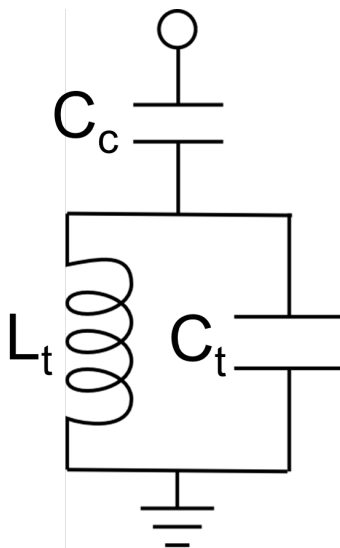
### 4.1.1 Ideal LC Tank Circuit

Here, we are interested in the use of a capacitively-coupled, parallel LC tank circuit. To understand how such a circuit behaves, we can begin with an ideal version consisting of coupling capacitance  $C_c$  and tank components  $L_t, C_t$ , as shown in Figure 4.1. This circuit has a completely reactive impedance given by

$$Z(\omega) = \frac{1}{i\omega C_c} + \left( i\omega C_t + \frac{1}{i\omega L_t} \right)^{-1}, \quad (4.1)$$

where the paranthetical term on the right-hand side is just the LC tank impedance. Such an impedance has two resonance frequencies: at  $\omega = 1/\sqrt{L_t C_t}$  the tank impedance goes to infinity (open circuit), and at  $\omega = 1/\sqrt{L_t(C_c + C_t)}$  the impedance goes to zero (short circuit).

Figure 4.1: Inductor-capacitor (LC) parallel tank circuit with components  $X_t$ , capacitively coupled by  $C_c$ . The impedance  $Z(\omega)$  of this ideal circuit is given by Equation 4.1.



### 4.1.2 Lossy LC Tank Circuit

The above model is a good start, but it makes the (idealistic) assumption that all of our circuit components are ideal, or lossless. There is bound to be dissipation somewhere in the system, and

— as described below — efficiently coupling this circuit to the outside world actually depends significantly on having some resistive element involved.

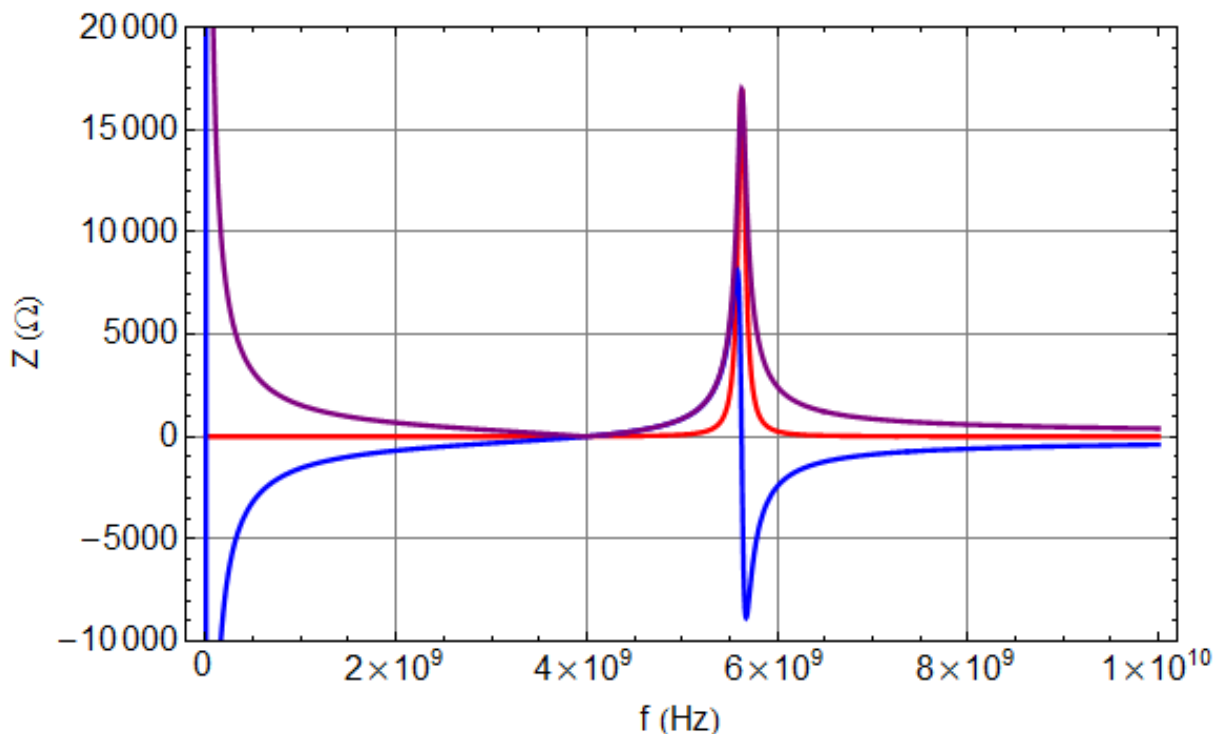
Short of inducing dielectric breakdown in our capacitors, they actually behave rather ideally. The conducting paths between the circuit elements (discussed in the fabrication portion of Chapter 5) are surely slightly resistive, but they are metallic and we treat them as ideal. For the sake of simplicity and calculation, we lump all of this low-level dissipation into the inductor,  $L_t$ , which is itself also a conceivable source of energy loss. One way to include this loss is to introduce a small imaginary component to  $L_t$ , proportional to the original value and scaled by a quality factor  $Q_L$ :  $L_t \rightarrow L_t - iL_t/Q_L$ . As a result, the corresponding impedance will have a small resistive component proportional to  $L_t$ . This modification has two related results: it forces the  $\omega = 1/\sqrt{L_t C_c}$  resonance impedance to be finite but still large (with an amplitude proportional to  $Q_L$  — in agreement with  $Z \rightarrow \infty$  in the limit  $Q \rightarrow \infty$ ), and the  $\omega = 1/\sqrt{L_t(C_c + C_t)}$  resonance to shift its impedance from that of a short to some finite resistive value. Matching this resistance to  $50 \Omega$  will later allow us to couple microwave signals into our system with minimal back- reflection.

A plot showing the real and imaginary components, and the magnitude of the non-ideal coupled LC tank impedance is shown in Figure 4.2, with component values somewhat similar to the actual values in our tank circuit. We will be operating near a tank resonance frequency of 3 GHz, where the corresponding microwave wavelength is on the order of 10 cm. Since most of the circuits fabricated for use in this work were on the order of  $1 \text{ cm}^2$ , we can consider lumped-element analyses of the circuit response. It is also worth noting that there will exist some amount of parallel, parasitic capacitance in the system. We can treat this as simply an additional capacitor in Figure 4.1, with the principle effect being a slight shift in the locations of the resonance frequencies. More details on the fabrication of some of these LC circuits is given in Section 5.1.1.

### 4.1.3 Microwave Network Analysis

For a comprehensive reference on microwave engineering, the reader is directed to Pozar's classic text [96] — most of the background material contained in this section is taken or derived

Figure 4.2: Calculated impedance  $Z(\omega)$  for the lossy LC tank resonator described in Section 4.1.2. Red, blue, and purple curves correspond, respectively, to the real component, imaginary component, and magnitude of the complex impedance. Here, the tank components  $L_t$  and  $C_t$  are, respectively, 8 nH and 0.1 pF, and the coupling capacitor,  $C_c$ , is 0.1 pF. The inductor has a  $Q$  of 60. Resonance behavior can be seen near 4 GHz ( $Z \rightarrow 0$ ) and 5.5 GHz (large  $Z$ ). The introduction of loss (through the inductor,  $L_t$ ) leads to finite impedance at the upper resonance frequency,  $\omega = 1/\sqrt{L_t C_c}$ , and non-zero impedance at the lower resonance frequency,  $\omega = 1/\sqrt{L_t(C_c + C_c)}$ .



from results in that work.

In order to analyze the microwave response of the LC tank system described thus far, we apply signals to – and measure the response from – our LC tank circuit using a Hewlett-Packard HP8510B vector network analyzer (VNA) capable of measuring the scattering parameters  $S_{ij}$  (magnitude and phase) of a one- or two-port microwave network. Though we will at times use one or both ports of the 8510 VNA, in both circumstances we will be measuring a microwave signal that has reflected from our LC circuit. The reflection coefficient,  $S_{11}$ , from a load with input impedance  $Z_{in}$  back into a characteristic (cable) impedance  $Z_o$  is given by:

$$S_{11} = \Gamma^{(1)} = \frac{Z_{in} - Z_o}{Z_{in} + Z_o}, \quad (4.2)$$

where in our system the characteristic impedances are typically  $50 \Omega$ .

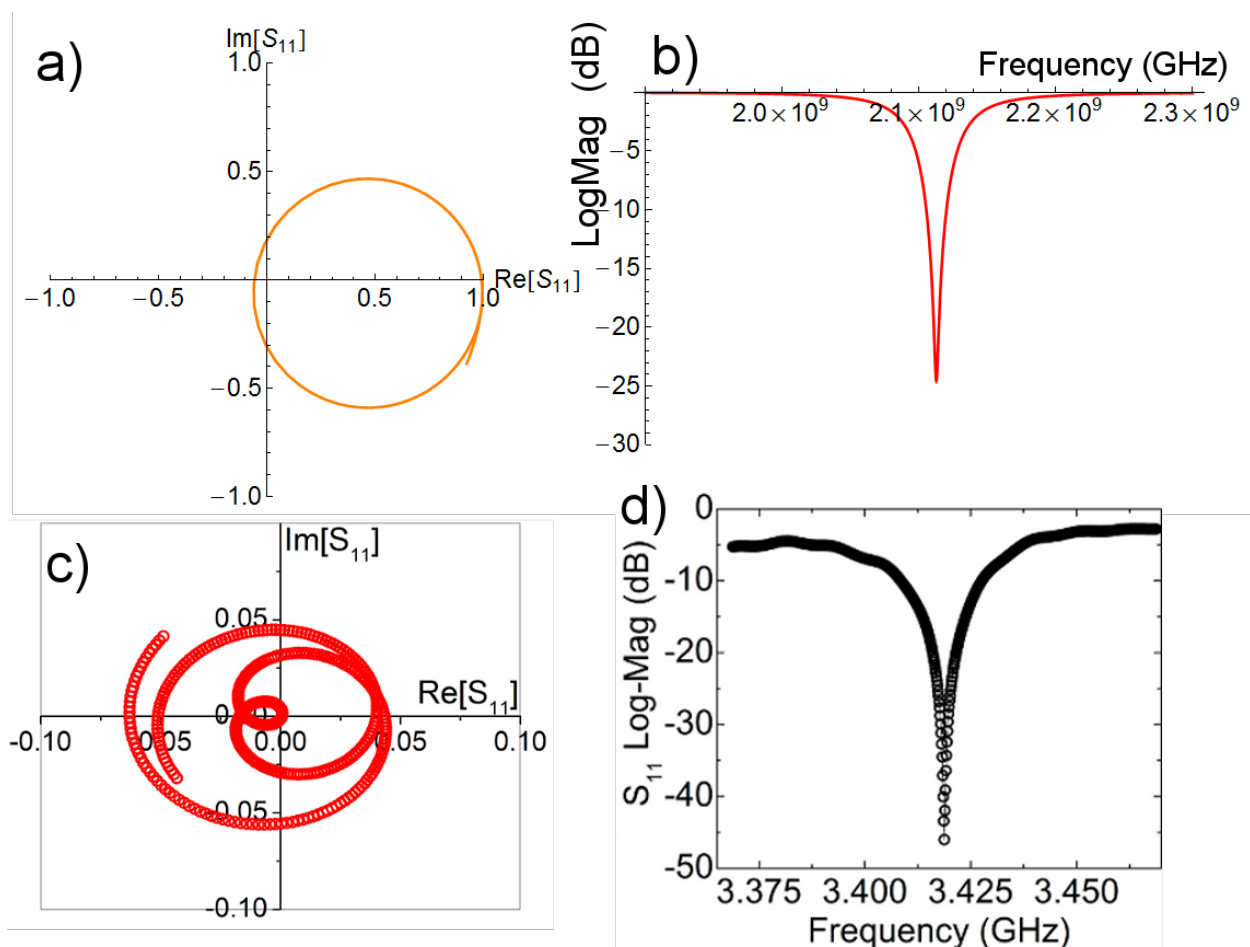
Equation 4.2 is correct if the load being tested with the 8510 VNA is connected directly to the test ports, where the path length is precisely calibrated. However, in a typical microwave system, a number of standard coaxial cables will lie between the load and the measurement ports. The evolution of the input impedance of a load  $Z_L$  on a lossless transmission line of length  $l$  can be found using the Telegrapher's Equations to be

$$Z_{in,l}(\omega, l) = Z_o \frac{Z_L + iZ_o \tan(\omega l)}{Z_o + iZ_L \tan(\omega l)}, \quad (4.3)$$

which reduces to  $Z_{in,l} \rightarrow Z_L$  when  $l \rightarrow 0$ .

With this information, we can now consider the measured reflection  $S_{11}$  given by Equation 4.2, but where the input impedance  $Z_{in}$  is replaced by the evolved  $Z_{in,l}$ . When it comes to representing the behavior of Equation 4.2 graphically, the 8510 VNA presents a number of display formats. For example, we can look at plots of the real and imaginary components, magnitude and phase, or a Smith chart of the reflected signal. Though they present effectively equivalent information, we will typically make use of the magnitude display (in logarithmic units (dB), referred to as 'log-mag'), and the Smith chart. The Smith chart displays the complex reflection coefficient plane. An example of both calculated (using Equations 4.2 and 4.3) and measured frequency trace of microwave reflection is shown in Figure 4.3. Typically, the Smith chart is normalized to a characteristic impedance (here, again,  $50 \Omega$ ), so a trace running through the origin represents proper impedance matching at a particular frequency. In this way, a perfectly matched load would lead to a reflection coefficient of zero — no signal is returned to the measurement port. Correspondingly, the log-mag plot also shown in Figure 4.3 displays a reflection amplitude that is reduced by approximately 25 dB from the incident signal near the resonance (and reduced very little off of resonance, where the impedance mismatch leads to large reflections).

Figure 4.3: Calculated and measured examples of the reflection parameter  $S_{11}$ . a) and b) are, respectively, calculations of the complex plane of the Smith Chart and the logarithmic magnitude as functions of frequency for a microwave resonance near 2 GHz. This resonance corresponds to a theoretical resonant circuit modeled by similar components to those described in our system in Section 4.2 and with a  $Q$  near 100. In the Smith Chart in a), the proximity of the resonance curve to the origin illustrates a near-critical coupling to the circuit as a  $50\text{-}\Omega$  load. Correspondingly, the log-mag plot (b) shows a large peak in the reflected signal indicating close impedance matching. c) and d) are an example of a Smith Chart and log-mag plot pair measured from our resonant circuit. The Smith Chart in c) also shows near-critical coupling by its close approach to the origin, but it also includes additional wrapping due to the physical length of the measurement line. The log-mag plot in d) shows a resonance peak near 3.42 GHz, and a  $-45\text{ dB}$  reflection of the microwave tone on resonance.



The proximity to the origin of the trace on the Smith chart or, equivalently, the depth of the log-mag resonance is said to represent the coupling of the load — here, the load is our LC tank circuit — to the transmission line. In our experiment, the coupling capacitor  $C_c$  is adjustable and provides the ability to tune the tank impedance and corresponding reflection coefficient  $S_{11}$  for optimal coupling. This tuning allows us to couple microwave signals into- and out of the LC tank and, ultimately, investigate variations in capacitance due to nanowire motion.

#### 4.1.4 Detecting Nanowire Motion As A Variable Capacitance

In order to detect a resonating GaN nanowire in the measurement system discussed thus far, we will consider it an additional small modulation of the pre-existing parallel tank capacitance  $C_t$  (cf. Figure 4.1). This modulation is ultimately observed via a chain of resultant modulations:  $C_t \rightarrow$  LC tank impedance  $Z_{in,t} \rightarrow$  complex reflection coefficient  $S_{11} \rightarrow$  reflected microwave tone. While the information about the resonating nanowire is encoded within this modulated, reflected tone, the size of these modulations are a small percentage of the tone amplitude. For this reason, we make use of an interferometric homodyne detection system.

Like the heterodyne technique described in Section 3.3.1, homodyne detection is also a technique involving nonlinear mixing of two signals. As the name suggests, however, this technique involves having RF and LO inputs of the same frequency. Recalling the products shown in Equation 3.1, we expect the IF signal to be at  $\omega = 0$  Hz, a dc signal at some voltage. Furthermore, our experiments make use of a quadrature double-balanced mixer (‘IQ mixer’) that provides both the typical IF port (I) and a ‘Q’ port, which is the quadrature phase of the mixed signal.

Given that the modulations in which we are interested are small, we would like to add gain stages to amplify these signals for easier measurement. However, arbitrarily large amounts of gain on a dc signal can easily saturate downstream amplifiers. Additionally, analyzing large signals that are not centered about zero can force digital measurement devices to use their resolution inefficiently by only utilizing bits on one end of their dynamic range. We can address this problem — in addition to obtaining more linear response to our desired capacitance modulations — by adjusting

the phase (equivalently, the path length) of the LO signal arm. We choose to manipulate the LO arm of homodyne detector in order to avoid any unnecessary – and potentially noise-inducing – components in the RF arm that carries our low-level, soon-to-be-amplified signal.

To properly choose the LO phase, we consider the response of our LC resonant tank with respect to frequency. As we sweep the incident tone frequency through the LC tank resonance, the reflected microwave signal (RF) will demonstrate an appropriate  $\pi$  phase shift. Similarly, when the LO arm of the mixing inputs is adjusted to match the phase of the RF arm, the quadrature phase of the mixer output will also show this transition. Figure 4.4 shows example voltage signals (plotted as a function of frequency - the sweeping incident/RF tone) from the I and Q phases of the mixer.

In this example, the LO arm has been phase-adjusted so it is nearly  $90^\circ$  out of phase with the RF signal. As such, the two measured phases correspond to the appropriate Lorentzian phases of a resonant circuit. When we narrow the sweep and center on the resonance, we see the quadrature output is approximately 0 V, symmetric about this point, and linear in frequency. Now we are also in a position to safely amplify the IF signal (since it has a 0-V mean value). Under these circumstances, we expect to observe linear response to perturbations in the LC tank impedance, such as by a modulated tank capacitance.

## 4.2 Capacitive Single-Nanowire Detection

The first successful use of the microwave system described in Section 4.1 for detection of a single GaN nanowire resonance is completed in collaboration with Scott Hoch, an undergraduate working on a thesis project [101] in the lab of Konrad Lehnert. This work would also result in subsequent journal article [66]. In these experiments, we create our simple resonant microwave tank circuit out of mostly off-the-shelf parts. We use a standard flange-mount SMA connector as the basis of our small circuit. On top of this, we connect a Coilcraft air-core inductor, create an air-gap capacitance between the inductor and the SMA central conductor, and the variable capacitance described in Section 4.1.4 will be between a modified platinum (Pt) scanning tunnelling microscope

(STM) tip and a GaN nanowire on the substrate. An image of the tank circuit and a schematic of the homodyne reflectometer are shown in Figure 4.5.

In this experimental setup we use an approximately 3-GHz tone (at the LC tank resonance frequency) at 32 mW – chosen to provide the largest power at the mixer RF port for which its response is still linear. With a measurement dynamic range of  $3 \times 10^7 \sqrt{\text{Hz}}$  and an electrical  $Q$  of about 100, we expect to be able to resolve fractional changes in capacitance of  $3 \times 10^{-9}$  in one second of integration time. For typical nanowire parameters (e.g. 50 nm radius and 10  $\mu\text{m}$  length), this resolution corresponds to a displacement sensitivity of  $1 \text{ pm}/\sqrt{\text{Hz}}$ .

To begin this experiment, a substrate of the GaN nanowires is mounted atop a similar PZT

Figure 4.4: An example of measured intermediate frequency (I) and quadrature (Q) mixer output signals plotted as a function of the incident tone frequency. The two output signals can be ‘rotated’ into the other’s appearance by adjusting the phase of the LO arm. The data is shown over a narrow bandwidth centered at the microwave resonance frequency (near 3 GHz). The two phases are very similar in shape to the phases of a typical Lorentzian response (cf. Figure 2.4). By observing these signals while simultaneously adjusting the phase (equivalently, the path length) of the LO arm, we can obtain approximately linear response in one mixer output (shown here, the black data) to modulations in the LC tank impedance. Modulations in the parallel tank capacitance (caused by resonant nanowire motion) can thus be expected to lead to an approximately linear response in the chosen mixer output. Furthermore, with the mixer output near 0 V, we can apply greater amounts of gain to our signal.

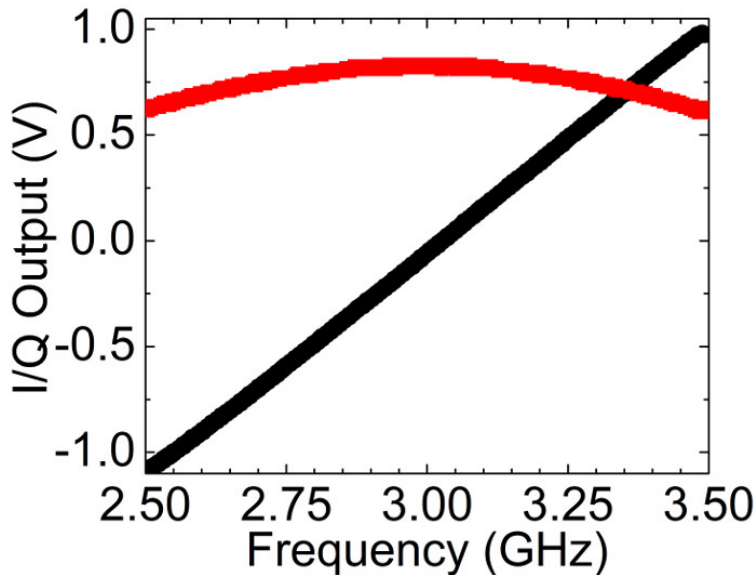
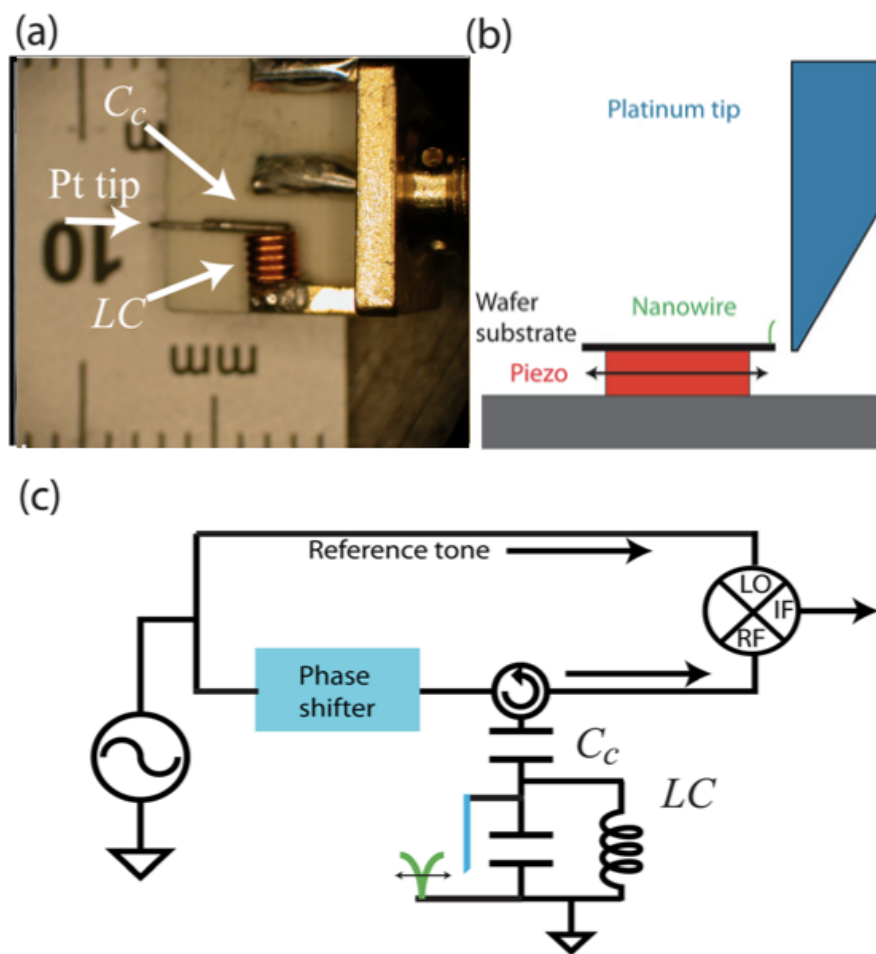


Figure 4.5: Capacitive detection of a single GaN nanowire using a microwave homodyne reflectometry. (a) A portion of the resonant LC tank circuit with labeled components assembled atop an SMA panel-mount connector.  $LC$ ,  $C_c$ , and 'Pt tip' are, respectively, a 12 nH surface-mount inductor, air-gap coupling capacitance, and modified platinum STM tip. (b) Schematic of the relationship between GaN nanowire and substrate, Pt STM tip, and PZT (not to scale). (c) Schematic of the LC tank circuit embedded within the microwave homodyne reflectometer system. The GaN nanowire is represented in green, the Pt STM tip in blue (not to scale). Figure adapted from [66].



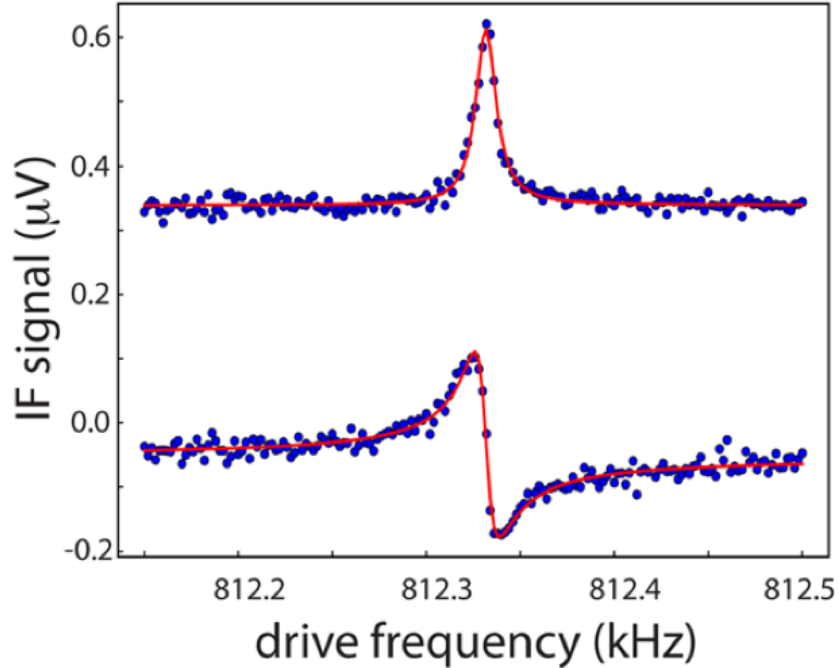
as first described in Section 3.2. The PZT is still driven by a standard function generator. The nanowires are capacitively coupled to the resonator circuit via the STM tip, which is manually adjusted using a three-axis translation stage. First, it is coarsely aligned to the chip under a low power optical microscope. While the PZT is driven, the tip is moved towards the substrate edge, approaching the nanowire region. When the STM tip is close enough to the edge, the motion of the PZT is observed on the output of the interferometer; when the PZT is driven with a sinusoidal signal at a particular frequency, we will see a relatively narrow peak in the spectrum of the interferometer output corresponding to that transduced drive frequency. At this point, we are typically within close enough proximity to observe nanowire motion. Optical microscope inspection of the experiment after such an alignment has shown the STM tip-nanowire substrate separation to be on the order of 10  $\mu\text{m}$ . After alignment, the entire apparatus (including nanowire substrate, PZT, and LC tank circuit with positioned STM tip) is then placed in a vacuum chamber. From here, we can perform the same type of phase-sensitive lock-in measurement previously described. Such a measurement leads to data as shown in Figure 4.6, precisely like that described in Section 3.3.2. The nanowire resonance frequencies remain in the vicinity of 1 MHz, and  $Q$  remains in the mid- $10^4$ s. After this initial success in demonstrating proof-of-concept with the homodyne reflectometer, we proceed to examine two additional aspects of the resonator system.

#### 4.2.1 Connecting Physical Deflection And Measured Signal

We next make a connection between our new, all-electrical (capacitive) experimental setup and the earlier SEM-based measurements (cf. Chapter 3). By comparing the amplitude of our measured electrical signals to observed nanowire tip deflection, we produce a form of calibration for our experiment.

While making a minimum of modifications to the existing measurement setup, we move the sample stage (with PZT, TEM tip, etc.) into the vacuum chamber of an SEM. From here, we carry out the measurement described in Section 4.2 with the SEM electron beam fully off (hence, not effecting our electrical measurement); in this scenario the SEM is effectively an overly complicated

Figure 4.6: An example of early two-phase lock-in resonance data for a single GaN nanowire mode providing proof-of-concept for detection via microwave homodyne reflectometry. Solid red curve is a simultaneous least-squares fit to both data-sets, resulting in  $f_o = 812,331.5 \pm 0.3$  Hz and  $Q = 62,000 \pm 1000$ . Figure adapted from [66].



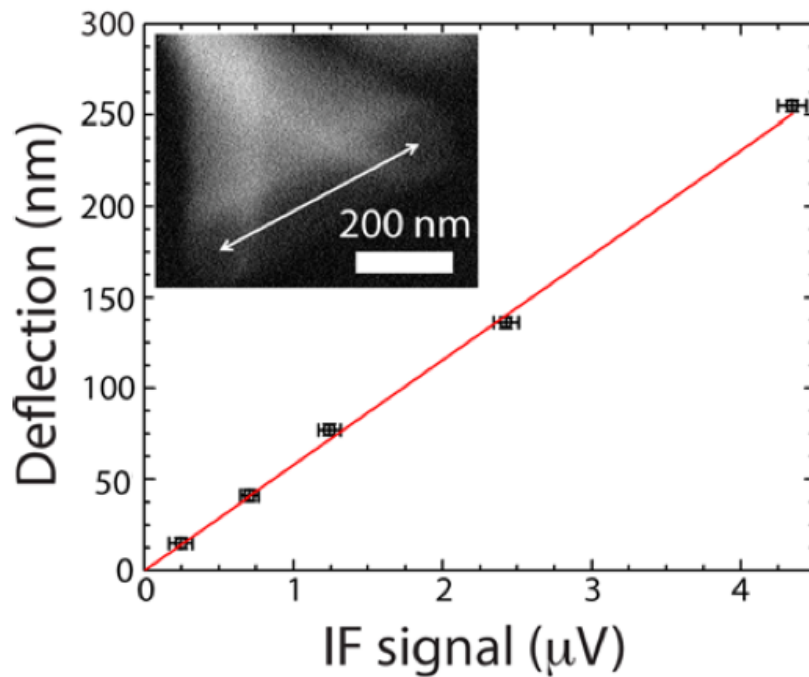
(and expensive) vacuum chamber. In this arrangement we conduct multiple lock-in measurements, each with different actuation amplitudes on the PZT, and each time detecting the phase-sensitive response of our chosen nanowire.

Following the acquisition of this data, the SEM electron beam is turned on and the capacitively-measured nanowire is located. This process is rather painstaking and involves manual, visual inspection of the sample edge closest to the STM tip while the known nanowire resonance frequency is applied to the PZT. By manually turning the PZT actuation (i.e. the function generator) on and off, we can look for a fanned nanowire tip amidst the forest of stationary ones. Once identified, we acquire electron micrographs of this nanowire while fanned out in resonance in response to the same PZT actuation amplitudes used for the phase-sensitive, capacitive measurements. With these two sets of data in hand, we carry out image analysis [102] on the micrographs to measure the

extent of the nanowire tip deflection at each actuation level.

The resulting comparison of tip deflection (as observed in – and measured from – the SEM micrographs) and resonance peak amplitude (as determined by the amplitude of the capacitive, phase-sensitive measurement data) provides a direct calibration between physical nanowire tip displacement and measured electrical signals for the nanowire being investigated. For one such nanowire (and choice of system gain) shown in Figure 4.7, this calibration was  $58 \pm 3 \text{ nm}/\mu\text{V}$ . Interestingly, the datasets acquired during this experiment all had similar appearance to Figure 4.6, fitting with reduced- $\chi^2$  of order 1 and suggesting reasonably linear resonator response in spite of the relatively large displacement amplitudes (cf. Figure 4.7). A more thorough investigation of the transition between the linear and nonlinear regime of these as-grown GaN nanowire resonators is certainly a prime target for future directions of this research project (cf. Chapter 6).

Figure 4.7: Deflection-signal calibration curve for the fanned nanowire shown in the inset. A plot of the nanowire tip deflection as measured from the SEM micrographs versus the amplitude of the electrical signal measured in our homodyne reflectometer results in a response of  $58 \pm 3 \text{ nm}/\mu\text{V}$ . Figure adapted from [66].

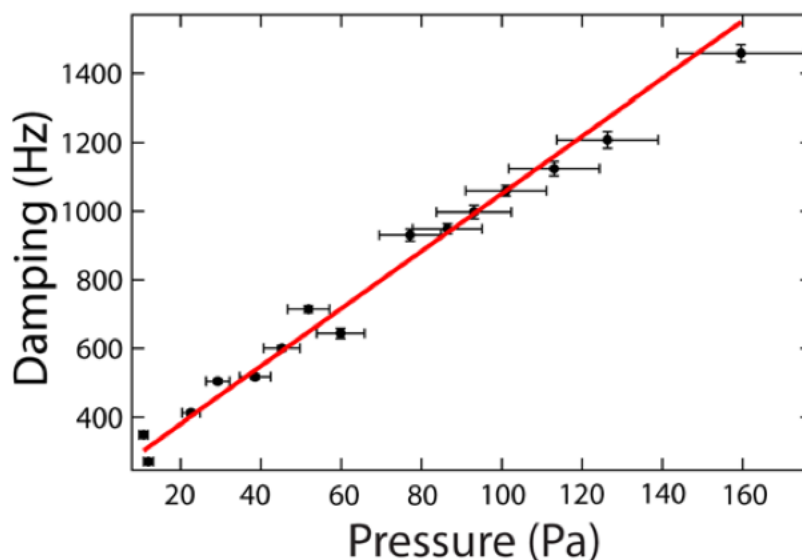


### 4.2.2 GaN Nanowire Mechanical Dissipation By Gas Damping

As discussed in Section 2.3.1, a common source of energy loss in nanoscale resonators is from friction due to gas damping. In our second experiment with this apparatus, we observe the dissipation of an as-grown GaN nanowire resonator while varying the pressure within our vacuum chamber. We begin by evacuating the measurement chamber to a pressure of 10 Pa (75 milliTorr) and making our standard measurement of the nanowire resonance. Next, we briefly open a nitrogen gas ( $N_2$ ) valve on the chamber, leading to a transient pressure spike before equilibration at a new, slightly increased level. Here, we carry out another resonance measurement, focusing on the same nanowire. After repeating this experiment at pressures from 10 Pa to 160 Pa (1.2 Torr), we obtain the data shown in Figure 4.8.

According to a model of low-pressure gas damping [86], the dissipation here is primarily caused by the independent collisions of noninteracting gas molecules. In this regime, the damping depends linearly on pressure with a functional form  $\Gamma = krp$ , where  $p$  is the pressure,  $r$  is the

Figure 4.8: Measurements of gas damping on an as-grown GaN nanowire resonator. Damping  $\Gamma/2\pi$  is shown as a function of vacuum chamber pressure at equilibrium (points). The solid red line is a linear fit to the data. According to a model of low-pressure damping [86], this fit allows us to extract an effective nanowire radius of  $49.5 \pm 0.5$ nm. Figure adapted from [66].



nanowire radius, and  $k$  is a constant describing the surrounding gas and is approximately  $3.5 \times 10^{-3}$  s/m for  $N_2$  [86]. In a plot of damping versus pressure, the free parameter is the effective radius of the nanowire being measured. Figure 4.8 shows the linear dependence of  $\Gamma$  on the chamber pressure, from which we can extract an effective nanowire radius of  $49.5 \pm 0.5$ nm. The specific nanowire measured in this study was not explicitly observed in an SEM, but the extracted radius is consistent with the range of previously observed nanowire geometries.

After this successful capacitive detection of as-grown GaN nanowire resonances, we next consider how to make these measurements faster and in larger volumes. We look toward a fusion of our noise- driven power spectra (used in the SEM as described in Section 3.3.1) and this hands-off, all-electrical capacitive detection scheme. This will allow us to make simultaneous measurements of a full ensemble of nanowires, without making physical contact with them.

## Chapter 5

### Capacitive Measurements: Ensemble Extension

After the success of Chapter 4, we are now confident that we can detect the mechanical resonance of as-grown GaN nanowire resonators using our microwave homodyne reflectometer, and we can also observe their response to environmental changes (i.e. pressure). Now, in the interest of making our measurements more efficient and statistically insightful, we extend this work to simultaneously detect the resonant motion of many nanowires. This will allow us – for the first time – to compare the simultaneous behavior of a full ensemble of nanowire resonators, and gain insight into the distribution of resonance parameters using a faster, parallel process. Qualitatively, we intend to use the same measurement technique as described in Section 4.1. However, instead of creating a variable capacitance between one nanowire and a specially-fashioned STM tip, we will use a large conducting plane that is adjacent to an entire substrate edge and all the nanowires along its edge. To begin, we'll first go discuss the measurement system and some of its assembly details.

#### 5.1 Microwave System Iteration

While the results of Chapter 4 demonstrate that the relatively simple LC tank circuit described in Section 4.2 works as intended, Figure 4.5 shows that the hand-assembled circuit is perhaps not as reproducible and versatile as it could be. In addition to allowing for ensemble detection through design modifications, our goal with the next version of this resonant circuit is to fabricate it in a more repeatable and controlled fashion.

### 5.1.1 Fabrication With Microwave Laminates

Here, we take a cue from the realm of industrial fabrication, where processes are made to be highly reproducible (and fast) through the use of lithography. However, we do not immediately go the route of silicon substrates and deposited-metal circuitry, as these types of processes can have a large upfront time requirement for accurate design iteration. Instead, we choose to use a system that has faster turn-around times for our implementations and a lower overhead cost: etching copper (Cu) laminates.

Though the physical layout of our microwave LC circuit takes on many different versions over time, they are all based on the printed Cu laminates from Rogers Corporation<sup>1</sup> [103]. Most commonly, we use the RT/duroid 5880 laminate. These products are designed for high-frequency applications, with low loss and water absorption properties. The version of 5880 laminate we typically use comprises 0.031” of Cu cladding on both sides of a PTFE (polytetrafluoroethylene) dielectric. These laminates are very easy to cut, shape, etch, and generally manipulate for our purposes.

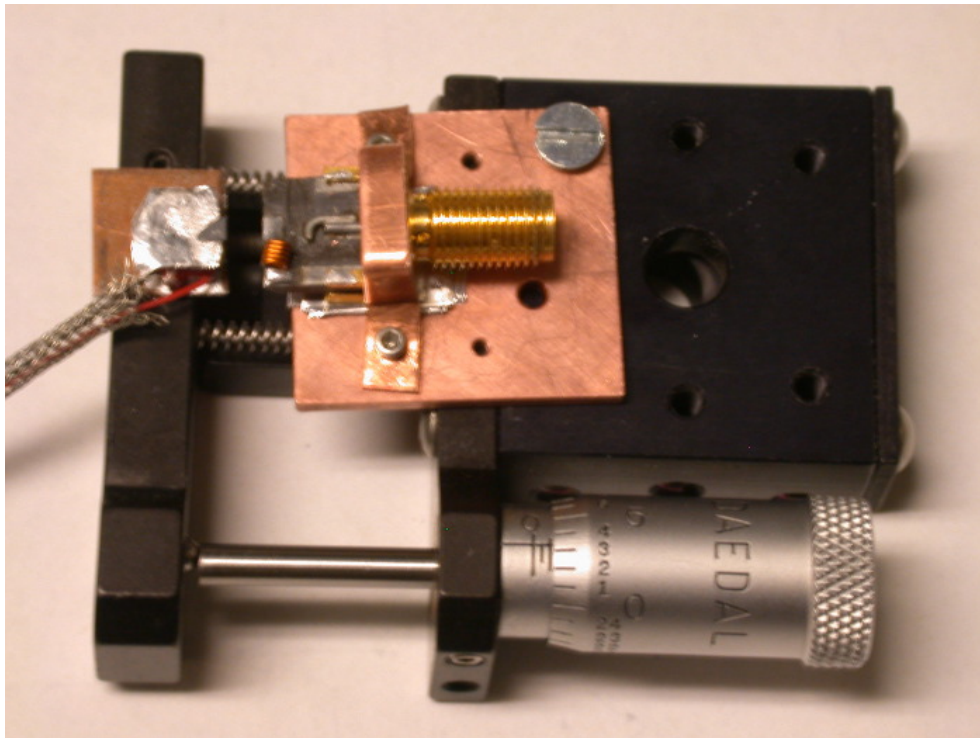
Fundamentally, we wish to improve upon the circuit layout shown in Figure 4.5, which we have shown effective at detecting these GaN nanowire resonators. As such, we look to maintain the approximate size scale and components involved in that previous implementation, while now taking advantage of our microwave laminate substrate. Ultimately, we intend to use standard photolithographic techniques to pattern and etch the top Cu surface and create electrically conducting paths (ideally, 50- $\Omega$  striplines, to minimize microwave losses). The Rogers Corporation website provides a tool for calculating the approximate impedance for a given stripline geometry. In order to simply show proof-of-concept, the first few iterations of this circuit layout were cut by hand with a simple razorblade. An example of an early laminate-based LC circuit is shown on the translation stage seen in Figure 5.1. The dark gray material attached to the SMA connector is the microwave laminate. The remaining Cu cladding has been covered with silver-colored solder while attaching the other components and also attaching the laminate substrate to the SMA connector.

---

<sup>1</sup> Rogers Corporation is not affiliated with Prof. Charles Rogers

An additional motivation for using the Cu-cladded microwave laminate is that a portion of our conducting circuit can now easily serve as the common sensing electrode (CSE) with which we hope to detect the simultaneous resonance of an ensemble of GaN nanowires. The device shown in Figure 5.1 is a working example and confirms that we can, indeed, design approximately 0.25 – 0.5-in<sup>2</sup> microwave circuits with resonance frequencies similar to our previous work (cf. Figure 4.3), and that such a device is capable of detecting nanowires in precisely the same manner as described in Chapter 4. Note that the CSE used in this epoch of experimentation is coplanar with the nanowire substrate. Given the thickness of the Cu cladding, however, it will still appear roughly

Figure 5.1: Mounted atop a uniaxial optical translation stage (black) is one of the first microwave laminate-based resonant LC circuits. The design is closely related to that used in Figure 4.5. The fixed coupling capacitance is through the air and half-plane of dielectric material between the small, L-shaped conductor attached to the SMA central conductor and the Cu laminate near the inductor (orange, 8 nH). In this example, the SMA connector is affixed and grounded to the translation stage with the use of an additional, pre-drilled, copper plate. The use of the translation stage enables us to adjust the distance and coupling between the common sensing electrode (CSE) at the edge of the laminate board and the nanowire substrate (left, small gray triangle) atop the PZT (covered in Al foil). The PZT is affixed to the translation stage via silver paste.

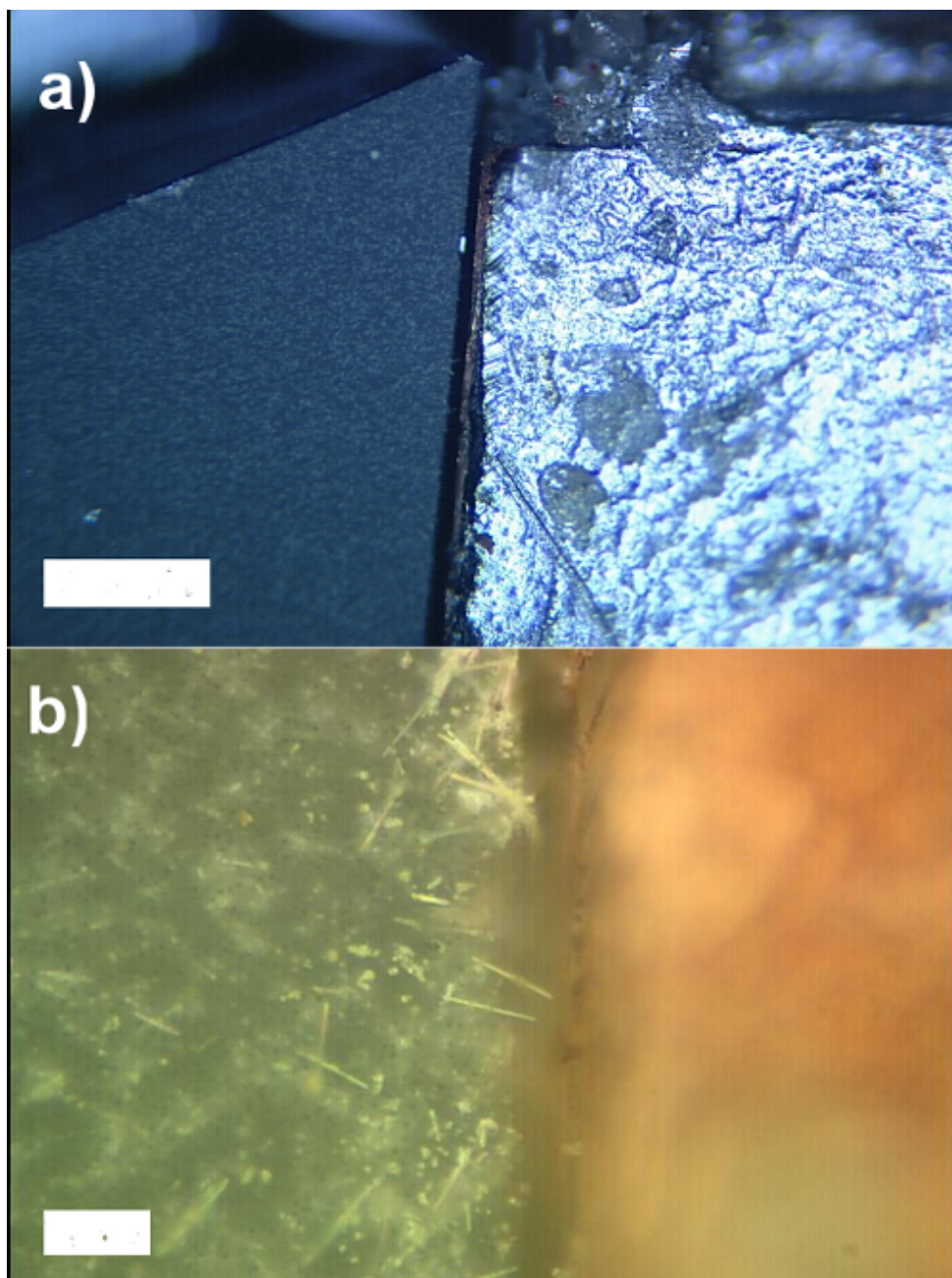


as a perpendicular plane relative to the nanowire  $c$  axis. However, this coplanar arrangement does require somewhat precise alignment of the relative heights of the nanowire substrate and CSE. In the example shown in Figure 5.1, the patterned circuit substrate is supported in a diving board-like geometry, which we quickly learn results in vertical position instability that is not particularly conducive to alignment of the far edge. We modify this design in later implementations of the circuit.

The choice of the optical micrometer stage in Figure 5.1 is made to allow for relatively fine-grained control over the gap between the CSE and the nanowires along the sample substrate edge. As seen in Equation 3.7, reducing this separation leads to greater fractional change in the parallel circuit capacitance due to nanowire motion and, hence, a larger signal to detect. Figure 5.2 shows optical microscope images of two examples of using this micrometer stage to bring the nanowire substrate into close coupling proximity to the CSE. We are able to use this device to improve our understanding of the capacitive detection technique, and discover areas for improvement. And while this particular device and technique work successfully and are incredibly useful, we recall that one goal is to make our fabrication process more standard and repeatable.

One problem we face with this project is that much of the photolithographic equipment available to us is designed for the use of thin substrates (silicon, sapphire, etc.) and glass masks (for extensive discussions of common lithographic processes, see Refs [95, 104]). Our choice of a more unconventional ‘substrate’ – the Cu-clad PTFE – requires some creativity on our part. The general concept of an exposure mask (photomask) is simply that there will be specific areas where ultraviolet light can (and cannot) interact and induce cross-linking in the photosensitive polymer (i.e. ‘photoresist’). Since, again, we would like a process that we can iterate faster and easier than the typical metal-on-glass photomask creation, we opt for the use of opaque, printed-ink circuit designs on plastic overhead transparencies (from a standard laserjet printer). These are obviously incredibly fast and inexpensive to create, and have sufficiently consistent output on the length scales we desire. Having created a number of the circuit designs by hand, we roughly know the dimensions for which we are aiming, and can simply specify these in our digital design and the

Figure 5.2: Optical microscope images illustrating the use of a micrometer stage to bring the nanowire substrate into close proximity to the CSE. At lower magnification (a), a larger portion of the nanowire substrate is visible (at left, in both images) on the order of 10  $\mu\text{m}$  from the solder-covered Cu electrode (right). Reflections from planar nanowire tips (cf. Figure 1.6) are seen as bright points in the otherwise-absorptive, high-aspect ratio nanowires. Scale bar is 100  $\mu\text{m}$ . On a different sample and at higher magnification (b) shows a region of the nanowire substrate (again, left) that is slightly less than 10  $\mu\text{m}$  from the CSE (again, right). At this level, we can make out broken portions of nanowires laying atop the larger forest. The focus plane is near the tips of the nanowires (again, reflective), and the narrow depth of field makes it difficult to resolve the nanowire-CSE separation in this particular image. The focus plane can, of course, be altered to emphasize any point along the nanowire (or CSE) height. The scale bar is 20  $\mu\text{m}$ .



resulting printout. An example of the kind of design we use is shown in Figure 5.3. More examples of these patterns are found in Appendix E.

First attempts at fabrication using this type of mask are conducted by using standard spin-on photoresist and physically overlaying the transparency on the laminate board within the aligner / exposer. After exposure and developing, the laminate is left with the desired Cu traces covered by hardened photoresist. The etch step makes use of a solution of dry, lump ferric chloride ( $\text{FeCl}_3$ ) and water. Initially, an approximately 500-mL solution of  $\text{FeCl}_3$  is created by stirring 8 – 10 1-cm<sup>3</sup> chunks of  $\text{FeCl}_3$  into DI water on a 90°C hotplate (under a fume hood). This is certainly more solution than is necessary for a single etch, but since it will be diluted very slowly, future etches should be able to simply reuse this batch (it has already been reused successfully a handful of times

Figure 5.3: An example of our laserjet-ink-printed, plastic transparency etch mask patterns for use on Cu laminate board. The laminate begins with Cu on both sides, so we selectively etch away material where desired. These, then, are representative of ‘positive’ etch masks. The dark regions will result in material (Cu) left behind for our surface circuitry. At left, the fully dark mask is for the bottom of the substrate and indicates that we intend to leave all of the Cu cladding to serve as a ground plane. We eventually learn, however, that it is easier to protect the bottom surface from etching via simple application of kapton tape. At right, the thin outline is only to guide the user in cutting out the laminate. This top surface design includes an ‘L’-shaped conducting path, the bottom (horizontal) piece of which is our common sensing electrode (CSE). The two parallel strips of Cu near the top are left to allow the laminate to be soldered to a standard SMA connector (cf. Figure 4.5). The small gap near the top of the L-shaped line allows a small air-core inductor to be soldered in-place. The coupling capacitance will be between the central pin of the SMA connector and the L-shaped line. These examples are not displayed at 1:1 scale. The actual rectangular board is approximately 0.5 in<sup>2</sup>.



since its creation). From this larger container, a smaller beaker of approximately 50 – 100 mL can be heated for any future etch (enough to submerge the substrate). While maintaining the hotplate temperature, the substrate is submerged in the solution with the use of plastic clamps (surgical tweezers). Conveniently, the luster of the Cu surface makes it is easy to inspect the progress of the etch and remove when desired. For a typical pattern on the 5880 Cu laminate, this etch might take approximately 30 – 45 minutes with periodic stirring. In order to have the most efficient etch, it is helpful to keep the substrate suspended in the solution so the etchant can circulate and remove the etched material from the newly-revealed regions.

Unfortunately, the results of using this photolithography procedure are mixed and, more often than not, poor. Furthermore, the alignment system is simply not designed to work on this sort of impromptu, odd-shaped substrate. The resulting layers of developed photoresist are ultimately thick and uneven, leading to very inconsistent etch patterns (precision thickness of photoresist is controlled by speed and ramp rate in a relatively straightforward method on standard round wafers). As a result, the conducting circuitry on top of these versions is inconsistent in electrical behavior and conductivity. After a handful of these attempts, we turn to a different pattern transfer process.

Conveniently, there is a large population of electronics and circuitry hobbyists in the world. We take a cue from this community and make use of ‘Press-n-Peel Blue’ mylar-backed PCB pattern transfer sheets from Techniks [105]. With this material, any image can be printed directly onto the (literally) blue sheets via a laser printer and then heat-pressed onto cleaned Cu board. This transfer process also requires a few iterations, but we can fast-forward to the last process recipe, which seems to work well.

First, warm a nearby hot-plate to 170°C and clean the pre-cut portion of Cu laminate board to be used by wiping with acetone, followed by isopropanol. The transfer process has a much higher success rate with a properly cleaned substrate. Place the substrate on the hot plate to warm up while cutting out the patterned Press-n-Peel film (as in Figure 5.3). Place the top-pattern film – ink side down – on the Cu substrate and using some sort of insulating object (e.g. a ceramic

block), apply continuous pressure to the film for 3 – 5 minutes. I seem to have better success when the pressure is applied while moving the block around atop the substrate. Avoid introducing relative displacement between the Cu substrate and film, however. After this time period is up, the substrate and film should be stuck together and you can move them with tweezers and run cold tap water over them to cool down before handling. When the blue film is gently peeled away, the black ink (which will have combined with the blue film under it) should be transferred to the Cu, also leaving a clear segment on the Press-n-Peel sheet. (A note: in order to get the most mileage out of the blue sheets, I advise printing only one or two examples of your circuit layout per sheet and carefully cutting those segments out in order to transfer the pattern. This way, you can reuse the remaining Press-n-Peel sheet with new patterns in the future by simply running them back through the printer.) If the top pattern is successfully transferred, then the substrate is nearly ready for the  $\text{FeCl}_3$  etch described above. Though the bottom, ground-plane pattern shown in Figure 5.3 would - in principle - lead to the correct design, we find that double-sided patterning is difficult to carry out properly. After some trial and error, we discover that standard kapton tape, too, is highly resistant to the  $\text{FeCl}_3$  Cu etchant. Once the top pattern is acceptable, simply covering the bottom surface with strips of this tape will allow only the top surface to etch. The patterns that result from this transfer and etch process are much more reliable and consistent than those from the previously-described photoresist and exposure process.

### 5.1.2 Key Electrical Circuit Features And Components

With a successfully-patterned Cu substrate, we can now talk about the remaining LC tank circuit components. The choice of components, too, undergoes many iterations and evolves over time. Each of these steps leads to some new understanding and sometimes additional flexibility. There are many small aspects to consider in calculating the electrical behavior of this circuit. We'll briefly discuss the more significant ones. The circuit shown in Figure 5.1 includes an air-core, surface-mount inductor from CoilCraft. In particular, we use an 8.1 nH model with a self-resonance near 5 GHz and a  $Q$  of about  $10^2$ . This particular company is chosen mainly because they ship out

free samples of their products if you request them. This inductance is used in combination with the coupling capacitor (discussed further below), the parallel nanowire-CSE capacitance, and parasitic parallel capacitance to lead to our overall microwave resonance near 3 GHz.

A portion of the parallel capacitance comes from the coupling of the surface Cu to the ground plane. The microwave board has a dielectric constant of approximately 10.2, and given the surface area of conducting paths, contributes approximately 1 pF to the parallel capacitance. This is also about the order of magnitude of most capacitances that we find in this circuit. The component of the parallel capacitance that we are most concerned with is that of the nanowire substrate and the nanowires themselves. A typical substrate cross-sectional area adjacent to the CSE is  $0.5 \times 2 \approx 1$  mm<sup>2</sup>. With an air gap between the nanowire substrate and the CSE, this also leads to a capacitance of about 0.1 pF. We can estimate the individual nanowire-CSE contribution by approximating the geometry as one of a cylinder near an infinite plane. With the values included in Table 2.1, the total capacitance from this geometry is approximately 0.1 fF, a small fraction of the overall parallel capacitance.

The original incarnation of the common sensing electrode (CSE) is seen in both Figures 5.1 and 5.2 in its coplanar (with the nanowire substrate) geometry. As mentioned earlier, this orientation leads to difficulties in obtaining vertical alignment of the conducting Cu of the CSE and the GaN nanowires atop the Si substrate. Often, many attempts must be made to get reasonably-close height matching. At best, alignment is done by eye and with incremental height adjustments – largely stacking of thin shims. One way around this situation would be to incorporate a second, vertical translation axis into the micrometer stage shown in Figure 5.1. However, this proposition ignores the position instability inherent in the diving-board-like microwave circuit. Instead, we eventually evolve the sample and holder orientation to implement a solution that deals with both of these issues.

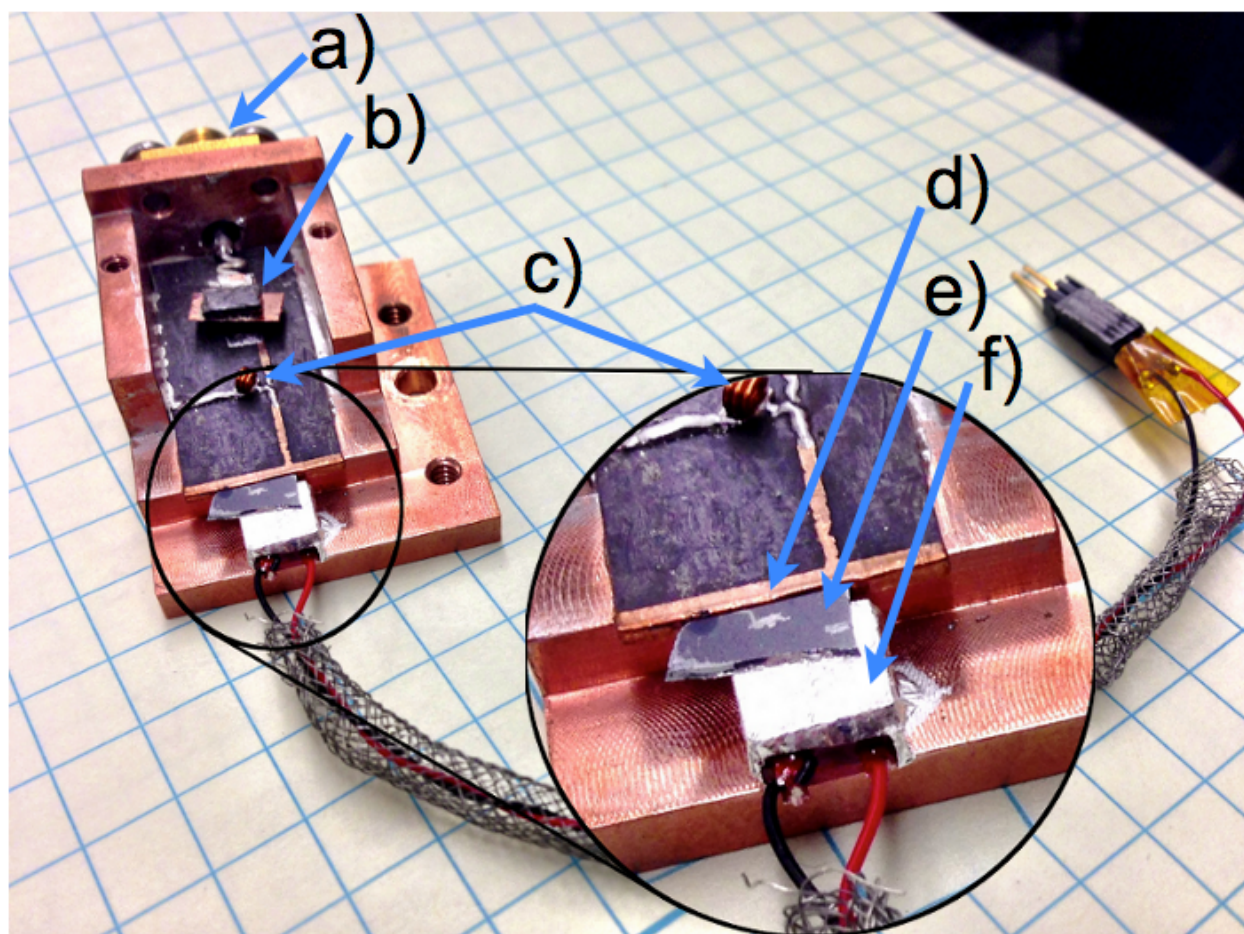
To begin, we increase the area of the CSE (via our heat-transfer pattern), such that its length (in the direction toward the SMA connector, cf. Figure 5.1) is now larger than the combined height of the Si nanowire substrate thickness plus the nanowire length (‘height’, if considering

it in the ‘up’ direction). Then, we imagine a sort of ‘underetch’ process wherein we remove the bottom Cu layer and the dielectric material from underneath most of the increased-size CSE. This removal of material can be carried out manually, with a razorblade. The now-suspended portion of Cu laminate (still electrically connected to the rest of the circuit) is then folded down over the dielectric material so the majority of its surface area is perpendicular to its original position, and a normal vector from this CSE would be pointed toward the nanowire substrate. The Cu ground plane is trimmed back sufficiently far so as to avoid short-circuiting with the CSE.

Now, proper alignment is as simple as roughly matching up the centers of the Si substrate and the CSE. As a result of this new arrangement, the precision needed to ensure sufficient overlap of the CSE and any nanowires along the substrate edge is significantly lower. Another benefit of this arrangement is that by placing the Si substrate and nanowires roughly in the center of the CSE, we have ensured that the full length of the nanowire will be as near as possible to the CSE. We expect that this ultimately leads to larger fractional changes in capacitance during resonator deflection, and also increases the number of potential nanowires in close proximity to the CSE. Finally, instead of suspending the CSE end of the microwave laminate substrate in air (the aforementioned ‘diving board’ geometry), we silver-paste the entire laminate at the bottom of a rigid Cu box. This removes the position instability and also provides a good sample holder for work that will be described in later sections. The most recent incarnation of the sample holder, with a nanowire sample near the CSE is shown in Figure 5.4. The SolidWorks model pattern for machining this sample holder is included in Appendix F.

When the notion of setting the separation between the nanowire substrate and CSE was first introduced (above, via the micrometer in Figure 5.1), one issue that was not discussed was why the separation was of order  $10\ \mu\text{m}$ . Why not  $1\ \mu\text{m}$ ? The answer lies in the fact that the Si substrate upon which the GaN nanowires are grown does not have a perfectly square edge. Our nanowire samples originate from larger (3-inch) wafers, which are cleaved to produce the approximately  $\text{mm}^2$  –  $\text{cm}^2$  samples we will measure. The crystal planes of the Si (111) wafers do not always break along nice straight lines (or, at least the author is not particularly good at breaking them along straight

Figure 5.4: An image of the final sample holder and microwave circuit used in this work, with an inset showing a blow-up of the CSE-nanowire substrate interface and PZT. The lid of the sample box has been removed in this image in order to expose the microwave circuit and coupling capacitor. The holder comprises a back plate – to which a standard flange-mount SMA connector is attached (a) for the introduction of microwave signals – and a larger, single piece of machined Cu with tapped holes for attaching the lid and attaching the box to other surfaces. The solid model we use to machine these parts is shown in Appendix F. Just above the black circle on the microwave board is the coupling capacitor (b). The bottom capacitor plate is a segment of Cu left unetched on the substrate. The top capacitor plate is a semi-rigid Cu sheet affixed to a block of dielectric material on a small serpentine spring. The height of the top plate is adjusted by the position of the threaded rod (not shown, see Figure 5.6). The air-core inductor is seen near the center of the microwave board (c). In the inset, the Cu CSE is seen (d) adjacent to the gray nanowire substrate (e), which is pasted to the top of the Al-covered PZT (f).



lines). Furthermore, upon breaking or cleaving the Si substrate, the cross-sectional profile of the Si wafer (that is, below the surface where the nanowires grow) varies.

As a result of this variable interface between the Si substrate and the CSE, the point of closest approach (i.e. the portion(s) of the Si substrate that contact the CSE) is not typically a useful region of nanowires. For example, in Figure 5.2, the micrometer has been adjusted until physical contact is made between the Si substrate and the CSE; they will not approach any closer. However, the region of nanowires in which we are interested (those shown in the image) are not as close. We have ‘preferred regions’ of nanowires, because often other regions of are damaged due to handling of the wafers or other deleterious events.

The final component of the circuit to be discussed is the coupling capacitor. This component, too, has undergone many iterations and improvements. Briefly, the important role of the coupling capacitor in determining the overall sensitivity to nanowire motion (cf. Section 4.1) leads us to prefer a capacitance that is adjustable (as opposed to the static capacitance seen in Figure 5.1). The adjustability of such a coupling capacitor allows us to obtain near-critical coupling to the microwave circuit and maximize our ability to detect nanowire motion. The first implementation of an adjustable capacitance is by way of a semi-rigid Cu flap, soldered to the central conductor of the SMA connector. This flap extends out over the long side of the L-shaped conducting path leading to the CSE (cf. Figure 5.3). By measuring the microwave reflection and its complex reflection coefficient in real time (as described in Section 4.1) we can manually adjust the coupling capacitance to our liking (e.g. with tweezers, on a lab bench). We call this process ‘tuning’ the microwave circuit, and occasionally refer to the capacitor as the tuning capacitor. Once adjusted to the preferred position, the rigidity of the Cu flap allows the coupling and circuit characteristics to remain relatively constant for a time. The overall behavior of the microwave circuit is of course dependent on the full environment, so some practice is needed in adjusting the coupling capacitance for the desired response also after the sample holder has been placed into the appropriate measurement environment (in an SEM chamber, vacuum chamber, etc).

For experiments that last on the order of one hour, this manually-adjusted coupling capacitor

seems to work sufficiently well. The resonance frequency of – and coupling to – the microwave circuit remain mostly constant. However, we see that for experiments that require a very long period of time, there is sufficient change in the coupling capacitance (determined to be the result of very slow, mechanical deformation) to warrant a hiatus in data acquisition for readjustment. Nevertheless, this setup works for us for a sufficient long period of time to acquire additional resonance data confirming both the functionality of the system and corroboration of previous results.

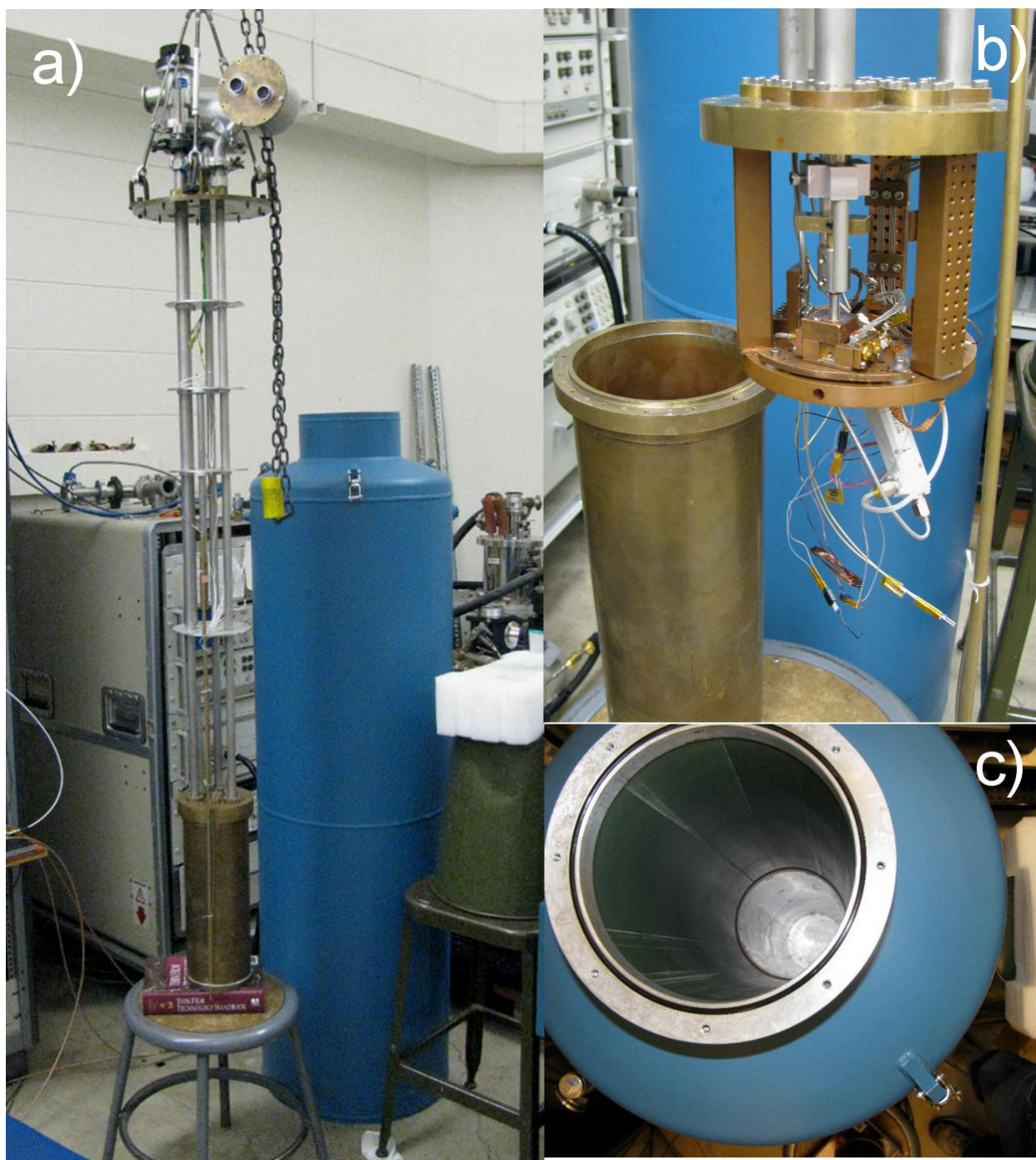
In parallel with the decision to create a more robust coupling capacitance, we also make a move toward making the first temperature-dependent measurements of the nanowire mechanical properties. This type of measurement has not been carried out in the Rogers lab for many years, so we make a diversion to briefly discuss the reintroduction of the vacuum cryostat. The development of a new (and useful) coupling capacitance is built into this design.

### 5.1.3 Resurrecting A $^4\text{He}$ Cryostat

In order to make measurements over a wide range of temperatures, we make use of an existing vapo-shielded, liquid helium (LHe) cryostat from Precision Cryogenics, Inc. [106] and a pre-existing, custom-built insert. These items are shown in Figure 5.5. As seen in Figure 5.5, on top of the insert plate are a number of ‘lollipops’ through which we make contact with the sample canister at the bottom of the insert. These include two lollipops for electrical connections: coaxial (SMA for microwave signals, BNC for low-frequency signals) and 26-pin (mil-spec). There is also a vacuum line with a valve at the top of the cryostat, and a feedthrough for a mechanical rod we will use to adjust our new microwave circuit tuning capacitor. Finally, there are also ports for the transfer and venting of LHe and liquid nitrogen ( $\text{LN}_2$ ).

From the insert plate, vacuum lines extend down toward the vacuum can at the bottom, where the sample is located. Support for these light, Al vacuum lines is provided by Al baffles spaced 6 – 12 in apart down their length. These baffles also help reduce circulation in the cryostat, allowing for longer periods of constant temperature at the base. Along the outside of these baffles and down along the vacuum can is a LHe level-meter, comprising a shielded superconducting element. This

Figure 5.5: Apparatus for low-temperature, vacuum, capacitive measurements of GaN nanowires. Blue dewar shown in a) is a Precision Cryogenics, Inc. vapo-shielded, liquid helium cryostat that allows us to make measurements down to around 6 K. The custom-built insert with electrical feedthroughs and vacuum line is suspended to the left of the dewar. At the base of the insert is the brass vacuum chamber/canister. b) A closer look at the two-part sample chamber. The brass vacuum can attaches to the upper lid where the feedthroughs are fixed. Atop the copper ring are the sample holder and various electrical components. A closer look at this region is provided in Figure 5.6. The aluminum fork for tuning the coupling capacitance can be seen in the center of the Cu posts. The sample holder is immediately below that, with its lid and tuning capacitor paddle above it. c) shows a view into the dewar, where the shinier portion is the magnetic shielding extending upward about three feet from the base – sufficient for shielding the brass vacuum chamber.



is read by the brown American Magnetics, Inc. LHe level monitor [107].

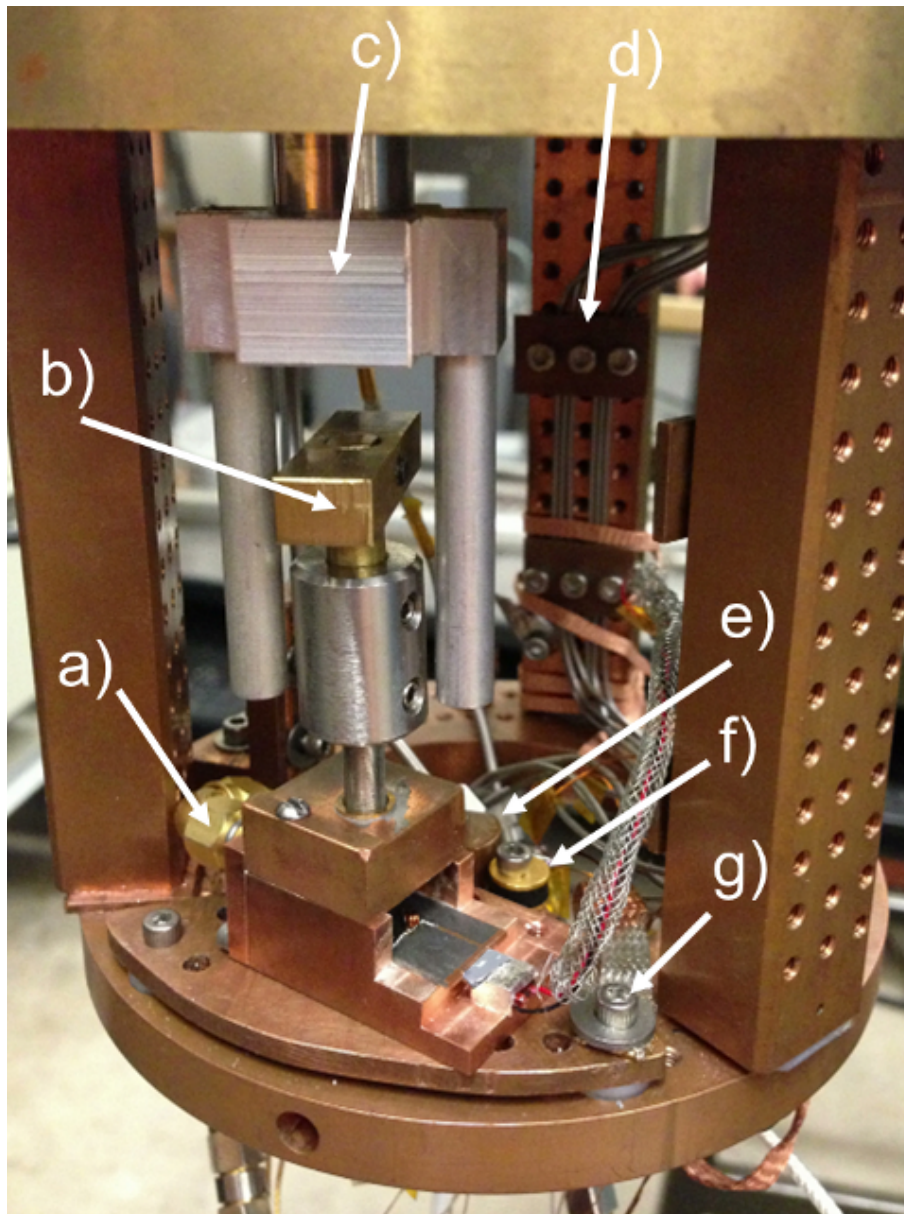
The brass vacuum chamber at the bottom comprises two pieces: a fixed lid (into which the vacuum lines and feedthroughs are connected), and a removable brass can that facilitates sample exchange and electrical circuit components. The vacuum seal between these two pieces is created by pressing a thin coil of lead-antimony wire. Suspended from the brass lid are Cu posts and a Cu ring onto which samples can be mounted.

As seen in Figure 5.6, the posts and ring contain many 4-40 tapped holes, allowing for a wide variety of attachment points. A Cu sample stage is stood-off from the ring with nylon washers in order to maintain local control of the sample temperature, but tied to the cryostat bath via a weak thermal link of meshed Cu. In close proximity to the sample holder, we also add a resistive heater and a silicon diode temperature sensor. The assorted electrical lines that enter the sample chamber (PZT control, microwave signal, etc) are all heat-sunk to the outer thermal mass. As Figure 5.6 shows, the sample box now interfaces with the larger cryostat structure via a ‘tuning paddle’ that manipulates a threaded rod, ultimately adjusting the separation between the two plates of the variable coupling capacitor. This is the top half of the variable capacitor shown in Figure 5.4. The threaded rod in use is 100-pitch, allowing for reasonably precise control over the inter-electrode spacing. The tuning paddle is rotated via an Al fork structure that extends down from the top of the cryostat through in a vacuum-sealed line. By rotating the fork prongs normal to the tuning paddle, we can maintain thermal isolation between the sample box and the outside world.

When all is said and done, the microwave circuit comprising our etched microwave laminate, capacitively-coupled GaN nanowires, and externally-controlled, variable coupling capacitance, is at the bottom of a LHe vacuum cryostat and has a typical resonance frequency near 3 GHz and a  $Q$  on the order of a few hundred. The typical power incident on the microwave circuit is approximately 5 dBm. On microwave resonance, the back-reflections from this system are typically around -30 dB. We can take these microwave signals from the cryostat and apply the same type of phase adjustment techniques described in Section 4.1.4 in order to amplify and record our data.

Figure 5.7 shows a schematic of the resulting system we have described, and Figure 5.8 shows

Figure 5.6: Close-up of the Cu ring within the cryostat vacuum canister, showing many of the essential components. a) SMA connector for incident and back-reflected microwave signals. These signals are carried on high-quality,  $50\text{-}\Omega$  semi-rigid coaxial cable. b) Tuning paddle for adjustable coupling capacitor in the microwave circuit (see Figure 5.4. Various set screws allow for adjustment of this composite structure. Extending down into the Cu sample box is the 100-pitch threaded rod that allows for fine control over the height the top capacitor plate. This paddle is manipulated by the corresponding Al fork, c). This fork is rotated by a rod that extends to the top of the cryostat insert and can be adjusted under vacuum and at any temperature. By rotating the Al fork away from the brass paddle, we can maintain better thermal isolation between the sample box and the outside world. d) Electrical lines carrying signals for e.g. the PZT are heat-sunk to the Cu posts. e) A small, bored, Cu block with a resistor (of order  $50\text{-}\Omega$ ) is affixed to the sample stage and serves as an in-situ heater for local temperature adjustment. f) A Si diode temperature sensor is affixed to the sample stage in close proximity to the nanowire sample. g) A weak thermal link is created by connecting meshed Cu thread from the larger sample canister (nominally at the internal temperature of the cryostat) to the isolated sample stage (Cu plate, stood-off from Cu ring by nylon washers seen e.g. below screw in g)).



SEM images of the CSE-nanowire interface. Over the course of this work, the external components (microwave components like amplifiers, mixers, etc) vary many times. But, as of the last experiments conducted, we are making use of the following set of components. The initial microwave tone (from the 8510 VNA) is divided by a Minicircuits power splitter [108]. One branch is sent through a variable phase shifter and used as the local oscillator (LO) in a Markii double-balanced IQ mixer [109]. The second branch is sent into the cryostat and is incident on the microwave circuit. The back-reflection from the cryostat lines is amplified by two low-noise Minicircuits amplifiers (ZX60-362GLN-S+, with a typical noise figure of 0.9 dB). The resulting signal becomes the RF input to the mixer. Both the I and Q mixer outputs are measured in the manner illustrated by Figure 4.4. We choose to use an IQ mixer mainly due to the fact that our current phase adjustment capability [110] on the LO mixer input is less than  $180^\circ$ . This can certainly be improved in future implementations of this experiment. Ultimately, one mixer output is chosen (by the criteria outlined in Section 4.1.4) to analyze after an additional stage of amplification (and sometimes filtering) by a Stanford Research Systems SR560 low-noise voltage preamplifier [111].

## 5.2 Capacitive Detection Of Nanowire Ensembles

With an appreciation for the building blocks of our measurement apparatus, we are now prepared to discuss some of the results obtained from it. A significant portion of the work that goes into these results is in the form of ‘behind-the-scenes’ work e.g. accurately observing and measuring specified levels of both signal and noise, maximizing signal-to-noise ratio, calibrating thermometry components, ..., and the list goes on. For the most part, though, these things are not particularly exciting. So, we will try to stick to some of the interesting experimental results.

The earliest significant observations that come out of the cryostat are resonance structures in high-vacuum, at room-temperature, that appear to have both appropriate resonance frequencies and  $Q$  factors. By systematically analyzing the response of these structures while e.g. varying drive levels, we confirm that they are, indeed, nanowire resonances of the type with which we are familiar. Significantly, this alone suggests that our approach of using a larger CSE to simultaneously

Figure 5.7: Schematic illustrating the experimental design of Chapter 5. As labeled, the GaN nanowires (NWs) are located a distance ( $d$ ) away from the CSE, creating a variable capacitance. The nanowires sit atop a Si substrate placed on the PZT actuator. The PZT is controlled, externally, by a signal generator ( $S_M$ ). Microwave signals at and near the electrical resonance of the LC tank circuit are provided by the 8510 SNA ( $S_G$ ). These tones are power split (PS) into two arms, one of which includes phase adjustment ( $\phi$ ) and becomes the local oscillator mixer signal (L). The other signal arm extends into the cryostat where it is incident on the microwave circuit via a directional coupler (DC), and back-reflects, through gain stages, to the RF mixer port (R). Either of the mixer outputs (I or Q, shown here as I) is then amplified again before being measured. Though labeled ‘PSD’ here, this setup can also be used to make phase-sensitive lock-in measurements of the nanowires, as well. The dashed blue box contains the items that are physically located within the cryostat and sometimes operate at low temperatures. An interesting note: the physical dimensions in this schematic cover a range of about seven orders of magnitude, from 100 nm (nanowire width) to 2 m (cryostat height).

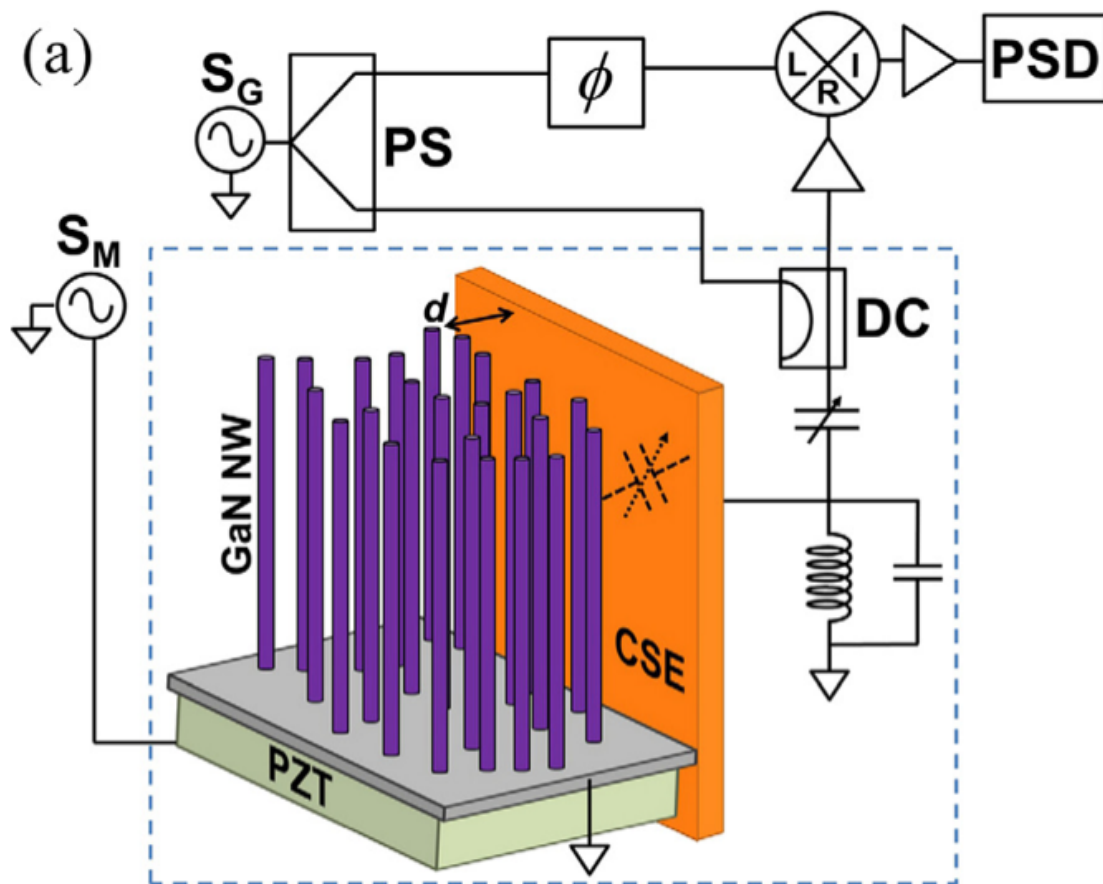


Figure 5.8: SEM images of the CSE-nanowire interface for an ensemble measurement. At left, the small nanowire substrate – pasted atop the PZT actuator – sits in close proximity to the large Cu CSE at the end of the laminate board microwave circuit. As shown, the scale bar is 1 mm. The small red box is enlarged at right to show detail near the interface where individual nanowires can now be resolved amidst the larger forest. The gap shown is slightly over 10  $\mu\text{m}$  as shown by the scale bar.

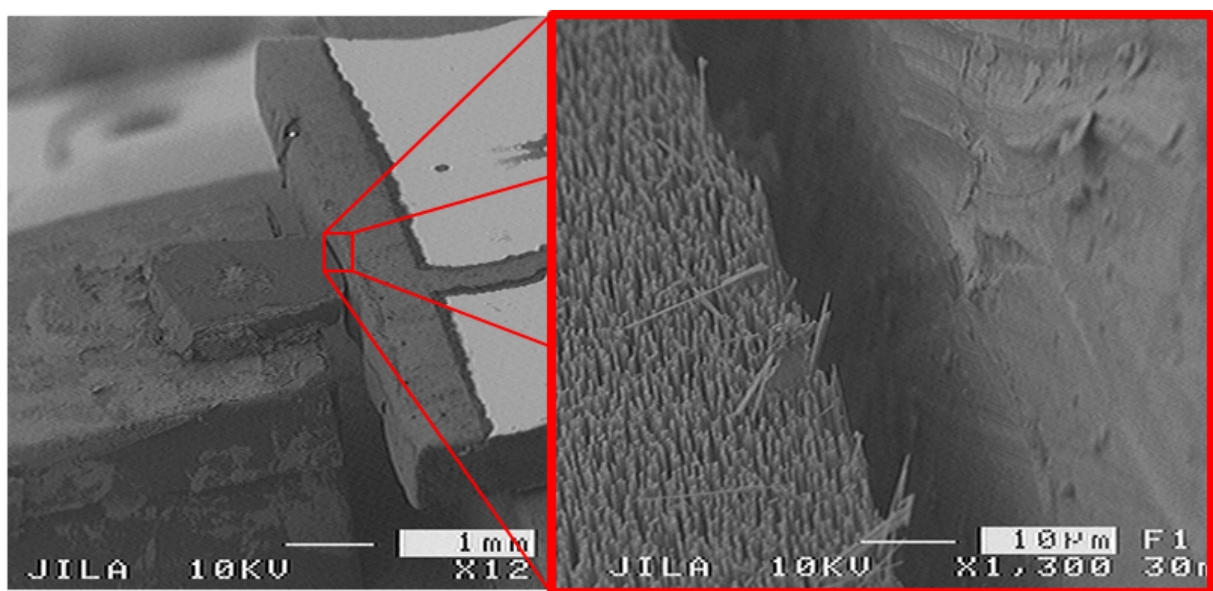
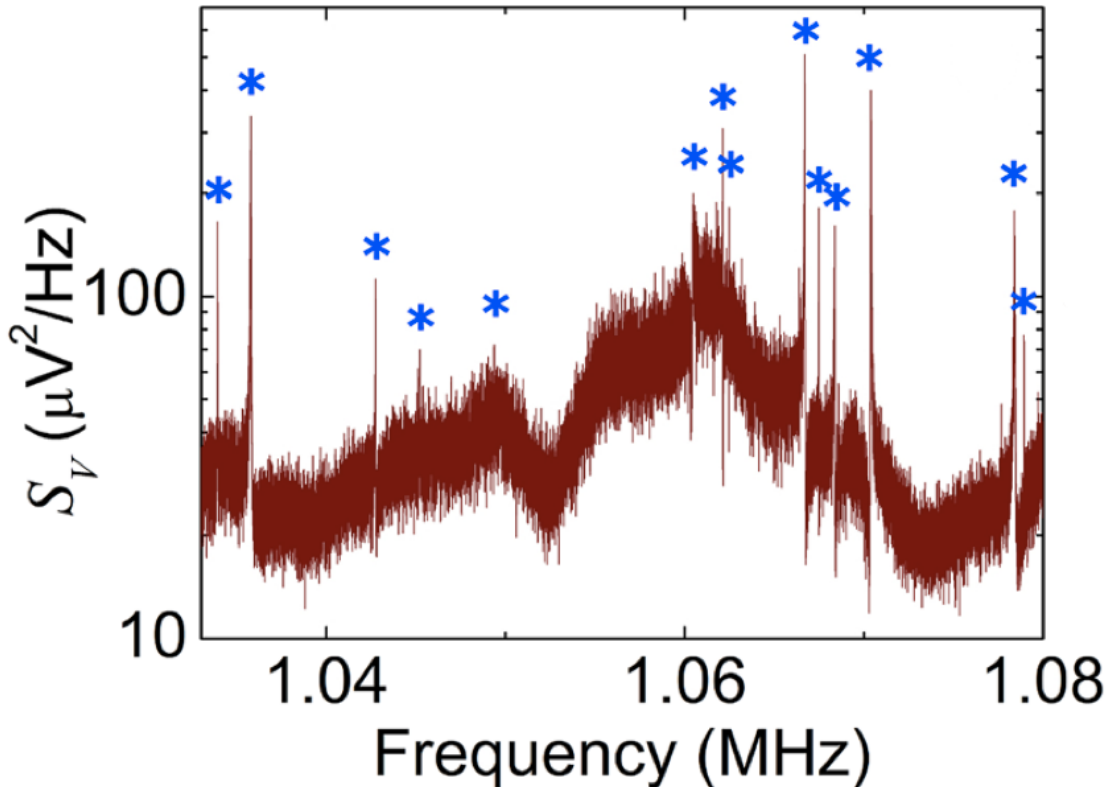


Figure 5.9: An approximately 45 kHz-wide region (near 1 MHz) of a voltage PSD,  $S_V$ , as detected by our homodyne reflectometry system. Seen atop the low- $Q$ , coherent structure from the PZT motion are fourteen resonance peaks corresponding to the mechanical modes of an ensemble of GaN nanowires. The ensemble measurement technique has observed up to about 300 simultaneous resonances. The nanowire resonance peaks are marked with blue stars. The sample is driven by 1 V<sub>rms</sub> white noise ( $\leq 10$  MHz) applied to the PZT. The asymmetrical resonance lineshape is as described in Section 2.2.2. Figure adapted from [112].



detect many nanowires does work as planned. An example of a PSD from the system is shown in Figure 5.9. In this PSD, we can see the correlated background signals described in Section 2.2.2 in addition to the narrow, high- $Q$  peaks of GaN nanowires (indicated by blue stars). This CSE-based ensemble measurement technique has observed up to about 300 simultaneous nanowire resonance modes.

A common calibration process that is often carried out on studies of nanomechanical resonators is that of measuring thermally-driven deflection (that is, changes in position due to the

fact that the resonator is in some arbitrary excited state as a result of its contact with a finite temperature bath). See, for example, Refs [60, 73, 113–118]. The measurement system described here succeeded on only two occasions in producing thermally driven nanowire resonance peaks. It appears that there is a combination of effects leading to this: insufficient apparatus stability and just enough sources of noise in and around our system. As a result, routinely producing such data is just out of reach for now. However, I believe that this situation can certainly be improved in future experiments using this setup or one like it (see Section 6.1).

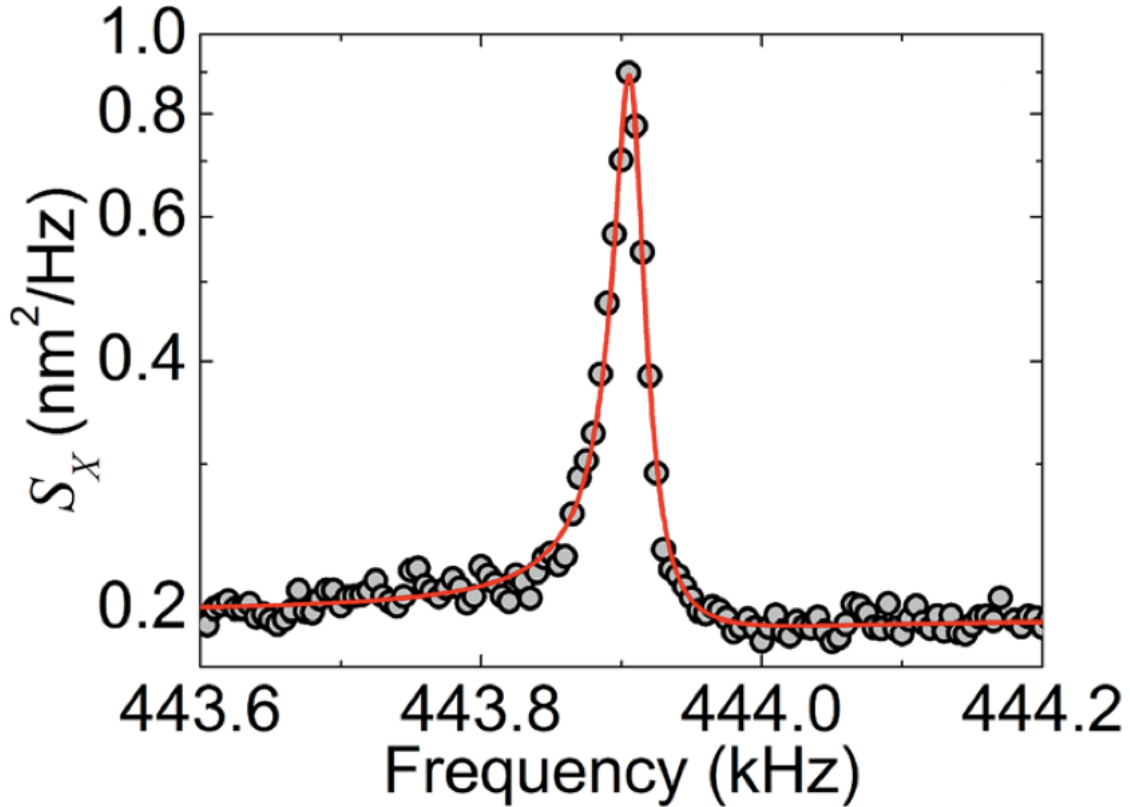
Nevertheless, as mentioned, we are able to measure the thermal deflection of two GaN nanowire modes. We initially corroborate the observed thermal resonance frequency by analyzing the response while providing increasing levels of excitation. By turning on and subsequently increasing the level of PZT actuation, we observe the resonance peak grow in amplitude with the drive level. We also observe the appropriate temperature dependence in the resonance frequency – an aspect discussed further in Section 5.2.3.

Using the equipartition theorem, we can calculate the root mean squared displacement for a resonator with  $k = 10^{-2}$  N/m and  $T = 300$  K (cf. Table 2.1) as

$$\langle \bar{x} \rangle = \sqrt{\frac{k_B T}{k}} \approx 7 \text{ \AA}, \quad (5.1)$$

where  $k_B$  is Boltzmann’s constant. With this value and the measured integral area from our thermally-driven resonance peak, we are able to calculate a conversion between the measured voltage level and physical displacement for this particular resonator. Subsequently, we can then drive this resonance mode and include a calibrated position PSD axis,  $S_X$ , along with the voltage PSD axis,  $S_V$ . An example of this data is shown in Figure 5.10. An important aspect of this calibration is that it is nanowire-dependent. That is, the integrated area under the thermally-driven resonance peak varies from one nanowire to another dependent on e.g. the sensitivity or distance. Ideally, this experiment will reach a point where each resonance can be calibrated by a corresponding thermal peak. Despite the fact that we don’t observe as many of these thermal peaks

Figure 5.10: Displacement PSD for a single, noise-driven (500 mV rms) GaN nanowire resonance mode near 444 kHz at 310 K. The solid red line is a fit to a Lorentzian lineshape with correlated noise from the PZT and an uncorrelated noise determined separately by an undriven spectrum. This uncorrelated noise signal arises from the front-end amplifiers. The Lorentzian contribution to the data yields fitted parameters of  $f_o = 443906.3 \pm 0.2$  Hz and  $Q = 22200 \pm 400$ .  $S_X$  is calibrated by measurement of a thermally driven resonance peak and application of the equipartition theorem. The integrated rms thermal deflection for this nanowire is approximately 7 Å. Figure adapted from [112].



as we would like, we still have much to learn about the nanowires and their ensemble properties.

### 5.2.1 Quick Inspection: Pressure Dependence

As discussed in Section 4.2.2, at high pressures we observe gas damping of the nanowire resonators. From our calculations in Section 2.3.1, we are confident that at our typical operating pressures ( $10^{-6} - 10^{-5}$  Torr), we are well below the threshold at which gas damping becomes a significant contribution to the overall dissipation. However, by briefly looking at the effects of

significantly higher pressures, we can get an estimate for when these effects are important.

Figure 5.11 shows two-phase lock-in data for one GaN nanowire resonance mode that is measured at a wide range of pressures. At pressures of order  $10^{-4}$  to  $10^{-1}$  Torr, the peak is observed to shift a bit in frequency, with minimal change in the observed linewidth. At  $10^0 = 1$  Torr, the peak is seen to quickly lose amplitude and becomes much wider. Then, additional data is acquired for a narrower range of pressures: 1 – 10 Torr. Here, we see that relative to the resonance amplitude at 1 Torr, at 2.5 to 5 Torr, the peak is all but invisible. By 10 Torr, the resonance is virtually indistinguishable from the background level. This particular set of data is not part of an extensive study. Rather, it is just to see that, indeed, air damping does become a significant contribution to the overall dissipation for these nanowires. In this short experiment, the pressure at which peak broadening is apparent – by eye – is of order 1 Torr. However, the effect of pressure on the central resonance frequency is apparent on the first step, to 1 mT ( $10^{-3}$  Torr).

### 5.2.2 Resonance Parameter Distributions

Recall our motivation for this Chapter has been the notion of ensemble measurements. A good way to look at these ensembles is via a histogram of the measured results. In Figure 5.12, such a histogram is shown illustrating the distribution of measured resonance frequencies for a typical sample. This set of data includes about 250 resonance modes. The resonance frequency data is divided into 10-kHz bins to see the aggregate behavior. The mode of the distribution is just under 1 MHz, consistent with our previous experiments.

There is an interesting ‘notch’ in the data around 1.3 MHz that we have also occasionally observed in other data sets. One possible explanation for this is a low level of response in the PZT at these frequencies. We have only taken data on a couple of these PZT actuators, and a thorough investigation of each one’s particular response as a function of frequency has yet to be determined. Another possible explanation comes from the nanowire growth, itself. Though no *a priori* reason exists why this particular bandwidth would be excluded, perhaps the growth process has a bimodal distribution in geometry. This kind of event could present in the form of preferred

Figure 5.11: Data from a quick inspection of the effects of gas damping on observed nanowire resonance curves. Two-phase lock-in measurements are shown for a single GaN nanowire mode at a range of sample chamber pressures. Increasing the chamber pressure from the typical  $10^{-6}$  Torr to  $10^{-4}$  Torr (not shown) shows no obvious difference in the lineshape. (a) At each step of increasing the pressure by a factor of ten, the central frequency is observed to shift, and at the level of  $10^0 = 1$  Torr, the peak becomes noticeably lower in amplitude. (b) Looking more closely at the pressures near 1 Torr, we see that the resonance peak becomes nearly indistinguishable from the background signal near 5 Torr.

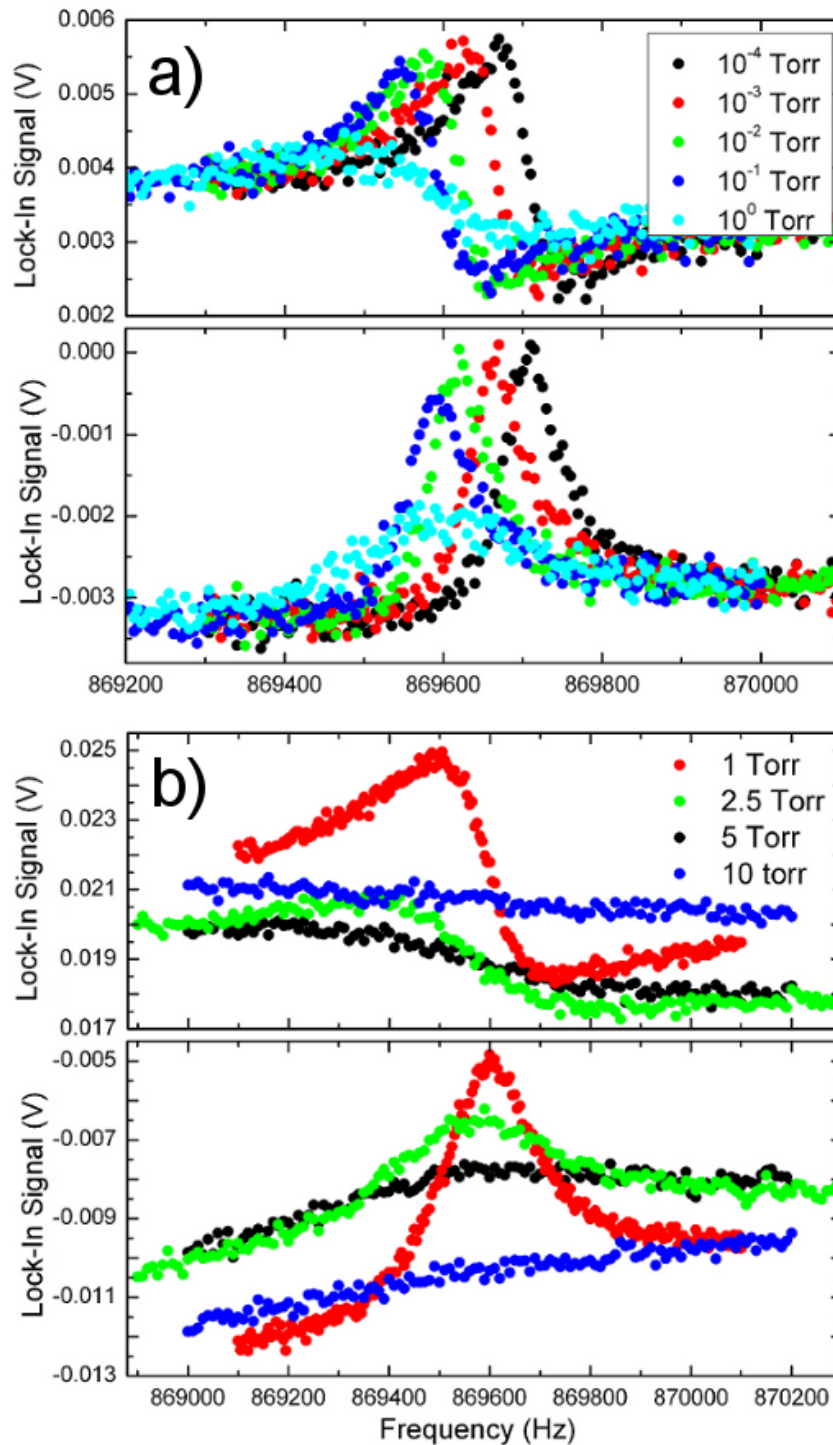
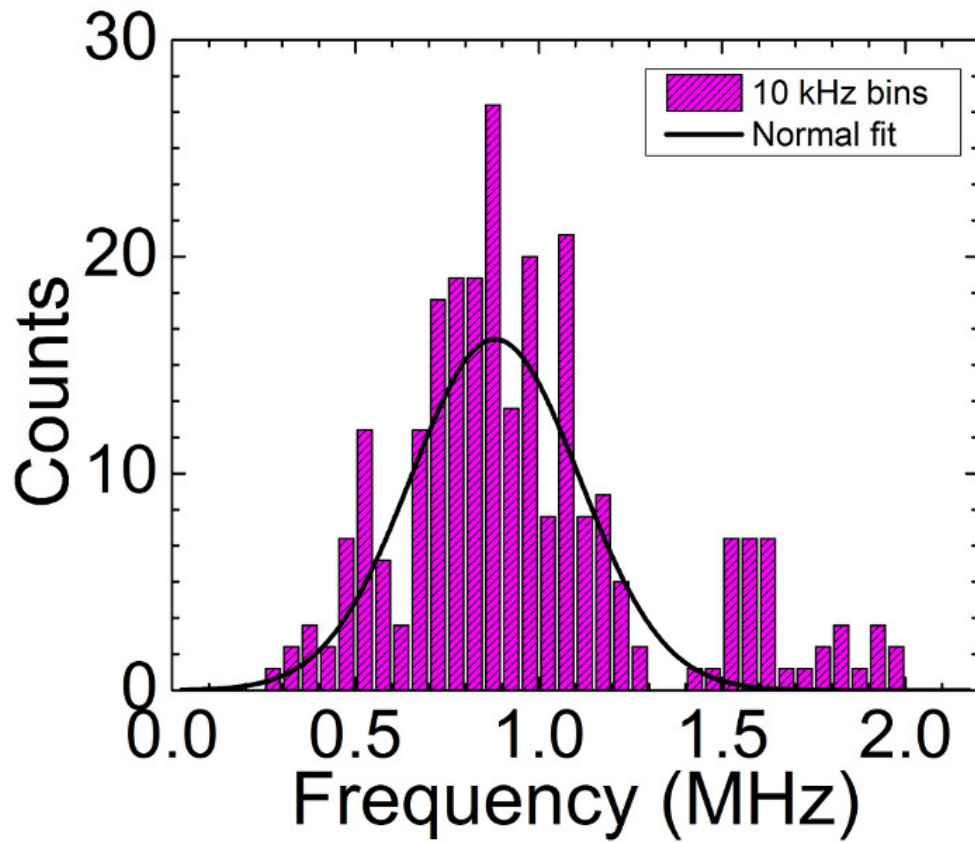


Figure 5.12: Histogram illustrating the distribution of 250 simultaneously measured resonance frequencies from a PSD using our CSE-based capacitive measurement technique. The frequencies are binned by 10 kHz, and the black curve is a normal fit to the distribution. The mode of the distribution is just below 1 MHz, and the corresponding normal fit result for resonance frequency is  $900 \pm 200$  kHz. The tails of these distributions consistently range from around 250 kHz to about 2 MHz.



regions of ‘allowed’ frequencies. The black line is a normal fit to the binned data (with  $1/\sqrt{N_{bin}}$  weights) and does a reasonable job of representing the data. The fit results for the center of this normal curve are  $900 \pm 200$  kHz. These numbers are consistent with previous results, as well.

We can explain the variation in observed resonance frequencies by considering the nanowire geometry. Recall Figure 1.6, where we can see that the nanowires have approximately the same length (plus or minus perhaps  $1 \mu\text{m}$ , less than 10%). But, the nanowire radii typically vary as approximately  $150 \pm 100$  nm (based on experience). If we take the mean value of the normal fit to the resonance frequency distribution as being correct, and calculate the range of frequencies that would follow from 100 nm of variation in radius, we find a range covering about 300 kHz to 1.5 MHz. Notice that this is very close to the observed range of frequencies in Figure 5.12. So, we can be fairly confident in attributing this distribution to geometrical differences amongst the nanowires.

Recalling that we are interested the intrinsic high  $Q$  factors of the nanowires, we can make a similar plot of the distribution of peak-widths (line-widths) (Figure 5.13). Then, using both of these datasets, we can plot the distribution of  $Q$  (Figure 5.14). The histogram data in Figure 5.13 is divided into 5-Hz bins, and we see a nice tight distribution of widths with a mode between 30 and 40 Hz. Again, we can fit a normal curve through the data to extract some additional quantitative insight from the histogram. Here, the resulting fit suggests the typical peak width is  $40 \pm 10$  Hz. Here, we note that though the normal curve does a reasonable job at describing the majority of the data – particularly near the mean – there are a handful of points in the upper tail.

In Figure 5.14, the histogram data shows the calculated  $Q$  factors for each of the resonances measured and shown in Figs 5.12 and 5.13. The individual resonance peak fitting provides the central frequency and linewidth. From these values, we calculate  $Q = \frac{f_o}{\Delta f}$  and use their uncertainties to calculate uncertainties in  $Q$ . The  $Q$  factors in Figure 5.14 are binned by 2500, and show the mode is around 25,000. The corresponding normal fit to the distribution gives a typical  $Q$  of  $23,000 \pm 8000$ . This data also has a small tail at higher  $Q$  factor, and matches our previous experience: the majority of the measured  $Q$  factors are in the low- to mid- $10^4$ , but occasionally they approach the high  $10^4$ s. One very clear opportunity for the continuation of this work is to

Figure 5.13: Histogram illustrating the distribution of 250 simultaneously measured resonance curve linewidths from a PSD using our CSE-based capacitive measurement technique. The widths are binned by 5 Hz and the black curve is a normal fit to the distribution. The mode of the distribution is between 30 and 40 Hz, and the corresponding normal fit result for peak width is  $40 \pm 10$  Hz.

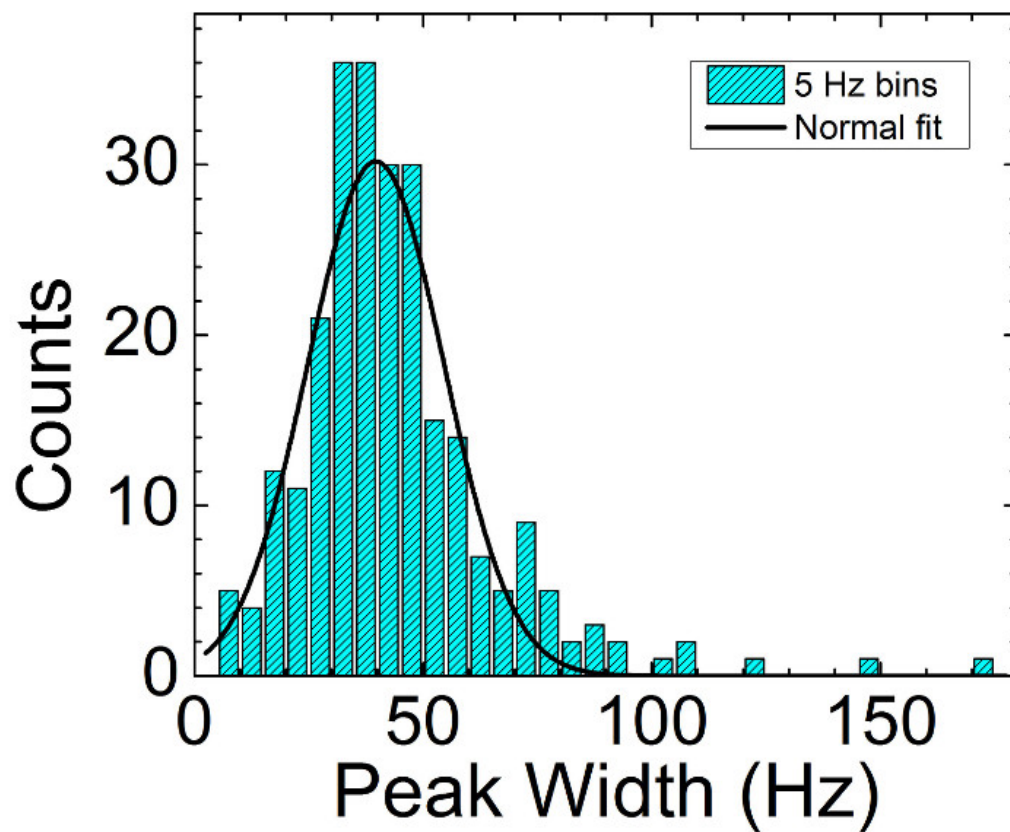
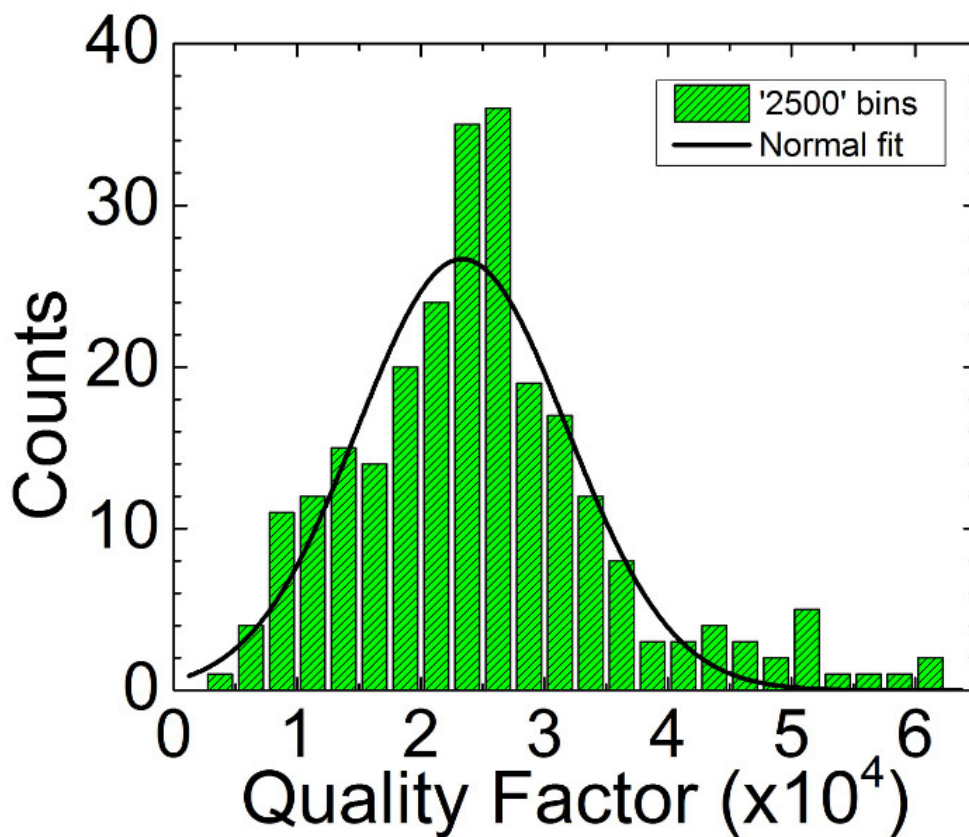


Figure 5.14: Histogram illustrating the calculated values of  $Q$  from a distribution of 250 resonance curves measured simultaneously from a PSD using our CSE-based capacitive measurement technique. The  $Q$  factors are binned by 2500 and the black curve is a normal fit to the distribution. The mode of the distribution is about 2500, and the corresponding normal fit result for  $Q$  factor is  $23,000 \pm 8000$ .



identify some of the correlations and similarities amongst these high- $Q$  nanowires and try to further skew this distribution toward that end.

Based on the discussion of a loss modulus in Section 2.1.1, we can also use these distributions of  $Q$  to estimate the magnitude of the imaginary component of the Young's modulus. Given the large  $Q$  factors we observe, we expect that the imaginary  $E_2 \ll E_1$  (where  $E = E_1 + iE_2$ ). As described in that section, we can approximate  $Q$  by the ratio  $\frac{E_1}{2E_2}$  (which is also an expansion of the ratio of the real to imaginary components of the complex frequency), and this functional form of  $Q$  should not have any of the geometrical dependence described above. Since we are reasonably confident about the value of  $E_1$  [50], we can use this formula and the observed distribution in  $Q$  to extract a corresponding distribution in  $E_2$ . The result is shown in Figure 5.15 and verifies that we are correct in assuming it would be small. This data has an obvious peak near 6 MPa, and a variation on the order of 2 MPa. Interestingly, it also has a pretty significant tail on the high end. Relative to the distribution in e.g.  $Q$  this is a significantly more narrow peak and is many orders of magnitude smaller than  $E_1$ , corroborating the low dissipation we observe via measured  $Q$  factors.

If both the  $Q$  factors and the resonance frequencies follow a nice distribution, an interesting question to ask is the following: what (if any) correlation should we expect between these two parameters? Given that  $Q$  is proportional to  $f_o$ , we might expect to see some kind of linear correlation between the two variables (with some variation, as we have already seen that both values are distributed).

Plotted in Figure 5.16 is a scatterplot of the measured resonance frequencies and  $Q$  factors for each nanowire in a new ensemble. This ensemble has just under 100 nanowire modes represented in it. Plotted along the sides are the corresponding histograms of the values in the scatterplot. Of note: this particular figure is created with low-temperature data and has very high  $Q$  values (to be discussed further in Section 5.2.3). However, the same scatterplot for room-temperature data looks very similar. The key aspect of this data is that the scatterplot of  $Q$  versus resonance frequency does not appear to follow any sort of trend line at all. There is no linear trend to the data, as might have been hypothesized. Instead, we observe a mostly normally distributed collection of resonance

Figure 5.15: Histogram illustrating the calculated values of the loss modulus,  $E_2$ , extracted from the distribution of  $Q$  and known  $E_1$ . The values are binned by 1 MPa and the peak value is 6 MPa, with an apparent nominal width of about 2 MPa. These are significantly smaller than established value of  $E_1 = 300$  GPa, corroborating the low dissipation we observe via measured  $Q$  factors.

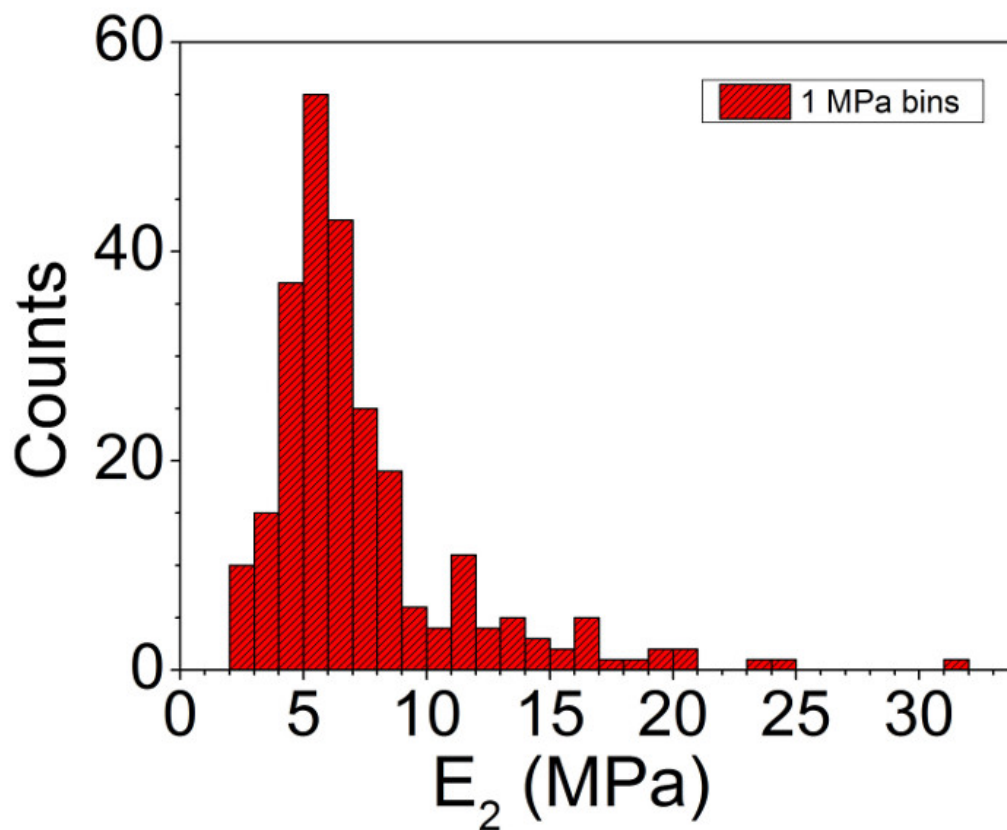
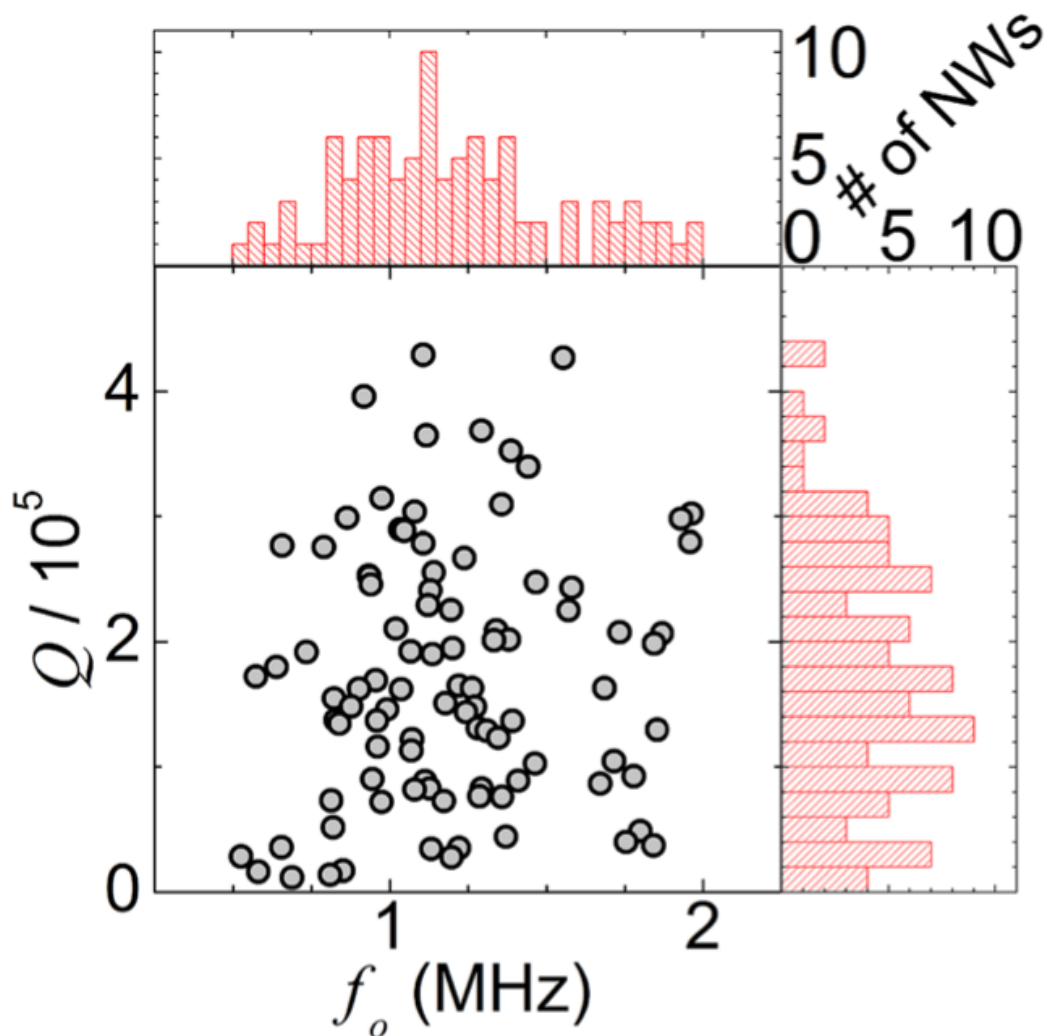


Figure 5.16: Scatterplot of the resonance fit parameters for an ensemble of about 100 GaN nanowires, detected simultaneously in a PSD. Histograms illustrating the distributions of the same parameters are shown alongside the graph. This data was collected at low temperature (cf. Section 5.2.3), leading to the high  $Q$  values in the plot. However, the same type of plot for room-temperature resonators looks very similar. There is no obvious correlation seen between the  $Q$  factors and the resonance frequencies. This is a useful and interesting result, suggesting that even the lower-frequency resonators can potentially have high  $Q$ .



parameters. Both histograms have shapes that appear very similar to those seen in Figs 5.12 and 5.14. This behavior suggests that the GaN nanowire resonators can potentially possess very high  $Q$  factors with a wide range of resonance frequencies. From an applications point of view, this is a potentially very useful opportunity.

### 5.2.3 Temperature Measurements: Setup

The final set of results that we discuss is an investigation of the temperature dependence of a nanowire ensemble. This experiment turns out to take an incredibly long time thanks to the complexities of building a cryogenic experiment. Hopefully, future recreations or replications of this work will benefit from the observations and findings discussed in my many notebooks. To begin, I'll go over some of the details required to get this type of experiment running. Then, I'll present some of the results.

In this experiment, we begin by observing an ensemble of resonances at typically high vacuum, and at room temperature. Having established the proper operation of our system, we begin the cooling process by transferring liquid nitrogen ( $\text{LN}_2$ ) into the cryostat. The insert has two additional ports on the top for the purpose of liquid transfer and venting. When the cryostat has been properly arranged adjacent to a  $\text{LN}_2$  dewar, an assembled transfer hose can be used. The transfer hose comprises a thin, L-shaped aluminum pipe, approximately seven feet tall. Attached to the upper end of this is an approximately six-foot length of plastic tubing, which ends in a metal fitting designed to match a standard low-pressure  $\text{LN}_2$  dewar. The pressure within the transfer hose is high when  $\text{LN}_2$  is flowing, so the plastic tubing is taped and hose-clamped onto the metal piping. Through a few freeze-thaw cycles, this tape will crack and begin to leak (as will the very end of the plastic tubing), so periodic maintenance is currently required. Also attached to the metal pipe is a standard rubber (beaker) stopper, at about the height of the cryostat insert top plate. For the transfer of  $\text{LN}_2$  into the cryostat, this is not used, but will be necessary when later removing  $\text{LN}_2$ .

With the transfer hose in place in the cryostat and connected to the liquid valve on the  $\text{LN}_2$  dewar, we open the valve to begin the flow into the cryostat. Since we have to cool the internal

components from about 300 K, a significant quantity of chilled N<sub>2</sub> gas will flow through the system before any liquid begins to transfer. In order to allow the cold gas time to remove heat energy, we keep the second cryostat insert port sealed (with a steel plug and rubber gasket) while letting pressurized N<sub>2</sub> escape around the metal pipe in the second port. This leads to a high-pressure jet coming out of the cryostat insert lid very close to the feedthroughs and electrical lollipops. To prevent the rubber gaskets in those assemblies from freezing and potentially introducing a dangerous leak, I typically attach a few sheets of ordinary printer paper, folded length-wise, around the metal pipe. These direct the cold gas up above the rubber gaskets and provide sufficient insulation during the transfer.

The plastic tubing that connects the dewar and metal pipe is certainly not the best solution, as it occasionally cracks and leaks from the cold. However, it works well enough that I have stuck with this process. In order to lengthen the lifetime of this system, it is suggested that the transfer not be attempted at incredibly fast rates. The combination of rapid cooling and high pressure will break the hose. With a modest transfer rate, the jet coming out of the cryostat will begin to cool immediately and the thermometry system will immediately begin to indicate that the vacuum can (which has a direct thermal link to the Cu ring inside – the location of the chamber temperature sensor) is cooling. Once liquid is flowing through the hose, the transfer rate can be increased and left alone for a time. In my experience, there is something on the order of fifteen minutes until the can temperature dips into the sub-200 K range. At some point in the high-100 K range, the LN<sub>2</sub> transfer can be stopped, allowing the collected liquid a chance to drag the cryostat's thermal mass down to an equilibrium temperature. If the experiment is intended to operate for a long period of time at 77 K, more liquid can of course be added. However, for efficient cooling to LHe temperatures, we try to avoid having excess LN<sub>2</sub> collect at the bottom.

If (and when) it is decided that the cryostat needs to be warmed while there is still liquid inside, the process for removing LN<sub>2</sub> is nearly opposite that of cooling. The same transfer hose can be used, only this time the rubber stopper is – as best as possible – sealed in-place in the second insert port. In my experience, this involves wedging the rubber (and the electrical tape that

keeps it together) into the opening as far as possible (note: this requires careful initial placement of the stopper on the metal pipe), followed by large quantities of electrical tape going over both the stopper and the brass insert port. The goal is to seal this opening from leaking when the cryostat is placed under high pressure. Trial and error here will be your friend. Assuming the second port (with the transfer hose) has been adequately sealed, the dewar connection end of the hose should be placed into a large bucket or insulated container to collect any removed LN<sub>2</sub>. In the vicinity of the cryostat, there is an additional coil of plastic tubing that has a fitting on the end for insertion in the first cryostat insert port and sealing there. The other end of this tubing has a fitting to connect to one of the pressurized, room-temperature N<sub>2</sub> gas canisters that typically live in the basement lab. While regulating the flow from the gas canister, the pressure will build in the cryostat, forcing the liquid up and out the transfer hose, into the waiting collection container. When the gurgling sound stops and warmer air is felt coming out the transfer hose, the hoses can all be taken out. Without liquid in the base of the cryostat, the vacuum can will begin to warm up. If the goal is to further lower the sample chamber to LHe temperatures, the crucial first step is to ensure there is no LN<sub>2</sub> remaining in the cryostat. Letting the can warm up to 90 K or so just to be sure is a wise choice. The LN<sub>2</sub> ‘slushy’ that results from starting a LHe transfer too early (and freezing solid the LN<sub>2</sub>) is a slow and expensive problem to deal with.

Also in the basement lab is the necessary LHe transfer system (long, awkward, U-shaped vacuum line). This process goes much easier with two people, but I will not explain this in detail. Essentially, one end of the transfer rod goes into the LHe dewar, the other fits carefully into the narrow funnel below the first cryostat insert port, and the liquid transfer goes quite quickly. While transferring, cold gas is again coming out of the second insert port, so a length of rubber tubing is helpful to direct the He gas away. Once the liquid transfer is complete, we place a one-way pressure valve (pop-off valve) on the rubber tubing to allow boil-off to escape but prevent atmosphere from entering the cryostat. A image from a LHe transfer is shown in Figure 5.17.

With the system described so far, we are capable of making measurements on nanowires samples that span the range of about 10 K to 320 K. The lower bound results from dissipation

of microwave power into the approximately  $50\text{-}\Omega$  load (resonant circuit). By turning down the incident power, we can attain this temperature but it also compromises our signal-to-noise ratio (SNR). Once the sample is warmed a few Kelvin, we can turn the microwave power back up for greater SNR. At each of the lowest temperature measurements, we make an effort to observe the effects of our current level of microwave power to avoid artificially inflating the sample temperature because we are observing the heating of the sample stage. The upper bound on temperature is not

Figure 5.17: The originally-red (now-white with frost) length of rubber hose attached to the second cryostat insert port is venting the He gas boil-off during a LHe transfer. The metal, vacuum transfer line runs out of the frame up and left of the vent hose. The top portion of the cryostat is seen to frost, as well. These frosted portions thaw quickly once the active transfer is over and the outer components reach a thermal equilibrium with the room atmosphere.



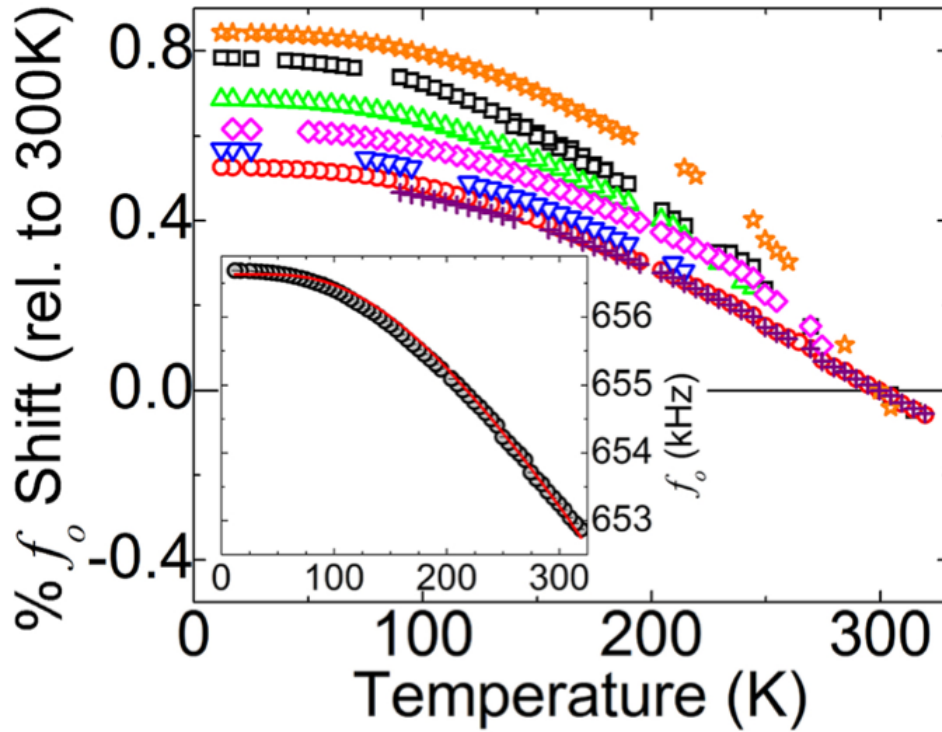
a hard one. Rather, it is simply as high as our experiments took the sample. Previous work on the GaN nanowire samples looked at still elevated temperatures (albeit in a different environment) and also saw interesting resonance behavior [47].

#### 5.2.4 Temperature Measurements: Results

The lengthy experiment described here consisted of a single GaN nanowire substrate with an ensemble of individual nanowire resonances observed over the temperature range 12 – 320 K [112]. At each temperature step (5 K), and the nanowire sample was actuated at a three to four different drive levels, and a PSD was recorded for each. After fitting the peaks in the dataset, we typically make an effort to choose the highest level of drive that does not excited the resonances into nonlinear response. This observation comes most easily from obtaining a poor fit to a standard Lorentzian. We choose to move up in temperature, as the ‘restoring force’ of the low-temperature bath makes it easier to maintain sample temperature stability at the 10 mK level (our typical level).

Figure 5.18 shows a subset of the resonance data for which we succeed in acquiring the corresponding peaks across the majority of the temperature range. This data shows the relative temperature dependence of the nanowire resonance frequencies. Since the nanowires plotted cover a range of room temperature resonance frequencies from about 500 kHz to about 2 MHz, the data shown is of the percent shift in resonance frequencies, relative to 300-K values (i.e. at 300 K, all data passes through  $y = 0$ ). The observed shift in resonance frequencies is consistent with the stiffening to due a temperature-dependent elastic modulus. A relative increase in resonance frequency of less than 1 % over the range 12 K – 320 K is observed for all NWs studied in this work. Near room temperature, the average measured frequency shift is  $40 \pm 20$  ppm  $\text{K}^{-1}$ , consistent with previously reported results for GaN nanowires [47], yet too large to be explained by observed thermal expansion alone [88]. Similar behavior has been observed in silicon [2, 119], and gallium arsenide [120] nanoscale resonators. We also fit some of our data to a semi-empirical model of temperature-dependent elastic moduli previously used on silicon microresonators (the Wachtman equation) [2]:

Figure 5.18: Percent resonance frequency shifts for a seven-nanowire subset of the measured GaN nanowire ensemble, relative to their 300 K values. All measured nanowires show less than 1 % change over the range 12 K–320 K. The average frequency shift near 300 K is  $40 \pm 20$  ppm  $\text{K}^{-1}$ . Room-temperature resonance frequencies are approximately: 573 kHz (black squares), 653 kHz (red circles), 733 kHz (green up-triangles), 1.12 MHz (blue down-triangles), 1.33 MHz (pink diamonds), 1.36 MHz (orange stars), and 2.44 MHz (purple crosses). The inset nanowire has a room-temperature resonance near 653 kHz. Solid red line is a fit to the data using an Euler-Bernoulli model for the resonance frequency with a temperature-dependent Young's modulus. Slight offsets in the single-nanowire data indicate temporal breaks in the experiment, where small amounts of adsorbed material likely modified resonance positions. Figure adapted from [112].



$$E(T) = E_o - BT e^{-\Theta_D/2T} \quad (5.2)$$

where  $E$  and  $E_o$  are, respectively, the temperature-dependent and zero-temperature Young's moduli,  $B$  is the bulk modulus,  $T$  is the temperature, and  $\Theta_D$  is the Debye temperature. In the inset, we include a fit for a damped, cantilever beam resonance frequency with this temperature-dependent elastic modulus and fixed, bulk GaN values of Debye temperature and zero-temperature Young's modulus.

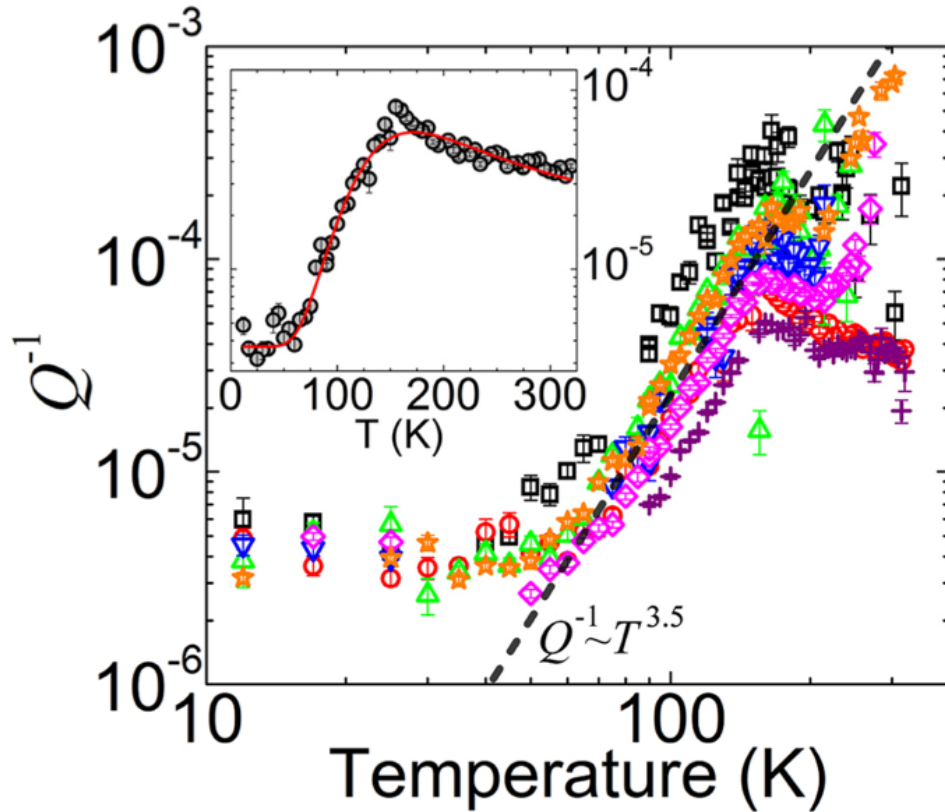
Interestingly, the ensemble data show a 20 ppm  $\text{K}^{-1}$  variation in the temperature-dependent relative resonance frequency shift at 300 K. We note that if all nanowires in the ensemble shared the same thermal expansion coefficient and temperature-dependent Young's modulus, then all relative resonance frequency shifts should lie on the same curve. They clearly do not, indicating nanowire-to-nanowire variations in either or both of these quantities within the ensemble. This echoes the ensemble distribution analysis discussed above.

Figure 5.19 shows the dissipation  $Q^{-1}$  for the same seven nanowire ensemble shown in Figure 5.18, with the same color- and symbol-coding. Near room temperature, typical values of  $Q^{-1}$  are near  $10^4$ . At slightly lower sample temperatures,  $Q^{-1}$  remains approximately constant, though there is a weak maximum for all nanowires near 150K. Below this point,  $Q^{-1}$  decreases more quickly with temperature until roughly 50 K where it reaches what appears to be a low-dissipation plateau. The peak near 150 K and lower-temperature reduction of dissipation is typical of all nanowires measured in this study. Below 100 K, we find that nearly all measured nanowire  $Q$  factors are near or above  $10^5$ .

In a typical model of thermally activated defect motion [121] the time constant  $\tau_{def}$  obeys an Arrhenius equation  $\tau_{def} = \tau_o \times \exp[E_b/(k_B T)]$ , where  $\tau_o^{-1}$  is an attempt frequency and  $E_b$  the associated activation energy (or barrier height). A fit to our  $Q^{-1}$  data with a single such Debye peak (Figure 5.19 inset) consistently results in activation energies of order of 0.1 eV and attempt frequencies of order 1 GHz. Though the energy scale is reasonable for point defects or surface species of a solid, the attempt frequencies are substantially lower than the typical 1 THz expected for solids. [83] It is worth noting that measured wurtzite GaN phonon modes [122] and calculated m-plane Ga adatom kinetics [123] have both been reported in this energy region. Additionally, previous studies have indicated a maximum in electron mobility in the vicinity of 140 K [124,125].

The general temperature dependence of nanowire dissipation is rather similar for the entire ensemble. In the region of 50 K – 200 K, we observe that the loss  $Q^{-1}$  appears approximately proportional to  $T^{3.5}$ . This is a stronger power law dependence than that previously reported for dissipation in nanostructure resonators composed of silicon carbide (temperature exponent =

Figure 5.19: Temperature dependence of GaN nanowire dissipation  $Q^{-1}$  for the seven-nanowire ensemble shown in Figure 5.18, with the same color- and symbol-coding. For all nanowires studied, a dissipation peak is observed near 150 K, accompanied by a decrease in dissipation to a low- $Q^{-1}$  plateau below 50K. The single-nanowire shown (inset) is the same as the Figure 5.18 inset, and demonstrates similar behavior to the full ensemble. Solid red line is a fit to the data using the Debye equation and giving an activation energy  $E_b \approx 70$  meV and attempt frequency  $\tau^{-1} \approx 0.1$  GHz. The dashed line shows a  $Q^{-1} = T^{3.5}$  approximation to guide the eye in the strongly temperature dependent region. Error bars are the results of nonlinear fitting to individual nanowires resonance peaks. Figure adapted from [112].



0.3) [126], nanocrystalline diamond (0.2) [17], gold (0.5) [81], carbon nanotubes and graphene (0.36) [127], and silicon (0.36) [78]. The data chosen for inclusion in Figs 5.18 and 5.19 span the observed ranges of their respective plots and are representative of the full ensemble. It is worth noting, however, that the full collection of data obeys the same scaling. See, for example, Figure 5.20 for a messier, but more data-rich plot. Appendix I includes an additional pair of these figures illustrating the volume of data.

Figure 5.21 illustrates that there is a correlation between greater relative resonance frequency shifts near room temperature and greater dissipation observed near a 150 K loss peak. This same correlation persists at all the temperatures we investigate. We also observe variations in the dissipation for nanowires of roughly equal relative frequency shift.

Figure 5.20: An extended version of the  $Q^{-1}$  data shown in Figure 5.19. This plot includes many disconnected records, where nanowires may or may not be observed at a number of temperatures. However, the key observation is that even in the aggregate, it is clear that all the resonators follow the same trend as that shown in Figure 5.19.

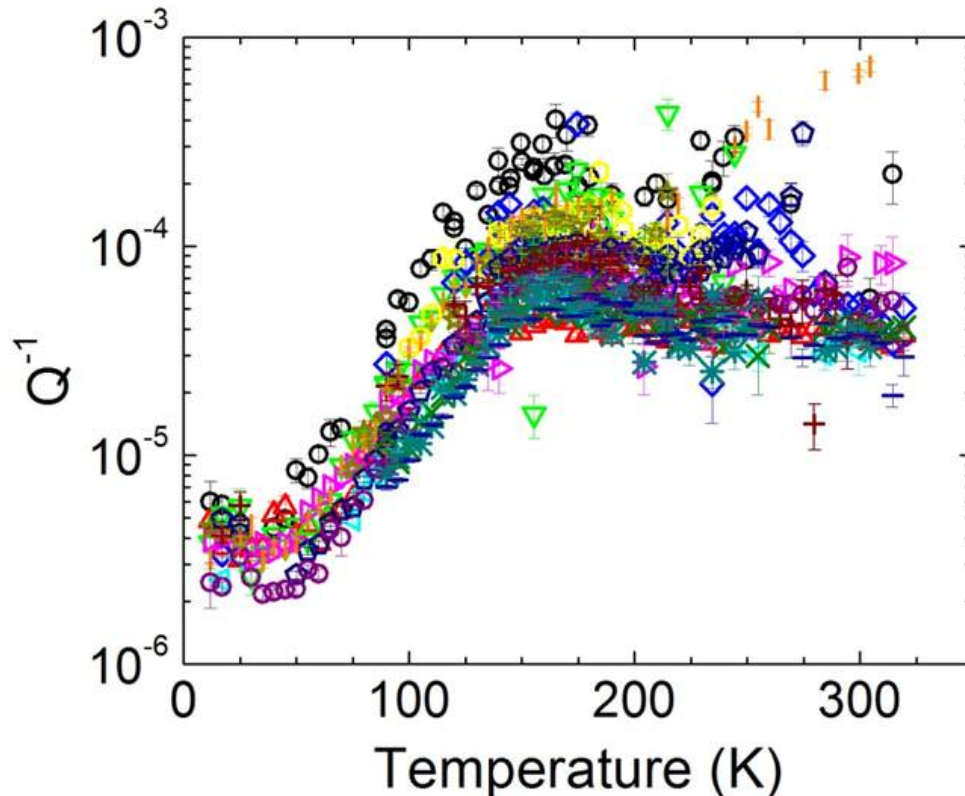
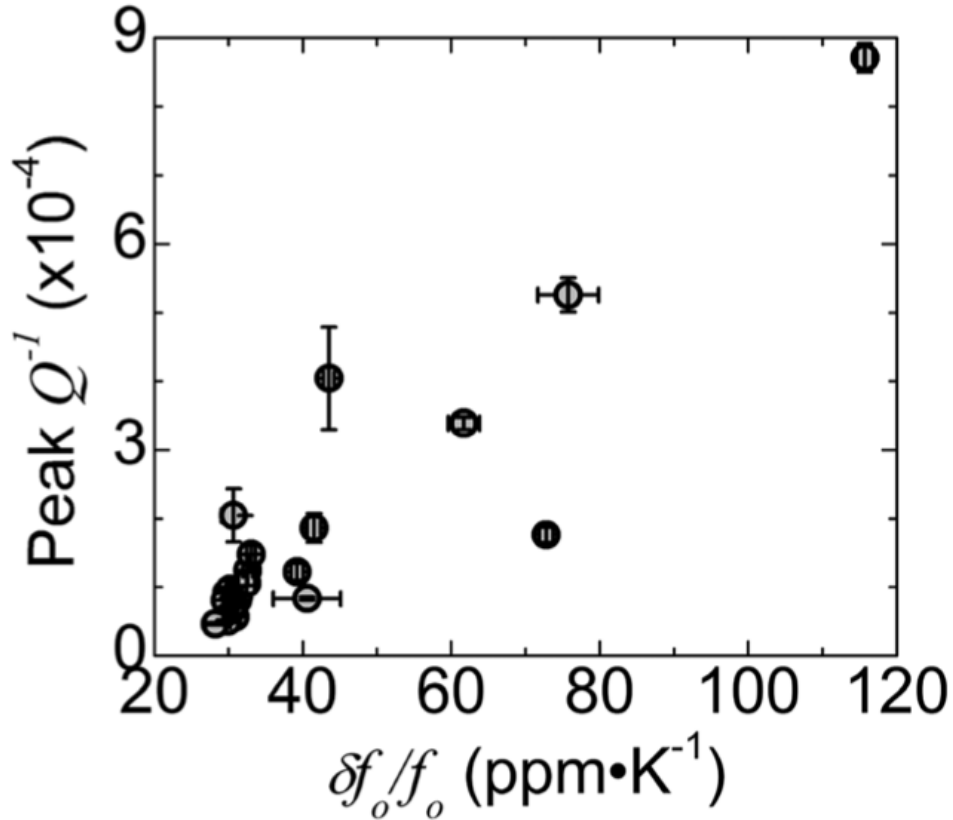


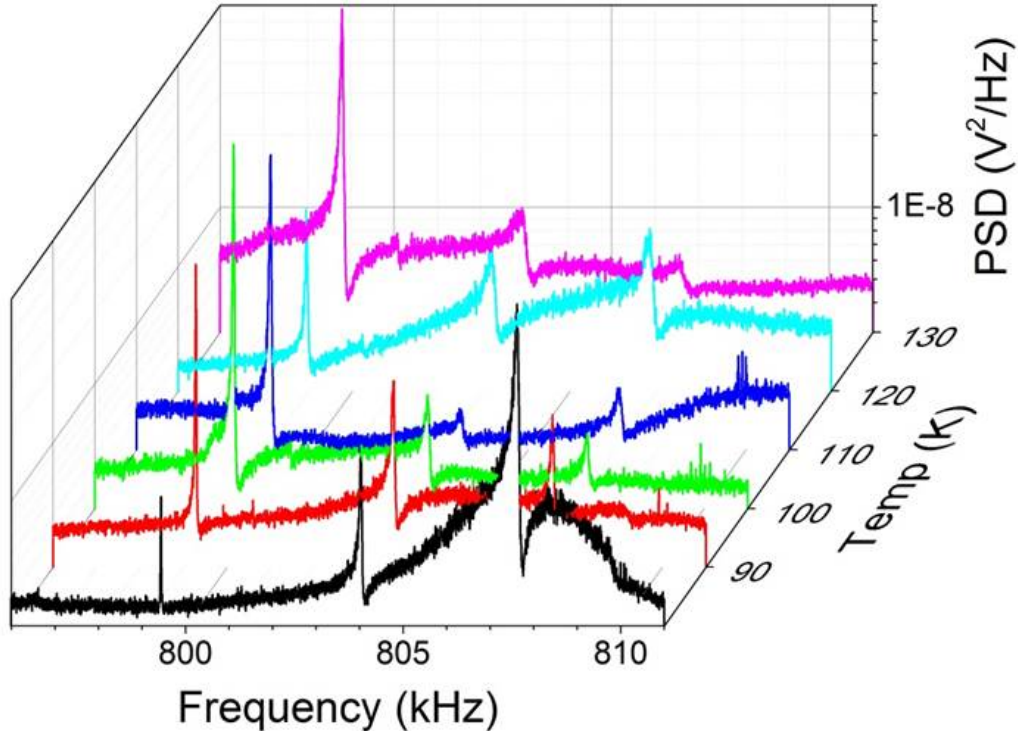
Figure 5.21: Variations in peak dissipation  $Q^{-1}$  in the region near 150 K appear to be correlated with relative resonance frequency shifts near room temperature. Shown are the twenty five GaN nanowire resonances with sufficient measurement data at both temperatures. Error bars are the results of nonlinear fitting to individual nanowire resonance peaks. Figure adapted from [112].



An additional interesting feature of our data is potentially part of the reason for the incomplete records described in Figure 5.20. Over many temperature-dependent measurements, we observe that nanowire resonance modes appear to ‘fade into-’ and ‘out of existence.’ That is, we see a resonance mode responding to a change in temperature as the rest of the ensemble, and then at some arbitrary measurement the resonance mode is no longer seen in the appropriate bandwidth. It may or may not also return to the PSD later, at different temperatures. After a number of observations, we begin to notice that the coherent background structure from the PZT is itself temperature dependent.

Figure 5.22 shows an example of the same approximately 15 kHz-wide region of five PSDs

Figure 5.22: A 15-kHz region of the ensemble PSDs from temperatures ranging from 90 K to 130 K illustrating a broad, low- $Q$  structure with apparent temperature dependence. This is possibly a sign of temperature dependence in the PZT actuator, though it is not as obvious as that of the nanowire resonance temperature dependence. When the broad, underlying structure overlaps with the nanowire peak, we see the nanowire peak apparently increase in amplitude in spite of the nominally identical actuation signal being applied to the PZT.



taken at temperatures from 90 K to 130 K. Three prominent nanowire resonance modes can be seen in the spectrum, and their central positions shift to slightly higher frequencies at lower temperatures (consistent with Figure 5.18). Interestingly, the amplitudes of these peaks vary as a function of temperature (for nearly identical levels of signal applied to the PZT actuator). Upon close inspection, however, we can see that there may be a broad (i.e. about 5 kHz), low- $Q$  structure that is also shifting through the PSD as a function of temperature. We believe that this temperature dependence of the PZT – though not as obvious as the temperature dependence of the nanowire resonances – may be behind the variations observed in nanowire resonance amplitudes.

### 5.2.5 Analysis Process

To this point, results have been presented without mention of precisely how they were attained. The process of turning a single broadband PSD, full of hundreds of nanowire resonances into a histogram (cf. Section 5.2.2) is nontrivial. The process of analyzing a single peak evolves over the many years they have been studied. But at the point which we decide to make simultaneous ensemble measurements, we need a new approach. As such, there is a significant amount of LabView software developed to assist in this process. Appendix H includes brief notes on the most useful of these programs.

Briefly, the analysis process begins to get sophisticated with windowed analyses of the full PSD bandwidth. Instead of knowing precisely where the resonance peaks are, we scan through the full PSD, block by block (e.g. 5 kHz windows at a time) with sufficient resolution to be able to manually, visually spot a nanowire resonance. Though this obviously relies strongly on the user, humans do have a very efficient pattern recognition system and this appears to work quite well.

As we continue to make progress on the efficiency of our detection system, the volume of simultaneously detected nanowires becomes very large. At a point (determined mostly by the attention span and time value of the user), it is simply no longer possible to keep up with the experiment. The time for (human) data analysis far exceeds the data acquisition time and becomes the bottleneck. It is at this point that we implement some rudimentary automation into the analysis system.

Even when analyzing the data by eye, there are always two sets of data: one PSD is taken without any actuation of the PZT and represents a sort of ‘background level’ to which we will compare a second PSD, taken while actuating the PZT. In this way, any persistent spikes or structures in the data (perhaps due to noise, electrical pulses, etc), can be discounted as non-nanowire structures – typically because they appear in both spectra. Beyond the phase rotation due to the coherent background signals (cf. Section 2.2.2), we observe that the nanowire resonances all share some bit of ‘family resemblance’. Furthermore, it is the distinct separations between the

background signal and the nanowire resonance that allows our eye to notice it in the first place. As a result, an automated peak-fitting routine is implemented that looks for just this: a region where the driven PSD continuously (e.g. some number of consecutive points, specified by the user) deviates from the background PSD. From this threshold point, a Levenberg–Marquardt least-squares fitting routine is implemented a distance ‘ahead’ in the data. This algorithm needs to know the functional form of the data, so we specify the function as well and point the fitting routine to it for reference.

This process, though crude and certainly not perfect, makes for incredible progress in our analysis. As an example, one particularly dense set of PSD data is analyzed by eye over an approximately 4 MHz bandwidth, identifying approximately 300 nanowire resonance modes in approximately two hours. With this as a benchmark, the automation tool described above is set on the same set of data and returns a 200-nanowire matching subset in approximately five minutes. A tradeoff of 33 % less data, but in 4 % of the time. This type of process can certainly be improved in the future, but it makes the majority of the later research conducted even remotely possible.

### 5.3 Conclusions

We have covered a lot of ground in this work. Some of the work is logical extension of earlier work, some is new ground in the field. In Chapter 3, the original SEM-based measurements were an extension of the techniques developed by Drs. Tanner and Gray, but the number of resonators measured was certainly higher than ever before. A systematic analysis of the effects of ALD on ensembles of nanowire resonators was a new aspect of the work, and appears to have provided a decent starting point for other research into ALD-nanowire composite structures [128–130].

By transitioning our studies to the ensemble capacitive measurements described in Chapters 4 and 5, we demonstrated that an unprecedented number of nanowires could be analyzed under a given set of parameters e.g. temperature. By the end of this work, we were measuring hundreds of unique resonances at a time; the volume of ensemble analysis was only limited by the time constraints of the user and the intelligence of the early-stage automation. While the former does not have a lot of flexibility, the latter certainly does. There is much room for improvement there.

In our studies of temperature dependence, we saw some unique and suggestive results. There appears to be a correlation between the observed temperature-dependent frequency shift (in the linear region), and the magnitude of the dissipation at its largest point. As discussed in e.g. Ref [121], such a correlation is an expected result of thermoelastic damping. On the other hand, as shown in Section 2.3, if thermoelastic damping was the dominant source of dissipation, we would expect much higher  $Q$  values. As mentioned in the same section, however, the dissipation attributed to support loss is predominantly temperature independent. In Figures 5.19 and 5.20, we see a clear low-temperature saturation in the dissipation. It is possible, therefore, that we are observing a limit imposed by such a temperature-independent mechanism. In Section 2.3, we estimated that for a typical GaN nanowire, this  $Q$  factor would be near  $3 \times 10^5$  which matches our observations quite well. If this is the case, then additional insight into the other loss mechanisms could also be gained by subtracting out the corresponding amount of temperature-independent dissipation. Additionally, it suggests that we may observe  $Q$  much higher if we remove the attachment point altogether (cf. Chapter 6).

The distributions of resonance parameters presented in e.g. Figure 5.12 reflect the observed variations in nanowire geometry, while those in e.g. Figure 5.14 suggest that there is unique nanowire-to-nanowire variation in structure or local environment (or possibly both) that is still to be understood. This is an exciting future direction for this work. At the lowest temperatures measured here, we observed GaN nanowire  $Q$  factors consistently above  $10^5$  (cf. Figure 5.19). Possibly more interesting, however, is that even at temperatures above 100 K, a number of the measured nanowires already show  $Q > 10^5$ . Related to the last point, this suggests that there is more work to be done in understanding the subtle differences between the individual nanowires. Perhaps growth parameters or post-growth processing can enable a greater fraction of nanowires on similar samples to have  $Q \geq 10^5$  right out of the gate.

Also in the vein of potentially increasing nanowire  $Q$  factors, it would seem worth exploring a concerted effort to remove trace oxides. We suspect that GaN is a unique resonator material due to its lack of native surface oxides. However, other high- $Q$  nanostructures have seen vast improvements

in  $Q$  after carefully preparing their surfaces [131]. Perhaps some incremental improvement in GaN nanowire  $Q$  could come of this type of treatment.

Finally, it is worth noting that behind the scenes of all of this work are the nanowire growth systems that our NIST collaborators developed and maintain. These systems have the capability to produce a large number of substrates with this incredible number of GaN nanowires. As such, our lab is in a niche position where we can continue to make significant progress in understanding the GaN nanowire system. I hope that the work presented here proves to be a useful addition to the collection of publications and dissertations that have grown out of this healthy collaboration.

## Chapter 6

### Future Work & Applications

There are many promising and potentially very interesting directions for work that follows up on some of the things discussed here. I began a number of experiments that ultimately got left behind in favor of others, and there are many things about which we have thought ‘Oh, X would be a neat thing to explore,’ along the way. Additionally, there are many conceivable extensions to work already done may be interesting and useful. This Chapter includes some of the thoughts and experiments that come to mind in this regard.

#### 6.1 Extensions Of This Work

- **Ringdown/Free Decay**

Many of the experiments on resonators (nano-, micro-, or even larger) found in the literature incorporate a measurement of  $Q$  known as ‘ring-down’ (see basically any of the References from the last five years). This is where the resonator is given an impulse and the resonance amplitude is observed to decay on the natural timescale of the structure  $\tau \approx 1/\Gamma$ . This technique provides an alternative method of calculating the  $Q$  factor by fitting the sinusoidal response with an exponentially decaying envelope. This would also allow for verification of the calculated  $Q = \omega_o/\Gamma$ .

Our experiment is somewhat unique relative to the many other nanoscale resonator experiments in the literature in that we use a PZT actuator. Other common forms of actuation are: electrostatic gating [18], magnetomotive forcing [42], and resistive/Joule heating [132].

These actuation techniques are often used because nanoscale resonators are fabricated, on-chip, via lithography; they are typically a mechanical component that also serves a role in the electrical circuitry of the system. Due to the elastic properties of the PZT we typically use, transducing an impulse to nanowires is somewhat difficult. Instead, we apply a pulse and the PZT responds with its own unique transfer function. The prescription, then, is to quantify the typical long-period, low- $Q$  response function of the PZT and include it in a composite fit with the high- $Q$  nanowire response. Some initial attempts of this were made, and there is some LabView code that begins this analysis (see Appendix H).

In a similar regard, another approach to accomplishing the ringdown measurement would be to replace the PZT actuation method with an electrostatic one. The advantages would include immediate response, larger range of control (in both amplitude and bandwidth), and simply having one less piece of equipment to troubleshoot. Since the system described in Chapter 5 already has an electrode adjacent to the nanowire resonators, the only requirement will be a re-engineering of the electrical configuration. By incorporating a bias tee, it should be possible to apply dc- to low-frequency signals (relative to the microwave frequencies) to either the CSE or the resonators for actuation.

- **ALD Nanowire Functionalization**

The studies of GaN nanowire-ALD composite resonator structures of Section 3.6 seem a really obvious direction to continue investigations. As the industrial uses of ALD continue to grow, it would seem that more organizations will be looking to fund any research in the direction of ALD functionalization. Due to the strong surface effects that GaN nanowires appear to show, it would seem a natural testbed for investigations into ALD properties.

An elusive result during the course of this work was to combine the lithographic notion of a sacrificial layer with an ALD deposition on the nanowires. That is, we consider a process by which we immerse (‘protect’) the lower portion of a nanowire substrate in some sacrificial material – we attempted to use photoresist – atop which we can do an evaporation or ALD

deposition. This would coat an arbitrary length at ends of the nanowires with the deposited material. The sacrificial layer could then be etched away leaving a cap of material on the end of the nanowire. The most obvious application of this technique is functionalization for e.g. medical sensing. Capturing or counting unique biological quanta e.g. proteins is only possible with a unique, inert chemistry.

A number of attempts were made in this regard with the GaN nanowires. Due to the small sample size typically used, a typical spin-on photoresist would often fail to create uniform layers (edge beads are a significant concern on a sub-cm<sup>2</sup>, square chip). As an example, Figure 6.1 shows inconsistent results from spinning photoresist onto a nanowire sample. In addition to uneven surfaces (which, for proof-of-concept, is probably not a big deal), we also observe some bizarre results involving the developing of such an unusual sample.

In his dissertation on creating nanowire diode structures, Dr. Cheng described an encapsulation process for the GaN nanowires using a spin-on (chemical) PCB material, and assorted combinations of mechanical polishing and plasma etching to expose nanowire tips [133]. The most notable difference is that his process did not intend for the encapsulation material to be removed. However, his thesis includes some recipes that could potentially be adapted for the purpose described here.

- **ALD-based Capacitive Sensors**

One particularly interesting experiment that we began was that of creating in-situ capacitive detectors. This type of arrangement could potentially allow for nanometer-scale separation between the resonator and electrode and subsequently large sensitivity to the displacements of the resonator. Figure 6.2 shows one of our attempts to create metallic electrodes on individual nanowire. The process used here is to start with a clean GaN nanowire sample, then deposit thin ALD alumina layer (some number of nanometers – a relatively short deposition time), e.g. as in Section 3.6.1. Since we are familiar with this material and know that it is easily etched, this serves as a sacrificial layer in this process. With uniform

Figure 6.1: SEM images after attempts at using photoresist as a sacrificial layer to mask the bottom portions of the GaN nanowires. a) Partially-exposed nanowire tips (bright) can be seen emerging from the rough photoresist applied to the substrate (dark). The extent of the exposed nanowire varies widely across this image. As indicated, the scale bar is 1  $\mu\text{m}$ . b) A surface layer of photoresist (approximately 1  $\mu\text{m}$  thick) appears to rest on top of the as-grown nanowires. This resulted from a drip-on technique, where the resist apparently was unable to extend down along the length of the nanowires. The surface layer has been torn by running tweezers along the sample. As indicated, the scale bar is 10  $\mu\text{m}$ .

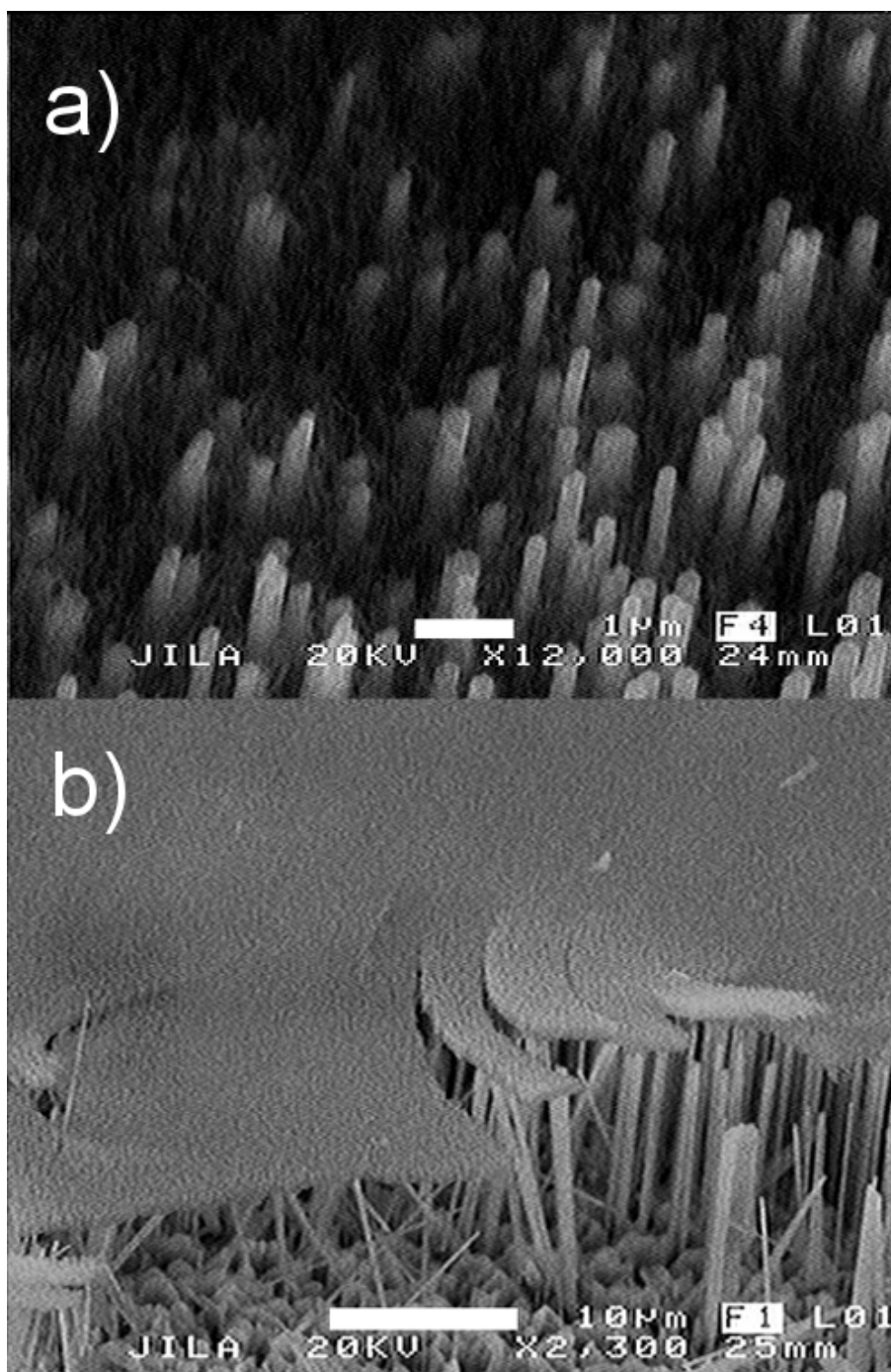
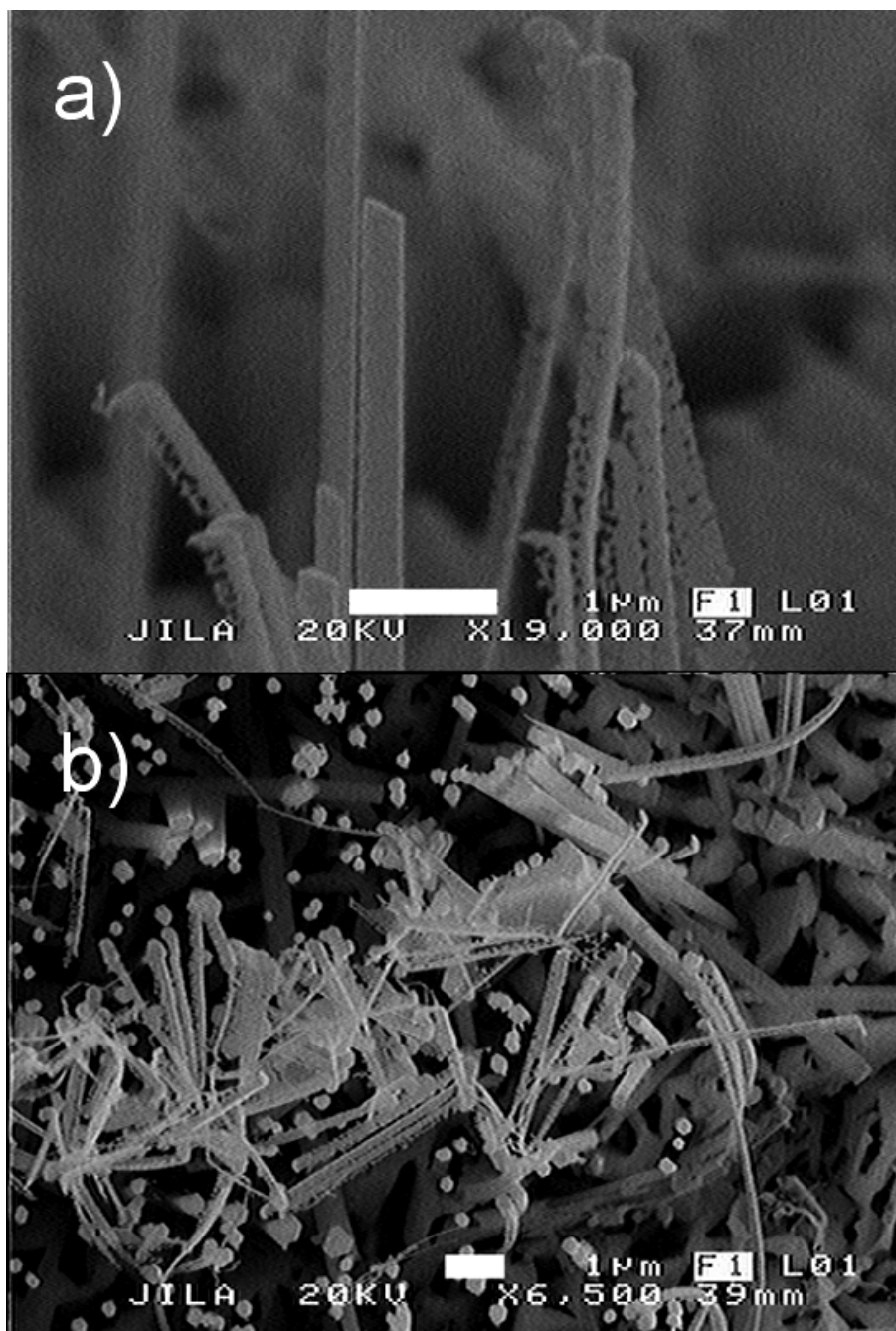


Figure 6.2: SEM images following an attempt to create in situ capacitive electrodes of Ag at each nanowire site. a) The metal film (with rough edges) is seen peeling away from the GaN nanowires. Presumably, the internal strain in the metal film led to this behavior. b) In some regions, the metal film also peeled up and was bundled together – perhaps by Van der Waals forces – on the surface of the nanowires.



surface coverage of the alumina, we can consider the fabrication of metallic electrodes. In this case, we do not want a uniform material coverage – in order to sense a change in the distance (capacitance) between the nanowire and electrode, we need it to be directional. The more conventional evaporative deposition is a line-of-sight method, and is the technique used below.

Following a metal (gold, Ag, for its resistance to the alumina etchant) deposition, the sacrificial alumina layer is etched away (in this case, via an aqueous HF and CO<sub>2</sub> critical point dry), and the electrodes are released. Due to the high aspect ratio of the nanowires, we expect that the sacrificial material between the electrode and nanowire will be removed, whereas at the base (on the substrate), the alumina will remain and maintain electrical isolation. As seen in Figure 6.2, it seems our thin evaporated films have excessive internal strain, leading to the apparent peeling of the shell away from the nanowire. It does appear that the sacrificial layer was successfully removed, though it was not clear whether the insulating layer remained on the substrate.

- **Additional Temperature Data**

Measuring ensemble temperature dependence for the GaN nanowire resonator system allowed us to observe aggregate behavior and, in a sense, each nanowire result served to corroborate the others. Though we made many measurements on the same sample, the next logical step is to reproduce this experiment on new and different samples. Potentially, the experiment could initially be repeated on a similar nanowire growth, and then on addition growths with different material properties e.g. doping levels. Furthermore, in his dissertation, Dr. Gray demonstrated interesting temperature dependence on doubly-clamped GaN nanowires depending on the direction in which the experiment was carried out (going up or down in  $T$ ) [95]. This would be an interesting observation to compare with the as-grown system.

- **Multiplexed Lock-in Detection**

The two primary means of data collection described here were the phase-sensitive lock-in technique (which measured nanowires one at a time), and the PSD technique (which simultaneously measured an ensemble of nanowires). The former lock-in technique allows much higher resolution in the acquired data, and as the resonators possess increasingly high  $Q$  factors, this becomes important. In this work, we remained just below the PSD resolution limit for the highest- $Q$  objects. One way around this would be to multiplex the lock-in stimulus and synthesize a composite waveform comprising a full ensemble of nanowire frequencies, and use this as the actuation. The resulting response could be read out and convolved with stimulus to back out the individual responses.

- **Identifying Nanowire Mode Pairs**

In the SEM measurement technique in Section 3.3, obtaining information about the two fundamental modes of a single nanowire is trivial. We see them both in the PSD and can drive and observe them both for confirmation. Using the capacitive technique – particularly when the sample is in the bottom of a cryostat, we get no such verification that any two resonance modes are tied to the same resonator.

An extension of the existing technology that could potentially resolve this issue is to combine two forms of actuation signal: both the broadband noise signal typically used for PSD measurements, and an additional tone at a known frequency. We see in the lock-in data that we can drive the resonators to nonlinear response regime e.g. Figure 3.7. If we identify a particular resonance frequency (by, say, an initial PSD), we could subsequently drive the sample with both broadband noise and that identified tone. If we increase the amplitude of the tone frequency, we expect the resonator response will also increase. It is conceivable that by driving the nanowire strongly in one of its fundamental modes, the other will be affected and we may see a change in its corresponding peak in a PSD.

- **Isolation / Noise Reduction**

As described in Section 5.2, our apparatus appears to be right near the edge of being capable

of routinely observing thermally driven resonator motion. This would be a nice compliment to future result reporting. The setup for these measurements was nearly the epitome of rough-and-ready; much can be done to improve the results. Additional vibrational isolation between the cryostat and the building would be a good start. Modifying the adjustment rod for the coupling capacitor for greater separation, as well. Doing a better job of shielding the sensitive electrical components, and working up to lower-noise amplifiers would all certainly increase the signal to noise ratio, as well.

- **Higher Mode Observations**

With the increased sensitivity that a future user is going to have (as a result of the previous bullet item), it would be logical to work toward observation of the higher resonance modes. As shown in Figure 2.3, the higher modes will likely result in smaller deflections. These modes will also lead to different internal strain fields, and additional data from which to analyze loss mechanisms. These higher modes will also provide further insight into the physical properties of the GaN nanowires themselves.

- **Nanowire Arrays**

The techniques and approaches described in this work can immediately be applied to a unique growth pattern that we have talked about with the NIST folks. Namely, a regularly patterned array of resonators. In fact, initial designs were sent off some time in 2011 for a sample of the GaN nanowires with regularly-spaced growth apertures. With luck, that sample will return someday and someone can study it as described here. The key benefit to the patterned array idea is that with a very finite collection of resonators, an incredibly detailed mapping can be made between the resonance behavior of a particular nanowire and its physical appearance. That is, each resonance (and resonance mode) can be identified as originating from a unique nanowire.

## 6.2 New Directions And Experiments

- **MUMPs**

The Multi-User MEMS Processes (MUMPs) is a commercial program to which you can submit design patterns for manufacturing. By designing patterns in a similar method to that of exposure mask design, you can submit – and have created for you – very complex MEMS structures. The process includes a fixed sequence of processes (depositions and removals), and the user can create incredibly complicated designs. The products are returned some number of months later, with approximately a dozen copies of your design.

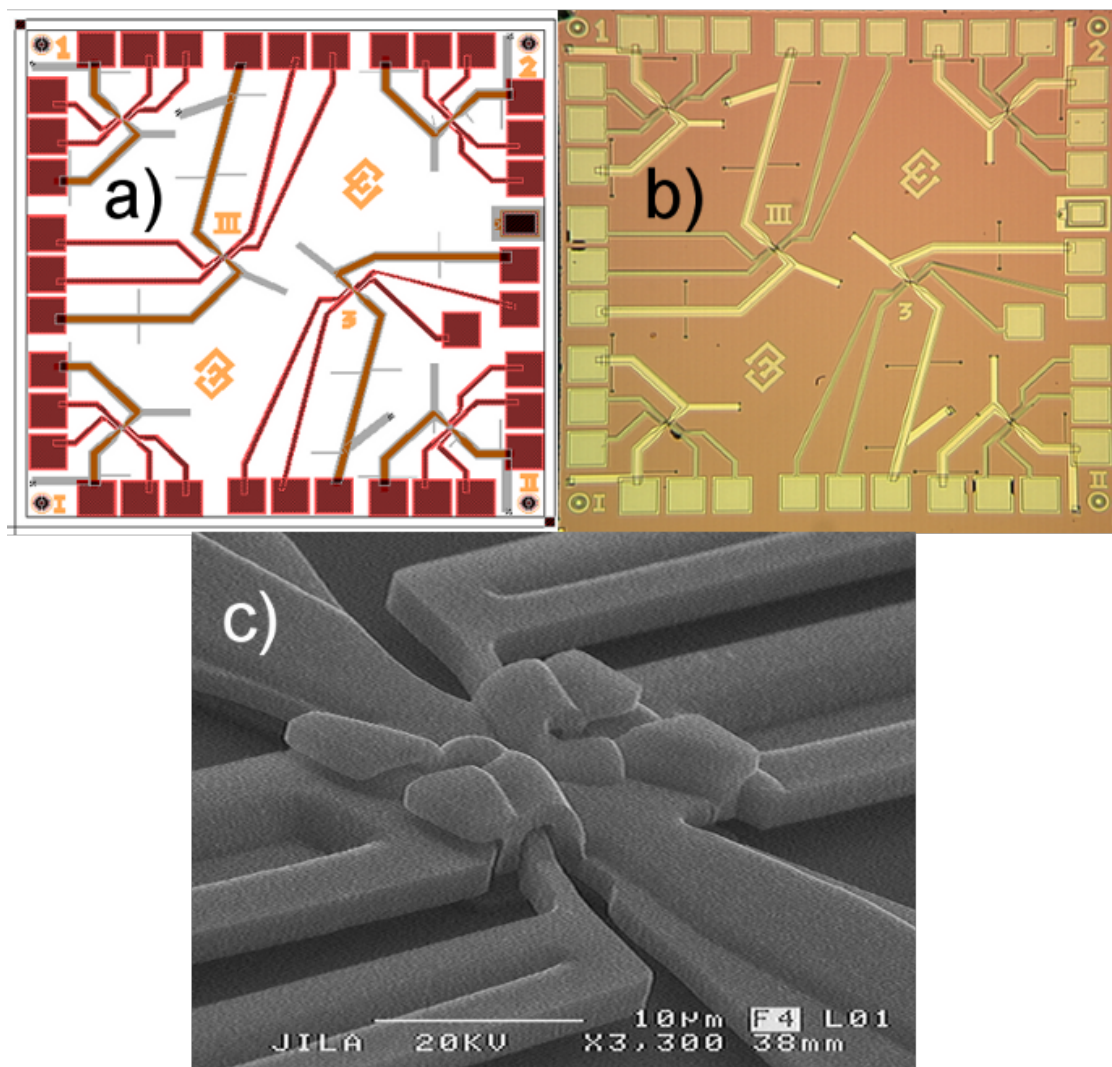
I submitted a design into which I planned to incorporate GaN nanowires in a fixed-fixed geometry (similar to Dr. Gray’s work [95]). The main difference would have been a significantly smaller footprint for the electrical and mechanical components in the experiment. The design would have only needed wire-bonded connections to address the electrical circuits on the few-mm<sup>2</sup> chip. Figure 6.3 shows some images of the design.

My first attempt at this process, however, included a design flaw that prevented good electrical contact from being made with the sample. The priority on this particular project was low, and a second attempt was never made. However, I believe this would be a very useful step for progressing this type of resonator system toward a useful, commercial application. The footprint of a typical MUMPs chip is essentially designed to be used with commercially-available chip packaging.

- **Attachment-Free Resonators**

Given the nearly defect-free structure of the GaN nanowires, we have long believed that the attachment point was one of the sources of the observed dissipation. The calculations in Section 2.3.2 also support the idea that reducing clamping losses would improve the measured  $Q$  factors. There is existing literature that shows an improvement in the measured  $Q$  factors for beams whose supports have been placed at the nodes of the resonant motion.

Figure 6.3: An example design created using the MUMPs fabrication process. a) Design layout, completed in LEdit, with layers appropriate for the MUMPs process. The large red squares along the outer edge are contact pads for wirebonded connections. The conductive lines from each of these pads run to one of the six experiments on the chip (difficult to see at this scale, but labeled 1, 2, 3, I, II, III). These were all variations on the electrode geometry. b) The resulting chip, returned from the fabrication process. The silicon substrate is seen in pink, while the deposited polysilicon layers appear gold in color. The full chip length in both a) and b) is about three millimeters. c) An SEM image showing a close-up of the center of one of the six experiments. The paths all lead to a central region where a nanowire was intended to be placed in a fixed-fixed geometry and electrostatically actuated. The portion of the design that appears to ‘flow’ over the others was a design flaw that left these chips unusable. As indicated, the scale bar is 10 $\mu$ m.



[70, 80, 134]

These beams are effectively free-free resonant structures. An experiment that we have long talked about (and is potentially in the early stages as of this writing), is to remove nanowires from the substrate and hold them in some version of an optical or magnetic trap. In such a system, it should be relatively easy to detect the motion of the nanowires via laser interferometry. In addition to being a new result and answering questions about the attachment losses, this would simply be a very neat experiment.

- **Nanoscale Quantum-Classical Transition**

One of the interesting aspects of the GaN nanowire systems described in this work is that their dimensionality is just above the atomic scale. In a sense, this makes it possible to apply straightforward classical mechanics to the analysis of the system. However, the nanowires could certainly be studied in smaller geometries (via shorter growths), at which point the smallest dimensions of these resonators could be on the order of angstroms. It would seem that this type of geometry could provide an interesting testbed for studies of the transition from the quantum oscillator to the classical simple harmonic oscillator.

- **Materials Science**

Similar to the unique scaling described above, by focusing in on such small size scales, it would seem that the nanowire structure could provide a good source of understanding for the basic materials science of GaN. While bulk GaN is in wide use for high-temperature and high-radiation electronic purpose, the nanowire structure may be found to diverge in some ways. There is already some theory work from groups doing simulations on this type of question [50]. It would be useful to meet them part-way with experimental results.

- **Portable Devices**

Finally, it would great to see this type of research be put to use in a practical setting. The research on composite ALD-GaN nanowire structures described in Section 3.6 is an

obvious first step toward developing a nanoscale deposition monitor. The quartz crystal microbalance (QCM) is an industry standard, but obviously the GaN nanowire system is orders of magnitude smaller. If similar precision could be attained in a package that scaled like the fundamental resonator, the full field of electronics using quartz resonators could take advantage of this size reduction. Though the graduate students in the George group (Chemistry) that I initially worked with are no longer around, I feel confident that this sort of collaboration would be easy to start again.

Similarly, for all of the parametric observations reported in this work (pressure, temperature, material deposition), it is at least conceivable to turn the measurement around and create a ‘sensor’ for that variable. This is a project that seems particularly appropriate for the kinds of defense funding that initially kicked off our research into GaN nanowires. Furthermore, it would be fantastic to see some of the results of this work put to use in the real world.

## Bibliography

- [1] A. Olkhovets, S. Evoy, D. Carr, and J. Parpia, "Actuation and internal friction of torsional nanomechanical silicon resonators," Journal of Vacuum Science & Technology B: Microelectronics and Nanometer Structures, no. June, pp. 3549–3551, 2000.
- [2] U. Gysin, S. Rast, P. Ruff, E. Meyer, D. Lee, P. Vettiger, and C. Gerber, "Temperature dependence of the force sensitivity of silicon cantilevers," Physical Review B, vol. 69, p. 045403, Jan. 2004.
- [3] M. Tudor, M. Andres, K. Foulds, and J. Naden, "Silicon resonator sensors: interrogation techniques and characteristics," IEE Proceedings - Nanobiotechnology, vol. 135, no. 5, p. 364, 1988.
- [4] J. Zook, D. Burns, H. Guckel, J. Sniegowski, R. Engelstad, and Z. Feng, "Characteristics of polysilicon resonant microbeams," Sensors and Actuators A: Physical, vol. 35, pp. 51–59, Oct. 1992.
- [5] B. L. Foulgoc, T. Bourouina, O. L. Traon, A. Bosseboeuf, F. Marty, C. Breluzeau, J.-P. Grandchamp, and S. Masson, "Highly decoupled single-crystal silicon resonators: an approach for the intrinsic quality factor," Journal of Micromechanics and Microengineering, vol. 16, pp. S45–S53, June 2006.
- [6] X. L. Feng, R. He, P. Yang, and M. L. Roukes, "Very High Frequency Silicon Nanowire Electromechanical Resonators," Nano Letters, vol. 7, pp. 1953–1959, July 2007.
- [7] M. Belov, N. J. Quitoriano, S. Sharma, W. K. Hiebert, T. I. Kamins, and S. Evoy, "Mechanical resonance of clamped silicon nanowires measured by optical interferometry," Journal of Applied Physics, vol. 103, no. 7, p. 074304, 2008.
- [8] S.-J. Kim, T. Ono, and M. Esashi, "Study on the noise of silicon capacitive resonant mass sensors in ambient atmosphere," Journal of Applied Physics, vol. 102, no. 10, p. 104304, 2007.
- [9] T. Ono and M. Esashi, "Energy dissipation in submicrometer thick single-crystal silicon cantilevers," Journal of Microelectromechanical Systems, vol. 11, pp. 775–783, Dec. 2002.
- [10] X. Feng, M. Matheny, R. Karabalin, C. Zorman, M. Mehregany, and M. Roukes, "Silicon carbide (SiC) top-down nanowire electromechanical resonators," in Solid-State Sensors, Actuators and Microsystems Conference, 2009. TRANSDUCERS 2009., pp. 2246–2249, IEEE, 2009.

- [11] S. Schmid and B. Malm, “Quality factor improvement of silicon nitride micro string resonators,” Micro Electro Mechanical Systems (, pp. 481–484, 2011.
- [12] L. Sekaric, D. Carr, S. Evoy, J. Parpia, and H. Craighead, “Nanomechanical resonant structures in silicon nitride: fabrication, operation and dissipation issues,” Sensors and Actuators A: Physical, vol. 101, pp. 215–219, Sept. 2002.
- [13] A. N. Cleland, M. Pophristic, and I. Ferguson, “Single-crystal aluminum nitride nanomechanical resonators,” Applied Physics Letters, vol. 79, no. 13, p. 2070, 2001.
- [14] M. K. Zalalutdinov, M. P. Ray, D. M. Photiadis, J. T. Robinson, J. W. Baldwin, J. E. Butler, T. I. Feygelson, B. B. Pate, and B. H. Houston, “Ultrathin single crystal diamond nanomechanical dome resonators.,” Nano Letters, vol. 11, pp. 4304–8, Oct. 2011.
- [15] M. Imboden, P. Mohanty, A. Gaidarzhy, J. Rankin, and B. W. Sheldon, “Scaling of dissipation in megahertz-range micromechanical diamond oscillators,” Applied Physics Letters, vol. 90, no. 17, p. 173502, 2007.
- [16] L. Sekaric, J. M. Parpia, H. G. Craighead, T. Feygelson, B. H. Houston, and J. E. Butler, “Nanomechanical resonant structures in nanocrystalline diamond,” Applied Physics Letters, vol. 81, no. 23, p. 4455, 2002.
- [17] A. B. Hutchinson, P. A. Truitt, K. C. Schwab, L. Sekaric, J. M. Parpia, H. G. Craighead, and J. E. Butler, “Dissipation in nanocrystalline-diamond nanomechanical resonators,” Applied Physics Letters, vol. 84, no. 6, p. 972, 2004.
- [18] J. M. Gray, C. T. Rogers, K. A. Bertness, and N. A. Sanford, “Gallium nitride nanowire electromechanical resonators with piezoresistive readout,” Journal of Vacuum Science & Technology B: Microelectronics and Nanometer Structures, vol. 29, no. 5, p. 052001, 2011.
- [19] J. Montague, M. Dalberth, J. Gray, D. Seghete, K. Bertness, S. George, V. Bright, C. Rogers, and N. Sanford, “Analysis of high-Q, gallium nitride nanowire resonators in response to deposited thin films,” Sensors and Actuators A: Physical, vol. 165, pp. 59–65, Jan. 2011.
- [20] H.-M. Kim, Y.-H. Cho, H. Lee, S. I. Kim, S. R. Ryu, D. Y. Kim, T. W. Kang, and K. S. Chung, “High-Brightness Light Emitting Diodes Using Dislocation-Free Indium Gallium Nitride/Gallium Nitride Multiquantum-Well Nanorod Arrays,” Nano Letters, vol. 4, pp. 1059–1062, June 2004.
- [21] C.-Y. Nam, D. Tham, P. Jaroenapibal, J. Kim, D. E. Luzzi, S. Evoy, and J. E. Fischer, “Gallium nitride nanowires: polar surface controlled growth, ohmic contact patterning by focused ion-beam-induced direct Pt deposition and disorder effects, variable range hopping, and resonant electromechanical properties,” Proceedings of SPIE, vol. 6370, pp. 63701F–63701F–12, 2006.
- [22] T. Henry, K. Kim, Z. Ren, C. Yerino, J. Han, and H. X. Tang, “Directed growth of horizontally aligned gallium nitride nanowires for nanoelectromechanical resonator arrays.,” Nano Letters, vol. 7, pp. 3315–9, Nov. 2007.
- [23] A. Motayed, A. V. Davydov, S. N. Mohammad, and J. Melngailis, “Experimental investigation of electron transport properties of gallium nitride nanowires,” Journal of Applied Physics, vol. 104, no. 2, p. 024302, 2008.

- [24] J.-W. Yu, C.-K. Li, C.-Y. Chen, Y.-R. Wu, L.-J. Chou, and L.-H. Peng, "Transport properties of gallium nitride nanowire metal-oxide-semiconductor transistor," Applied Physics Letters, vol. 99, no. 15, p. 152108, 2011.
- [25] J. T. M. van Beek and R. Puers, "A review of MEMS oscillators for frequency reference and timing applications," Journal of Micromechanics and Microengineering, vol. 22, p. 013001, Jan. 2012.
- [26] M. Poot and H. S. van der Zant, "Mechanical systems in the quantum regime," Physics Reports, vol. 511, pp. 273–335, Feb. 2012.
- [27] K. Williams, K. Gupta, and M. Wasilik, "Etch rates for micromachining processing-part II," Journal of Microelectromechanical Systems, vol. 12, pp. 761–778, Dec. 2003.
- [28] C. J. Summers and Z. L. Wang, "Large-Scale Hexagonal-Patterned Growth of Aligned ZnO Nanorods for Nano-optoelectronics and Nanosensor Arrays," Nano Letters, vol. 4, pp. 423–426, Mar. 2004.
- [29] J. Bao, M. a. Zimmler, F. Capasso, X. Wang, and Z. F. Ren, "Broadband ZnO single-nanowire light-emitting diode.," Nano Letters, vol. 6, pp. 1719–22, Aug. 2006.
- [30] S. Hersee, M. Fairchild, A. Rishinaramangalam, M. Ferdous, L. Zhang, P. Varangis, B. Swartzentruber, and A. Talin, "GaN nanowire light emitting diodes based on templated and scalable nanowire growth process," Electronics Letters, vol. 45, no. 1, p. 75, 2009.
- [31] M.-C. Jeong, B.-Y. Oh, M.-H. Ham, and J.-M. Myoung, "Electroluminescence from ZnO nanowires in n-ZnO film/ZnO nanowire array/p-GaN film heterojunction light-emitting diodes," Applied Physics Letters, vol. 88, no. 20, p. 202105, 2006.
- [32] M. H. Huang, S. Mao, H. Feick, H. Yan, Y. Wu, H. Kind, E. Weber, R. Russo, and P. Yang, "Room-temperature ultraviolet nanowire nanolasers.," Science, vol. 292, pp. 1897–9, June 2001.
- [33] A. V. Maslov and C. Z. Ning, "Reflection of guided modes in a semiconductor nanowire laser," Applied Physics Letters, vol. 83, no. 6, p. 1237, 2003.
- [34] S. Gradecak, F. Qian, Y. Li, H.-G. Park, and C. M. Lieber, "GaN nanowire lasers with low lasing thresholds," Applied Physics Letters, vol. 87, no. 17, p. 173111, 2005.
- [35] C.-C. Nguyen, L. Katehi, and G. Rebeiz, "Micromachined devices for wireless communications," Proceedings of the IEEE, vol. 86, no. 8, pp. 1756–1768, 1998.
- [36] M. S. Arnold, P. Avouris, Z. W. Pan, and Z. L. Wang, "Field-Effect Transistors Based on Single Semiconducting Oxide Nanobelts," The Journal of Physical Chemistry B, vol. 107, pp. 659–663, Jan. 2003.
- [37] A. B. Greytak, L. J. Lauhon, M. S. Gudixsen, and C. M. Lieber, "Growth and transport properties of complementary germanium nanowire field-effect transistors," Applied Physics Letters, vol. 84, no. 21, p. 4176, 2004.
- [38] C. T. Black, "Self-aligned self assembly of multi-nanowire silicon field effect transistors," Applied Physics Letters, vol. 87, no. 16, p. 163116, 2005.

- [39] P.-C. Chang, Z. Fan, C.-J. Chien, D. Stichtenoth, C. Ronning, and J. G. Lu, "High-performance ZnO nanowire field effect transistors," Applied Physics Letters, vol. 89, no. 13, p. 133113, 2006.
- [40] R. He, X. L. Feng, M. L. Roukes, and P. Yang, "Self-transducing silicon nanowire electromechanical systems at room temperature.," Nano letters, vol. 8, pp. 1756–61, June 2008.
- [41] A. Boisen, S. Dohn, S. S. Keller, S. Schmid, and M. Tenje, "Cantilever-like micromechanical sensors," Reports on Progress in Physics, vol. 74, p. 036101, Mar. 2011.
- [42] K. L. Ekinci and M. L. Roukes, "Nanoelectromechanical systems," Review of Scientific Instruments, vol. 76, no. 6, p. 061101, 2005.
- [43] Y. Huang, X. Bai, and Y. Zhang, "In situ mechanical properties of individual ZnO nanowires and the mass measurement of nanoparticles," Journal of Physics: Condensed Matter, vol. 18, pp. L179–L184, Apr. 2006.
- [44] S. Perisanu, P. Vincent, M. Choueib, A. Ayari, S. T. Purcell, M. Bechelany, and D. Cornu, "High Q factor for mechanical resonances of batch-fabricated SiC nanowires," Applied Physics Letters, vol. 90, no. 4, p. 043113, 2007.
- [45] C.-Y. Nam, P. Jaroenapibal, D. Tham, D. E. Luzzi, S. Evoy, and J. E. Fischer, "Diameter-dependent electromechanical properties of GaN nanowires.," Nano Letters, vol. 6, pp. 153–8, Feb. 2006.
- [46] E. Givargizov, "Fundamental aspects of VLS growth," Journal of Crystal Growth, vol. 31, pp. 20–30, 1975.
- [47] S. M. Tanner, J. M. Gray, C. T. Rogers, K. A. Bertness, and N. A. Sanford, "High-Q GaN nanowire resonators and oscillators," Applied Physics Letters, vol. 91, no. 20, p. 203117, 2007.
- [48] M. Brubaker, "Growth And Characterization Of Gallium Nitride Nanowire LEDs For Application As On-Chip Optical Interconnects". PhD thesis, University of Colorado, 2012.
- [49] E. F. Schubert, T. Gessmann, and J. Kyu Kim, Light Emitting Diodes. John Wiley & Sons, Inc., 1997.
- [50] R. A. Bernal, R. Agrawal, B. Peng, K. A. Bertness, N. A. Sanford, A. V. Davydov, and H. D. Espinosa, "Effect of growth orientation and diameter on the elasticity of GaN nanowires. A combined in situ TEM and atomistic modeling investigation.," Nano Letters, vol. 11, pp. 548–55, Feb. 2011.
- [51] [Http://jmol.sourceforge.net/](http://jmol.sourceforge.net/), "Jmol: an open-source Java viewer for chemical structures in 3D."
- [52] C. Wetzel, M. Zhu, J. Senawiratne, T. Detchprohm, P. Persans, L. Liu, E. Preble, and D. Hanser, "Light-emitting diode development on polar and non-polar GaN substrates," Journal of Crystal Growth, vol. 310, pp. 3987–3991, Aug. 2008.
- [53] K. A. Bertness, A. Roshko, L. Mansfield, T. Harvey, and N. A. Sanford, "Mechanism for spontaneous growth of GaN nanowires with molecular beam epitaxy," Journal of Crystal Growth, vol. 310, pp. 3154–3158, June 2008.

- [54] O. Landré, D. Camacho, C. Bougerol, Y. M. Niquet, V. Favre-Nicolin, G. Renaud, H. Renevier, and B. Daudin, “Elastic strain relaxation in GaN/AlN nanowire superlattice,” Physical Review B, vol. 81, p. 153306, Apr. 2010.
- [55] Z. Zhong, F. Qian, D. Wang, and C. M. Lieber, “Synthesis of p-Type Gallium Nitride Nanowires for Electronic and Photonic Nanodevices,” Nano Letters, vol. 3, pp. 343–346, Mar. 2003.
- [56] A. Sanders, P. Blanchard, K. Bertness, M. Brubaker, C. Dodson, T. Harvey, A. Herrero, D. Rourke, J. Schlager, N. Sanford, A. N. Chiaramonti, A. Davydov, A. Motayed, and D. Tsvetkov, “Homoepitaxial n-core: p-shell gallium nitride nanowires: HVPE overgrowth on MBE nanowires.,” Nanotechnology, vol. 22, p. 465703, Nov. 2011.
- [57] T. J. Kippenberg and K. J. Vahala, “Cavity optomechanics: back-action at the mesoscale.,” Science, vol. 321, pp. 1172–6, Aug. 2008.
- [58] J. D. Thompson, B. M. Zwickl, A. M. Jayich, F. Marquardt, S. M. Girvin, and J. G. E. Harris, “Strong dispersive coupling of a high-finesse cavity to a micromechanical membrane.,” Nature, vol. 452, pp. 72–5, Mar. 2008.
- [59] D. K. Armani, T. J. Kippenberg, S. M. Spillane, and K. J. Vahala, “Ultra-high-Q toroid microcavity on a chip.,” Nature, vol. 421, pp. 925–8, Feb. 2003.
- [60] C. A. Regal, J. D. Teufel, and K. W. Lehnert, “Measuring nanomechanical motion with a microwave cavity interferometer,” Nature Physics, vol. 4, pp. 555–560, May 2008.
- [61] N. Flowers-Jacobs, D. Schmidt, and K. Lehnert, “Intrinsic Noise Properties of Atomic Point Contact Displacement Detectors,” Physical Review Letters, vol. 98, pp. 2–5, Mar. 2007.
- [62] M. Li, W. Pernice, and H. Tang, “Broadband all-photonic transduction of nanocantilevers,” Nature Nanotechnology, vol. 4, pp. 377–82, June 2009.
- [63] D. DeVoe, “Piezoelectric thin film micromechanical beam resonators,” Sensors and Actuators A: Physical, vol. 88, no. August 2000, pp. 263–272, 2001.
- [64] A. N. Cleland and M. L. Roukes, “Fabrication of high frequency nanometer scale mechanical resonators from bulk Si crystals,” Applied Physics Letters, vol. 69, no. 18, p. 2653, 1996.
- [65] M. Poot, S. Etaki, I. Mahboob, K. Onomitsu, H. Yamaguchi, Y. Blanter, and H. van der Zant, “Tunable Backaction of a DC SQUID on an Integrated Micromechanical Resonator,” Physical Review Letters, vol. 105, p. 207203, Nov. 2010.
- [66] S. W. Hoch, J. R. Montague, V. M. Bright, C. T. Rogers, K. A. Bertness, J. D. Teufel, and K. W. Lehnert, “Non-contact and all-electrical method for monitoring the motion of semiconducting nanowires,” Applied Physics Letters, vol. 99, no. 5, p. 053101, 2011.
- [67] A. N. Cleland, Foundations of Nanomechanics: From Solid-State Theory to Device Applications, vol. 2002. Berlin Heidelberg: Springer-Verlag, 2003.
- [68] S. Timoshenko, D. H. Young, and W. Weaver Jr., Vibration Problems In Engineering. New York: John Wiley & Sons, Inc., 1 ed., 1974.

- [69] O. Erginçan, G. Palasantzas, and B. J. Kooi, “Viscous damping of microcantilevers with modified surfaces and geometries,” Applied Physics Letters, vol. 101, no. 6, p. 061908, 2012.
- [70] P.-L. Yu, T. Purdy, and C. Regal, “Control of Material Damping in High-Q Membrane Microresonators,” Physical Review Letters, vol. 108, p. 083603, Feb. 2012.
- [71] S. Schmid and C. Hierold, “Damping mechanisms of single-clamped and prestressed double-clamped resonant polymer microbeams,” Journal of Applied Physics, vol. 104, no. 9, p. 093516, 2008.
- [72] S. Schmid, K. Jensen, A. Boisen, and K. Nielsen, “Damping mechanisms in high-Q micro and nanomechanical string resonators,” Physical Review B, vol. 84, pp. 1–6, Oct. 2011.
- [73] A. Eichler, J. Moser, J. Chaste, M. Zdrojek, I. Wilson-Rae, and A. Bachtold, “Nonlinear damping in mechanical resonators made from carbon nanotubes and graphene,” Nature Nanotechnology, vol. 6, pp. 339–42, June 2011.
- [74] Q. Unterreithmeier, T. Faust, and J. Kotthaus, “Damping of Nanomechanical Resonators,” Physical Review Letters, vol. 105, pp. 1–4, July 2010.
- [75] Y. Sun, A. Soh, and D. Fang, “Thermoelastic damping in micro-beam resonators,” International Journal of Solids and Structures, vol. 43, pp. 3213–3229, May 2006.
- [76] H. Hosaka, K. Itao, and S. Kuroda, “Damping characteristics of beam-shaped micro-oscillators,” Sensors and Actuators A: Physical, 1995.
- [77] G. D. Cole, I. Wilson-Rae, K. Werbach, M. R. Vanner, and M. Aspelmeyer, “Phonon-tunnelling dissipation in mechanical resonators,” Nature Communications, vol. 2, p. 231, Jan. 2011.
- [78] G. Zolfagharkhani, A. Gaidarzhly, S.-B. Shim, R. Badzey, and P. Mohanty, “Quantum friction in nanomechanical oscillators at millikelvin temperatures,” Physical Review B, vol. 72, pp. 1–5, Dec. 2005.
- [79] S. S. Verbridge, J. M. Parpia, R. B. Reichenbach, L. M. Bellan, and H. G. Craighead, “High quality factor resonance at room temperature with nanostrings under high tensile stress,” Journal of Applied Physics, vol. 99, no. 12, p. 124304, 2006.
- [80] B. Kim, M. a. Hopcroft, R. N. Candler, C. M. Jha, M. Agarwal, R. Melamud, S. a. Chandorkar, G. Yama, and T. W. Kenny, “Temperature Dependence of Quality Factor in MEMS Resonators,” Journal of Microelectromechanical Systems, vol. 17, pp. 755–766, June 2008.
- [81] A. Venkatesan, K. J. Lulla, M. J. Patton, A. D. Armour, C. J. Mellor, and J. R. Owers-Bradley, “Dissipation due to tunneling two-level systems in gold nanomechanical resonators,” Physical Review B, vol. 81, pp. 1–4, Feb. 2010.
- [82] R. A. Barton, B. Ilic, A. M. van der Zande, W. S. Whitney, P. L. McEuen, J. M. Parpia, and H. G. Craighead, “High, size-dependent quality factor in an array of graphene mechanical resonators,” Nano Letters, vol. 11, pp. 1232–6, Mar. 2011.
- [83] A. N. Cleland and M. L. Roukes, “Noise processes in nanomechanical resonators,” Journal of Applied Physics, vol. 92, no. 5, p. 2758, 2002.

- [84] I. Wilson-Rae, “Intrinsic dissipation in nanomechanical resonators due to phonon tunneling,” Physical Review B, vol. 77, pp. 1–31, June 2008.
- [85] A. Venkatesan, K. J. Lulla, M. J. Patton, A. D. Armour, C. J. Mellor, and J. R. Owers-Bradley, “Dissipation in a Gold Nanomechanical Resonator at Low Temperatures,” Journal of Low Temperature Physics, vol. 158, pp. 685–691, Sept. 2009.
- [86] F. R. Blom, S. Bouwstra, M. Elwenspoek, and J. H. Fluitman, “Dependence of the quality factor of micromachined silicon beam resonators on pressure and geometry,” Journal of Vacuum Science & Technology B: Microelectronics and Nanometer Structures, vol. 10, p. 19, Jan. 1992.
- [87] R. Lifshitz and M. Roukes, “Thermoelastic damping in micro- and nanomechanical systems,” Physical Review B, vol. 61, pp. 5600–5609, Feb. 2000.
- [88] M. E. Levinshtein, S. L. Rumyantsev, and M. S. Shur, Properties of Advanced Semiconductor Materials: GaN, AlN, InN, BN, SiC, SiGe. Hoboken: John Wiley & Sons, 2001.
- [89] C. Zener, “Internal Friction in Solids. I. Theory of Internal Friction in Reeds,” Physical Review, vol. 52, pp. 230–235, Aug. 1937.
- [90] C. Zener, “Internal Friction in Solids II. General Theory of Thermoelastic Internal Friction,” Physical Review, vol. 53, pp. 90–99, Jan. 1938.
- [91] C. Zener, W. Otis, and R. Nuckolls, “Internal Friction in Solids III. Experimental Demonstration of Thermoelastic Internal Friction,” Physical Review, vol. 53, pp. 100–101, Jan. 1938.
- [92] K. Yasumura, T. Stowe, and E. Chow, “Quality factors in micron- and submicron-thick cantilevers,” Systems, Journal of, vol. 9, pp. 117–125, Mar. 2000.
- [93] P. Poncharal, Z. L. Wang, and W. A. de Heer, “Electrostatic Deflections and Electromechanical Resonances of Carbon Nanotubes,” Science, vol. 283, pp. 1513–1516, Mar. 1999.
- [94] D. Carr and S. Evoy, “Measurement of mechanical resonance and losses in nanometer scale silicon wires,” Applied Physics Letters, vol. 75, no. 7, pp. 920–922, 1999.
- [95] J. M. Gray, Gallium Nitride Nanowire Electromechanical Resonators. PhD thesis, 2011.
- [96] D. M. Pozar, Microwave Engineering. Wiley, 1990.
- [97] S. George, A. Ott, and J. Klaus, “Surface chemistry for atomic layer growth,” The Journal of Physical Chemistry, vol. 3654, no. 95, pp. 13121–13131, 1996.
- [98] M. Tripp, C. Stampfer, D. Miller, T. Helbling, C. Herrmann, C. Hierold, K. Gall, S. George, and V. Bright, “The mechanical properties of atomic layer deposited alumina for use in micro- and nano-electromechanical systems,” Sensors and Actuators A: Physical, vol. 130–131, pp. 419–429, Aug. 2006.
- [99] J. Zhang, Y. Wu, G. Cheng, M. Moskovits, and J. Speck, “Dislocation-Free GaN Nanowires,” Microscopy and Microanalysis, vol. 9, no. S02, pp. 342–343, 2003.

- [100] R. Zhu, D. Wang, S. Xiang, Z. Zhou, and X. Ye, “Piezoelectric characterization of a single zinc oxide nanowire using a nanoelectromechanical oscillator.,” *Nanotechnology*, vol. 19, p. 285712, July 2008.
- [101] S. Hoch, “Capacitive measurement of the intrinsic damping of a gallium nitride nanowire”. Undergraduate thesis, University of Colorado, 2010.
- [102] W. S. Rasband, “ImageJ”, <http://imagej.nih.gov/ij/>.
- [103] <Http://www.rogerscorp.com/acm/producttypes/2/Rogers-High-Frequency-Laminates.aspx>, “Rogers Corporation.”
- [104] S. Tanner, *Electrostatically Actuated Cantilevers Processing and Measurement*. PhD thesis, 2007.
- [105] <Http://www.techniks.com/>, “Techniks.”
- [106] <Http://www.precisioncryo.com/dewarvapo.html>, “Precision Cryogenic Systems, Inc.,”
- [107] <http://www.americanmagnetics.com/level.php>, “American Magnetics, Inc.”
- [108] <Http://www.minicircuits.com/homepage/homepage.html>, “Minicircuits, Inc..”
- [109] <Http://www.markimicrowave.com/>, “Marki Microwave.”
- [110] <Http://www.nardamicrowave.com/east/>, “Narda Microwave.”
- [111] <Http://www.thinksrs.com/>, “Stanford Research Systems, Inc..”
- [112] J. R. Montague, K. A. Bertness, N. A. Sanford, V. M. Bright, and C. T. Rogers, “Temperature-dependent mechanical-resonance frequencies and damping in ensembles of gallium nitride nanowires,” *Applied Physics Letters*, vol. 101, no. 17, p. 173101, 2012.
- [113] J. D. Teufel, T. Donner, M. A. Castellanos-Beltran, J. W. Harlow, and K. W. Lehnert, “Nanomechanical motion measured with an imprecision below that at the standard quantum limit.,” *Nature Nanotechnology*, vol. 4, pp. 820–3, Dec. 2009.
- [114] L. B. Biedermann, R. C. Tung, A. Raman, and R. G. Reifenberger, “Flexural vibration spectra of carbon nanotubes measured using laser Doppler vibrometry.,” *Nanotechnology*, vol. 20, p. 035702, Jan. 2009.
- [115] J. Chan, T. P. M. Alegre, A. H. Safavi-Naeini, J. T. Hill, A. Krause, S. Gröblacher, M. Aspelmeyer, and O. Painter, “Laser cooling of a nanomechanical oscillator into its quantum ground state.,” *Nature*, vol. 478, pp. 89–92, Oct. 2011.
- [116] J. Teufel, J. Harlow, C. Regal, and K. Lehnert, “Dynamical Backaction of Microwave Fields on a Nanomechanical Oscillator,” *Physical Review Letters*, vol. 101, pp. 1–4, Nov. 2008.
- [117] A. D. O’Connell, M. Hofheinz, M. Ansmann, R. C. Bialczak, M. Lenander, E. Lucero, M. Neeley, D. Sank, H. Wang, M. Weides, J. Wenner, J. M. Martinis, and A. N. Cleland, “Quantum ground state and single-phonon control of a mechanical resonator.,” *Nature*, vol. 464, pp. 697–703, Apr. 2010.

- [118] J. E. Sader, J. Sanelli, B. D. Hughes, J. P. Monty, and E. J. Bieske, "Distortion in the thermal noise spectrum and quality factor of nanomechanical devices due to finite frequency resolution with applications to the atomic force microscope," The Review of Scientific Instruments, vol. 82, p. 095104, Sept. 2011.
- [119] S. Evoy, A. Olkhovets, L. Sekaric, J. M. Parpia, H. G. Craighead, and D. W. Carr, "Temperature-dependent internal friction in silicon nanoelectromechanical systems," Applied Physics Letters, vol. 77, no. 15, p. 2397, 2000.
- [120] P. Mohanty, D. Harrington, K. Ekinici, Y. Yang, M. Murphy, and M. Roukes, "Intrinsic dissipation in high-frequency micromechanical resonators," Physical Review B, vol. 66, pp. 1–15, Aug. 2002.
- [121] A. S. Nowick and B. S. Berry, Anelastic Relaxation in Crystalline Solids. London: Academic Press, Inc., 1 ed., 1972.
- [122] D. Manchon, "Optical studies of the phonons and electrons in gallium nitride," Solid State Communications, vol. 8, pp. 1227–1231, Aug. 1970.
- [123] L. Lymperakis and J. Neugebauer, "Large anisotropic adatom kinetics on nonpolar GaN surfaces: Consequences for surface morphologies and nanowire growth," Physical Review B, vol. 79, pp. 1–4, June 2009.
- [124] D. Look, J. Sizerlove, S. Keller, Y. Wu, U. Mishra, and S. DenBaars, "Accurate mobility and carrier concentration analysis for GaN," Solid State Communications, vol. 102, pp. 297–300, Apr. 1997.
- [125] A. Anwar and R. Webster, "Temperature dependent transport properties in GaN, Al/sub x/-Ga/sub 1-x/N, and In/sub x/Ga/sub 1-x/N semiconductors," IEEE Transactions on Electron Devices, vol. 48, pp. 567–572, Mar. 2001.
- [126] X. L. Feng, C. A. Zorman, M. Mehregany, and M. L. Roukes, "DISSIPATION IN SINGLE-CRYSTAL 3C-SiC ULTRA-HIGH FREQUENCY NANOMECHANICAL RESONATORS NEMS," in Solid-State Sensors, Actuators and Microsystems Workshop (Hilton Head 2006), (Hilton Head Island, SC), pp. 86–89, 2006.
- [127] C. Chen, S. Rosenblatt, K. I. Bolotin, W. Kalb, P. Kim, I. Kymissis, H. L. Stormer, T. F. Heinz, and J. Hone, "Performance of monolayer graphene nanomechanical resonators with electrical readout.," Nature Nanotechnology, vol. 4, pp. 861–7, Dec. 2009.
- [128] J. Mei and L. Li, "A Self-Tuning Mechanism of Zinc Oxide Nanoelectro-Mechanical Resonator Based on Joule Heating," Procedia Engineering, vol. 47, pp. 462–465, Jan. 2012.
- [129] W. L. Johnson, S. A. Kim, R. Geiss, C. M. Flannery, K. A. Bertness, and P. R. Heyliger, "Vibrational modes of GaN nanowires in the gigahertz range.," Nanotechnology, vol. 23, p. 495709, Dec. 2012.
- [130] J. Mei and L. Li, "Frequency self-tuning of ZnO nanoresonator," Physica E: Low-dimensional Systems and Nanostructures, vol. 46, pp. 206–212, Sept. 2012.

- [131] H. Lee, T. Chen, J. Li, K. Y. Yang, S. Jeon, O. Painter, and K. J. Vahala, “Chemically etched ultrahigh-Q wedge-resonator on a silicon chip,” Nature Photonics, vol. 6, pp. 369–373, May 2012.
- [132] J. Mei and L. Li, “A Self-Tuning Mechanism of Zinc Oxide Nanoelectro-Mechanical Resonator Based on Joule Heating,” Procedia Engineering, vol. 47, pp. 462–465, Jan. 2012.
- [133] J.-H. L. Cheng, “Atomic Layer Deposition Enabled Interconnect and Packaging Technologies for As-Grown Nanowire Devices”. PhD Thesis, University of Colorado, 2010.
- [134] X. M. H. Huang, X. L. Feng, C. A. Zorman, M. Mehregany, and M. L. Roukes, “VHF, UHF and microwave frequency nanomechanical resonators,” New Journal of Physics, vol. 7, pp. 247–247, Nov. 2005.

## Appendix A

### Research Contributions

#### A.1 Peer-Reviewed Publications

- ‘Temperature-dependent mechanical-resonance frequencies and damping in ensembles of gallium nitride nanowires,’ J.R. Montague, K.A. Bertness, N.A. Sanford, V.M. Bright, C.T. Rogers, Applied Physics Letters, **101**, 173101 (2012).
- ‘Non-contact and all-electrical method for monitoring the motion of semiconducting nanowires,’ S. Hoch, J.R. Montague, V.M. Bright, C.T. Rogers, K.A. Bertness, J. Teufel, K. Lehnert, Applied Physics Letters, **99**, 053101 (2011).
- ‘Analysis of high- $Q$ , gallium nitride nanowire resonators in response to deposited thin films,’ J.R. Montague, M. Dalberth, J.M. Gray, D. Seghete, K.A. Bertness, S.M. George, V.M. Bright, C.T. Rogers, Sensors and Actuators, A **165**(1), 59 (2011).

#### A.2 Presentations And Conference Proceedings

- American Physical Society (APS), March Meeting 2012 (oral presentation)
- American Society of Mechanical Engineers (ASME), International Mechanical Engineering Congress and Exposition 2011 (oral presentation & published conference proceedings)
- APS, March Meeting 2010 (oral presentation)

- IEEE, International Conference on Solid-State Sensors, Actuators, and Microsystems 2009  
(poster & published conference proceedings)

## Appendix B

### Calculation Of Hexagonal Beam $I_y$

In Section 2.1, we present the derivation of the eigenfrequencies for the hexagonal cross-section GaN nanowires. There, we mention that the two possible – nominally orthogonal – directions for the fundamental mode are degenerate (for regular cross-section). This result is not necessarily intuitive, so here we include the calculations illustrating this fact. To begin, consider the orientation of the prismatic beam that will displace (in this two-dimensional cross section) in the  $y$ -direction. Figure B.1 includes sketches of the two orientation under consideration.

Beginning with the sketch in part a), we consider that the longest cross-sectional direction is aligned with the  $x$ -axis. The motion of the nanowire will be orthogonal to this, along  $y$ . The integral calculation for the second moment in this direction  $I_x$  – though it is generically referred to as  $I_y$  in e.g. [67] – is over the cross-sectional area:

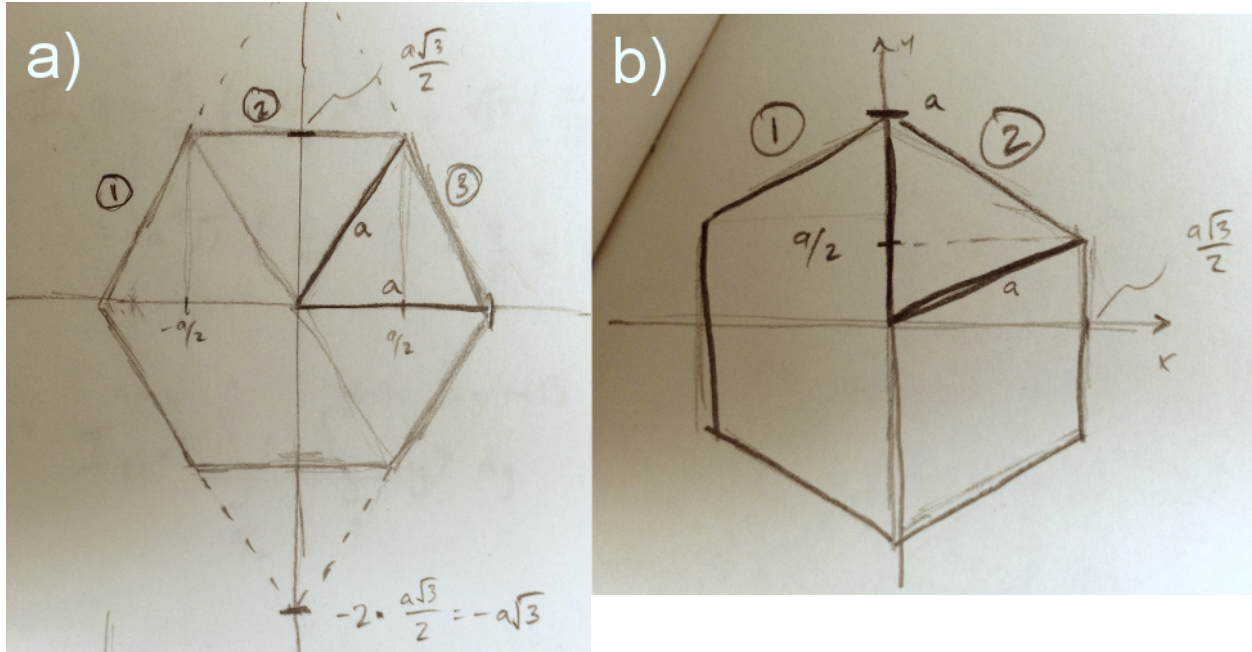
$$I_x = \int y^2(x) \, dA. \quad (\text{B.1})$$

Referring to Figure B.1, we will divide this area integral into three components (labeled (1), (2), and (3) in the Figure). By symmetry, we can also save some effort by calculating the area integral for only the top half and doubling the result.

The slope of the line below section (1) is  $y(x) = \sqrt{3}x + a\sqrt{3}$ , so the contribution from this section of the area integral is given by

$$I_1 = \int_{-a}^{-a/2} dx \int_0^{\sqrt{3}x+a\sqrt{3}} y^2 \, dy, \quad (\text{B.2})$$

Figure B.1: Calculations of the second moment of area for the eigenfrequency of a resonator in the two orthogonal vibratory directions.



which evaluates to  $I_1 = \frac{\sqrt{3}}{64}a^4$ .

Section (2) is a simple rectangle, but we can also use the proper formulation to calculate its contribution:

$$I_2 = \int_{-a/2}^{a/2} dx \int_0^{a\sqrt{3}/2} y^2 dy, \quad (\text{B.3})$$

which evaluates to  $\frac{\sqrt{3}}{8}a^4$ .

Finally, section (3) is identical to section (1), so  $I_3 = \frac{a^4\sqrt{3}}{64}$ . When we combine these sections and multiply by two (to account for the bottom half) we find  $I_{total} = \frac{5\sqrt{3}}{16}a^4$ .

For the other mode – moving in the other direction, with the displacement of the nanowire in the direction orthogonal to a line that bisects the sidewalls – we simply rotate our coordinates. Figure B.1 shows that we can break the integral into two components. In this case, we can see that symmetry allows us to calculate just the ‘top’ half, and also just the ‘left’ half, then multiply our result by four. The function for the edge in section (1) is given by  $y(x) = \frac{x}{\sqrt{3}} + a$ , and so the

integral to evaluate is

$$I_1 = \int_{-\frac{a\sqrt{3}}{2}}^0 dx \int_0^{\frac{x}{\sqrt{3}}+a} y^2 dy, \quad (\text{B.4})$$

which evaluates to  $\frac{5a^4\sqrt{3}}{64}$ . Multiplying this result by four, the total value for  $I_y$  here is  $\frac{5\sqrt{3}}{16}a^4$ , precisely the same as for the orthogonal orientation.



```

/CLEAR                                !default conditions
/PREP7                                !enter input preprocessor
Refine = 2                            !refinement: 1=coarse , 5=fine
nwR = .2                              !nanowire radius (major, microns)
length = 17                           !nw/ald length (microns)
!Ald = 0.005                          !ald thickness

!!!!!!!!!!!!!! solution data !!!!!!!!!!!!!!!
NOM = 10                              !number of modes to find
MINFREQ = 0                           !settings for solving?
MAXFREQ = 10e9                        ! " " "

!!!!!!!!!!!!!! material data !!!!!!!!!!!!!!!
ET,1,SOLID187                         !element type
MPTEMP,,,,,,,,                        !temperature field
MPTEMP,1,0                            ! set all to 0
MPDATA,EX,1,,300E3                    !elastic modulus (MPa)
MPDATA,PRXY,1,,.3                     !poisson's ratio
MPDATA,DENS,1,,6.150e-15              !density (kg/um^3)
MPTEMP,,,,,,,,                        !<--- redundant?
MPTEMP,1,0                            !<--- " " "

!!!!!!!!!!!!!! create area & offset !!!!!!!!!!!!!!!
RPR4,6,0,0,nwR,                       !n-gon area for NW
!RPR4,6,0,0,Ald+NanR,                 ! Ald Shell
!VOFFST,3,Length,,                   ! for use with ALD
VOFFST,1,length,,                    !offset

```

```

!----->
! Mesh and extrude
!----->
MSHKEY,0                                !free meshing (?)
MSHAPE,1,3d                             !specify element shape & dim
VSEL,, , , all                          !select subset of volumes
MAT,1                                    !set mat'l pointer
VMESH,ALL                                !generate nodes & vol elements
EREFINE,ALL, , , Refine,0,1,1           !refine mesh around everything

!----->
! Apply boundary conditions
!----->
DA,1, all, 0                             !DOF constraints (fix end?)

!----->
! Modal Solution and Solve
!----->
ANTYPE,2                                 !set analysis type (2=nodal)
!!!!!!! is this necessary?
!MODOPT,LANB,3                           !modal analysis options
!EQLV,SPARSE                             !type of eqn solver
!MXPAND,0, , , 0                         !modes to expand on
!LUMPM,0                                  !lumped mass matrix (?)
!PSTRES,0                                 !prestress effects
!!!!!!!!!!!!!!!!!!!!!!!!!!!!!!

```

```

MODOPT,LANB,NOM,MINFREQ,MAXFREQ,,OFF    !# of modes, frequency range
FINISH

/SOLU                                     !enters soln processor
SOLVE                                     !start solution
/POST1                                    !enter postproc
FINISH

```

## C.2 File #2

This file is included mainly as a resource. It was the first modal solution script that we came up with and includes some shorthand, some additional code, and is not particularly well-commented. The results, however, should be very similar to the previous file.

```
FINI
```

```
fname='NanoWire_Resonance'
```

```
/title , %fname%
```

```
/out , fname , out
```

```
/filename , fname
```

```
WPSTYLE, , , , , , 0
```

```
!uMks units
```

```
/cle
```

```
/PREP7
```

```
Refined = 2    !level of refinemnt 1 = coarse , 5 = max
```

```

NanR    = .1      !nano wire radius (outer radius of hexagon)
Ald     = .005   !Ald thickness
Length = 18

NOM = 10                !number
MINFREQ = 0           !
MAXFREQ = 10e9

btol = 1e-3

ET,1 ,SOLID187
MPTEMP, , , , , , ,
MPTEMP,1 ,0
MPDATA,EX,1 , ,300 E3
MPDATA,PRXY,1 , ,.2
MPTEMP, , , , , , ,
MPTEMP,1 ,0
MPDATA,DENS,1 , ,6.15E-15
MPTEMP, , , , , , ,
MPTEMP,1 ,0
MPDATA,EX,2 , ,400 E3
MPDATA,PRXY,2 , ,.28
MPTEMP, , , , , , ,
MPTEMP,1 ,0
MPDATA,DENS,2 , ,19.3E-14

```

```

RPR4,6,0,0,Ald+NanR,          ! Ald Shell
RPR4,6,0,0,NanR,             ! Nano Wire

ASBA,1,2,,2    ! Subtraction for use with ALD coatings
RPR4,6,0,0,NanR,

RPR4,6,0,0,NanR,

VOFFST,1,Length, ,          ! for use with ALD
VOFFST,3,Length, ,

!RPR4,6,0,0,Ald+NanR,
!voffst,5,Length
!voffst,5,Length+Ald
!vsbv,4,3,,3

VGLUE,ALL

!----->
! Mesh and extrude
!----->

MSHKEY,0
MSHAPE,1,3d
VSEL,, ,1
mat,1
vmesh,1

```

VSEL,ALL

MSHKEY,0

MSHAPE,1,3d

VSEL,,,3

mat,2

vmesh,ALL

VSEL,ALL

!EREF,ALL,,,Refined,0,1,1

!—————>

! Apply boundry conditions

!—————>

da,1,all,0

DA,24,ALL,0

!—————>

! Modal Solution and Solve

!—————>

ANTYPE,2

MODOPT,LANB,3

EQSLV,SPAR

MXPAND,0,,,0 ! modes to expand on, none

LUMPM,0

PSTRES,0

MODOPT,LANB,NOM,MINFREQ,MAXFREQ, ,OFF !# of modes, frequency range

FINISH

/SOL

SOLVE

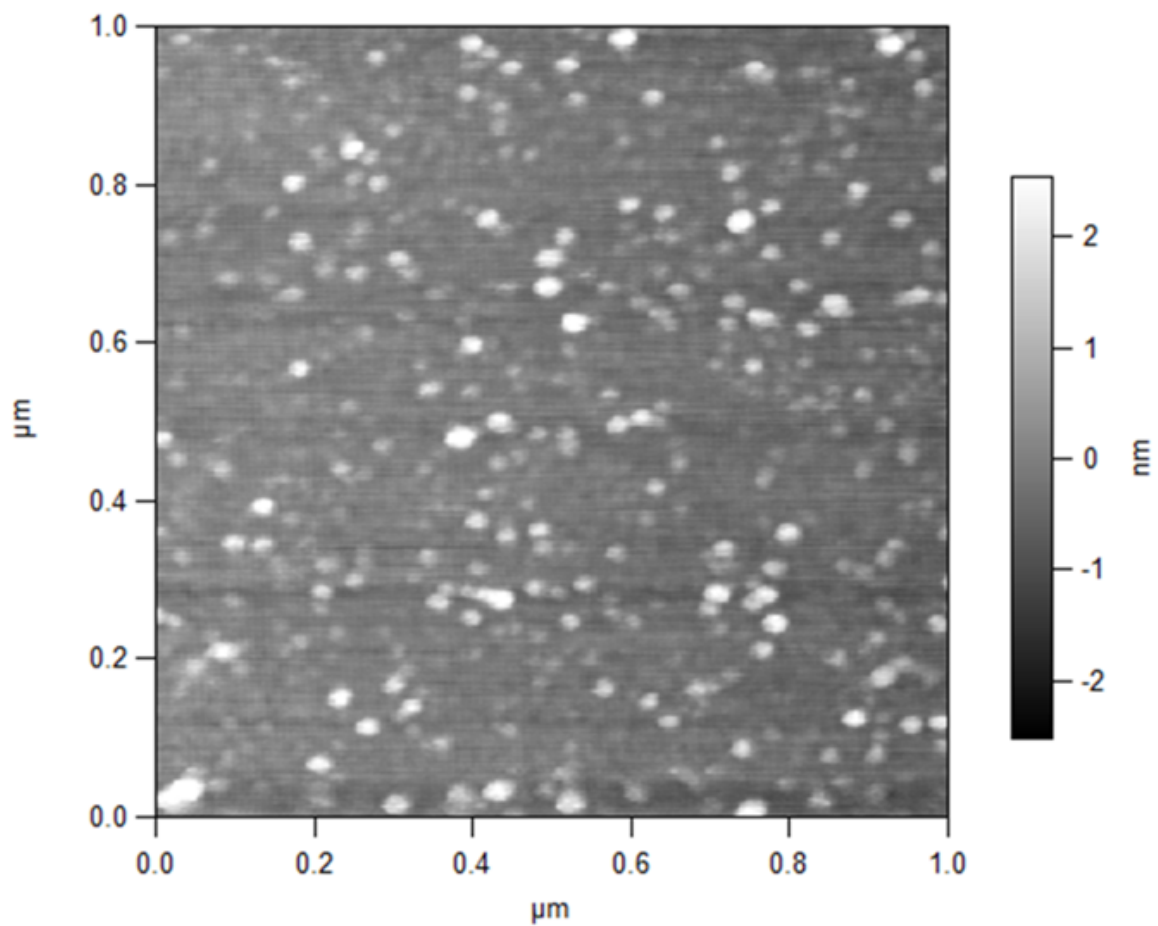
/POST1

fini

## Appendix D

### Atomic Force Microscope Scan of ALD Ruthenium

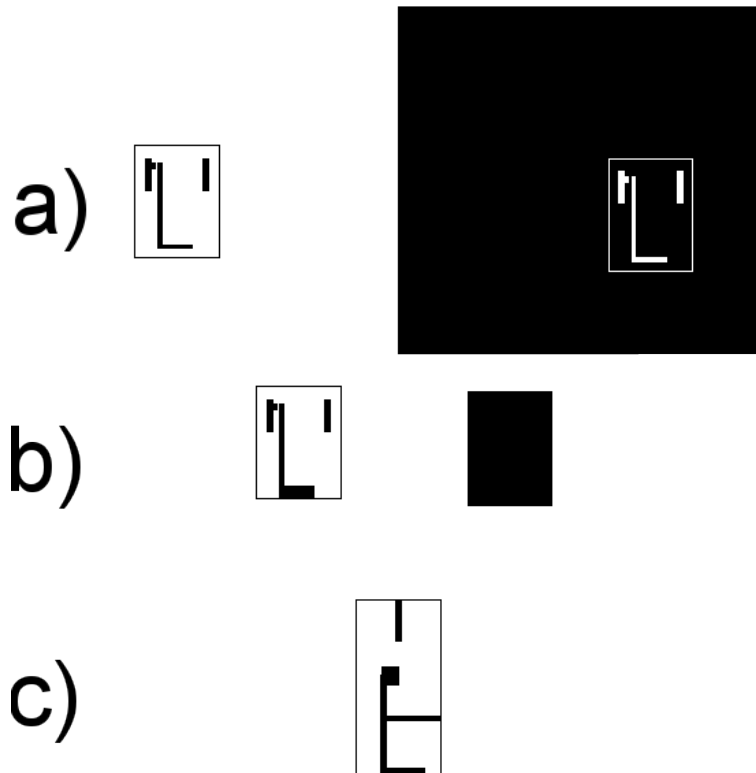
Figure D.1: AFM scan showing ALD Ru on a witness substrate placed in the deposition chamber with the GaN nanowire sample. The observed island growth indicates that the Ru film has not yet coalesced into a continuous layer. This is corroborated by the mass-loading effects discussed in Section 3.6.3.



## Appendix E

### Microwave Circuit Lithography Masks

Figure E.1: In Section 5.1.1, we describe the use of overhead transparencies as lithography masks, and printable designs for heat transfer. This is the evolution of these patterns. a) The initial positive (left) and negative (right) masks. These were created in preparation for use with photoresist. b) The top (left) and bottom (right) masks used once the CSE area was increased. c) The final design used in this work, where the bottom Cu was protected by kapton tape. The central square in the mask served as the bottom capacitor plate for the variable coupling capacitance. For any future printing and modifications, these images are saved on the Win7 desktop in `josh/posters papers presentations conferences/PPT illustrations/printed circuit.ppt`.



## Appendix F

### SolidWorks Sample Holder Model

Figure F.1: Exploded view of Cu sample holder machined for use in capacitive nanowire measurements. The two pieces are manually screwed together by use of shown through- and tap-holes. The base plate is  $1.5 \times 1.5 \text{ in}^2$ . The design is such that a panel-mount SMA connector can be screwed onto the back via the four square-positioned holes.

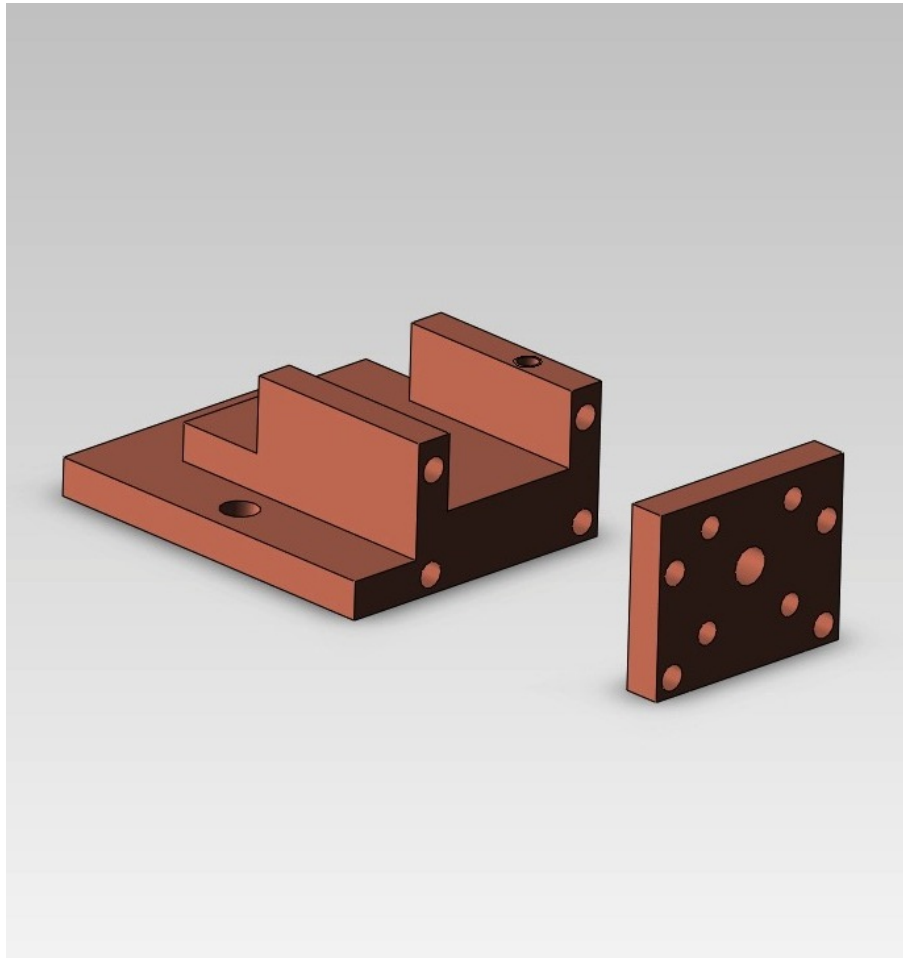
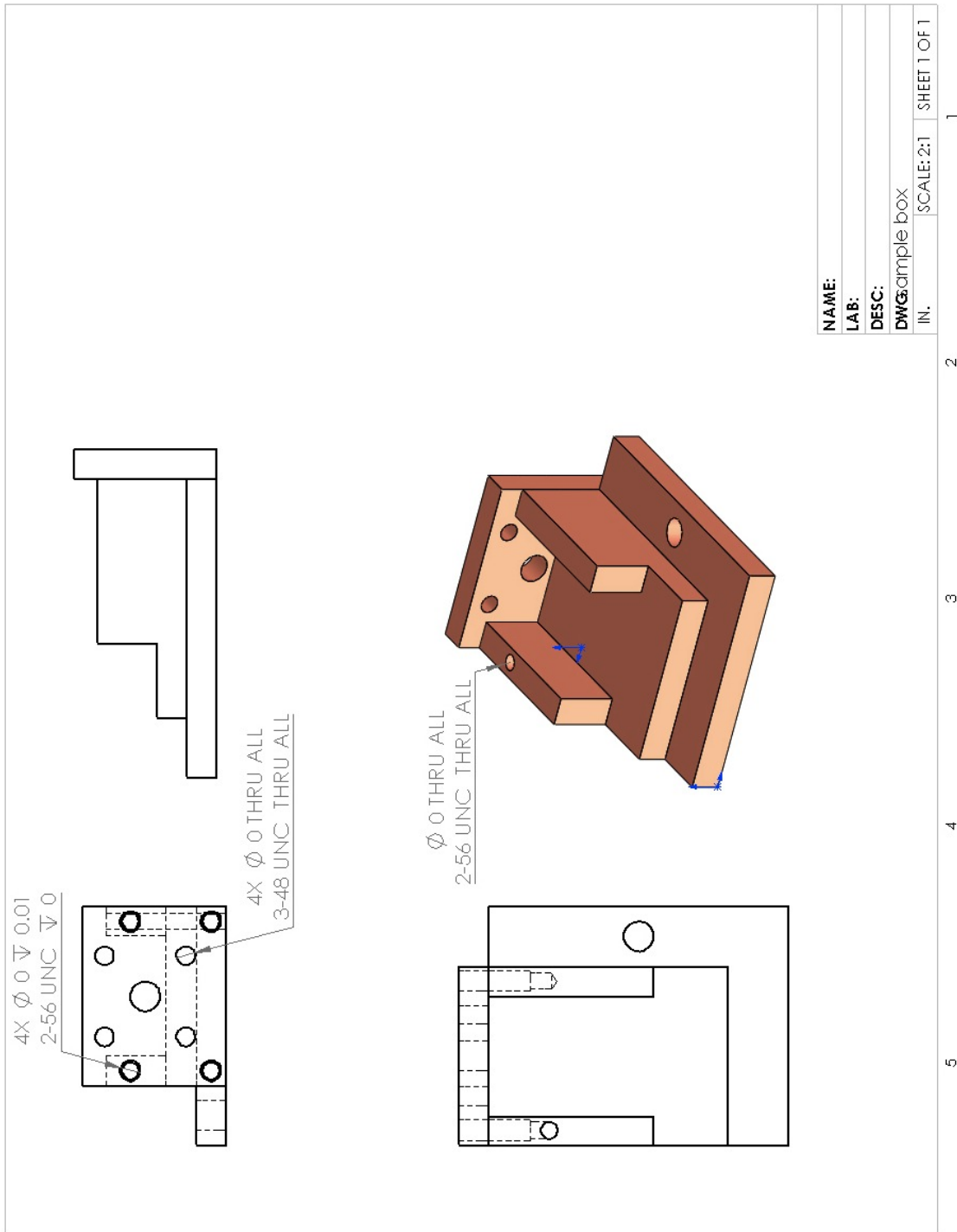


Figure F.2: Schematic of final iteration of Cu sample holder used for capacitive detection of nanowires. Machined from two blocks of solid Cu – one for base plate, one for back plate – and screwed together manually. Through- and tapped-holes are indicated by arrows and labels. This piece is fabricated by the physics department machine shop. The Solidworks model files used to create this are in `josh/SolidWorks/sample holder 08202012/`.



## Appendix G

### OriginPro Data, Scripts, And Fitting Functions

#### G.1 OriginPro Data Files

Data collection for the work described in this work began in the summer of 2008. There are at least three separate hard disks in the basement lab that contain all of the raw and analysis data. Since there are far too many individual OriginPro projects (\*.opj) to list, the curious reader is directed to the Word document I created in preparation for my Comprehensive III examination. In the 2B basement, there is a desktop machine on a blue cart (as of this writing). Inside the enclosure are two 3.5" hard disk drives. The primary-use drive boots into Windows 7 and has a folder (appropriately) named 'josh' on the desktop. This folder contains everything that I created on this particular disk. In this directory is a Word document (CompsIII outline.doc) that outlines the chronology of my work with references to notebook and page numbers of major results, calculations, derivations, and other noteworthy events. From this information, one can locate the origin data if so desired.

On both the primary drive (Windows 7, data from the last couple of years) and the secondary drive (Windows XP, data from 2008 to approximately 2011), the data files are organized chronologically and by date (typically 'year/month/day/'). Note that this motherboard does not support dual SATA connections, so in order to access data stored on the other hard drive, you have to open the case and physically move the SATA and power supply connections to the disk you want. Both disks are bootable into their respective operating system. Finally, there is an additional computer – a Sony Vaio laptop running Windows 7 – that also has a lot of the data on it. As is described in a

README in the ‘josh’ directory on that machine, there should be very little (if any) unique data, programs, scripts, or files saved there that are not also replicated somewhere on the Windows 7 desktop hard disk. The laptop was used for (less noisy) data acquisition and all the data acquired there was copied to the desktop on a near-daily basis. Nevertheless, the data was also kept on the laptop for a form of backup (the desktop Windows 7 hard drive also uses Windows Backup with an external USB drive that sits on the same cart). Additionally, all but the last couple of months worth of data is backed up at ADrive.com, with the various logins listed in my lab notebooks.

## G.2 OriginPro Scripts

Most of the programs written and used for the purpose data acquisition ultimately save the data in a format that can be simply imported to OriginPro (either through the menus or a direct drag-and-drop of the data file). Occasionally, the data was saved in a slightly more efficient manner e.g. when saving a time or PSD record of 2 – 4 million double-precision floats, also writing the independent variables to file unnecessarily doubled the memory required. Instead, the programs often write the information needed to reconstruct the independent variable. For example, if the data is a time record, often the initial time (typically 0) and the time increment  $dt$  will be stored as the first two rows of a single-column data file. After manually keying in the commands to reconstruct this independent variable via the clickable menus a few times, I realized it would be much faster and more efficient to script the process.

OriginPro has an essentially deprecated proprietary scripting language called LabTalk. Though it is superceded by various other systems (I think OriginC is what they want users to use now), LabTalk is pretty quick to learn and can accomplish my tasks with minimal effort. Included below are the two LabTalk scripts that I used very frequently in order to reconstruct time and frequency independent variable records. In order to run these scripts (assuming you have the appropriately-structured file imported into an active worksheet, click through the menus to find the ‘Show Classic Script Window’ option. Open and copy the entirety of the desired script, paste it into the Classic Script Window, highlight all of that text in the Script Window, then hit enter. This entire process

should take three clicks, four keyboard commands, and a few seconds to calculate the results. These scripts should be located in josh/origin things/ (or something very similar).

### G.2.1 Independent Variable: Time

File name: makeTimeX.txt

This code is used in conjunction with e.g. data acquired by the ‘NIScope 2chan time record.vi’ program. It assumes that the column data starts with the time increment (assumes the start is at  $t = 0$ ), and then the array of y values. It outputs a two-column array with time (in seconds, by default) in the first column and y values in the second column. Both columns should also be labeled appropriately.

```
type Begin ...;
double dt = col(1)[1];           // set x step size
type dt is $(dt);              // verify it's working
range rc1 = col(1)[2:end];      //get rows 2 through end of imported data
type length is $(rc1.getSize()); // verify length
col(2) = rc1;                   // copy data into col B
col(1) = data(0, dt*rc1.getSize(), dt); // fill regular data for X
wks.col1.name$ = "time";        // rename cols
wks.col2.name$ = "signal";
del -ra r*;                     //delete range vars
type Done!;
```

### G.2.2 Independent Variable: Frequency

File name: makePSDx.txt

This code is used in conjunction with e.g. data acquired by any of the various PSD VIs e.g. ‘NIScope PSD v8.vi’ (the most recent incarnation of an evolving set of VIs). It assumes the column

data begins with the initial frequency (typically 0), and the frequency increment  $df$ , followed by the y value array. It outputs a two-column array with frequency in the left-hand column and PSD values in the right-hand column. Both columns should be labeled appropriately.

```
//type Begin;
double df = col(1)[2]; // set freq step
type df is $(df); // verify it's working
//sec -p 0.1; // experiment with timing
range rc1 = col(1)[3:end]; //get rows 3 through end of imported data
type $(rc1.getSize()); // verify length
col(2) = rc1; // copy data into col B
col(1) = data(0, df*rc1.getSize(), df); // fill regular data for X
wks.col1.name$ = "Freq"; // rename cols
wks.col2.name$ = "PSD";
del -ra r*;
//type Done;
```

### G.3 OriginPro Fitting Functions

Additionally, there are many fitting functions that have been created over the years. OriginPro of course comes preloaded with many functions that work well, but we have also added a number of Lorentzian- and loss-type functions. Unfortunately, with each new release or upgrade of OriginPro, we must import our fitting functions again. There are too many of these functions to list them all here – plus, any fitting function that I wrote will have documentation throughout it. The most-used fitting functions are the two-phase Lorentzian and the PSD fit. In order to locate the fitting functions (which are stored in OriginPro’s own internal directory structure), simply use the Fitting Function Organizer, found in the menus of the graphical interface. From here, you can see the existing functions, create your own, or modify existing ones.

## Appendix H

### LabView Tools

It is possible that nearly as much time was spent developing programs in LabView as was spent acquiring data with said programs. Many powerful tools have been created for data acquisition in this work. Due to the quantity and resolution of the data, we have had to – at times – be cognizant of our system resources and design around these. In particular, the programs for acquiring and saving long-average PSDs pay attention to this. As such, more of the software developed toward the end of this work will have efficiency in mind, and fewer brute-force tactics.

The folder `josh/labview` (on the desktop and laptop computers) contains somewhere between 300 and 400 files in it. Some of these are hold-overs from previous graduate students and were never used. Occasionally, bits and pieces of these types of programs are recycled into new tools, so they are kept around just in case. Due to the sheer number of utilities available, I will not try to list all of them here. Instead, I will point out the most useful of these tools. And again, much of the software that I have developed will (hopefully) have reasonable comments to guide some understanding if it gets complicated inside.

Note: with every new academic year, National Instruments releases a new edition of LabView. Each and every year, this upgrade renders earlier programs inoperable. And, the oldest versions of code (those just-in-case programs from generations of grad students ago) will slowly deprecate to the point of not even being readable. Therefore, it is advised to periodically open all the random VIs that are stored in the depths of these computers. Not only will this expose the user to new (potentially insightful, potentially terrifying) examples of LabView programming, but it will often

allow LabView to automatically make the necessary changes in order to maintain the compatibility of these VIs with future version of LabView.

These VIs are listed in approximately the order they are used during a typical data acquisition. As we reach back in time, the VIs get progressively more spaghetti-like in their design. Take more design inspiration from the later code than the earlier. You will prefer it as well as any future user.

- **8510 res read2.vi**

Queries the HP8510 VNA for the measured signal (i.e. displays and optionally saves the data that is displayed on the 8510 LCD). Requires the scan bandwidth to be specified on the 8510. Designed to calculate and stay centered on a resonance frequency. If no local minimum is displayed on the screen, this VI will run off to unwanted frequencies. With local minimum on-screen, repeated calculates resonance frequency and 3-dB points.

- **8510 set 2.vi**

Sets up the 8510 output. Allows user to either scan a specified bandwidth at a specified power level, or output a continuous tone at a specified power and frequency.

- **circuit watch + T.vi**

Repeatedly queries the 8510 for resonance properties (frequency, width) of the circuit under test, while also querying the temperature monitor for the sample temperature. Primarily used for monitoring the cool-down of the system and optimizing PID levels for temperature control.

- **NIScope 2chan time record.vi**

Samples both inputs of the USB-5133 NI digitizer (NIScope) with a user-specified record length, sampling rate, digital gain, coupling, etc. Optionally saves the time records to file with via a single-column technique to save memory (time increment and y values). Used for observation of mixer output while adjusting phase for linear system response.

- **NIScope PSD v8.vi**

Principle PSD acquisition tool. State machine design that has been iterated many times in the interest of speed and efficiency. Acquires time records via user-specified parameters, calculates PSD (in both one-shot and averaging modes), optionally averages PSDs for specified number of averages and with weight and windowing. Writes files via single-column technique described above.

- **add freq list.vi**

Reconstructs two-column data file from saved PSD e.g. from 'NIScope PSD v8.vi'. User selects single-column data file and two-column data is written to new file.

- **PSD analysis align count.vi**

Manual PSD peak identification and analysis program. User specifies some parameters for scanning through the data and for notating files as they are saved to disk. Requires both driven and undriven PSDs to be previously saved and converted to two-column format via 'add freq list.vi'. This VI will open and read from those data files. Provides interface for fitting PSD data via user-defined Lorentzian function (see code) and least-squares routine, and also saving fit to file with data.

- **NW PSD analysis Auto slope TOP.vi**

Not the most elegant naming convention, but this is the first implementation of automated peak identification, fitting, and saving to file. User specifies a portion of the PSD to begin and the files are read sequentially, fitting and saving along the way. Parameters used for peak classification are user-specified on Front Panel and are based on trial and error. Peak is classified by observing drive PSD with 'peak points' consecutive data points that are ( $\text{'threshold'} \times \text{rolling-}'N \text{ avg'-datapoints-standard-deviation-of-linear-background-fit}$ ) away from rolling- $'N \text{ avg'-datapoints-linear background-fit}$ . Some of these values then get passed into the fitting algorithm as starting parameters. This VI has miles of room for

improvement but certainly provided a much-needed boost in productivity.

- **NIScope lockin dual FG.vi**

Software replication of lock-in amplifier capabilities of e.g. the SRS830 or 844. Has many of the same controls, and labeled as such. Records data in forward/backward sweeping passes (in addition to averaging) in order to have a saved record in case of crash. Also saves information from temperature controllers and sensors. Data acquisition parameters are set via the same NIScope controls as many other VIs. Capable of interfacing with SRS DS345 function generator or Rigol DG5000 function generator via Front Panel selection.

- **SRS lockin multi scan stdev.vi**

Very similar to previous VI except intended for use with SRS 844 high frequency lock-in amplifier. Slightly less control over hardware in this one. Requires some data acquisition parameters e.g. time constant to be set manually on the 844 front panel.

## Appendix I

### Additional Ensemble Data

Figure I.1: Additional GaN nanowire ensemble data showing all measured resonance frequencies over a range of temperatures from 12 – 325 K. Data points are the result of individual peak fits from an ensemble PSD measurement at each temperature. The resonances in this experiment are observed to span the range of approximately 600 kHz to 3 MHz. The higher-temperature data (red) is acquired after the introduction of new data acquisition hardware, enabling us to observe higher-frequency resonances. We can see, however, that the majority of the frequencies are below the 2 MHz level. Recalling that the overall changes observed are of order 1 %, no obvious temperature dependence is visible at this scale. These data are not connected; in order to observe the behavior of a single resonance mode, we must reconstruct that data by hand. The plot contains on the order of 5,000 data points.

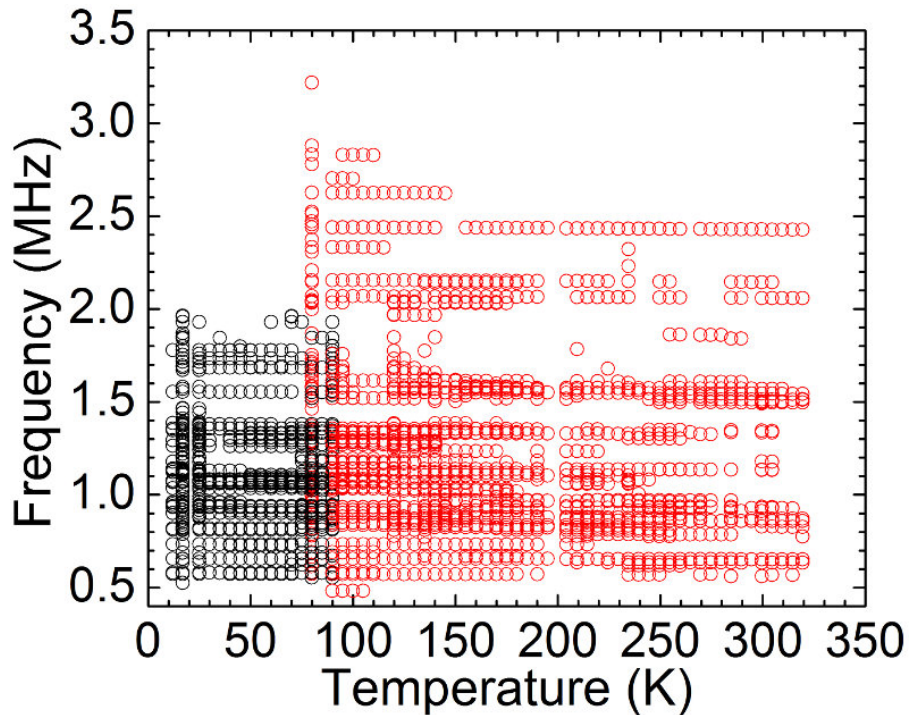


Figure I.2: Additional GaN nanowire ensemble data showing all measured  $Q$  factors over a range of temperatures from 12 – 325 K. Data points are the result of individual peak fits from an ensemble PSD measurement at each temperature. The  $Q$  factors in this experiment are observed to span the range of approximately  $10^3$  – mid- $10^5$ . A few data points are at or above  $Q = 10^6$ , but do not have sufficient resolution to justify any strong statements. The higher-temperature data (red) is acquired after the introduction of new data acquisition hardware, enabling us to observe higher-frequency resonances. Though the collection of  $Q$  factors cover an order of magnitude at each temperature, the overall behavior of the ensemble is quite consistent. These data are not connected; in order to observe the behavior of a single resonance mode, we must reconstruct that data by hand. The plot contains on the order of 5,000 data points.

